LOCAL AND REMOTE DRIVERS OF GREENLAND ICE SHEET SURFACE MASS LOSS UNDER ARCTIC AMPLIFICATION

by

JONATHON R. PREECE

(Under the Direction of Thomas L. Mote)

ABSTRACT

The rapidly melting Greenland Ice Sheet (GrIS) has been one of the most visible changes in the climate system during the current era of global warming. An extensive body of work links the abrupt increase in meltwater runoff to a shift in summer atmospheric circulation, characterized by more frequent and intense bouts of Greenland blocking. While these stalled circulation patterns and the persistent, anomalous weather conditions that follow have clearly played a leading role in driving recent GrIS surface mass balance trends, the precise mechanisms by which blocking encourages melt are still an active area of research. Moreover, there is no consensus on why summer Greenland blocking has increased in recent decades. The timing of the change, set against a backdrop of amplified Arctic warming, has naturally sparked questions regarding whether it may be a dynamical response to anthropogenic climate change that should be expected to continue.

This dissertation investigates the drivers of GrIS surface mass loss within the context of amplified Arctic warming. First, this research provides a more comprehensive look at the mechanisms by which blocking promotes GrIS melt by identifying

common Greenland blocking patterns and considering spatiotemporal differences in the synoptic-scale forcing of GrIS surface conditions between them. This analysis demonstrates that more frequent high-amplitude Omega blocking patterns have promoted melt of the northern GrIS by generating above-normal downwelling longwave radiation and enhanced sensible heat flux in the region. Next, this work investigates remote forcing of summer atmospheric circulation over Greenland, revealing two potentially synergistic mechanisms by which amplified Arctic warming favors Greenland blocking: (1) Disproportionate high-latitude warming promotes wavier atmospheric circulation over the North Atlantic—conditions that are conducive to the formation of blocking anticyclones. (2) Low spring North American snow cover generates a stationary Rossby wave response that favors anticyclonic conditions over Greenland. Through regional climate modeling, this work then estimates the contribution of the change in local thermodynamic background conditions to observed GrIS surface mass loss. The results demonstrate that surface mass loss would have been reduced by $\sim$62% had the recent dynamical forcing of the GrIS occurred in a preindustrial climate.

INDEX WORDS: [Climatology, Greenland Ice Sheet, Regional Climate Models, Climate Change, Cryosphere, Snow Cover, Artificial Neural Networks]

Local and Remote Drivers of Greenland Ice Sheet Surface Mass Loss Under Arctic Amplification

by

Jonathon R. Preece

B.S., University of Utah, 2014

M.A., University of Wyoming, 2018

A Dissertation Submitted to the Graduate Faculty of the
University of Georgia in Partial Fulfillment of the Requirements for the Degree.

Doctor of Philosophy

Athens, Georgia

2022

©2022

Jonathon R. Preece

All Rights Reserved

Local and Remote Drivers of Greenland Ice Sheet Surface Mass Loss Under Arctic Amplification

by

Jonathon R. Preece

Major Professor: Thomas L. Mote

Committee: Andrew J. Grundstein
John A. Knox
Gabriel J. Kooperman

Electronic Version Approved:

Ron Walcott
Vice Provost for Graduate Education and Dean of the Graduate School
The University of Georgia
December 2022

ACKNOWLEDGMENTS

There is no doubt that I would not have realized this achievement without the help of the many that I have been so fortunate to forge relationships with along the way. First, I want to thank my family. Their unwavering support and emphasis on the value of an education has been the foundation of my success. I owe a special debt of gratitude to my siblings, Chris and Jill, for successfully completing their undergraduate education, and to my brother Russell, who demonstrated what was possible by becoming the first in my family to obtain a graduate degree. I developed a deep admiration for their accomplishments at an early age and their example has been a sustained source of motivation that has propelled me to where I am now.

It is hard to believe the extent to which each stage of my postgraduate education has been tailored to my needs in a way that has maximized my chances at success. As a diffident master's student, I was fortunate to land under the advisement of Dr. J. J. Shinker at the University of Wyoming. I could not imagine a better mentor to build confidence in my academic abilities while also providing a strong motivation to embark on my doctoral studies by demonstrating just how fulfilling a career in academia can be. For that, I will never be able to repay her. Thank you also to Dr. Gerald Webster for expressing his belief in me and my academic potential, and to the self-proclaimed "accidental PhD," Dr. William Gribb, for sharing his story, which resonated with me so.

Upon leaving the University of Wyoming, I was thrilled to join the Department of Geography at the University of Georgia, as I had learned of its reputation for cultivating a supportive environment. That reputation was confirmed in each of my interactions with department faculty and fellow graduate students. I want to share a particular note of thanks to my advisory committee. Thank you to Dr. John Knox for all your invaluable advice and for being an exemplar of what it is to truly inspire through teaching, to Dr. Andy Grundstein for your unique perspective and for being an advocate for my success, and to Dr. Gabe Kooperman, who not only provided critical guidance for my dissertation research but also crafted and taught one of the most practical and experientially rich courses of my graduate studies. I am also grateful to my lab mates for a camaraderie that is defined by an unwavering willingness to lend a hand, even from those who have moved on to the next stages of their careers.

Finally, nobody has embodied the culture of support within the department more than my advisor, Dr. Thomas Mote. Equipped with a renewed motivation and sense of self-efficacy from my time at the University of Wyoming, I was privileged to work with Dr. Mote as he provided endless opportunities to apply these virtues to a new frontier in my personal growth. Whether it be through collaborations with outside institutions or numerous workshops and conferences, he approached it all with wholehearted encouragement and a focus on my professional development. Thank you, Dr. Mote, for treating all your advisees not just as students, but as equal colleagues and friends.

CONTENTS

Acknowledgments **iv**

List of Figures **vii**

List of Tables **xxiii**

1 Introduction **1**

1.1 Greenland Ice Sheet Mass Loss in a Rapidly Warming Arctic 1

1.2 Local Thermodynamic Forcing of Accelerated GrIS Runoff 3

1.3 Dynamical Forcing of GrIS SMB and its Potential Remote Origins . . 5

1.4 Study Motivation and Objectives 16

2 Summer Greenland Blocking Diversity and its Impact on the Surface Mass Balance of the Greenland Ice Sheet **21**

2.1 Introduction 23

2.2 Data and Methods 26

2.3 Results 30

2.4 Discussion and Conclusions 50

3 Summer Atmospheric Circulation Over Greenland in Response to Arctic Amplification and Diminished Spring Snow Cover **68**

3.1 Introduction 70

3.2 Results 73
3.3 Discussion 93
3.4 Data and Methods 97

4 Estimating the Thermodynamic Contribution to Recent Greenland Ice Sheet Surface Mass Loss **107**

4.1 Introduction 109
4.2 Experimental Design 114
4.3 Results 123
4.4 Discussion 144

5 Conclusion **151**

Bibliography **158**

LIST OF FIGURES

1.1 Cumulative anomaly of total GrIS mass balance as well as the individual contributions of SMB and ice dynamics as color-coded in the legend to the bottom-left. SMB anomalies calculated with respect to a 1980–1990 reference period. Shading indicates the 1σ uncertainty for each time series. Right axis shows the equivalent sea-level contribution for a given amount of mass change (left axis). Figure reprinted by permission from Springer Nature: Nature, IMBIE Team (2020), © 2020. 2

1.2 November atmospheric response to low sea ice in the region stretching between the Barents and East Siberian seas as simulated by an atmospheric general circulation model. All quantities shown represent the difference in simulated conditions between model runs with light and heavy prescribed sea ice concentrations. (a) Vertical cross-section showing the geopotential height differences [m] (shading and contours) and associated wave activity flux [$m^2 s^{-2}$] (vectors). (b) Difference in turbulent heat flux (shading in [Wm^{-2}]). Vectors show horizontal component of the associated wave activity flux; contours show the vertical component. Figure reprinted from Honda et al. (2009), with permission granted by the American Geophysical Union usage permissions policy: https://www.agu.org/Publish-with-AGU/Publish/Author-Resources/Policies/Permission-policy. 9

1.3 September atmospheric response in years of low spring snow cover over Eurasia. Contours show difference in monthly 300 hPa geopotential height at a 20 m interval for early minus late snow cover years during a study period of 1986–2004. Light and dark shading indicate significant differences at $\alpha = 0.10$ and $\alpha = 0.05$ respectively. Vectors indicate the horizontal component of the associated wave activity flux. Figure reprinted from Matsumura and Yamazaki (2012), © American Meteorological Society. Used with permission. 12

1.4 Comparison of GCM-simulated and observed trends in Greenland blocking. As indicated by the legend, observed trends are obtained from NCEP/NCAR Reanalysis 1 (NCEP-NCARv1), NOAA 20th Century Reanalysis Version 2c (20CRv2c), and ERA 20th Century Reanalysis (ERA-20C), while GCM projections are obtained from an ensemble of RCP4.5 and RCP8.5 CMIP5 simulations. Figure reprinted from Hanna et al. (2018a), with permission granted by the Creative Commons Attribution 4.0 License 17

1.5 Comparison of observed and GCM-projected contributions to sea level rise by the Antarctic and Greenland ice sheets combined, as well as broken down by the dynamic and SMB contributions for each ice sheet separately. Observed values (black) are based on estimates from the IMBIE Team (IMBIE Team, 2018, 2020). GCM projections are broken down into the 95th (maroon), 50th (orange), and 5th (yellow) percentile of simulations from the IPCC Fifth Assessment Report. The range included with each data point indicates 1 standard deviation about the average annual rate. Figure reprinted by permission from Springer Nature: Nature Climate Change, Slater et al. (2020), © 2020. 18

2.1 Composite-anomaly maps for all JJA GBI-PH03 overlap blocking episode days. (Continued on the following page.) 33

2.2 Composite anomalies (shading) and composite means (contours; 60 m interval) of Z500 during JJA blocking episode days assigned to each SOM node. The frequency of each node with respect to all blocking episode days is displayed in the upper-left corner. Map outlines indicate subjective groupings: Omega (dark blue), CWB (medium blue), or SR (light blue). Inset maps show MEaSUREs surface melt frequency for each node less the 1981–2010 mean JJA melt frequency. Elevation contours as in Figure 1. 35

2.3 Chord diagram of SOM node transitions. Nodes labeled radially along outside of diagram. Outer bar denotes total number of daily transitions into and out of a node as indicated by the axes. Inner bar denotes the proportion of total transitions that are outgoing. Arcs point from origin to destination nodes for paths in the top quartile of transition frequency for each node. Arc width indicates the number of transitions along a given path. 37

2.4 Anomalous SWD composited by SOM BMU. Stippling indicates significant ($\alpha = 0.05$) differences between days assigned to a given node and 1981–2010 JJA conditions. Map outlines as in Figure 2. Elevation contours as in Figure 1. 41

2.5 Anomalous LWD composited by SOM BMU. Map outlines as in Figure 2. Elevation contours as in Figure 1. Stippling as in Figure 4. 42

2.6 Magnitude (shading) and direction (vectors) of IVT composited by SOM BMU. IVT calculated from eastward and northward components of ERA5 vertical integral of water vapor flux. Vectors shown for $\geq 40\ kg\ m^{-1}\ s^{-1}$. Map outlines as in Figure 2. Stippling as in Figure 4. 44

2.7 Anomalous SHF composited by SOM BMU. Map outlines as in Figure 2. Elevation contours as in Figure 1. Stippling as in Figure 4. . . 45

2.8 Anomalous SMB composited by SOM BMU. Map outlines as in Figure 2. Elevation contours as in Figure 1. Stippling as in Figure 4. 47

2.9 Composite-anomaly ME for each SOM node less the composite anomaly for all blocking episode days. Stippling indicates significant ($\alpha = 0.05$) differences between each node and all other blocking episode days. Map outlines as in Figure 2. Elevation contours as in Figure 1. 48

3.1 Maps illustrating the synoptic setting and S_{ag} parameters for (a) a case of low S_{ag} occurring August 16, 2001, and (b) a case of high S_{ag} occurring July 11, 2012. The value of S_{ag} as well as the sinuosity of each individual isohypse is listed to the right of each map. For each case, the calculation for the isohypse of maximum sinuosity (blue line) is shown as an example, where the blue shading shows the area used to calculate the equivalent latitude (red dashed line). Dashed gray lines show the longitude boundaries of the regional domain. 74

3.2 Temporal comparison of spring SCE and summer circulation over Greenland. (a) Timeseries of JJA S_{ag} (orange), GBI (gray), and PH03 (blue) plotted alongside June Northern Hemisphere SCE (green). Dashed lines show raw data. Solid lines show 5-year running means. (b) Correlation matrix comparing each of the raw timeseries in (a). White numbering presents the correlation coefficient for each variable pair and color shading corresponds to the strength of correlation . . 75

3.3 Daily standardized values of S_{ag} plotted against the corresponding standardized values of the GBI. Dashed line marks the 1:1 line. Solid line shows the linear best-fit line. Data points are color-coded according to the corresponding monthly value of the principal-component-based NAO (Hurrell et al., 2003) as shown in the color bar to the right. The associated Pearson's correlation coefficient (r) is provided in the upper-left corner. 76

3.4 Moving linear trends for (a) 500 hPa sinuosity, (b) 850 hPa meridional temperature gradient, and (c) 500 hPa zonal wind. For each latitude along the y-axis, the shading indicates the linear trend from the start year indicated on the x-axis through the end of the study period (i.e., 2019). All quantities calculated for the North Atlantic domain (0–90°W). Stippling indicates significance at $\alpha = 0.05$. 78

3.5 Lagged correlation plots relating (column a) June, (column b) July, and (column c) August atmospheric circulation over Greenland to antecedent monthly SCE area over (row d) the Northern Hemisphere, (row e) Eurasia, and (row f) North America. The color-coded bars in each panel document the correlation coefficient relating PH03 (blue), GBI (black), and S_{ag} (orange) measured during the summer month labeled at the top of each column to lagged monthly SCE area as noted along the x-axis. Likewise, triangles note the correlation between the principal-component-based NAO (Hurrell et al., 2003) and lagged monthly SCE area. Filled bars and bold triangles indicate statistical significance at $\alpha = 0.05$. 80

3.6 Stationary Rossby wave response to low North American SCE. (a) Anomalies of July Z300 regressed against inverted May North American SCE (contours: solid, positive; dashed, negative) presented alongside the 300 hPa horizontal component (vectors) and average 850–150 hPa vertical component (shading) of the associated WAF. Stippling (crosshatching) indicates horizontal divergence (convergence) of the Z300 WAF exceeding $\pm 10^{-7}\, m\, s^2$ (b) Vertical cross-section along the thick gray line in (a), where vectors indicate WAF, shading indicates the geopotential height anomaly, and solid (dashed) white contours indicate WAF divergence (convergence). Contour interval: $10^{-7}\, m\, s^2$, zero contour omitted. The horizontal component of the vectors in (b) is 100 times that of the vertical component. 83

3.7 North American SCE variability as measured by the NOAA SCE CDR and its relationship with Greenland blocking. Panels a–c show the 1979–2019 frequency of weekly snow cover at each grid point during (a) May, (b) June, and (c) July. Panel (d) presents grid point Pearson correlation coefficients relating the total number of weeks with snow cover from April to June of each year and the monthly mean GBI for the following July. Note that negative values are shaded red to reflect an increase in blocking associated with a decrease in snow cover duration. Stippling indicates statistical significance at the 95% confidence level. 86

3.8 North American surface conditions following low spring SCE. Anomalies of ERA5 (column a) volumetric soil water to a depth of 28 cm and (column b) 2 m air temperature obtained from a linear regression of (row c) May, (row d) June, and (row e) July surface variables against inverted and standardized May North American SCE area. Stippling indicates significance at the 95% confidence level. 88

3.9 Vertical cross-section of the average 40–60 °N anomalous eddy geopotential height (shading) obtained from a linear regression against standardized, inverted May North American SCE area. The –2, 0, and 2 hPa isopleths are shown in black to more clearly visualize the vertical structure of the eddy height anomalies. Vectors show the meridional average of the associated WAF. 89

3.10 GrIS surface conditions in July following low spring SCE. (Continued on following page.) 91

3.11 Illustration of the link between North American snow cover and atmospheric circulation over Greenland. Low spring snow cover causes early depletion of soil moisture over eastern North America (brown shading). The dry conditions that follow produce a warm surface anomaly that persists into July (orange shading). This anomalous heating of the near-surface atmosphere induces a stationary Rossby wave response that propagates northeastward (yellow arrow) and favors high-pressure ridging over Greenland—conditions which augment melt of the Greenland Ice Sheet (blue shading) 95

4.1 Model diagram illustrating the design of the control run (gray outlines) pseudo-global warming experiments (blue outlines). 116

4.2 Climate change perturbation fields for surface air temperature (top row) and specific humidity (bottom row) shown for a selection of months equally spaced throughout the year as labeled at the top of each panel. Perturbation fields shown for the lowermost model level after vertically interpolating to the same ECMWF L137 hybrid sigma-pressure levels as the ERA5 boundary conditions. Contour interval: 500 m. Range: 1000–3000 m. 118
4.3 Comparison of observed sea ice concentration on June 15, 2018 (shading) and the corresponding CESM-LE climate perturbation signal (contours, 5% interval). 119
4.4 Change in sea-surface conditions around Greenland. Maps show the difference in SST (shading) and the location of the sea ice edge (black contours) between the prescribed 1880–1899 Hadley-OI fields used in the PGW experiments and the 2000–2019 ERA5 sea-surface conditions used in the control. Differences are shown for a selection of months equally spaced throughout the year as labeled at the top of each panel. Positive values (red shading) indicate warmer SST during the preindustrial period than during the control. Solid contour demarcates the sea ice edge for the control period, dashed for the preindustrial period. Sea ice edge is defined using a threshold of $\geq 50\%$ SIC. 121

4.5 Temporal evolution of the GrIS SMB under contrasting thermodynamic background conditions. Shown are the cumulative SMB anomaly time series for the control (gray), PGW1 (blue dashed), and PGW2 (green dashed) simulations. Anomalies calculated with respect to the 1980-1989 reference period. Left axis shows cumulative SMB anomaly; right axis shows the equivalent sea-level contribution. Annotations detail the difference in the final cumulative SMB between each of the PGW simulations and the control. 124

4.6 Spatial distribution of GrIS SMB change under contrasting thermodynamic background conditions. (a) The observed cumulative SMB over the full study period of 2000–2019 as represented by the control simulation. (b) PGW1 cumulative SMB minus the control. (c) PGW2 cumulative SMB minus the control. Contour interval: 500 m. Range: 1000–3000 m. 125

4.7 Seasonal evolution of GrIS SMB under contrasting thermodynamic background conditions. (Continued on following page.) 127

4.8 The SEB of the GrIS under contrasting thermodynamic background conditions. (Continued on following page.) 130

4.9 Melt season katabatic wind field under contrasting thermodynamic background conditions. (a) 2000–2019 long-term mean May–Sep 10 m wind speed (shading) and direction (vectors). (b) Difference in 10 m wind speed between PGW1 and the control. (c) Difference in the 10 m wind speed between PGW2 and the control. $\Delta = PGW - Control$. Contour interval: 500 m. Range: 1000–3000 m. 132

4.10 Thermodynamic mechanisms of GrIS SMB change. (Continued on following page.) 134

4.11 The impact of thermodynamic change on GrIS melt timing. The observed median date of (a) melt onset, (b) freeze onset and (c) median melt season duration for the control simulation alongside (d–f) the difference between the PGW simulations (PGW1, left; PGW2, right) and the control ($\Delta = PGW - Control$) for each metric as organized by row and labeled on the left. Contour interval: 500 m. Range: 1000–3000 m. 137

4.12 Thermodynamic contribution to surface mass loss during years of exceptional GrIS melt. Panels show (a, e) the cumulative SMB anomaly spanning the Sep–Aug hydrological year alongside (b, f) meltwater runoff, (c, g) average daily near-surface air temperature anomaly, and (d, h) integrated water vapor anomaly during the exceptional melt years of (a–d) 2012 and (e–h) 2019. In all panels, time series are presented for the control (gray), PGW1 (blue dashed), and PGW2 (green dashed) simulations. Bottom portion of b–d and f–h shows the difference between each PGW simulation (PGW1, blue; PGW2, green) and the control ($\Delta = PGW - Control$). Red vertical shading highlights periods of strong synoptic-scale forcing. Anomalies calculated with respect to the entire 2000–2019 study period. Cumulative anomalies calculated with respect to the 1980–1989 reference period. 140

4.13 Comparison of GrIS melt frequency between PGW simulations during years of exceptional GrIS surface mass loss. (a, c) The number of days in which the control simulation indicated $\geq$5 mm melt in a given grid cell and (b, d) the difference between the PGW simulations and the control (PGW1, left; PGW2, right) for the exceptional melt years of (a, b) 2012 and (c, d) 2019. $\Delta = PGW - Control$ Contour interval: 500 m. Range: 1000–3000 m. 143

5.1 The change in conditions accompanying the recent GrIS SMB decline. Panels show the difference in the 1991–2017 summer (A) 500 hPa geopotential height (contours), winds (vectors), and mid-tropospheric cloud cover, (B) downward shortwave radiation, and (C) downward longwave radiation relative to that of 1958–1990. The annotations in panel (C) note the change in 2 m temperature for each of the sectors illustrated by the gray outlines. Figure reprinted from Noël et al. (2019), with permission granted by the Creative Commons Attribution 4.0 License 153

LIST OF SUPPLEMENTARY FIGURES

2.1 Integration domain for the MARv3.11 output utilized in the analysis. . 56
2.2 All instances of large-scale blocking as identified by PH03 (blue), GBI (red), and GBI-Z (black) from 1979–2019. Gray shading marks GBI-PH03 overlap blocking episodes. 57
2.3 5-day lead-lag of composite-anomaly (shading) and composite-mean (contour with interval of 60 m) 500 hPa geopotential height for GBI-PH03 overlap blocking episodes. Lags noted at top of each plot are with respect to the first day of overlap between PH03 and GBI for each event. Teal polygon delineates the GBI domain. 58
2.4 Composite anomalies (shading) and composite means (contours: 60m interval) of 500 hPa geopotential height for all JJA blocking episode days identified using a blocking episode duration criterion of (a) 6 days and (b) 8 days. Anomalies were calculated with respect to the 1981–2010 long-term daily mean and values were composited by SOM BMU. 59

2.5 Composite anomalies (shading) potential temperature at 2 PVU for all blocking event days identified separately by PH03 and GBI and composited by SOM BMU. The percentage of all days assigned to each node that were identified by the GBI (PH03) is displayed in black (red) in the upper left (right) corner of each map. Map outline colors are as in Figure 2. 60

2.6 Left: Composite anomalies (shading) and composite means (contours: 60 m interval) of 500 hPa geopotential height for all JJA blocking episode days identified by GBI (top row) and PH03 (bottom row). Values were composited according to each day's BMU for SOMs conducted separately for each blocking index. The frequency of each node with respect to all blocking episode days identified by each index is displayed in the upper right corner. Right: Chord diagrams illustrating the transitions between nodes for each SOM (symbolized as in Figure 3). 61

2.7 Anomalous snowfall (SF) composited by SOM node. Contours denote MAR elevation data. Contour interval of 500 m from 1000–3000 m. Stippling indicates significant difference between days assigned to given node and 1981–2010 JJA conditions at 95% confidence level. 62

2.8 Anomalous rainfall (RF) composited by SOM node. contours denote MAR elevation data. Contour interval of 500 m from 1000–3000 m. Stippling indicates significant difference between days assigned to given node and 1981–2010 JJA conditions at 95% confidence level. 63

2.9 Anomalous meltwater production (ME) composited by SOM node. Contours denote MAR elevation data. Contour interval of 500 m from 1000–3000 m. Stippling indicates significant difference between days assigned to given node and 1981–2010 JJA conditions at 95% confidence level. 64

2.10 Number of blocking episode days per year (bars) and long-term linear trends (red lines) for each blocking type (columns) during JJA and for each month individually (rows). Shading indicates 95% confidence level for the best-fit lines. The Pearson's correlation coefficient (R), slope, and p-value (P) of the linear models are annotated in the upper-left corner of each panel. 65

2.11 Anomalous surface albedo (AL2) composited by SOM node. contours denote MAR elevation data. Contour interval of 500 m from 1000–3000 m. Stippling indicates significant difference between days assigned to given node and 1981–2010 JJA conditions at 95% confidence level. 66

2.12 Anomalous absorbed shortwave (SWnet) composited by SOM node. contours denote MAR elevation data. Contour interval of 500 m from 1000–3000 m. Stippling indicates significant difference between days assigned to given node and 1981–2010 JJA conditions at 95% confidence level. 67

3.1 Climatology of Northern Hemisphere Z500 for (a) all days (b) JJA days during the 1979–2019 study period. Boxplots summarize daily zonal means grouped into 5° latitudinal bins spanning the midlatitudes as labeled along the x-axis. Dashed horizontal lines mark aggregate sinuosity isohypse values used in Vavrus et al. (2017). Solid green horizontal lines in (b) mark JJA S_{ag} isohypses used here. 104

3.2 A representation of the two blocking detection methods employed herein. The red dashed line shows the sampling area of the GBI. Solid blue lines show PH03 parameters. 105

4.1 Comparison of individual SMB terms between the PGW simulations and the control. (Continued on following page.) 149

LIST OF SUPPLEMENTARY TABLES

3.1 Long-term (1979–2019) seasonal trends in the mean and select percentiles of S_{ag}. Percentiles computed from daily S_{ag} for each season and year. 106

CHAPTER 1

INTRODUCTION

1.1 Greenland Ice Sheet Mass Loss in a Rapidly Warming Arctic

The Arctic has undergone drastic change in conjunction with a recent acceleration of warming at high latitudes. Since 1979, annual mean surface air temperature in the Arctic has warmed at approximately four times the rate of the global average (Rantanen et al., 2022). This pronounced warming at high latitudes, known as Arctic amplification (AA), is inseparably linked to a rapidly changing cryosphere. As both a manifestation of, as well as a contributor to, rising temperatures, observations have displayed marked reductions in sea ice and even more dramatic losses in spring snow cover (Cohen et al., 2014; Derksen & Brown, 2012; Pithan & Mauritsen, 2014; Stroeve & Notz, 2018).

Widespread thawing at high latitudes has also impacted the Greenland Ice Sheet (GrIS), where the consequences of AA have been especially apparent since the turn of the century—since the early 1970s, the GrIS has transitioned from a state of near-neutral mass balance, that persisted into the 1990s, to a state of consistent mass loss (Figure 1.1) (IMBIE Team, 2020; Mouginot et al., 2019). The

status of the GrIS has several globally relevant implications: According to recent estimates, GrIS mass flux to the ocean has accounted for over 10 mm of sea-level rise since 1972 (Figure 1.1) (IMBIE Team, 2020; Mouginot et al., 2019), and complete melt of the ice sheet would provide enough runoff to raise sea level by over 7 meters (Aschwanden et al., 2019). Freshwater from the ice sheet has the potential to weaken thermohaline circulation and thus the poleward transport of relatively warm water in the North Atlantic (Fichefet et al., 2003). Lastly, freshwater runoff from the GrIS has been shown to increase primary production, thus modulating the exchange of carbon between the ocean and atmosphere (Arrigo et al., 2017; Oliver et al., 2018). Given these far-reaching impacts, there is a clear impetus to understand the physical mechanisms that govern GrIS mass balance.

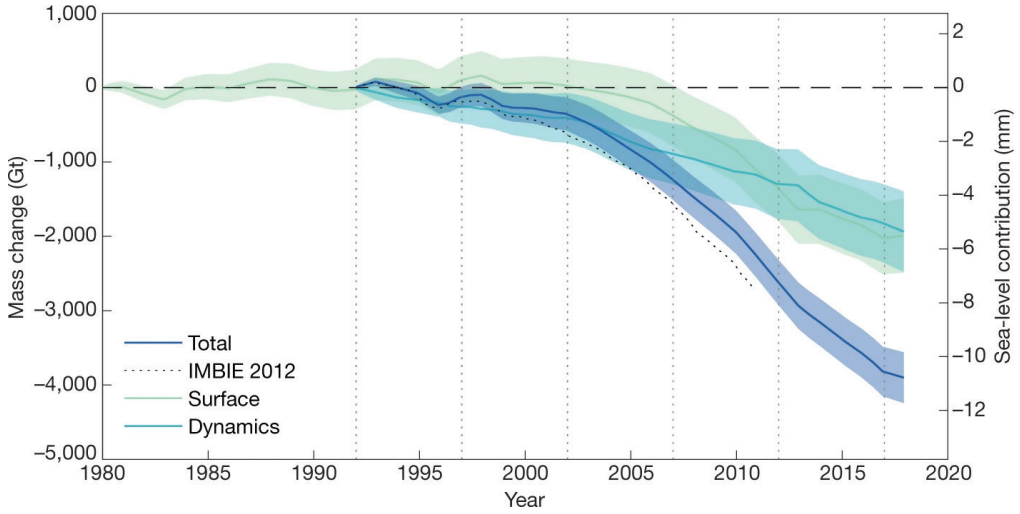


Figure 1.1: Cumulative anomaly of total GrIS mass balance as well as the individual contributions of SMB and ice dynamics as color-coded in the legend to the bottom-left. SMB anomalies calculated with respect to a 1980–1990 reference period. Shading indicates the 1σ uncertainty for each time series. Right axis shows the equivalent sea-level contribution for a given amount of mass change (left axis). Figure reprinted by permission from Springer Nature: Nature, IMBIE Team (2020), © 2020.

The total mass balance of the GrIS is the sum of contributions from 1) dynamic loss, which occurs as ice discharge from marine terminating glaciers; and 2) the surface mass balance (SMB), which is primarily the difference between snow

accumulation and the portion of surface melt that exits the ice sheet as runoff. Both these components have contributed to the shift to persistently negative annual mass balance over the past two decades (Figure 1.1)(van den Broeke et al., 2009a). At the start of the 21st Century, declining sea ice and warm ocean waters caused calving fronts to recede, in turn, reducing glacial back stress, which resulted in the acceleration of ice discharge (Hanna et al., 2009; Joughin et al., 2008; Khan et al., 2014; Mouginot et al., 2019; Rignot & Kanagaratnam, 2006). Over the same time period, cumulative SMB anomalies have become increasingly negative due to a pronounced acceleration of surface melt (Hanna et al., 2014; IMBIE Team, 2020; Mote, 2007; Mouginot et al., 2019; Tedesco et al., 2016; van den Broeke et al., 2009a). In fact, the decline in SMB has outpaced the surge in ice discharge, with surface melt superseding dynamic loss as the majority source of total GrIS mass loss around the turn of the century (Mouginot et al., 2019).

1.2 Local Thermodynamic Forcing of Accelerated GrIS Runoff

A portion the observed trend in GrIS surface melt can be attributed to increasing background temperatures (Hanna et al., 2008; Rajewicz & Marshall, 2014). The rapid decline in SMB over just the past two decades is reflective of the nonlinear relationship between air temperature and surface melt that arises as a consequence of multiple positive radiative feedbacks that operate locally within the Arctic (Pithan & Mauritsen, 2014; Serreze & Barry, 2011; Trusel et al., 2018). Perhaps the most well-established of these is the ice-albedo feedback, which describes how enhanced melt due to increasing temperatures acts to decrease surface albedo—either by uncovering the more absorptive underlying land surface, sea surface, or

glacial ice, or by lowering the albedo of the snow itself—all of which promote further warming and melt (Box et al., 2012; Serreze & Barry, 2011; Tedesco et al., 2011).

Not only is the ice-albedo feedback evident in the retreat of snow and sea ice cover, and thus rising temperatures, throughout the arctic (Serreze & Barry, 2011), but it has also played a key role in more directly augmenting melt of the GrIS. Over sub-annual timescales, early melt onset combined with low snow accumulation has conditioned the ice sheet for sustained melt during years of exceptional GrIS surface runoff (Box et al., 2012; Tedesco et al., 2011; Tedesco & Fettweis, 2020; Tedesco et al., 2016). Over the long term, an expansion of the low-albedo ablation zone has caused a disproportionate increase in runoff from the most northern portions of the ice sheet (Noël et al., 2019).

In addition to the ice-albedo feedback, reductions in sea ice can also contribute to elevated temperatures in the lower troposphere through the water vapor feedback. Higher air temperature allows for increased atmospheric water vapor—a greenhouse gas—which results in greater downwelling longwave radiation and, consequently further warming at the surface (Pithan & Mauritsen, 2014). While this feedback mechanism is active as a global response to a warming atmosphere, the increase in atmospheric humidity can be regionally exacerbated by reductions in sea ice cover (Screen et al., 2013). Thus, there is the potential for local advection of moist marine air from the seas surrounding Greenland to encourage GrIS surface melt, and previous work has yielded statistical evidence of such a relationship (Pedersen & Christensen, 2019; Rennermalm et al., 2009; Stroeve et al., 2017). However, in apparent contradiction to these results, investigations of this same question using regional climate models have demonstrated low GrIS sensitivity to local sea surface conditions, as ubiquitous katabatic winds originating over the ice sheet's interior inhibit onshore flow from the adjacent marine layer (Hanna et al., 2009; Hanna et al., 2014; Noël et al., 2014).

1.3 Dynamical Forcing of GrIS SMB and its Potential Remote Origins

While increasing background temperatures have undoubtedly contributed to the increase in GrIS surface runoff, several studies have pointed to recent behavior of the summer North Atlantic Oscillation (NAO) and its correspondence with GrIS SMB as being suggestive of a potential dynamical feedback between AA and atmospheric circulation that may play a key role in influencing total mass balance response (Bevis et al., 2019; Fettweis et al., 2013; Liu et al., 2016; Mote, 1998; Trusel et al., 2018; van Angelen et al., 2014). Specifically, observations have revealed a greater incidence of negative summer NAO conditions since the start of the century (Bevis et al., 2019; Fettweis et al., 2013; van Angelen et al., 2014). This period of predominately negative summer NAO has been characterized by more frequent high-amplitude, quasi-stationary planetary wave configurations, known as atmospheric blocks, that have promoted the recent upswing in surface melt via greater insolation, anomalously warm surface temperatures, reduced surface albedo, and strong advection of warm, moist air from lower latitudes (Hanna et al., 2014; Hofer et al., 2017; Liu & Barnes, 2015; Mattingly et al., 2018; McLeod & Mote, 2016; Neff et al., 2014; Tedesco & Fettweis, 2020; Tedesco et al., 2016). Indeed, this shift in summer atmospheric circulation over Greenland has been recognized as the dominant source of accelerated mass loss in recent decades (Delhasse et al., 2018; Fettweis et al., 2013; Rajewicz & Marshall, 2014). The timing of this dynamical change and its connection to GrIS SMB raises the question of how AA may be influencing atmospheric circulation over Greenland and throughout the Northern Hemisphere more generally.

1.3.1 Atmospheric Response to Arctic Amplification: A shift to more persistent weather?

At the hemispheric scale, AA weakens the meridional near-surface temperature gradient which, as dictated by the thermal wind equation, should translate to reduced westerlies aloft (Cohen et al., 2014; Francis & Vavrus, 2012). Indeed, modeling efforts (Cvijanovic & Caldeira, 2015; Deser et al., 2015; Vavrus et al., 2017) and observation-based analyses (Coumou et al., 2015; Francis & Vavrus, 2012, 2015; Vavrus et al., 2017) have shown reductions in upper-level westerlies accompanying weaker temperature gradients in the mid-latitudes. It has been proposed that the reduction in the zonal flow has resulted in a wavier jet, which has consequently led to more persistent, high-amplitude weather patterns (Cohen et al., 2014; Francis & Vavrus, 2012), such as the blocking events that have promoted melt of the GrIS (McLeod & Mote, 2016; Neff et al., 2014; Tedesco et al., 2016). In rebuttal, others have argued that early results indicating a positive trend in wave amplitude were an artifact of methodology (Barnes, 2013; Screen & Simmonds, 2013); however, several recent studies have confirmed a wavier circulation regime using various metrics (Cattiaux et al., 2016; Di Capua & Coumou, 2016; Vavrus et al., 2017), providing a more robust body of evidence in support of the proposed jet stream response to AA.

Additional theories of how AA may lead to more persistent, meridional circulation have been put forth, some of which may be more consequential in summer (Coumou et al., 2018). These theories focus on mechanisms that reduce the dispersion of Rossby wave energy, thus leading to amplification of the wave (Coumou et al., 2018, and references therein). One such mechanism is that enhanced heating of the continental landmasses relative to the Arctic Ocean in summer leads to the formation of an Arctic front jet that, together with the subtropical jet, acts as a

waveguide that encourages resonance between free and forced waves (Coumou et al., 2018).

Focusing on summer, Coumou et al. (2015) found a decline in phase speed for the wavenumber most frequently accompanied by synoptic disturbances—a finding that supports a shift to more persistent weather; however, contradicting the theoretical framework outlined above, the decline in phase speed was met by a reduction in wave amplitude. Subsequent work likewise found that summer geopotential height patterns have recently become less sinuous throughout the Northern Hemisphere as a whole, while conversely revealing an increase in sinuosity over North America, thus demonstrating strong regional variability in mid-latitude circulation trends (Di Capua & Coumou, 2016). Together these results indicate a summer trend toward a more pronounced quasi-stationary wave pattern upstream of Greenland (Di Capua & Coumou, 2016) accompanied by slower propagating transitory waves (Coumou et al., 2015)—conditions that may have favored the anomalous weather events that have facilitated accelerated GrIS surface melt since the turn of the century.

The regional diversity of atmospheric change under AA may be related to the spatiotemporal heterogeneity of surface cover response to rising temperatures. Recent research suggests that sea ice and snow cover have played an important role in driving both hemispheric and regional circulation trends at high latitudes via their commanding influence on the surface energy balance (SEB) (Bader et al., 2011; Cohen et al., 2014; Coumou et al., 2018). Hence, the locations of greatest sea ice and snow cover response to AA and their relation to the background state of the atmosphere may be an important factor in dictating regional and interannual differences in circulation response (Francis et al., 2017; Kidston et al., 2011; Overland & Wang, 2018).

1.3.2 Atmospheric Response to Sea Ice Variability

Sea ice affects the state of the atmosphere by altering surface albedo and acting as an insulator that suppresses sensible and latent heat fluxes from the underlying sea surface; although, the albedo effect is less impactful in winter when insolation is minimized across the high latitudes (Bader et al., 2011; Deser et al., 2000). In response to rising temperatures, the Arctic has experienced earlier melt onset and perennial reductions in sea ice extent (SIE) (Stroeve & Notz, 2018). These changes reduce surface albedo causing more incoming shortwave radiation to be absorbed by the sea surface, increasing SST, and delaying freeze-up in the fall (Cohen et al., 2014; Markus et al., 2009; Stroeve et al., 2012). The combination of more open water and warmer SST then increases sensible and latent heat fluxes to the atmosphere (Deser et al., 2010; Screen et al., 2013). Although the greatest reductions in SIE occur in late summer, the forcing to the atmosphere is small at this time due to the weak temperature gradient between the sea surface and the overlying air mass; rather, SIE-related heat flux anomalies and the associate atmospheric response are greatest in the cool season when the temperature difference between ocean and atmosphere is maximized (Deser et al., 2010; Screen, 2017; Screen et al., 2013).

The first-order, thermodynamic response to sea ice loss is a warming and moistening of the lowermost troposphere that is then advected over adjacent coastal landmasses, with resulting temperature anomalies that are largest during winter (Alexander et al., 2004; Deser et al., 2010; Screen et al., 2013). Indeed, pan-arctic sea ice reductions are responsible for the majority of winter Arctic warming in recent decades (Screen & Simmonds, 2010) and, by association, are primarily responsible for the weakening of the near-surface meridional temperature gradient throughout the Northern Hemisphere.

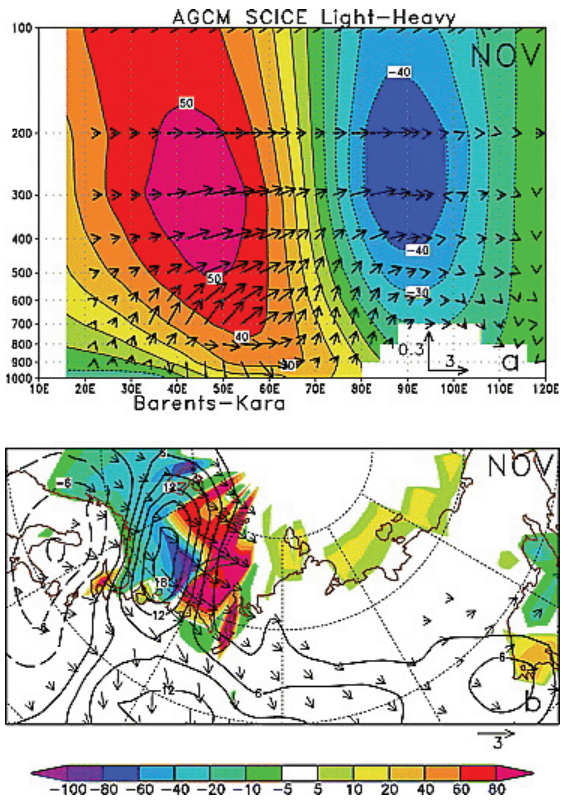


Figure 1.2: November atmospheric response to low sea ice in the region stretching between the Barents and East Siberian seas as simulated by an atmospheric general circulation model. All quantities shown represent the difference in simulated conditions between model runs with light and heavy prescribed sea ice concentrations. (a) Vertical cross-section showing the geopotential height differences [m] (shading and contours) and associated wave activity flux [m^2s^{-2}] (vectors). (b) Difference in turbulent heat flux (shading in [Wm^{-2}]). Vectors show horizontal component of the associated wave activity flux; contours show the vertical component. Figure reprinted from Honda et al. (2009), with permission granted by the American Geophysical Union usage permissions policy: https://www.agu.org/Publish-with-AGU/Publish/Author-Resources/Policies/Permission-policy.

Heating of the lower troposphere can also affect dynamic change by causing an upward inflation of geopotential heights, forcing an anomalous ridge aloft (Cohen et al., 2019; Kim et al., 2014; Screen et al., 2013). This clearly has implications for local conditions, but thermal forcing at the surface may also exert a remote influence by exciting a stationary Rossby wave train (Walter et al., 2001). Thus, the location of sea ice loss is an important factor in determining the spatial character of the atmospheric response.

Regions known to induce a winter dynamical response to fall and winter SIE variability include the Barents and Kara seas along the Siberian coast, as well as the Sea of Okhotsk in the North Pacific. Several studies have examined the role of Barents-Kara sea ice loss as an explanation for the recent winter cooling in Eurasia that is ostensibly inconsistent with a globally warming climate (Cohen et al., 2012; Cohen et al., 2014; Honda et al., 2009; Overland et al., 2015; Petoukhov & Semenov, 2010). Turbulent heat flux accompanying low

fall SIE in the Barents and Kara seas induces a stationary wave response that emanates southeastward (Figure 1.2), with a high-pressure ridge aloft and a trough over eastern Eurasia that weakens the climatological westerly flow, causing below-normal surface temperature over the continental interior (Honda et al., 2009; Liptak & Strong, 2014; Petoukhov & Semenov, 2010; Wu & Smith, 2016). Elsewhere, winter SIE variability in the Sea of Okhotsk elicits a local baroclinic response, triggering a stationary wave that propagates eastward along 60 °N into North America, causing a weakened Aleutian Low under low sea ice conditions (Honda et al., 1999; Honda et al., 1996).

In addition to the tropospheric mechanisms outlined above, sea ice variability is believed to influence primary modes of Northern Hemisphere atmospheric variability via a stratospheric pathway. A growing body of research supports a conceptual model in which sea ice loss in the Barents and Kara seas in late fall generates a forced Rossby wave response that constructively interferes with the climatological stationary wave pattern, thus enhancing the upward propagation Rossby waves into the stratosphere (Cohen et al., 2019; Jaiser et al., 2016; Kim et al., 2014; McKenna et al., 2018). The ensuing wave-mean flow interaction decelerates the polar stratospheric vortex, which exerts a downward influence on the troposphere, manifesting as a negative Arctic Oscillation (AO) / NAO in late winter and early spring (Cohen et al., 2019; Jaiser et al., 2016; Kim et al., 2014; Sun et al., 2015). Conversely, sea ice loss in the North Pacific generates a forced wave that destructively interferes with the climatological stationary wave pattern and, consequently, strengthens the stratospheric polar vortex, leading to a positive AO / NAO over the same timeframe (McKenna et al., 2018; Sun et al., 2015). Here, again, the geographic region of sea ice loss is a crucial factor in determining atmospheric response.

Investigations of remote influences on atmospheric circulation by regional changes in SIE are far less prevalent for summer compared to winter (see Vihma, 2014), potentially due to the relatively weak forcing of the summer atmosphere by SIE-related surface-energy fluxes (Bhatt et al., 2013). However, there is some evidence of a relationship between SIE and summer circulation over Greenland. Several studies using both observations and prescribed modeling have demonstrated a wave train response to low Arctic sea ice that favors ridging over Greenland and wetter-than-normal conditions in Northern Europe (Petrie et al., 2015; Screen, 2013; Wu et al., 2013).

1.3.3 Atmospheric response to snow cover variability

Snow cover acts to modulate the SEB by increasing surface albedo and elevating latent heating at the expense of sensible heating (Cohen & Rind, 1991). Accordingly, the presence of snowpack depresses the near surface temperature of the overlying air mass (Mote, 2008; Vavrus, 2007; Walsh et al., 1982). As was the case for sea ice, alteration of the SEB and, thus, the forcing of the atmosphere at the surface by changes in snow cover extent (SCE) has the potential to prompt a dynamical response.

In winter, Eurasian SCE may act in concert with Barents-Kara SIE to modulate the AO / NAO via the stratospheric pathway outlined in the previous section. The proposed mechanism linking the two surface variables is that the more open water and the above-normal air temperatures that accompany decreased fall Barents-Kara SIE increase the moisture content of the atmosphere, which translates increased snowfall and expanded fall SCE over Eurasia (Cohen et al., 2012; Cohen et al., 2014; Yao et al., 2017). More extensive snow cover depresses the temperature of the overlying air mass, which generates an upper-tropospheric trough over eastern Eurasia, thus reinforcing the aforementioned stationary wave pattern

that decelerates the polar vortex and encourages a negative winter AO / NAO (Cohen, 2016; Cohen et al., 2007; Cohen et al., 2014; G. Gong et al., 2007; Saito et al., 2001).

An essential condition for this hemispheric-scale response is that Eurasian snow cover variability is geographically aligned with a location of strong climatological stationary wave forcing—a condition that is not present for North American snow cover (G. Gong et al., 2003). Consequently, studies have revealed a weaker winter circulation response to North American SCE variability (see Henderson et al., 2018). Even so, some studies have documented a dynamical tropospheric response to more expansive North American SCE that resembles a positive winter AO / NAO (G. Gong et al., 2003; Klingaman et al., 2008).

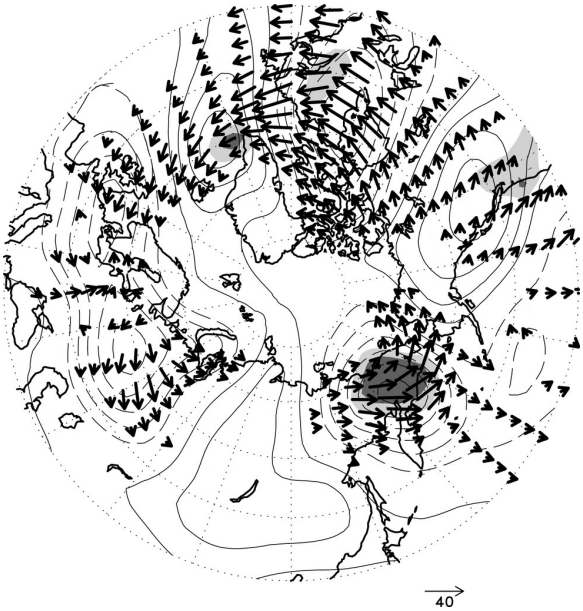


Figure 1.3: September atmospheric response in years of low spring snow cover over Eurasia. Contours show difference in monthly 300 hPa geopotential height at a 20 m interval for early minus late snow cover years during a study period of 1986–2004. Light and dark shading indicate significant differences at $\alpha = 0.10$ *and* $\alpha = 0.05$ *respectively. Vectors indicate the horizontal component of the associated wave activity flux. Figure reprinted from Matsumura and Yamazaki (2012), © American Meteorological Society. Used with permission.*

Spring and summer snow cover extent (SCE) has undergone rapid decline spurred by earlier snowmelt onset (Estilow et al., 2015; Hernández-Henríquez et al., 2015). In addition to its direct impact on albedo and the partitioning of sensible and latent heating at the surface, snow cover also exerts a residual influence on the atmosphere via the snow-hydrological effect—snow cover enhances soil moisture, which decreases surface temperature and increases atmospheric mois-

ture throughout summer (Matsumura & Yamazaki, 2012; Yasunari et al., 1991). In fact, while the influence of snow cover on air temperature is greatest in spring when widespread snowmelt occurs, the snow-hydrological effect that follows exerts a greater control on air temperature than does the snow-albedo effect during winter (Xu & Dirmeyer, 2011). Thus, the timing of greatest observed snow cover decline has coincided with that of greatest snow-atmosphere coupling.

The first-order impact of reduced snow cover on the summer atmosphere is enhanced heating of continental air masses, which is projected to drive anomalous ridging over Northern Hemisphere mid-to-high latitudes (Alexander et al., 2010; Vavrus, 2007; Vavrus et al., 2017). As was the case for winter, much of the work examining a summer dynamical atmospheric response to interannual snow cover variability has focused on Eurasia. Early snowmelt over Eurasia has been linked to a stationary wave response that persists through summer with increased blocking over eastern Siberia and enhanced ridging over southeast Greenland in September (Figure 1.3) (Matsumura & Yamazaki, 2012). At the hemispheric scale, Overland et al. (2012) found a persistent negative Arctic Dipole pattern during June from 2007 to 2012, where the negative phase of the Arctic Dipole is characterized by above-normal sea-level pressure spanning the North American Arctic coastline, including Greenland, and below-normal pressure over Siberia. The authors pointed to concurrent, widespread reductions in spring snow cover as a potential causal mechanism behind this shift in circulation. Subsequently, Matsumura et al. (2014) revealed a similar pattern when regressing 1000 hPa geopotential heights against June Eurasian SCE; however, they likened the pattern to a negative AO phase. Furthermore, the study presented evidence of a causal mechanism by showing that diminished spring snow cover over Eurasia enhances the poleward propagation of Rossby waves, which acts to decelerate the subpolar jet, thereby forcing a negative summer AO.

1.3.4 Implications for Atmospheric Circulation Over Greenland

The dynamical responses to surface cover variability outlined above can be drawn upon to infer general implications for GrIS SMB. The negative SMB trend has been a consequence of amplified runoff during the melt season, as precipitation inputs to the ice sheet have remained consistent over time (Noël et al., 2017). Accordingly, the focus here centers on potential impacts on summer atmospheric circulation over Greenland. Since the stratospheric polar vortex typically breaks down by early May (Kelleher et al., 2020), a stratospheric pathway linking surface cover to atmospheric conditions over Greenland is unlikely. Thus, this discussion is limited to tropospheric mechanisms.

Consistent with the jet stream response to AA hypothesized by Francis and Vavrus (2012), studies have measured an increase in the waviness of summer atmospheric circulation over North America and the North Atlantic (Cattiaux et al., 2016; Di Capua & Coumou, 2016; Vavrus et al., 2017). While this suggests AA may foster conditions in the region that encourage Greenland blocking, these studies have examined domains that dissect Greenland itself and none have specifically examined the increase in Greenland blocking through this lens of a wavier jet stream under AA.

Concerning more direct surface atmosphere coupling, the flux of energy to the atmosphere associated with sea ice anomalies is an order of magnitude less in summer than it is in winter (Bhatt et al., 2013), reducing the magnitude of any sea-ice-induced atmospheric response (Screen, 2017). Conversely, the relative influence of terrestrial snow cover on the atmosphere is thought to be greater in summer than in winter (Coumou et al., 2018), and its retreat has been cited as a likely reason for observed changes in summer circulation (Coumou et al., 2015; Overland et al., 2012).

Snow cover may impact GrIS conditions through its influence on hemispheric-scale circulation. The negative phase of the summer AO / NAO is characterized by a more meridional flow regime (Di Capua & Coumou, 2016; Vavrus et al., 2017), with an anomalous ridge over Greenland that promotes above-normal temperatures and below-normal snowfall (Box et al., 2012; Fettweis et al., 2013). Furthermore, a negative AO / NAO is associated with both an increased frequency and higher latitude of blocking highs throughout the Northern Hemisphere (Hassanzadeh & Kuang, 2015; Thompson & Wallace, 1998), including more frequent Greenland blocking (Hanna et al., 2015; Hanna et al., 2014). Hence, the results of Matsumura et al. (2014) showing a negative AO during summers of low Eurasian SCE suggest diminishing spring and summer SCE may have contributed to the increase in Greenland blocking that has elevated GrIS surface melt in recent decades.

Additionally, the stationary wave response to low spring Eurasian SCE documented by Matsumura and Yamazaki (2012) raises the possibility of a more direct tropospheric connection with conditions over Greenland. Their results show anomalous ridging near southeast Greenland in September following instances of low spring Eurasian SCE (Figure 1.3) which could contribute to the decline in GrIS SMB by encouraging anticyclonic conditions over Greenland in early fall. However, while this demonstrates the ability of Eurasian SCE variability to impact Greenland, their analysis was focused on the Eurasian subarctic and, consequently, the region around Greenland was not included in the results they presented for summer months. Thus, more work is needed to fully understand the implications of terrestrial snow cover variability for GrIS SMB.

1.4 Study Motivation and Objectives

There is extensive evidence establishing the central role of Greenland blocking in supporting the recent upswing in GrIS surface runoff (Ballinger et al., 2019; Häkkinen et al., 2014; Hanna et al., 2013; Henderson et al., 2021; McLeod & Mote, 2016); however, studies have offered differing explanations of the precise mechanisms by which blocking episodes encourage melt. Some have pointed to cloud-suppressing subsidence within the blocking anticyclone that reduces snow accumulation and encourages melt by allowing for greater insolation at the surface (Box et al., 2012; Hofer et al., 2017). Conversely, others have emphasized the importance of southerly moisture transport upstream of the ridge which, upon ascent of the ice sheet, increases cloud cover and attendant downwelling longwave radiation—a mechanism that is particularly effective at producing melt of the northern ice sheet and over the accumulation zone where surface albedo is high (Gallagher et al., 2018; Hahn et al., 2020; Neff, 2018; Noël et al., 2019; Wang et al., 2019). Furthermore, the filaments of intense moisture transport—termed atmospheric rivers—that often accompany blocking onset can impart distinct SEB and SMB signatures depending on where they make landfall (Mattingly et al., 2018; Mattingly et al., 2020). It follows that the progression and orientation of the blocking anticyclone with respect to the ice sheet is likely an important determinant of the precise mechanisms of melt production and their overall efficacy during a given blocking episode. However, previous studies of the impact of blocking on the GrIS have often used case studies of individual melt events or have employed composite means that indiscriminately average across many blocking episodes. A more thorough accounting of spatiotemporal differences in the progression of Greenland blocks is therefore needed to better understand the different mechanisms of melt

production between individual blocking episodes and, by extension, how blocking has facilitated the observed decline in GrIS SMB.

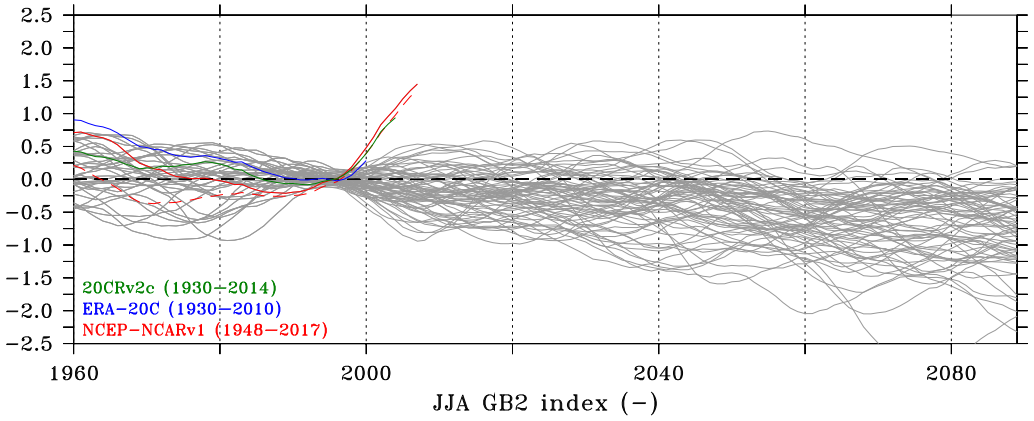


Figure 1.4: Comparison of GCM-simulated and observed trends in Greenland blocking. As indicated by the legend, observed trends are obtained from NCEP/NCAR Reanalysis 1 (NCEP-NCARv1), NOAA 20th Century Reanalysis Version 2c (20CRv2c), and ERA 20th Century Reanalysis (ERA-20C), while GCM projections are obtained from an ensemble of RCP4.5 and RCP8.5 CMIP5 simulations. Figure reprinted from Hanna et al. (2018a), with permission granted by the Creative Commons Attribution 4.0 License: https://creativecommons.org/licenses/by/4.0/legalcode.

Given the recent increase in summer Greenland blocking that has coincided with an acceleration of GrIS mass loss (Hanna et al., 2018a; Hanna et al., 2018b; IMBIE Team, 2020; McLeod & Mote, 2016), a critically important question is whether this shift in regional circulation should be expected to continue as a consequence of climate change. Contrary to observations, the latest global climate model (GCM) projections yield a robust decline in summer blocking in the North Atlantic (Figure 1.4) (Delhasse et al., 2021; Hanna et al., 2018a; Masato et al., 2013). However, weather prediction models and historical GCM simulations fail to adequately represent blocking events, with both model types underestimating blocking frequency and duration (Vial & Osborn, 2012; Woollings et al., 2018). This underrepresentation carries significant implications for climate change projections throughout the mid-to-high latitudes, as atmospheric blocking plays an instrumental role in regulating surface conditions and facilitating climate extremes (Woollings et al., 2018, and

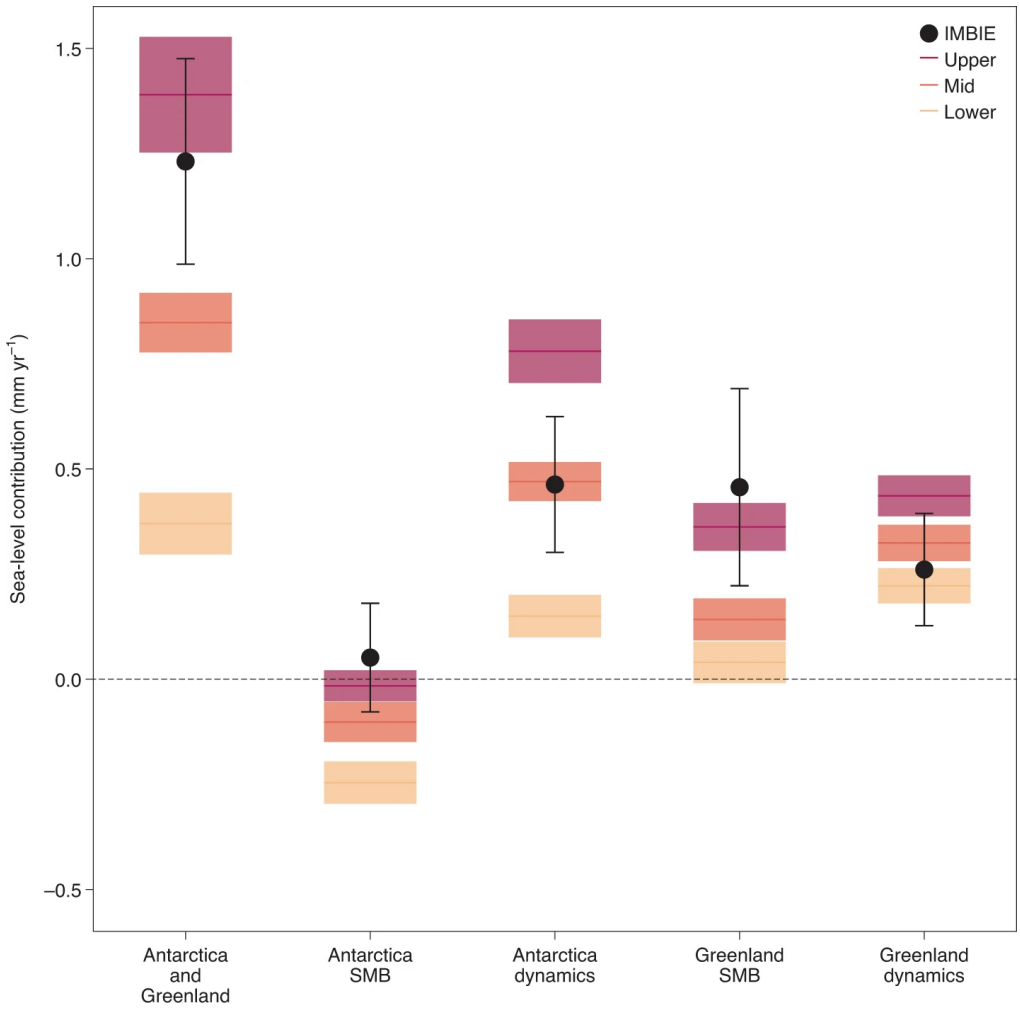


Figure 1.5: Comparison of observed and GCM-projected contributions to sea level rise by the Antarctic and Greenland ice sheets combined, as well as broken down by the dynamic and SMB contributions for each ice sheet separately. Observed values (black) are based on estimates from the IMBIE Team (IMBIE Team, 2018, 2020). GCM projections are broken down into the 95th (maroon), 50th (orange), and 5th (yellow) percentile of simulations from the IPCC Fifth Assessment Report. The range included with each data point indicates 1 standard deviation about the average annual rate. Figure reprinted by permission from Springer Nature: Nature Climate Change, Slater et al. (2020), ©2020.

references therein). Indeed, accurate representation of regional circulation over Greenland is essential for GrIS SMB projections. The failure of GCMs to resolve the recent shift in summer circulation over Greenland has led to an underestimation of surface mass loss from the GrIS (Figure 1.5) and, as a result, the combined contributions of Greenland and Antarctic mass loss to global sea-level rise has most closely tracked the upper bound of projections from the IPCC Fifth Assessment Report (Slater et al., 2020). Furthermore, one pertinent analysis found that, if the recent increase in blocking that is not captured in CMIP5 were to continue (see Hanna et al., 2018a), SMB losses will be more than twice than what is currently estimated by downscaled GCM projections (Delhasse et al., 2018). Thus, if AA does in fact act to augment blocking over the ice sheet, estimates of future Greenland SMB obtained from GCMs may contain substantial error due to a failure to resolve this important feedback.

Much of the scientific focus on atmospheric response to AA has been centered on implications for weather in the mid-latitudes, where population density is high. While this previous work can indirectly inform on the consequences of AA-induced surface cover change for GrIS mass balance via established associations with synoptic-to-global-scale circulation, a direct examination of the relationship between high-latitude surface cover variability and GrIS SMB is lacking. Furthermore, although past efforts have compared the relative impacts of dynamical forcing against that of increasing background temperatures (Delhasse et al., 2018) and local SIE / SST change (Hanna et al., 2014; Noël et al., 2014) separately, no study has presented a combined analysis of the complete thermodynamic contribution to recent GrIS surface mass loss. A comprehensive examination of the dynamical and thermodynamic consequences of AA for the GrIS could provide insight on the discrepancy between the recently observed increasing trend in summer anticyclonic conditions over Greenland and the decreasing trend represented in climate

model projections (Hanna et al., 2018a) and, further, would inform the near-term GrIS SMB outlook. Here, I seek to elucidate these relationships by pursuing the following research objectives:

1. *Classification of Greenland blocking episodes and their impact on GrIS SMB*: What are the predominant blocking patterns that impact Greenland during the summer? How do differences in the spatial configuration and temporal progression of these common Greenland blocking patterns influence the SEB and SMB response of GrIS? Has the relative frequency of different Greenland blocking types changed with time and, if so, what are the implications for GrIS mass balance?

2. *Dynamical consequences of AA and retreating SCE for GrIS SMB*: Has the upper-level flow over the North Atlantic become wavier during the current period of AA and how strong is the relationship between atmospheric waviness in the region and Greenland blocking? Does retreating spring snow cover under AA exert an influence on blocking frequency over Greenland in summer?

3. *Estimating the local thermodynamic contribution to GrIS surface mass loss*: What portion of SMB losses in recent years can be attributed to local thermodynamic change (i.e., the combined influence of increasing background temperatures and contributions from local sea-surface conditions)? Moreover, what portion of the thermodynamic influence is due to adjacent SIE / SST change alone?

CHAPTER 2

SUMMER GREENLAND BLOCKING DIVERSITY AND ITS IMPACT ON THE SURFACE MASS BALANCE OF THE GREENLAND ICE SHEET[1]

[1] Preece, J. R., Wachowicz, L. J., Mote, T. L., Tedesco, M., & Fettweis, X. (2022). Journal of Geophysical Research: Atmospheres, 127(4), e2021JD035489. https://doi.org/10.1029/2021JD035489. Reprinted here with permission of the publisher.

Abstract

The increase in Greenland Ice Sheet (GrIS) surface runoff since the turn of the century has been linked to a rise in Greenland blocking frequency. However, a range of synoptic patterns can be considered blocked flow and efforts that summarize all blocking types indiscriminately likely fail to capture consequential differences in GrIS response. To account for these differences, we employ ERA5 reanalysis to identify summer blocking using two independent blocking metrics: the Greenland Blocking Index (GBI) and the blocking index of Pelly and Hoskins (2003). We then conduct a self-organizing map analysis to objectively classify synoptic conditions during Greenland blocking episodes and identify three primary blocking types: (1) a high-amplitude Omega block, (2) a lower-amplitude, stationary summer ridge, and (3) a cyclonic wave breaking pattern. Using Modèle Atmosphérique Régional output, we document the spatiotemporal progression of the surface energy and mass balance for each blocking type. Relative to all blocking episodes, summer ridge patterns produce more melt over the southern ice sheet, Omega blocks produce more melt across the northern ice sheet, and cyclonic wave breaking patterns produce more melt in northeast Greenland. Our results indicate that the recent trend in summer Greenland blocking was largely driven by an increase in Omega patterns and suggest that Omega blocks have played a central role in the recent acceleration of GrIS mass loss. Furthermore, the GBI exhibited a relative bias toward Omega patterns, which may help explain why it has measured stronger trends in summer Greenland blocking than other blocking metrics.

2.1 Introduction

Atmospheric blocking is characterized by a pronounced, quasi-stationary anticyclone that diverts incoming synoptic disturbances that would otherwise bring a change in weather conditions. In summer, persistent, widespread subsidence within the blocking ridge suppresses cloud cover and increases radiative warming at the surface, resulting in warm extremes (Tedesco & Fettweis, 2020; Tedesco et al., 2016; Woollings et al., 2018). Given their impact on summer surface temperature more broadly, it is not surprising that blocking anticyclones over Greenland show a strong association with Greenland Ice Sheet (GrIS) surface melt and runoff over synoptic-to-decadal timescales (Ballinger et al., 2019; Häkkinen et al., 2014; Hanna et al., 2014; Hanna et al., 2013; Hermann et al., 2020; McLeod & Mote, 2016). Indeed, Greenland blocking was instrumental in promoting exceptional surface melt in 2012 and 2019 that extended to Summit Station (Cullather et al., 2020; Hanna et al., 2021; Nghiem et al., 2012; Tedesco & Fettweis, 2020)—a phenomenon that has occurred, on average, only once every 153 years throughout most of the Holocene (Alley & Anandakrishnan, 1995).

Blocking events encourage melt through their spatially varying influence on the surface energy balance (SEB). The poleward extension of the blocking ridge transports warm, moist air aloft that may then be mixed through the stable boundary layer to the surface (Duynkerke & van den Broeke, 1994; Gorter et al., 2014; van den Broeke & Gallée, 1996). Southerly flow along the upstream flank of the blocking anticyclone often generates strong water vapor transport to northern Greenland through the Davis Strait (Ballinger et al., 2019; Barrett et al., 2020; Mattingly et al., 2018; Ward et al., 2020). Not only can this warm, southerly flow amplify turbulent heat flux along the western ablation zone (van den Broeke & Gallée, 1996), but as it rounds the crest of the ridge and ascends the northwest ice sheet, it cools

adiabatically and generates cloud cover that enhances downwelling longwave radiation over high elevations of the northern ice sheet (Hahn et al., 2020; Mattingly et al., 2020; Ward et al., 2020). Thus, blocking-related enhancement of longwave radiation often occurs at higher latitudes and over the accumulation zone of the GrIS, where surface albedo is high and, consequently, the SEB is more susceptible to changes in longwave radiation than shortwave radiation (Lenaerts et al., 2019; Wang et al., 2018; Wang et al., 2019). Indeed, several studies have pointed to moisture transport and the presence of low-level clouds as being essential for melt production over high elevations of the ice sheet (Bennartz et al., 2013; Gallagher et al., 2018; Neff et al., 2014; Tedesco & Fettweis, 2020). Meanwhile, subsidence within the ridge acts in concert with downslope flow to suppress cloud cover over southern Greenland, thereby increasing incoming shortwave radiation (Hahn et al., 2020; Ward et al., 2020). Unlike the northern ice sheet, shortwave cloud radiative effects dominate the SEB of the southern ice sheet due to a lower surface albedo (Lenaerts et al., 2019; Wang et al., 2019) and it has been argued that blocking-related reductions in cloud cover have driven GrIS surface mass loss in recent decades (Hofer et al., 2017). However, anomalously warm conditions and exceptional melt throughout the southwest ablation zone have also been linked to increased cloud cover and anomalous rainfall during blocked circulation patters that bring southerly moisture transport to western Greenland (Doyle et al., 2015; Gallagher et al., 2020; Neff, 2018)—observational evidence that contradicts a strictly inverse relationship between cloud cover and surface mass loss and underscores the need for a more complete understanding of the atmospheric dynamics that drive GrIS surface mass balance (SMB) variability.

Much of the work relating Greenland blocking to GrIS surface conditions has quantified blocking using the Greenland Blocking Index (GBI) (Fang, 2004; Hanna et al., 2016), which shows a significant increase in summer blocking in recent

decades (Hanna et al., 2018b). However, because the GBI is simply a measure of average geopotential height over Greenland, it does not account for differences in the type or location of the blocking anticyclone. Several efforts have revealed an Omega blocking pattern, in which an amplified ridge of high pressure is bounded on either side by two low-pressure centers, during periods of high GBI (Barrett et al., 2020; McLeod & Mote, 2016) and in association with GrIS surface melt (Fettweis et al., 2013; Hanna et al., 2014; Hermann et al., 2020; van den Broeke et al., 2017). However, other blocking types have also accompanied extensive GrIS melt. One recent example occurred in late July 2019 when a cyclonic wave breaking pattern was instrumental in transporting an anticyclone to Greenland from the east where it was previously responsible for the record setting heatwave that beset Western Europe that same year (Cullather et al., 2020; Tedesco & Fettweis, 2020). Estimates of maximum daily surface melt during this event range from 62–73% of the GrIS surface (Cullather et al., 2020; Tedesco & Fettweis, 2020), demonstrating that a diversity of Greenland blocking types can cause extensive GrIS melt. Considering this blocking diversity, the prominence of Omega patterns during periods of high GBI suggests this blocking type may be overrepresented in the GBI.

In contrast to the robust increase in summer GBI, a positive trend is less evident when blocking is detected using the flow-reversal-based method of Pelly and Hoskins (2003) (Wachowicz et al., 2021). These disparate results raise the question of how the definition of blocking imparted by a given blocking metric may influence observed trends by emphasizing certain circulation patterns. Here, we apply an objective classification technique to characterize the predominate summer Greenland blocking types as identified by these two independent metrics. Utilizing this classification, we examine how long-term trends vary among differing blocking patterns and assess relative biases in the blocking metrics toward these patterns.

In doing so, we aim to detail the synoptic conditions captured by each blocking index and clarify the differences in measured trends between them.

Given that the impact of blocking on the SEB of the GrIS is dictated by the position of the blocking anticyclone (Ward et al., 2020), the resulting interaction between large-scale flow and the topography of the ice sheet (Hahn et al., 2020), and geographical variations in surface albedo (Wang et al., 2019), efforts that indiscriminately summarize all blocking events as a single group likely fail to capture consequential differences in SEB and SMB response. To account for these factors, we also contrast the influence of differing Greenland blocking types—herein referred to as blocking diversity—on the surface of the GrIS. Thus, another primary objective of this analysis is to provide a more spatially nuanced surface climatology of Greenland blocking and to frame these results within the context of the recent acceleration of GrIS mass loss.

2.2 Data and Methods

2.2.1 Identifying summer Greenland blocking

Here we utilized ERA5 reanalysis (Hersbach et al., 2020) to identify June–August (JJA) blocking from 1979–2019 using two independent blocking metrics: 1) the GBI and 2) a modified version of the blocking index of Pelly and Hoskins (2003), hereafter abbreviated as PH03. The GBI is defined as the average 500 hPa geopotential height (Z500) over a domain spanning 60–80° N and 20–80° W (Figure 2.1a, black dashed line). We calculated the GBI by taking the mean daily Z500 within the GBI domain while weighting each observation by the cosine of its latitude. We then standardized the index by day of year and identified large-scale blocking as any day where the GBI exceeded one positive standardized anomaly. We define Greenland blocking episodes as cases where large-scale blocking persisted for

$\geq$ 4 days to be consistent with the duration criteria of PH03. Thus, we identified Greenland blocking episodes as instances of persistent, anomalous anticyclonic circulation—a commonly invoked defining feature of atmospheric blocking (Charney et al., 1981; Dole & Gordon, 1983; McLeod et al., 2018; Woollings et al., 2018).

Our use of PH03 complements the GBI by focusing on another frequently used defining characteristic of blocking—the disruption of midlatitude jet stream and embedded synoptic disturbances (PH03; Lejenäs & Økland, 1983; Tibaldi & Molteni, 1990; Woollings et al., 2018). As an indicator of a disrupted jet, PH03 identifies reversals in the meridional potential temperature gradient at the two potential vorticity unit (PVU) surface around a longitudinally varying central blocking latitude. The blocking index, B, was calculated at each longitude as in PH03:

$$B = \frac{2}{\Delta\phi}\int_{\phi_0}^{\phi_0+\Delta\phi/2} \theta \,\mathrm{d}\phi - \frac{2}{\Delta\phi}\int_{\phi_0-\Delta\phi/2}^{\phi_0} \theta \,\mathrm{d}\phi$$

Where θ is potential temperature on the 2 PVU surface, ϕ_θ is the central blocking latitude, and $\Delta\phi = 30^\circ$ is the latitude range over which the index is calculated (Figure 2.1a, thick gray lines). To ensure that $B > 0$ signals a disruption of the climatological storm track, ϕ_0 is defined as the latitude of maximum 1981–2010 long-term mean JJA 300 hPa eddy kinetic energy (EKE):

$$EKE = \frac{1}{2}(u' + v')^2$$

Where u' and v' are the 2.5–10 day bandpass filtered zonal and meridional winds. While PH03 use the annual mean EKE to define ϕ_θ, we followed Wachowicz et al. (2021) who found it was necessary to use a seasonally defined ϕ_θ to sufficiently capture summer blocking over Greenland. As in PH03, for each longitude we calculated B at ϕ_θ as well as $\phi_\theta \pm$ 4°, then retained the maximum of the three values. Here, we define large-scale blocking as any day where $B > 0$ across 12°

longitude or more within the GBI domain (i.e., 20–80 $^\circ$ W) and blocking episodes as large-scale blocks that persist for $\geq$ 4 days. This duration threshold corresponds to the number of days after which a flow reversal is more likely to persist into the next day, suggesting the existence of distinct blocking dynamics (PH03).

2.2.2 Greenland blocking and GrIS SEB/SMB

Though the GBI and PH03 effectively indicate the presence of blocked conditions over Greenland, they do not distinguish intra- or inter-episode variability in the type or position of the blocking anticyclone. We therefore performed a self-organizing map (SOM; Kohonen, 1990) analysis to document the SEB/SMB response to the full diversity of Greenland blocking. The SOM is an artificial neural network architecture that reduces dataset dimensionality through an iterative, unsupervised classification of the input data into a user-defined number of characteristic patterns, referred to as nodes, that represent the full range of physical states present in the record (Kohonen, 1990; Miljković, 2017; Reusch et al., 2005; Sheridan & Lee, 2011). For climatological applications, the SOM is typically organized into a two-dimensional array where, as a feature of the iterative learning process, neighboring nodes are more similar than distant nodes and corner nodes represent opposing extremes within the record (Hewitson & Crane, 2002; Kohonen, 1990; Sheridan & Lee, 2011; Tedesco & Fettweis, 2020). We refer the reader to Hewitson and Crane (2002) for a more comprehensive comparison between SOMs and the clustering methods that have historically been applied in synoptic typing, wherein they summarize the main differences as follows: (1) Rather than prioritizing the minimization of within group differences and the maximization of differences between groups, SOM nodes are effectively positioned in the data space such that they reflect the multidimensional distribution function of the input data and (2)

The topological ordering of SOM nodes makes them a more effective means of visualizing relationships between groups.

We utilized the SOM to classify daily ERA5 Z500 for all identified JJA blocking episode days. The geopotential height data were remapped to a 100 km EASE2 grid (Brodzik et al., 2012, 2014) using bilinear interpolation to ensure that all latitudes were given equal weight during the SOM training process. We tested several SOM configurations ranging in size from 5x5 to 3x3 nodes and found little difference in the quantization error—a measure of the difference between the input data and the nodes to which they map. As is common for climatological analyses (Sheridan & Lee, 2011), we then proceeded with a 4x3 array based on a subjective evaluation of its ability to clearly present the range of Greenland blocking configurations while also limiting the number of low-frequency nodes.

As a product of the SOM analysis, each blocking episode day is assigned a best matching unit (BMU) indicating the node (e.g., class) into which it is classified. We displayed the synoptic setting and attendant surface conditions that characterize each node by compositing daily values of relevant variables by common BMU assignment. Because we examined variables that are not normally distributed, we employed the nonparametric Wilcoxon rank-sum test with $\alpha = 0.05$ to assess the statistical significance of the composites.

We examined SEB and SMB response using the regional climate model, Modèle Atmosphérique Régional (MAR). MAR is fully coupled to a one-dimensional surface-atmosphere energy and mass transfer scheme that employs a multilayered snowpack model that accounts for changes in surface albedo due to snow metamorphism and has been extensively verified over the GrIS (Brun et al., 1992; Brun et al., 1989; Fettweis et al., 2005; Fettweis et al., 2020; Lefebre et al., 2005). Moreover, MAR was found to reproduce GrIS surface observations better than leading reanalysis products during the type of extreme moisture transport events that often

accompany blocking (Mattingly et al., 2018; Mattingly et al., 2020). It is therefore particularly well suited for analyses of GrIS SMB. We used output from MARv3.11 forced by 6-hourly ERA5 reanalysis data (Fettweis, 2022). The model was integrated over a 165x300, 10-km grid (Supplementary Figure 2.1) with 24 vertical sigma levels spanning 2 m to 17 km above the surface and an integration timestep of 60 s. MAR was forced at its lateral boundaries by surface pressure, wind (u and v components), specific humidity and temperature. Along its upper boundary, the model was forced by wind and temperature but only for its top three vertical levels, which are in the stratosphere. Over the ocean, ERA5 sea-ice extent and sea-surface temperature were prescribed. A full description of MARv3.11 is available in Amory et al. (2021). With respect to Amory et al. (2021), however, the blowing snow module was switched off here. To provide a comparison of MAR-derived surface melt with observations, we utilized the National Snow and Ice Data Center MEaSUREs Greenland Surface Melt record of daily melt extent, which is derived from satellite passive microwave observations (Mote, 2014).

2.3 Results

Our application of the GBI identified 623 days of JJA large-scale blocking from 1979 to 2019, while PH03 identified 963 (Supplementary Figure 2.2). Both indices indicate an increase in blocking in the latter half of the record; however, the increase in GBI-identified blocking is much more pronounced—the GBI indicated a 92% increase in large-scale blocking days per year in 2000–2019 relative to 1979–1999, while PH03 underwent only a 14% increase over the same period. The disproportionate increase in GBI-identified blocking in the latter half of the record is likely driven, in part, by a global increase in geopotential height from anthropogenic

warming of the troposphere rather than an increase in blocking frequency (Christidis & Stott, 2015; Hanna et al., 2018a; Wachowicz et al., 2021).

To investigate this possibility, we also applied an adjusted version of the GBI (see Hanna et al., 2018a; Wachowicz et al., 2021), which we call GBI-Z (Supplementary Figure 2.2), that accounts for the increase in the background geopotential height by taking the difference between the GBI and the latitude-weighted mean Z500 for the zonal band spanning 60–80°N. According to GBI-Z, there was a 51% increase in large-scale blocking days per year from 1979–1999 to 2000–2019, suggesting that while some of the difference between GBI and PH03 can be attributed to globally increasing geopotential height, other factors are likely at play. Furthermore, while there are periods of strong agreement between the two indices, there are also considerable differences that likely reflect the biases that individual detection methods exhibit toward specific blocking types (see PH03; Barriopedro et al., 2010; Woollings et al., 2018). Acknowledging this, we explore the hypothesis that the GBI may be more sensitive to a particular blocking type and that blocking type may have experienced a disproportionate increase in recent years. The remainder of this analysis will focus on the standard definition of the GBI for a more direct comparison with the existing literature in which it has been predominately used.

2.3.1 GBI-PH03 overlap episodes

To provide a reference climatology of the impact of Greenland blocking on GrIS surface conditions, we first focus on instances of four or more consecutive days where both the GBI and PH03 identify large-scale blocking. By requiring that the blocking criteria of both indices are satisfied, these GBI-PH03 overlap episodes effectively constitute a hybrid index that is analogous to that of Dunn-Sigouin and Son (2013) in that it requires both a flow reversal and the presence of a persistent,

anomalous anticyclone. Application of these criteria resulted in 165 episode days occurring across 33 blocking episodes (Supplementary Figure 2.2).

Figure 2.1 documents the mid-tropospheric circulation during the 33 JJA GBI-PH03 overlap episodes using ERA5 Z500 and the associated GrIS surface response as resolved by MAR. The composite anomalies for each variable represent the mean daily anomaly for all GBI-PH03 overlap episode days relative to the 1981–2010 long-term daily mean. On average, these blocking episodes are characterized by an upper-level ridge with strongest high-pressure anomalies centered over southwest Greenland (Figure 2.1a). High pressure aloft is met by widespread above-normal surface air temperature with anomalies that are maximized over high elevations (Figure 2.1b). While the surface air temperature response is uniformly positive, blocking episodes produce a spatially variable SEB signature (Figure 2.1, middle row). Blocking enhances downward shortwave radiation (SWD) in southeast Greenland while reducing SWD and increasing downward longwave radiation (LWD) in northern Greenland (Figure 2.1c,d). This anomalous radiative forcing along with a positive latent heat flux (LHF) anomaly along the northwest perimeter of the ice sheet (Figure 2.1f) is consistent with the delivery of warm, moist air to northern Greenland via southerly advection upstream of the high-pressure center documented in previous studies (Hermann et al., 2020; Mattingly et al., 2018; Neff et al., 2014; Ward et al., 2020). Positive sensible heat flux (SHF) anomalies are maximized along the steep margins of the ice sheet and are most extensive in southern and eastern Greenland (Figure 2.1e). Together these results demonstrate the importance of longwave radiative forcing to the SEB in northern Greenland and at high elevations throughout the ice sheet, while SHF and SWD dominate surface heating in south and east Greenland during blocking episodes.

The bottom row of Figure 2.1 documents the impact of GBI-PH03 overlap episodes on the SMB. The integrated contributions of snowfall (SF) and meltwater

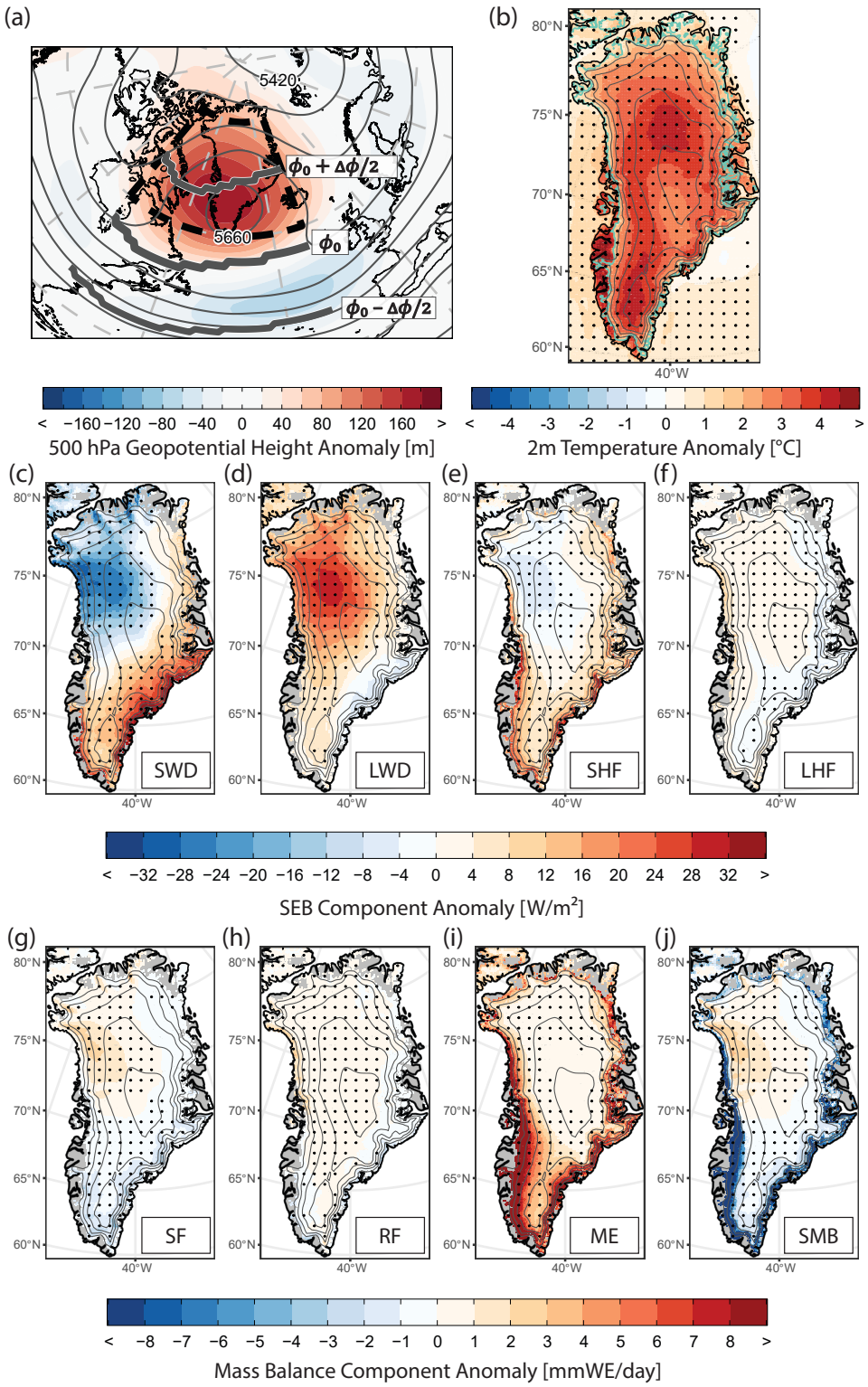


Figure 2.1: Composite-anomaly maps for all JJA GBI-PH03 overlap blocking episode days.
(Continued on the following page.)

Figure 2.1: Composite-anomaly maps for all JJA GBI-PH03 overlap blocking episode days: (a) Z500, (b) 2-m temperature, (c) downward shortwave radiation, (d) downward longwave radiation, (e) sensible heat flux to surface, (f) latent heat flux to surface, (g) snowfall, (h) rainfall, (i) meltwater production, (j) surface mass balance. Stippling indicates significant differences between surface conditions during blocking episode days and average 1981-2010 JJA conditions at $\alpha = 0.05$. In (a) contours denote composite-mean Z500 (60 m interval); dashed polygon delineates the GBI domain; thick gray lines show the JJA PH03 index parameters. PH03 is calculated for the parameters as pictured as well as at $\pm$ 4° latitude. In (b) teal line denotes land ice extent. In (b)-(j) contours denote MAR elevation data. Contour interval: 500 m. Range: 1000–3000 m.

production (ME) to the SMB are visible in Figure 2.1j. Blocking encourages above-normal SMB over high elevations of northwest Greenland by enhancing snowfall while the opposite is true in southern Greenland (Figure 2.1g,j). Greater-than-normal meltwater production (ME) extends above 2500 m in southern Greenland (Figure 2.1i); however, negative SMB anomalies are contained below 1500 m along the ice sheet margins (Figure 2.1j) as melt at higher elevations is retained as meltwater refreezes within the snowpack. Below 2000 m in northwest Greenland, above-normal rainfall (RF) appears to increase the SEB through enhanced LHF (Figure 2.1f,h), thus contributing to ME in the ablation zone.

2.3.2 SOM classification of Greenland blocking

To document the diversity of Greenland blocking episodes, rather than focus exclusively on blocking events of overlap, we applied each blocking detection method separately and retained all days where either the GBI or PH03 indicated four or more consecutive days of large-scale blocking. This resulted in the identification of 759 total JJA blocking episode days that were then used to subset daily Z500 to be classified via SOM. By subsetting only those days which occur during blocking episodes, we aim to more precisely characterize the exceptional atmospheric conditions captured by the two blocking indices (see Gibson et al., 2017).

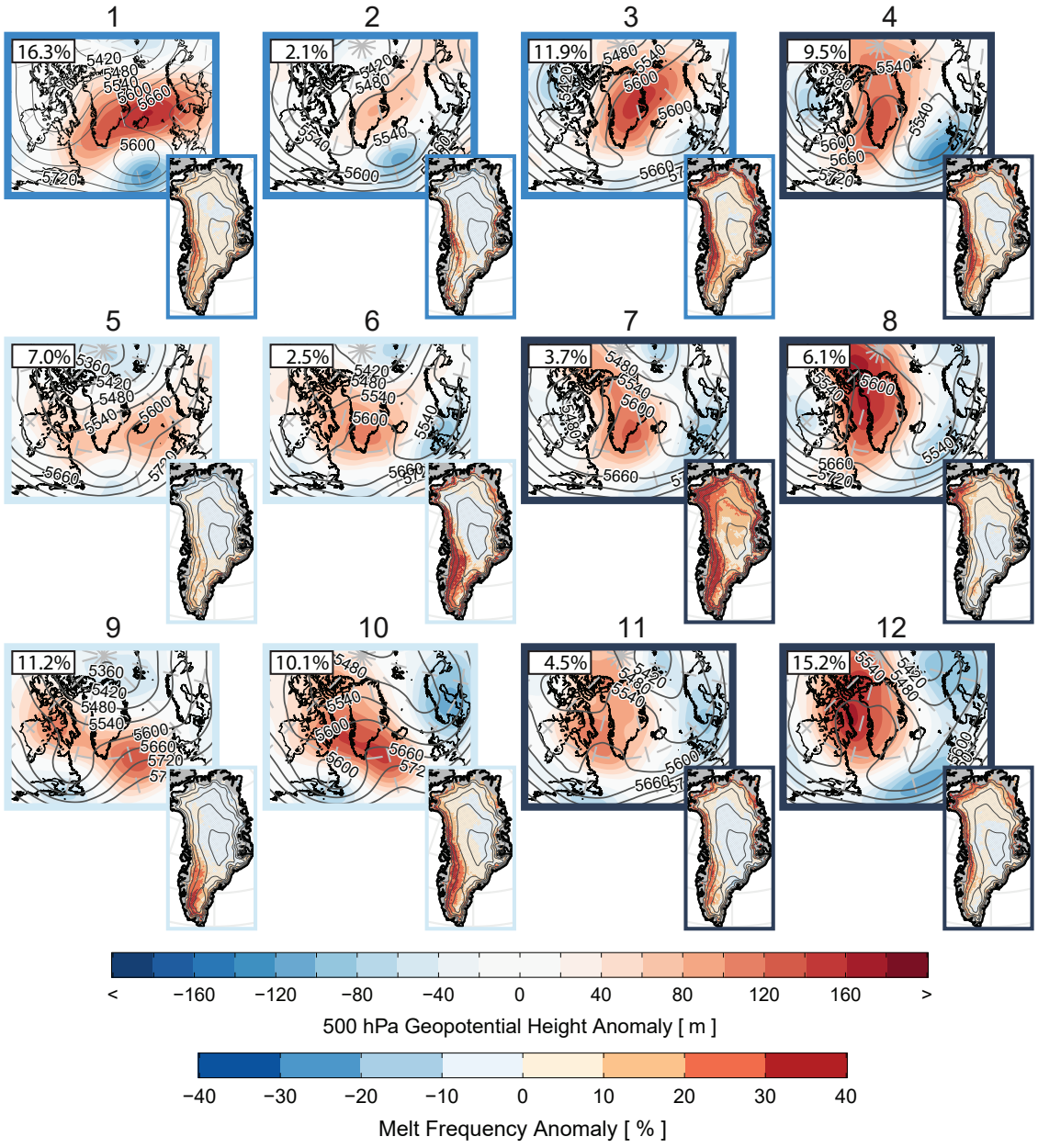


Figure 2.2: Composite anomalies (shading) and composite means (contours; 60 m interval) of Z500 during JJA blocking episode days assigned to each SOM node. The frequency of each node with respect to all blocking episode days is displayed in the upper-left corner. Map outlines indicate subjective groupings: Omega (dark blue), CWB (medium blue), or SR (light blue). Inset maps show MEaSUREs surface melt frequency for each node less the 1981–2010 mean JJA melt frequency. Elevation contours as in Figure 1.

The nodes of the SOM represent the continuous range of atmospheric circulation states identified as a blocking episode by either detection method. We visualize the characteristic patterns identified by the SOM by displaying the average Z500 on days assigned to a given node and present the associated anomalies in satellite-observed melt frequency (Figure 2.2). The percentage of all identified blocking episode days assigned to each node is displayed in the upper-left corner of each map. These percentages indicate how prevalent a given circulation pattern is on days when blocking is detected. For example, node 1 is the pattern most frequently identified during blocking episodes, comprising 16.3% of all blocking episode days, and resembles a wave breaking pattern with a ridge over Iceland and a cutoff low near the Azores. Node 12 is the next most frequent pattern, comprising 15.2% of all blocking episode days, and resembles an Omega block centered over Baffin Bay. There are clear differences in surface melt between nodes, where the northernmost extent of increased melt frequency appears to reflect the amplitude of the blocking ridge. We discuss these differences and their associated SEB forcing in detail in section 3.4.

As a blocking episode progresses, it may pass through more than one node. We therefore calculated one-day lead transition frequencies to illustrate the temporal relationships between all 12 nodes. The arcs of the chord diagram in Figure 2.3 symbolize the transition frequencies, where the size of the arc indicates the number of days in which a given transition occurs and the color of the arc indicates the node of origin as labeled radially along the outside of the diagram. We direct the reader to the gold arcs of node 9 as an example. Along the axis, the outer bar indicates that the sum of the transitions into and out of node 9 totaled 145, while the inner bar shows that 70 of those transitions were outgoing. The largest transition arc both starts and ends in node 9 demonstrating that subsequent blocking episode days typically remain in the origin node. An examination of the full diagram shows this

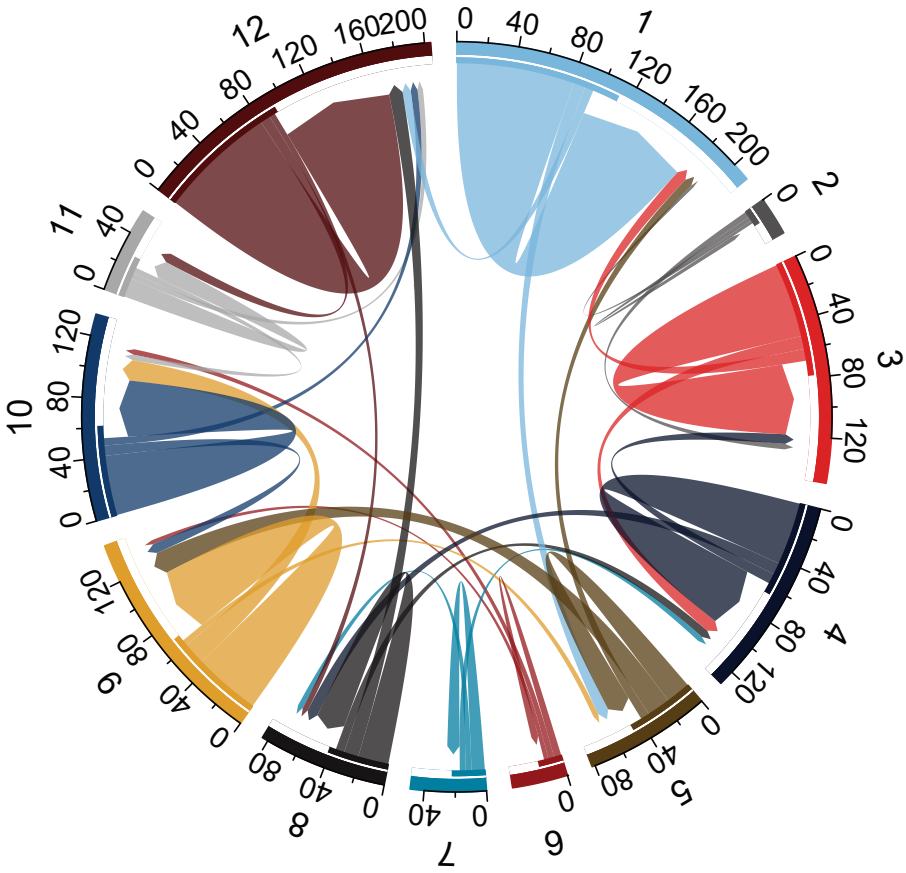


Figure 2.3: Chord diagram of SOM node transitions. Nodes labeled radially along outside of diagram. Outer bar denotes total number of daily transitions into and out of a node as indicated by the axes. Inner bar denotes the proportion of total transitions that are outgoing. Arcs point from origin to destination nodes for paths in the top quartile of transition frequency for each node. Arc width indicates the number of transitions along a given path.

is true for all nodes, consistent with the quasi-stationary nature of blocking. When node 9 does transition to another node, the remaining gold arcs indicate that it most often transitions to node 10, followed by node 5. Focusing on the arcs terminating in this sector, nodes 5 (brown), 10 (blue), and 6 (red) most frequently transition to node 9.

The transitions depicted in Figure 2.3 inform on how often the circulation patterns represented by individual nodes are temporally related over synoptic timescales. It follows that nodes with a high transition frequency between them are more likely

to represent the progression of a common blocking type. We utilized these temporal relationships along with a visual interpretation of the Z500 patterns in Figure 2.2 to group the SOM nodes into three representative blocking types based on resemblance to commonly recognized blocking patterns (see Woollings et al., 2018) as well as to illustrate the typical progression of each type. The map frames in Figure 2.2 are color coded to indicate the node groupings for each blocking type: (1) Omega blocking (dark-blue outlines) in which a large-amplitude ridge brings a strong anticyclonic anomaly to northernmost Greenland, (2) cyclonic wave breaking (CWB; medium-blue outlines) in which the anticyclone approaches Greenland from the east as it moves along the poleward flank of a cutoff low, and (3) a summer ridge pattern (SR; light-blue outlines) in which a lower-amplitude stationary ridge tracks the southern half of Greenland.

The SR transition frequencies reveal a tendency for node 5 to transition to node 9, indicating that the ridge typically first emerges over Iceland then builds toward the southeast coast of Greenland. Node 9 then tends to transition to node 10, suggesting the ridge continues to track westward, bringing a strong anticyclonic anomaly to the Labrador Sea. A retrograde motion is more evident for Omega blocks, as node 4, with a large-amplitude ridge over south-central Greenland, transitions through node 8 to node 12 with the ridge extending over Baffin Bay. In an alternative approach, we generated lead-lag composites of Z500 during GBI-PH03 overlap episodes. These composites confirmed the westward migration of the blocking anticyclone (Supplementary Figure 2.3), increasing confidence in the conclusions drawn from the SOM node transitions.

We repeated the SOM classification using an extended domain (20–85° N, 10–80° W), as well as using blocking duration thresholds of 6 and 8 days to assess the robustness of these results. While the start and end dates of individual episodes vary with domain size, 82% of the episodes identified using the extended

domain overlap with those identified using the original domain. Accordingly, the SOM classification yielded consistent results between the two domains (not shown). As the duration criterion is increased, lower-amplitude SR patterns become less evident and, rather, Omega blocks and the dipole structure of mature CWB patterns begin to dominate the SOM (Supplementary Figure 2.4)—a result that reflects the direct relationship between blocking intensity and duration (Cheung et al., 2013; Tyrlis & Hoskins, 2008). We therefore follow the empirical basis presented in PH03 and proceed with a minimum blocking episode duration criterion of 4 days.

Using all blocking episode days identified by either detection method enables the assessment of biases in each index toward any of the blocking types outlined in Figure 2.2. In Supplementary Figure 2.5, we present the atmospheric patterns represented by each SOM node from the perspective of the potential vorticity framework utilized in PH03 and note the percentage of all blocking episode days assigned to a given node that are identified by each blocking index. Except for node 7, all Omega blocking patterns are more frequently identified by the GBI than PH03. In contrast, three of the four SR nodes are more frequently identified by PH03. Similarly, the CWB patterns in nodes 1 and 2 are more frequently identified by PH03 while the pattern in node 3 features anomalously high pressure throughout more of the domain and consequently is more likely to be detected by the GBI (Figure 2.2,Supplementary Figure 2.5).

These biases clarify the differences in detected blocking between the two indices (Supplementary Figure 2.2). PH03 is more likely to identify SR and CWB patterns that, while they cause a large-scale flow reversal, do not bring anomalous high pressure to as much of the domain and, thus, are less probable to meet the threshold for large-scale blocking applied to the GBI. Conversely, while their amplitude is likely to generate a high GBI, Omega blocks produce weaker and less extensive easterly flow and are therefore less visible to flow-reversal-based metrics

(PH03; Barriopedro et al., 2010). Thus, while the more detailed view of the atmosphere afforded by a potential vorticity perspective has demonstrated substantial improvement over geopotential-height-based reversal metrics (PH03), these results suggest PH03 may still suffer from under detection of Omega patterns.

To further substantiate these findings, we also classified GBI-detected and PH03-detected blocking episode days separately (Supplementary Figure 2.6). The two separate SOMs reinforce the primary conclusions drawn from the combined SOM: (1) Omega, CWB, and SR blocking types are evident between the GBI-only and PH03-only SOMs; (2) The transition frequencies for the separate SOMs indicate a retrograding anticyclone, particularly for Omega patterns; (3) The GBI-only SOM exhibits a relative bias toward higher-amplitude Omega blocks while the PH03-only SOM detects more CWB and lower-amplitude SR patterns.

2.3.3 SEB response to Greenland blocking diversity

To document the variability in GrIS surface response accompanying the range of synoptic patterns revealed by the SOM classification, we calculated daily anomalies of MAR surface variables on all JJA blocking episode days relative to the 1981–2010 long-term daily mean, then composited the resulting anomalies by SOM node. Considered in conjunction with the node transitions, the MAR composites document the spatiotemporal GrIS SEB/SMB response to the three Greenland blocking types. We also examine SOM composites of ERA5 integrated water vapor transport (IVT) to elucidate the physical mechanisms underlying the SEB/SMB response.

Focusing on the radiative terms, SWD for all three CWB nodes exhibits a west–east dipole with negative anomalies to the west and positive anomalies to the east (Figure 2.4), while the LWD anomalies show an inverse pattern (Figure 2.5). This is consistent with the IVT composites (Figure 2.6), which show moisture

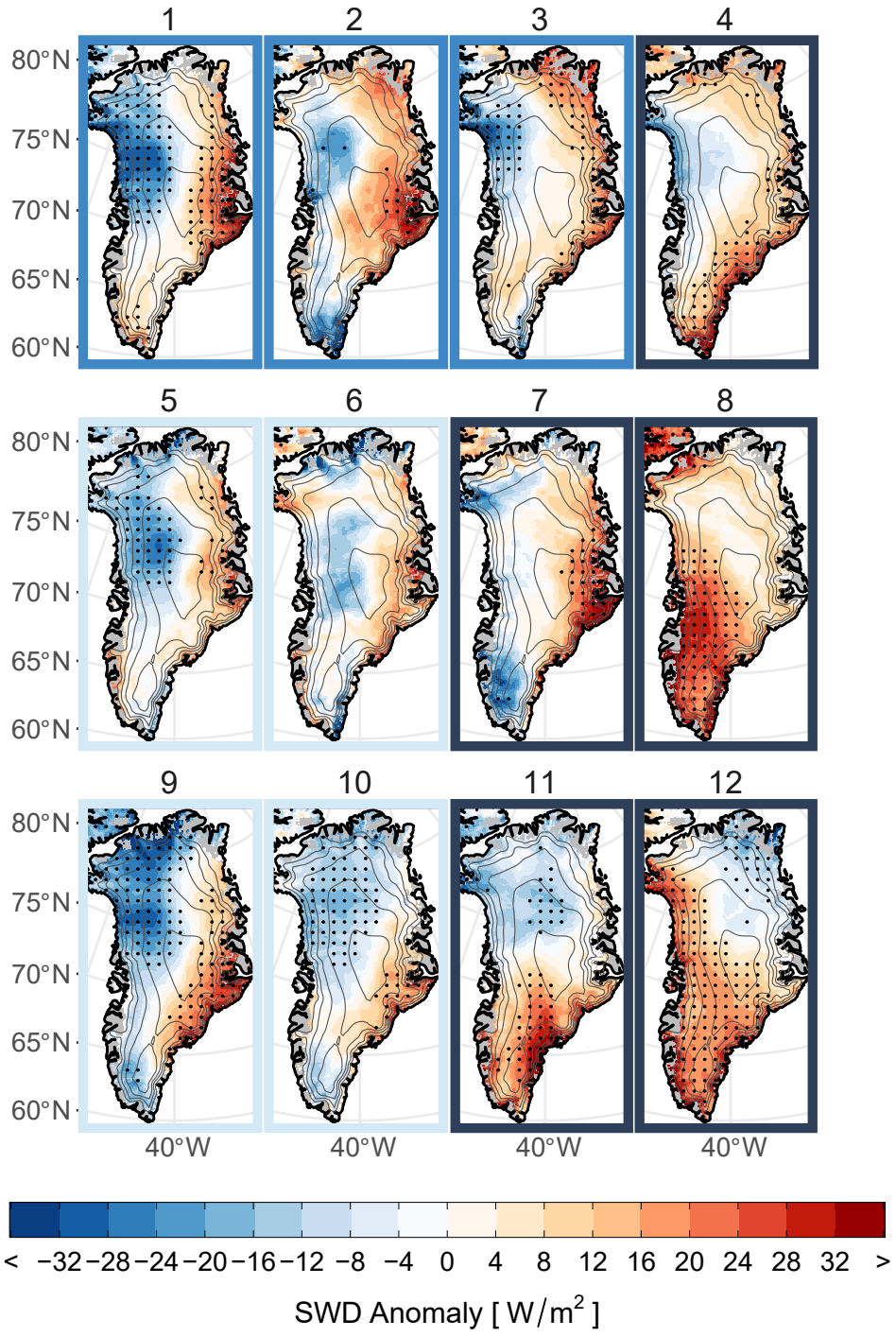


Figure 2.4: Anomalous SWD composited by SOM BMU. Stippling indicates significant ($\alpha = 0.05$) differences between days assigned to a given node and 1981–2010 JJA conditions. Map outlines as in Figure 2. Elevation contours as in Figure 1.

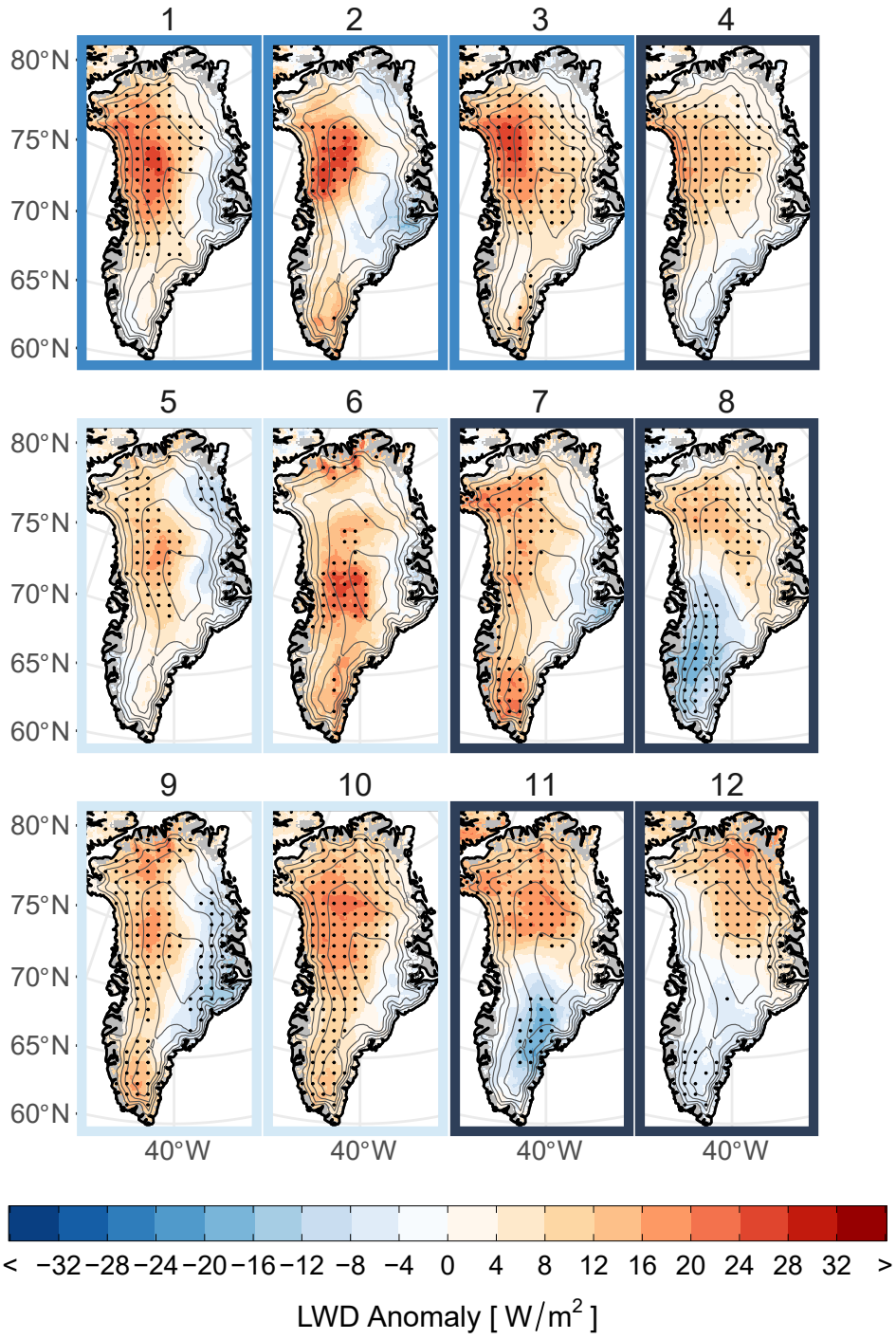


Figure 2.5: Anomalous LWD composited by SOM BMU. Map outlines as in Figure 2. Elevation contours as in Figure 1. Stippling as in Figure 4.

delivery through the Davis Strait after wrapping anticyclonically around the southern tip of Greenland from its origin over the northeast Atlantic. The resulting onshore moisture advection over northwest Greenland is favorable to cloud formation that would decrease SWD and increase LWD. Conversely, the cross-barrier IVT over northern Greenland is conducive to lee-side subsidence in northeast Greenland that would increase SWD and reduce LWD. Anomalous positive SHF is most evident in northeast Greenland, where relatively strong anomalies extend to elevations above 3000 m, and southwest Greenland, where they extend to above 2500 m (Figure 2.7).

The radiative terms in nodes 5 and 6 of SR patterns exhibit a similar west–east dipole as during CWB patterns (Figures 2.4, 2.5). However, as the ridge builds westward (Figures 2.2, 2.3; nodes 9,10), below-normal (above-normal) SWD (LWD) extends across northwest Greenland as the new ridge position allows for increased moisture transport through the Davis Strait (Figure 2.6). Coincidently, SWD and SHF increases along the southeast margin of the ice sheet as northwesterly winds downstream of the ridge axis generate downslope flow (Figures 2.2, 2.7).

Like SR and CWB patterns, there is a west–east oriented dipole in the anomalous radiative forcing associated with moisture delivery to northwest Greenland through the Davis Strait when Omega blocking is centered over eastern Greenland (Figures 2.4-2.6; nodes 4,7). As the ridge axis migrates west, southerly IVT to northwest Greenland gives way to northerly IVT over northern Greenland (Figures 2.2, 2.3, 2.6; nodes 8,11,12). Consequently, negative SWD anomalies extend across the northern ice sheet and positive SWD anomalies occupy the southern ice sheet, while the inverse pattern is apparent for LWD (Figures 2.4, 2.5). Above-normal SHF during Omega blocking is greatest in west-central ablation zone (Figure 2.7).

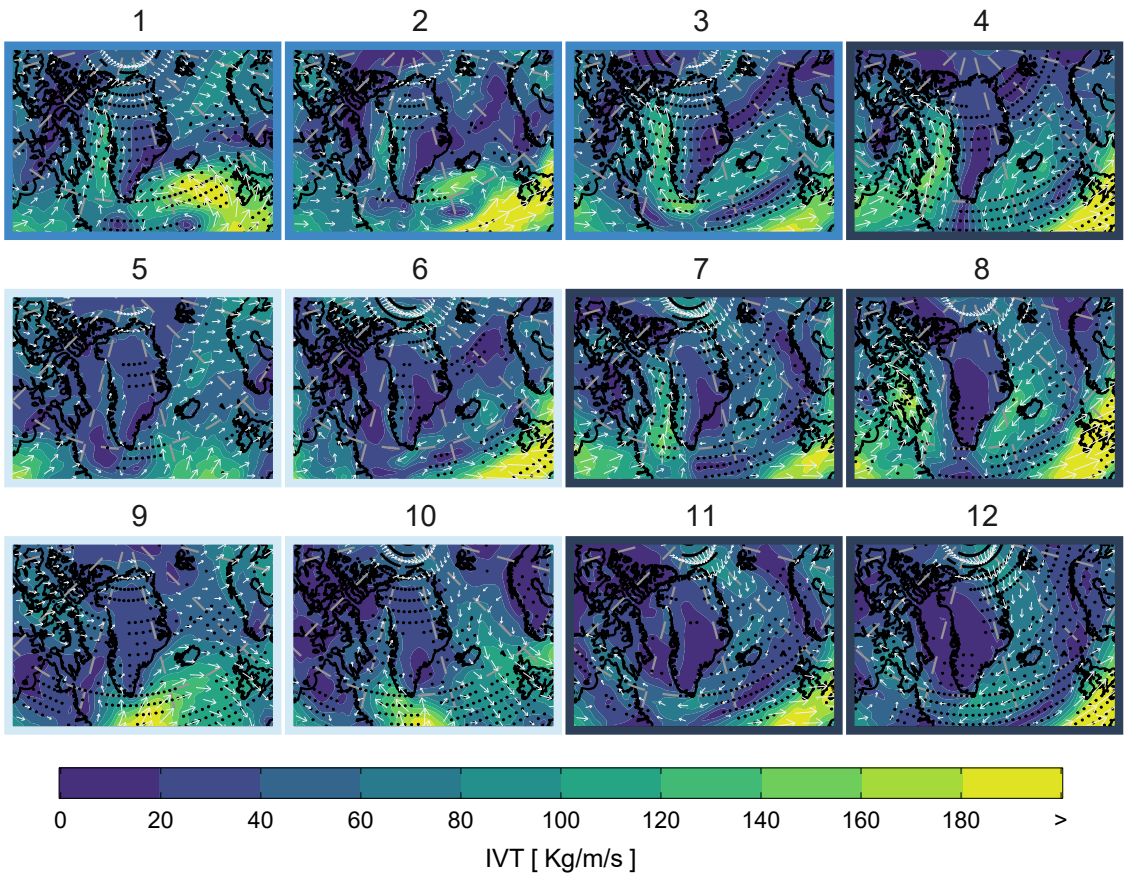


Figure 2.6: Magnitude (shading) and direction (vectors) of IVT composited by SOM BMU. IVT calculated from eastward and northward components of ERA5 vertical integral of water vapor flux. Vectors shown for $\geq 40\ kg\ m^{-1}\ s^{-1}$*. Map outlines as in Figure 2. Stippling as in Figure 4.*

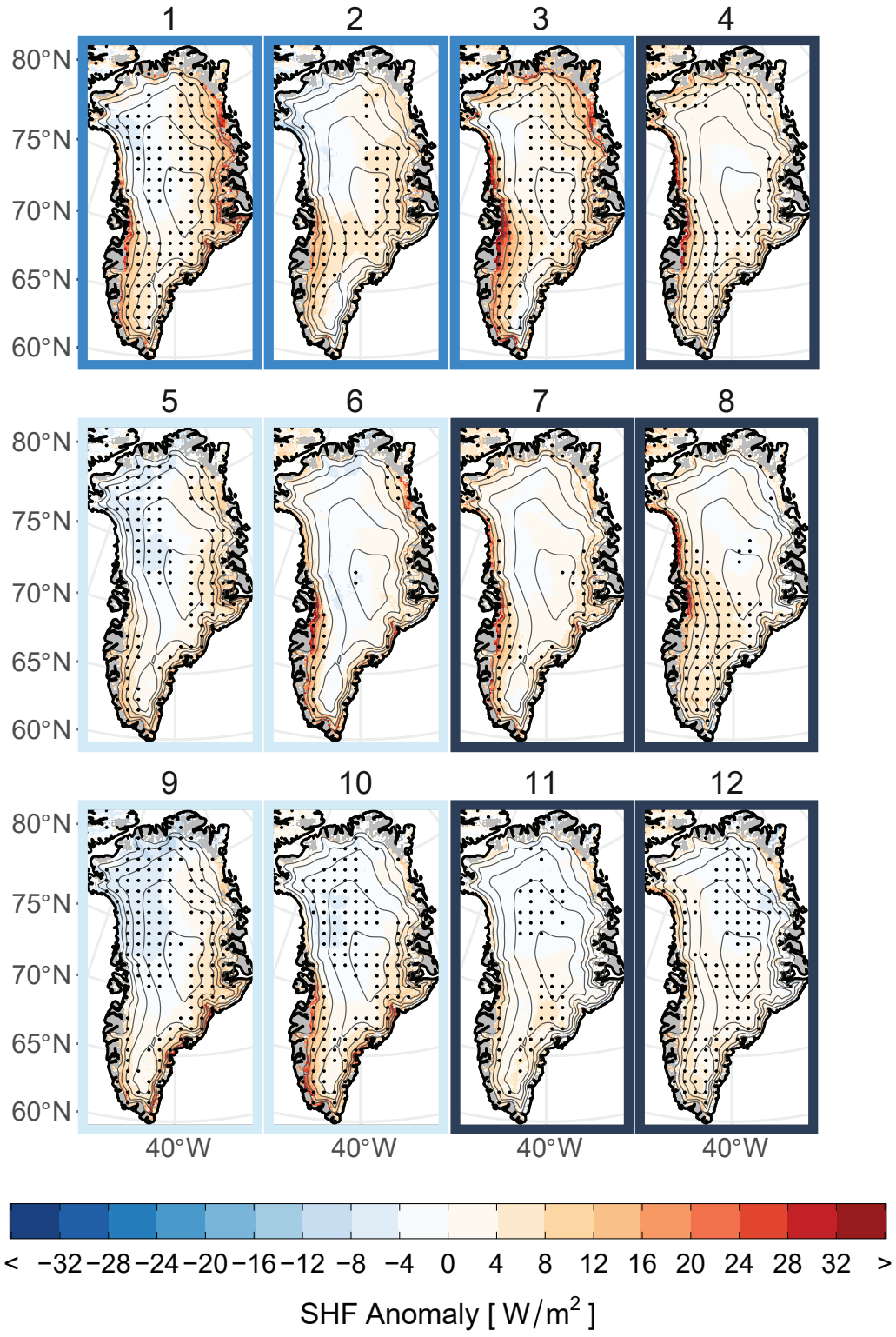


Figure 2.7: Anomalous SHF composited by SOM BMU. Map outlines as in Figure 2. Elevation contours as in Figure 1. Stippling as in Figure 4.

2.3.4 SMB response to Greenland blocking diversity

Focusing on the SMB response, anomalies above 1500 m are driven by changes in SF that align with onshore IVT (Figures 2.6, 2.8,Supplementary Figure 2.7). Blocking typically leads to an increase in SF over the northern ice sheet and a decrease over the southern ice sheet. The increase in SF and SMB above 1000 m in northwest Greenland is notably more extensive for CWB and SR blocks than Omega blocks. Strong, positive RF anomalies are generally limited to warmer locations below 2000 m (Supplementary Figure 2.8) and closely track locations of onshore moisture transport along the upstream flank of the blocking ridge (Figures 2.2, 2.6).

The spatial distribution of anomalous ME resembles that of below-normal SMB, except that ME anomalies extend to higher elevations where it is refrozen within the snowpack (Figure 2.8,Supplementary Figure 2.9), and there is strong agreement between the patterns of anomalous ME as simulated by MAR and the satellite record of anomalous melt frequency (Figure 2.2,Supplementary Figure 2.9). Below-normal SMB is predominantly focused below 1500 m along the narrow ablation zone (Figure 2.8), making it difficult to distinguish spatial differences in mass loss between blocking types. Recognizing that mass loss is driven by surface melt, we present the difference between the composite-mean ME for each node and the mean ME for all blocking episode days in Figure 2.9 to better highlight differences in melt production, and thus mass loss, between nodes.

The magnitude and extent of surface melt during CWB patterns is highly variable between individual nodes; however, nodes 1–3 consistently display enhanced ME in the eastern ablation zone relative to all blocking episode days (Figure 2.9). This appears to be driven by greater SWD (Figure 2.4) and enhanced SHF (Figure 2.7). Relative to all blocking episodes, SR patterns generate greater surface

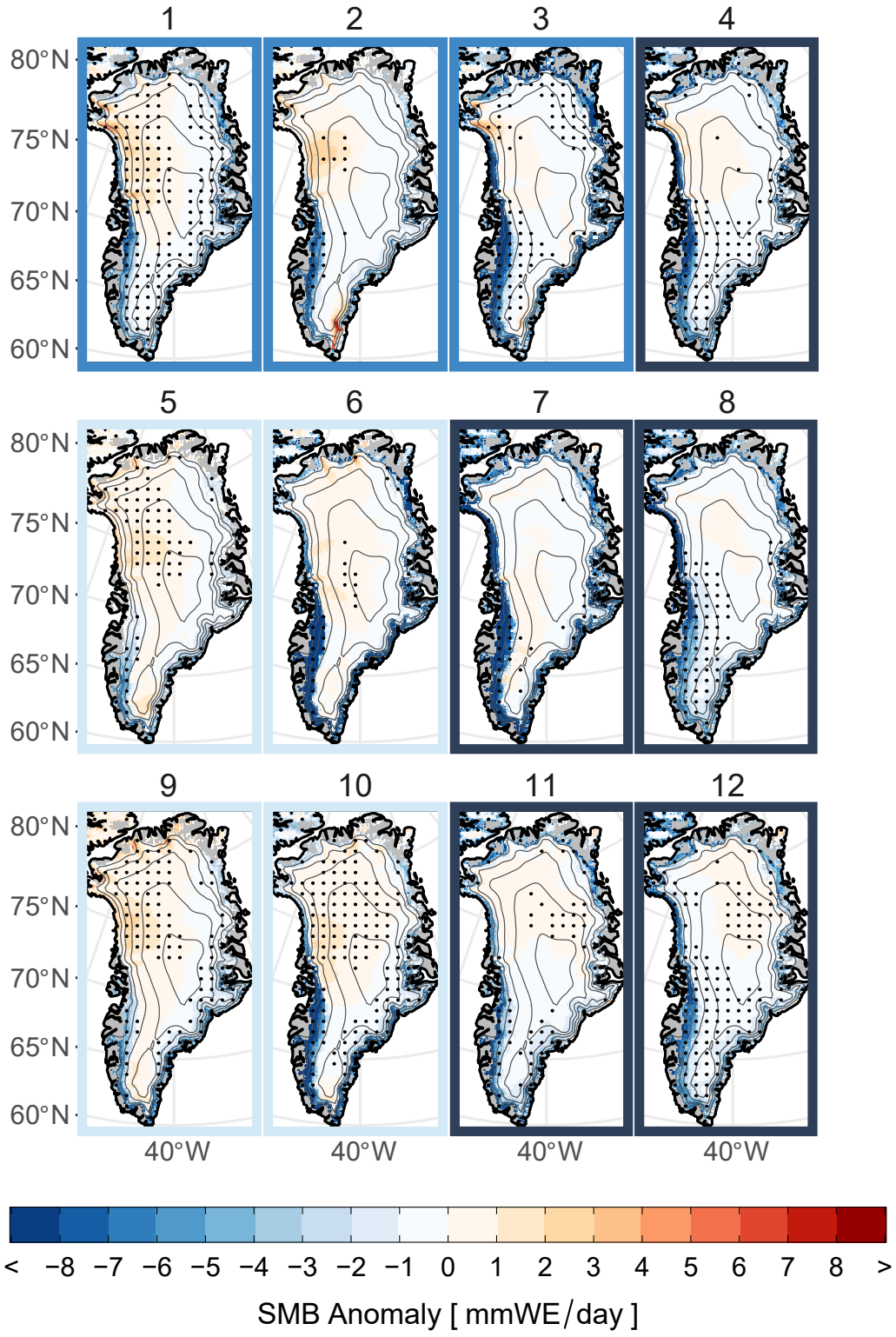


Figure 2.8: Anomalous SMB composited by SOM BMU. Map outlines as in Figure 2. Elevation contours as in Figure 1. Stippling as in Figure 4.

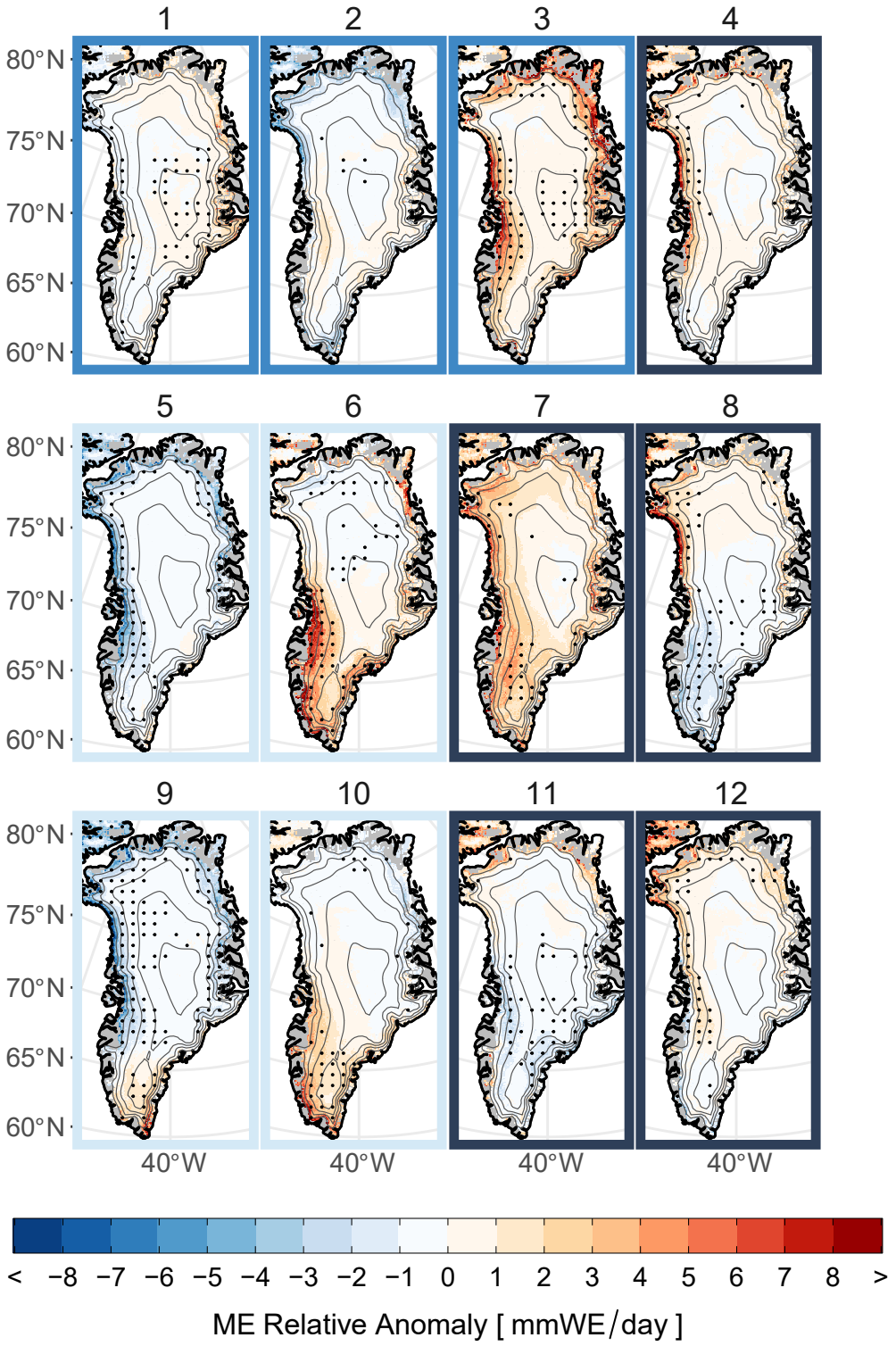


Figure 2.9: Composite-anomaly ME for each SOM node less the composite anomaly for all blocking episode days. Stippling indicates significant ($\alpha = 0.05$) differences between each node and all other blocking episode days. Map outlines as in Figure 2. Elevation contours as in Figure 1.

melt in southern Greenland, where the northernmost extent of the strongest melt anomalies closely tracks the position of the anticyclone (Figures 2.2, 2.9). Melt anomalies are greatest in the southwest ablation zone (Figure 2.9), where SR blocking is associated with increased LWD (Figure 2.5) and enhanced SHF (Figure 2.7). Omega blocking brings greater surface melt to northern Greenland than other blocking episodes (Figure 2.9), where the strongest ME is generally aligned with locations of enhanced LWD above 1000 m (Figure 2.5) and enhanced SHF below 1000 m (Figure 2.7). Nodes 7 and 8, in particular, show enhanced ME extending to $>$2000 m in northwest Greenland. Conversely, Omega blocks generally produce less meltwater across the southern ice sheet than other blocking episodes (Figure 2.9).

2.3.5 Partitioning long-term trends by blocking type

For each blocking type, we performed least-squares linear regression to quantify any long-term trend in the number of JJA blocking episode days per year from 1979 to 2019 (Supplementary Figure 2.10). The linear models indicate significant ($\alpha = 0.05$) positive trends of 0.22 Omega blocking episode days per year and 0.15 CWB days per year. Of the blocking episode days that occurred between 1979 and 1999, 37% were classified as Omega patterns, 27% as CWB, and 36% as SR. During 2000–2019, the percent of blocking episode days classified as Omega and CWB patterns increased to 40% and 32% respectively, while the share of SR patterns declined to 28%. Thus, higher-amplitude patterns have become more prevalent in recent years and Omega patterns have shown the strongest trend. Partitioning the data by month reveals that the trend in summer Omega blocking is driven by more frequent blocking later in the season, particularly in August, where over 80% of August Omega blocking episode days have occurred since the year 2000 (Supplementary Figure 2.10).

2.4 Discussion and Conclusions

This research documented the spatiotemporal diversity of summer Greenland blocking and its impact on the SEB/SMB of the GrIS. To this end, we identified Greenland blocking episodes using two complementary blocking metrics, then classified atmospheric circulation on blocking episode days into three primary blocking types and contrasted their respective SEB/SMB signatures. Referring to this new climatology, we now discuss potential dynamical and physical mechanisms behind the observed surface response and consider the implications of temporal variability and trends in blocking type for GrIS mass balance.

One feature of summer Greenland blocking that is apparent in the transition frequencies (Figures 2.2, 2.3) and confirmed in the lead-lag composites for GBI-PH03 overlap episodes (Supplementary Figure 2.3) is the retrograde motion of the blocking anticyclone—a feature that is particularly evident during Omega blocks. This behavior has been observed in previous work and attributed to the influence of transient, synoptic-scale eddy forcing of the blocking high (Hanna et al., 2018b; Luo, 2005; Luo & Yao, 2014; Mullen, 1987; Overland et al., 2021). Recent efforts have specifically highlighted the role of moist dynamics, where divergent outflow aloft associated with diabatic ascent in the warm conveyor belt of an approaching cyclone advects low potential vorticity air westward, acting to extend the blocking ridge against the background westerly flow (Pfahl et al., 2015; Steinfeld & Pfahl, 2019). These diabatic processes play a larger role in North Atlantic blocking than in other regions (Steinfeld & Pfahl, 2019), which could help explain the robust westward progression of Greenland blocks.

The retrograde motion of Greenland blocks is evident in the temporal progression of the SEB anomalies. This is particularly apparent for Omega blocks, during which the radiative anomalies exhibit a west-east dipole pattern when the

ridge is positioned to the east that is consistent with previous work documenting the cloud radiative effects of blocking highs over southeast Greenland (Ward et al., 2020). Southerly moisture advection along Greenland's west coast gives way to moisture delivery across the northern shoreline as the block tracks west and Greenland becomes embedded in northerly flow on the downstream side of the ridge (Figures 2.2, 2.6). The resulting onshore flow brings positive LWD anomalies to the Northern half of the GrIS with enhanced SWD to the south (Figures 2.4, 2.5)—a SEB signature that resembles previously documented cloud radiative effects accompanying adiabatic ascent (descent) of the northern (southern) GrIS during extreme GBI events (Hahn et al., 2020). Thus, the position of the blocking anticyclone exerts a critical influence on the SEB signature by dictating the interplay between GrIS topography, the path of moisture transport, and the extent of large-scale subsidence.

Generally, surface melt during summer Greenland blocking drives mass loss that is greatest at lower elevations and collocated with regions of anomalous SHF (Figures 2.7–2.9); however, this low-elevation mass loss also aligns with regions of reduced albedo (Supplementary Figure 2.11) and above-normal absorbed shortwave radiation (Supplementary Figure 2.12). Thus, the ice-albedo effect (e.g., either due to grain size metamorphism or to the appearance of liquid water on the surface) is likely a key factor in producing the observed surface melt patterns. For example, it appears non-radiative fluxes may initiate melt and lower the surface albedo, allowing for above-normal absorbed shortwave radiation even in regions with cloud-related reductions in SWD (Figure 2.4, Supplementary Figure 2.12). These findings align with work demonstrating that turbulent heat flux and net shortwave radiation drive melt in the ablation zone (Fausto et al., 2016a; Fausto et al., 2016b; Wang et al., 2021).

The SOM analysis revealed notable differences in surface melt and associated mass loss between blocking types. Intense moisture transport into Baffin Bay and western Greenland is typically facilitated by cyclonic Rossby wave breaking (Liu & Barnes, 2015)—a dynamical process that is apparent in the IVT anomalies associated with CWB patterns (Figure 2.6, nodes 1–3). Relative to all blocking episodes, however, CWB patterns consistently produce greater ME in northeast Greenland through an increase in lee side SHF and SWD that is concomitant with westerly IVT poleward of the ridge (Figures 2.4, 2.6, 2.7). Our results therefore corroborate previous work demonstrating that melt of the northeast GrIS is supported by a Foehn effect whereby westerly flow suppresses cloud cover and mixes warm air to surface as it descends the lee side of the ice sheet (Cullather & Nowicki, 2018; Mattingly et al., 2020; Noël et al., 2019).

The lower amplitude of SR patterns produces inland moisture transport at lower latitudes of the GrIS, which drives relatively more ME in southern Greenland by increasing SHF and LWD over the southwest ablation zone—results that support previous work on the role of intense moisture transport and attendant opaque cloud cover in producing exceptional mass loss over the southwest GrIS (Doyle et al., 2015; Gallagher et al., 2020; Neff, 2018). That these processes produce more melt over the southern ice sheet than higher-amplitude Omega patterns that bring anomalous SWD demonstrates that turbulent heat flux and cloud-longwave radiation can combine to produce greater mass loss, even in the lower-albedo ablation zone where shortwave cloud radiative effects normally dominate (Wang et al., 2019). A closer look at the SR transition frequencies suggests cloud-longwave forcing may play a greater role earlier in the progression of the block. Nodes 5 and 9 display positive LWD anomalies accompanying enhanced IVT over the southwest ablation zone (Figures 2.5, 2.6). These nodes then typically transition to node 10 where a stark decline in surface albedo results in strong positive anomalies in

absorbed shortwave radiation despite below-to-near-normal values of SWD (Figure 2.4, Supplementary Figures 2.11, 2.12). This temporal progression is suggestive of the hypothesis offered in Mattingly et al. (2020) that intense water vapor transport at blocking onset may act to precondition the GrIS, allowing for greater absorbed shortwave radiation as the block matures.

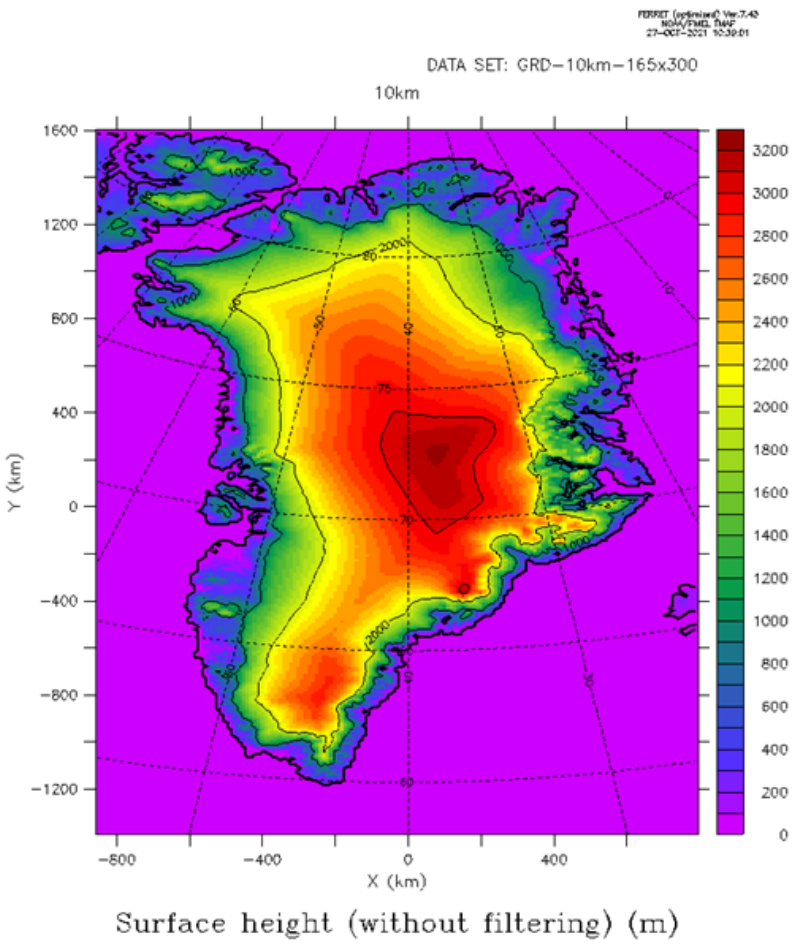
Conversely, the higher amplitude of Omega blocks supports relatively high melt in northern Greenland that is collocated with areas of enhanced SHF and above-normal LWD (Figures 2.5, 2.7), pointing to the importance of cloud-longwave radiative effects to melt production in this region of high surface albedo (Noël et al., 2019; Wang et al., 2019). Furthermore, while SR and CWB patterns both produced above-normal SF at elevations > 1000 m in northwest Greenland that, to some degree, compensate for mass loss elsewhere, above-normal SF contributions were far less prevalent during Omega patterns (Figure 2.8, Supplementary Figure 2.7).

While these findings describe the characteristic Greenland blocking types and their typical progression, it is important to note that the behavior of individual blocking episodes may deviate from the description presented here. Furthermore, the blocking detection criteria employed in this analysis may not capture all significant dynamical situations relating to GrIS mass loss. For example, intense moisture delivery upstream of an open ridge that did not meet the blocking episode duration criterion applied here was responsible for an exceptional rainfall event in late August of 2011 that produced 8–15% of the annual surface melt measured at locations along the Kangerlussuaq sector in southwest Greenland (Doyle et al., 2015; Neff, 2018). However, while it was not included in our classification, we note that this melt event was dominated by turbulent heat flux and longwave radiative forcing (Doyle et al., 2015), which is consistent with the mechanisms of melt in southwest Greenland during SR events.

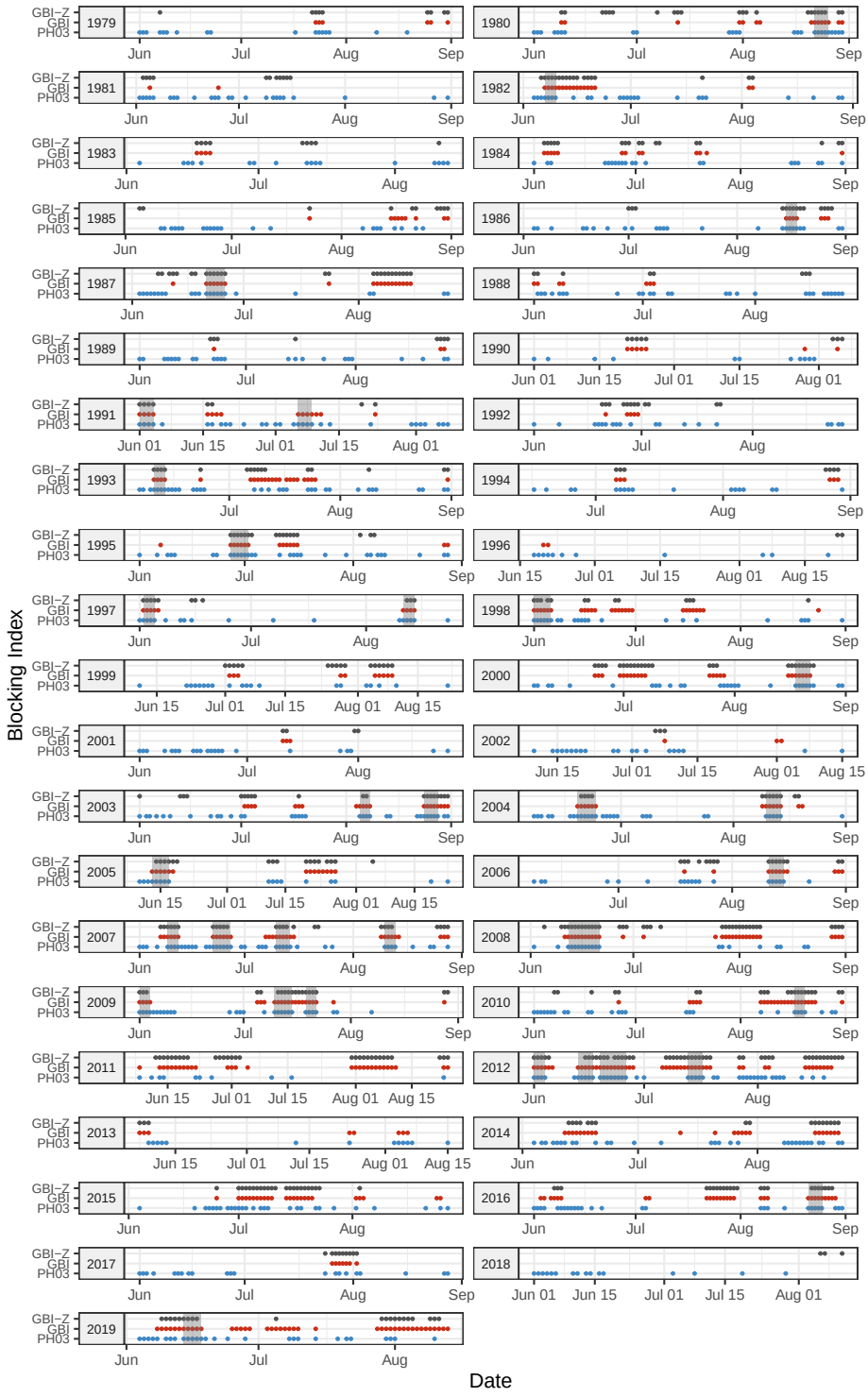
It is well documented that the sharp decline in GrIS SMB since the turn of the century has coincided with a more persistently negative North Atlantic Oscillation and a rise in Greenland blocking frequency (Bevis et al., 2019; Fettweis et al., 2013; Hanna et al., 2018a; McLeod & Mote, 2016; van Angelen et al., 2014). Our results demonstrate more precisely that this increase in Greenland blocking was primarily driven by an increase in Omega patterns (Supplementary Figure 2.10). Furthermore, because the GBI is an integrated measure of the extent and magnitude of high pressure over Greenland, efforts to quantify blocking frequency using this metric are prone to emphasize Omega patterns because they are more likely to produce above-normal pressure throughout the domain. That the GBI is biased toward Omega patterns likely contributes to the fact that it shows a stronger positive trend in recent decades than other metrics (Wachowicz et al., 2021), such as PH03, that more frequently identify CWB and lower-amplitude SR patterns.

Recent modeling efforts have demonstrated that accelerated SMB decline has been driven by a disproportionate increase in surface melt and runoff from northcentral and northwestern drainages of the ice sheet (Noël et al., 2019). Furthermore, these same efforts show that augmented runoff in northern Greenland is a consequence of enhanced longwave radiative forcing over the northern ice sheet in recent decades that has caused the rapid ablation of snow cover and exposure of the underlying glacial ice at lower elevations while also reducing diurnal variability in surface temperature and thus meltwater refreeze at higher elevations. We show that Omega blocks, specifically, enhance LWD and generate greater surface melt over the northern ice sheet than other blocking types which, in turn, depresses the surface albedo (Supplementary Figure 2.11). Thus, our results suggest that the increase in Omega patterns since the turn of the century has played a central role in augmenting GrIS mass loss.

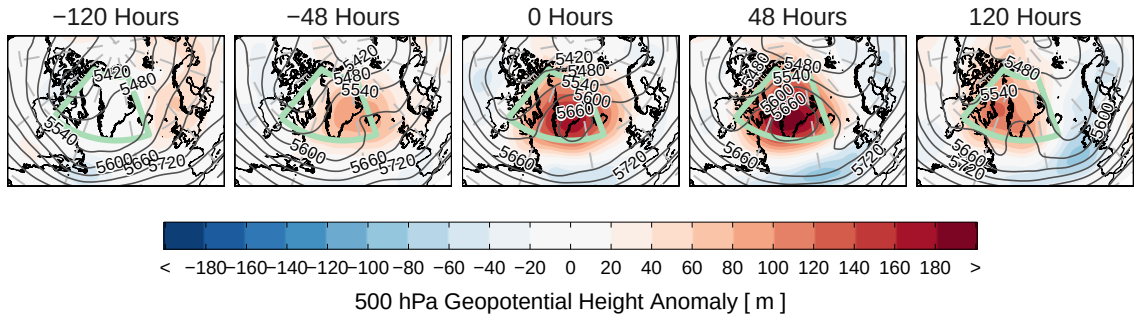
These results underscore the importance of considering the range of atmospheric settings that can be considered blocked flow. Changes in the character of blocking, such as an increase in amplitude or a shift in the predominate ridge-trough configuration, can have substantial, application- and site-specific consequences even if there is little change in overall blocking frequency. Researchers should be cognizant of these factors and how a chosen blocking metric may emphasize or obfuscate impacts on relevant physical processes when investigating trends in blocking.



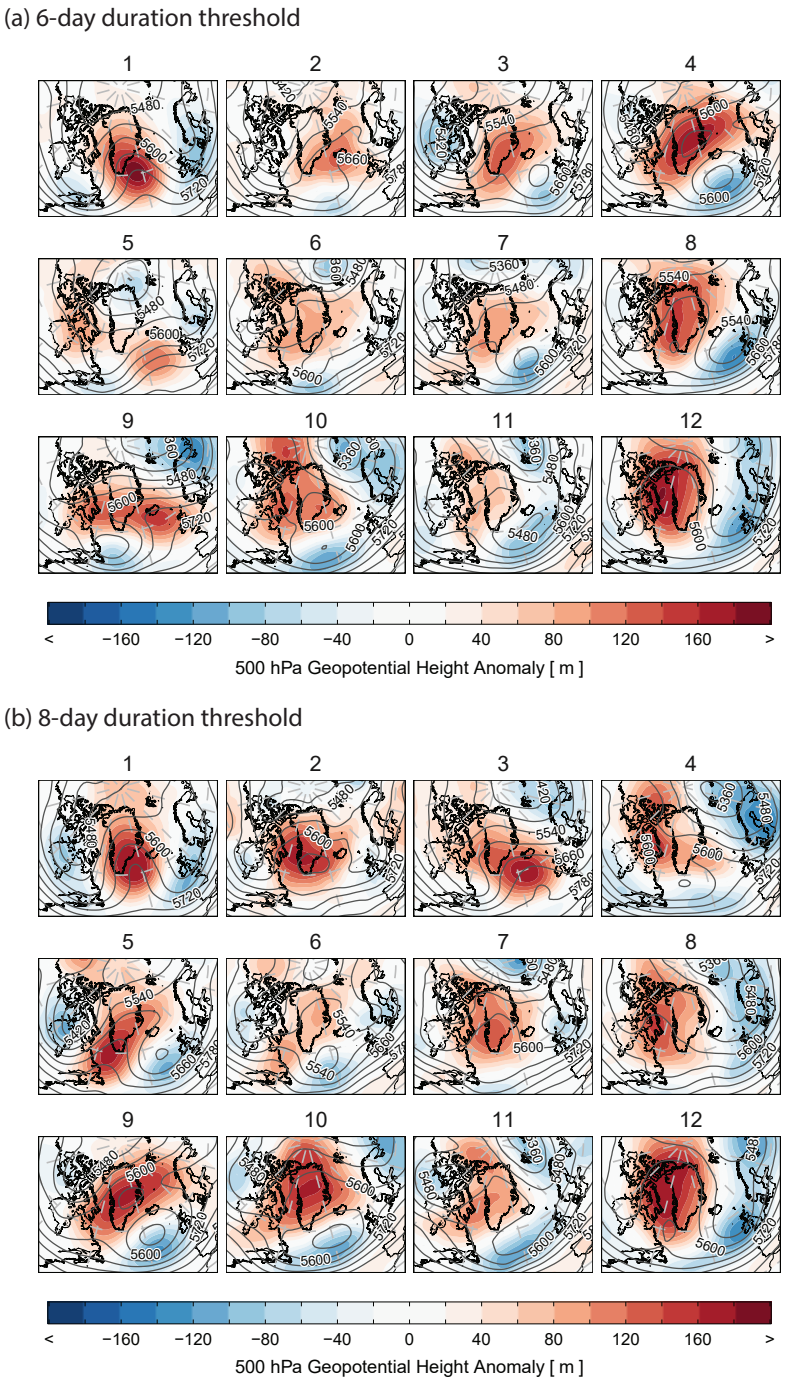
Supplementary Figure 2.1: Integration domain for the MARv3.11 output utilized in the analysis.



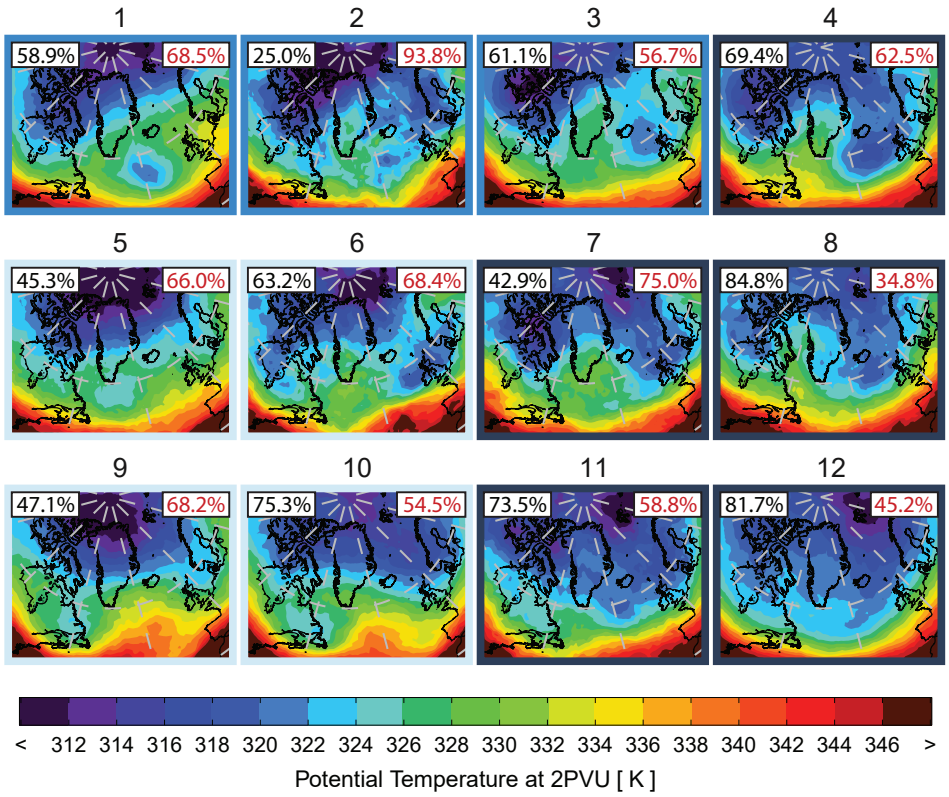
Supplementary Figure 2.2: All instances of large-scale blocking as identified by PH03 (blue), GBI (red), and GBI-Z (black) from 1979–2019. Gray shading marks GBI-PH03 overlap blocking episodes.



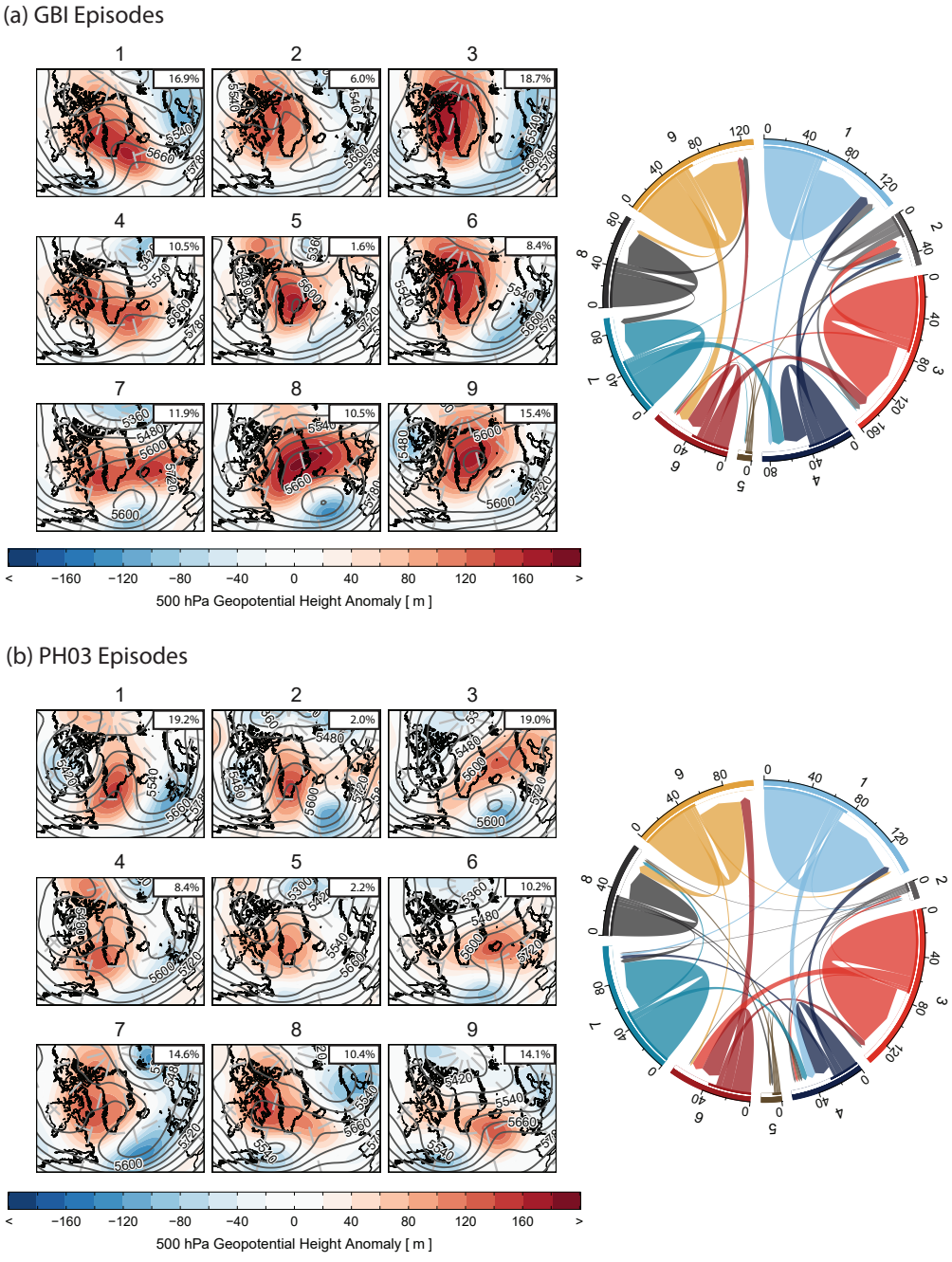
Supplementary Figure 2.3: 5-day lead-lag of composite-anomaly (shading) and composite-mean (contour with interval of 60 m) 500 hPa geopotential height for GBI-PH03 overlap blocking episodes. Lags noted at top of each plot are with respect to the first day of overlap between PH03 and GBI for each event. Teal polygon delineates the GBI domain.



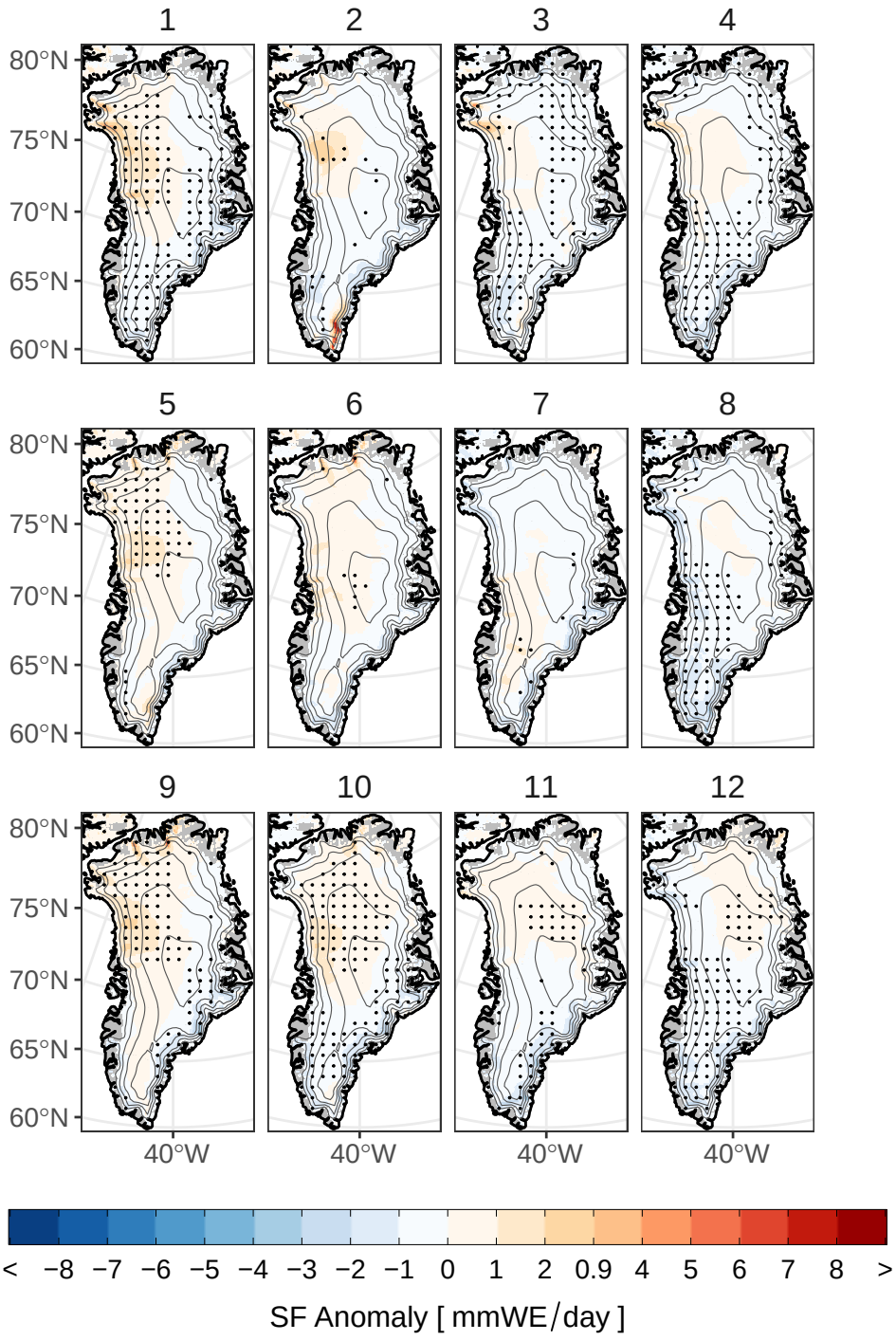
Supplementary Figure 2.4: Composite anomalies (shading) and composite means (contours: 60m interval) of 500 hPa geopotential height for all JJA blocking episode days identified using a blocking episode duration criterion of (a) 6 days and (b) 8 days. Anomalies were calculated with respect to the 1981–2010 long-term daily mean and values were composited by SOM BMU.



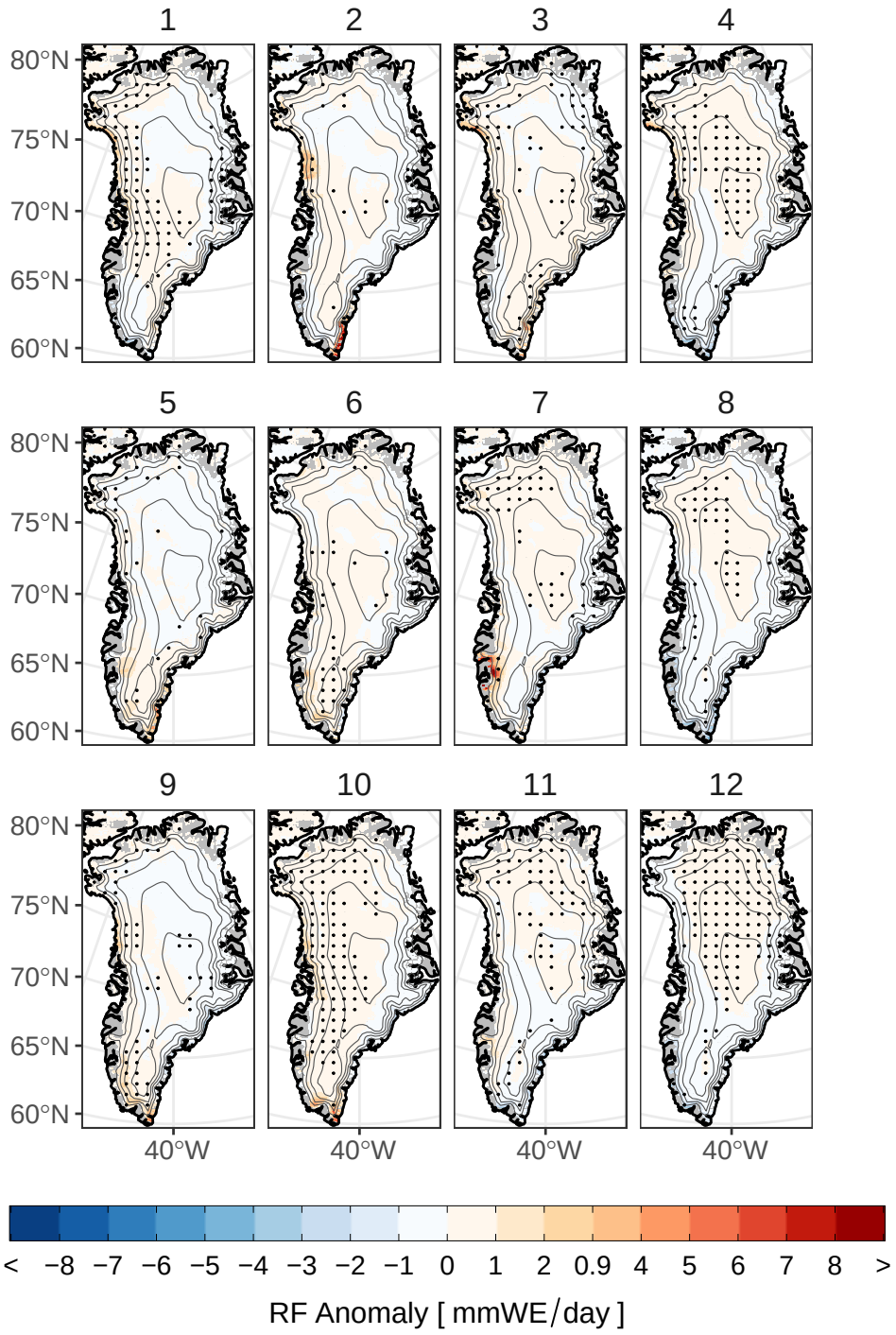
Supplementary Figure 2.5: Composite anomalies (shading) potential temperature at 2 PVU for all blocking event days identified separately by PH03 and GBI and composited by SOM BMU. The percentage of all days assigned to each node that were identified by the GBI (PH03) is displayed in black (red) in the upper left (right) corner of each map. Map outline colors are as in Figure 2.



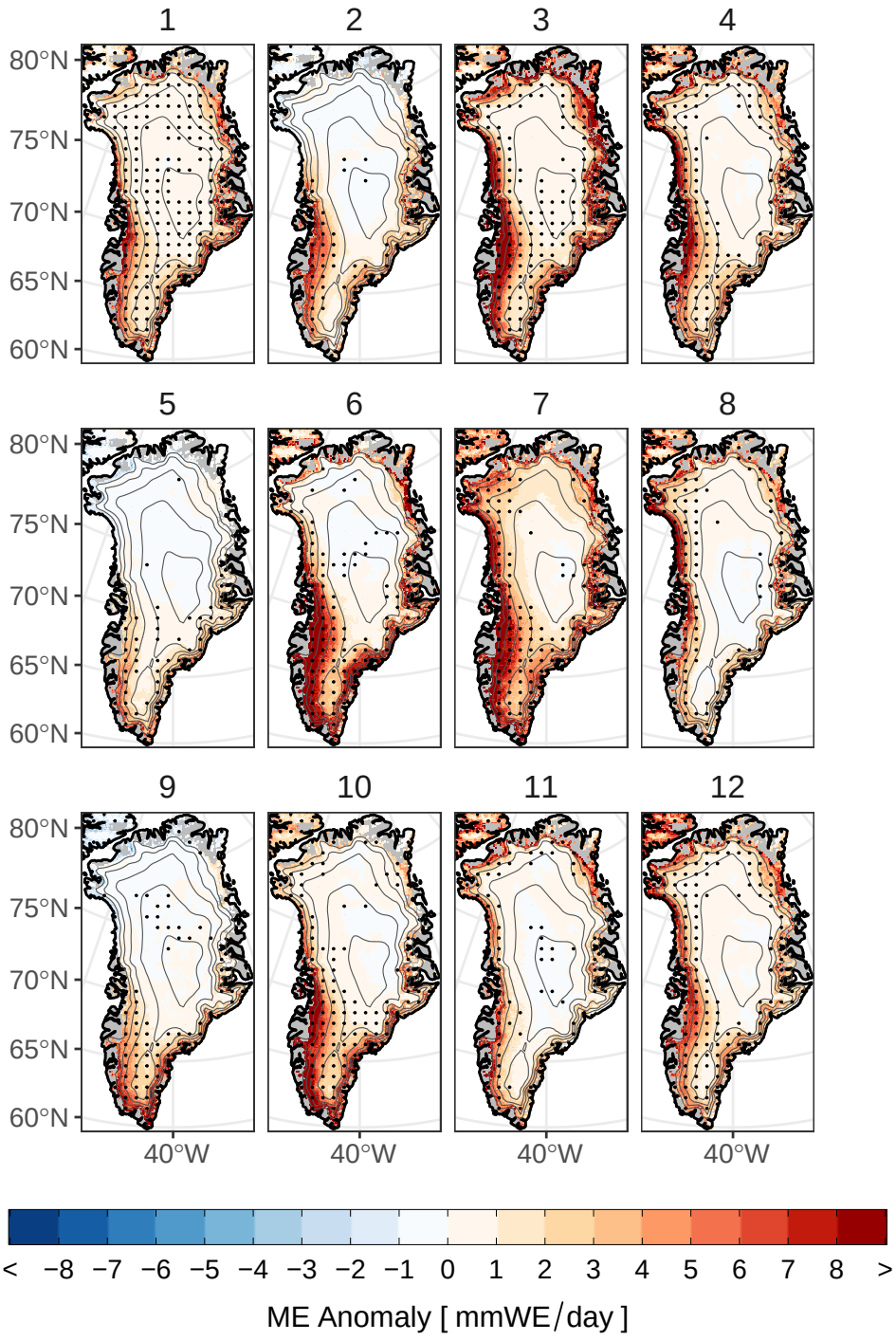
Supplementary Figure 2.6: Left: Composite anomalies (shading) and composite means (contours: 60 m interval) of 500 hPa geopotential height for all JJA blocking episode days identified by GBI (top row) and PH03 (bottom row). Values were composited according to each day's BMU for SOMs conducted separately for each blocking index. The frequency of each node with respect to all blocking episode days identified by each index is displayed in the upper right corner. Right: Chord diagrams illustrating the transitions between nodes for each SOM (symbolized as in Figure 3).



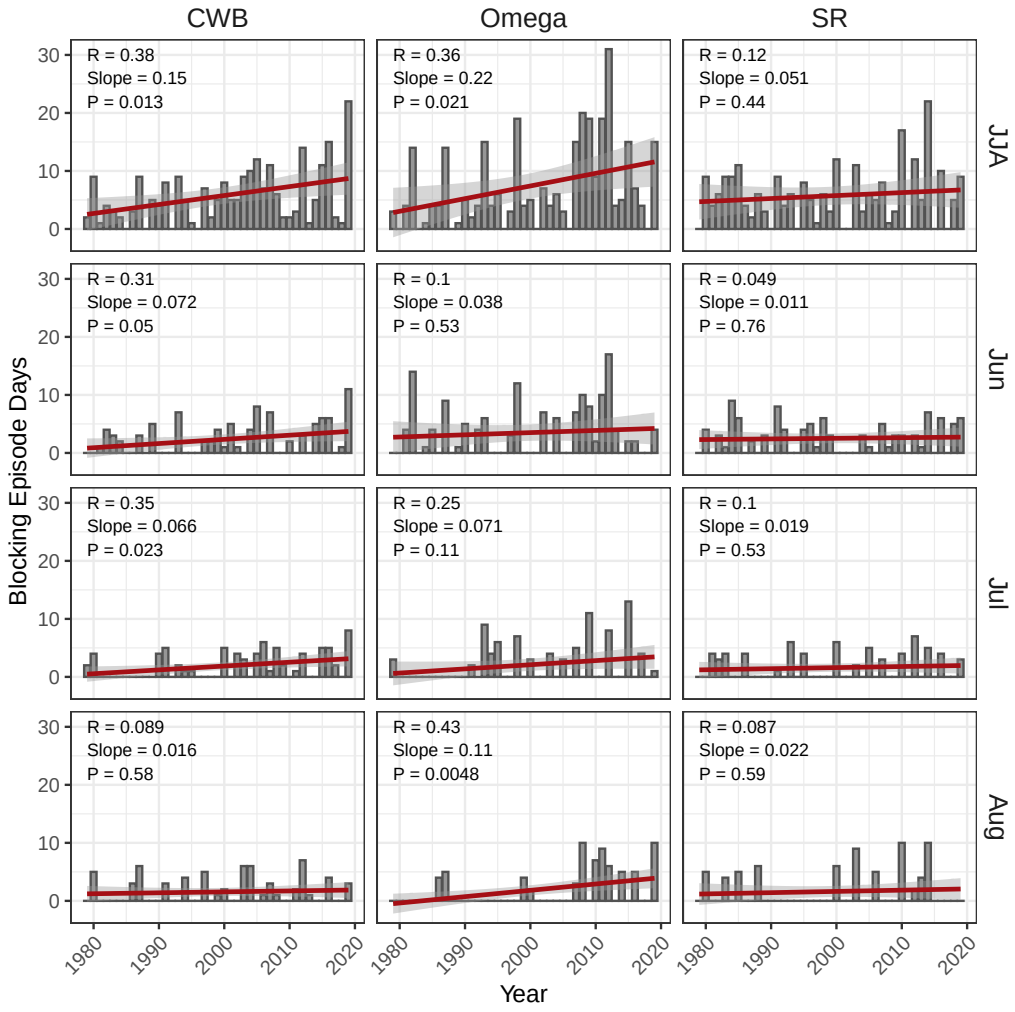
Supplementary Figure 2.7: Anomalous snowfall (SF) composited by SOM node. Contours denote MAR elevation data. Contour interval of 500 m from 1000–3000 m. Stippling indicates significant difference between days assigned to given node and 1981–2010 JJA conditions at 95% confidence level.



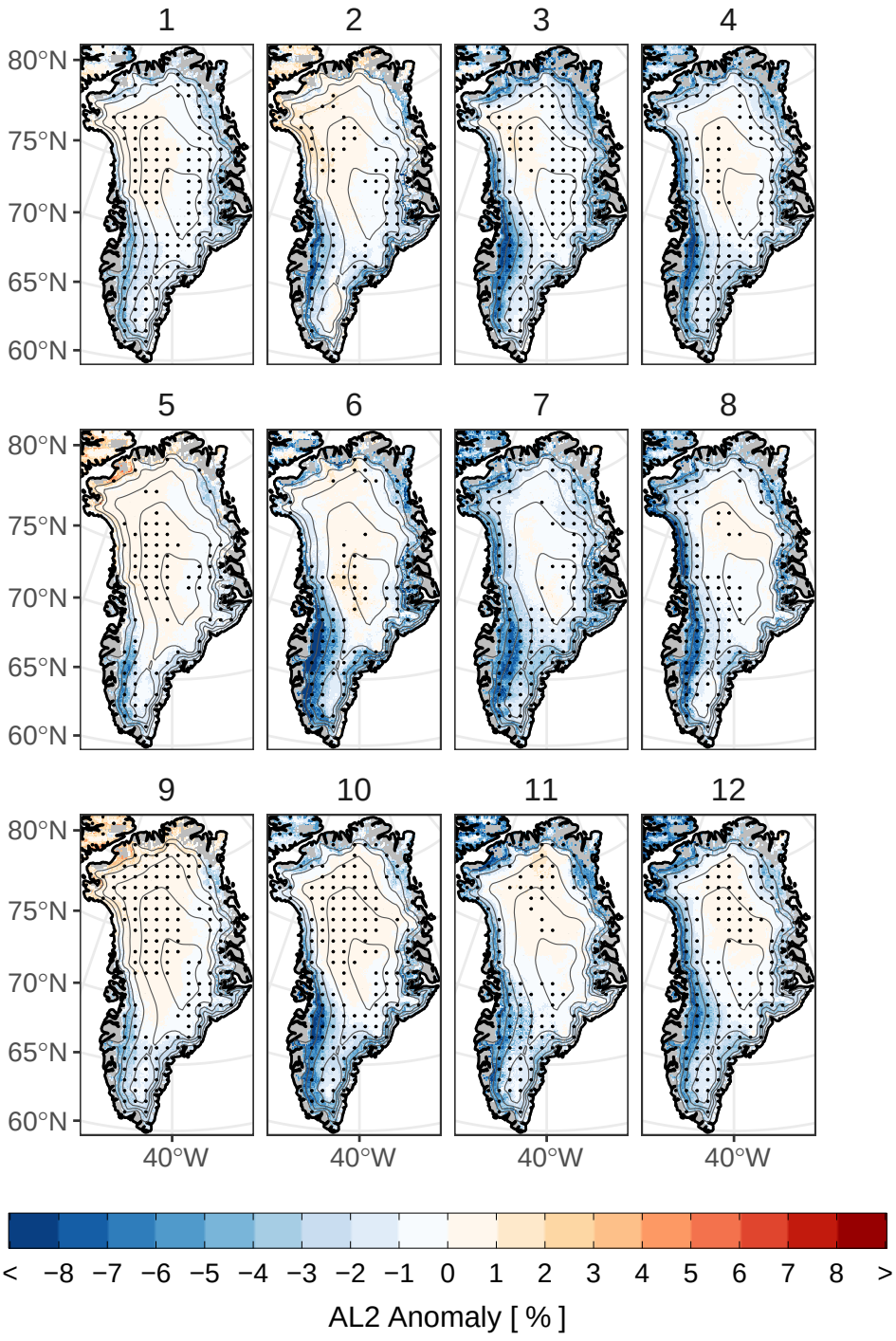
Supplementary Figure 2.8: Anomalous rainfall (RF) composited by SOM node. contours denote MAR elevation data. Contour interval of 500 m from 1000–3000 m. Stippling indicates significant difference between days assigned to given node and 1981–2010 JJA conditions at 95% confidence level.



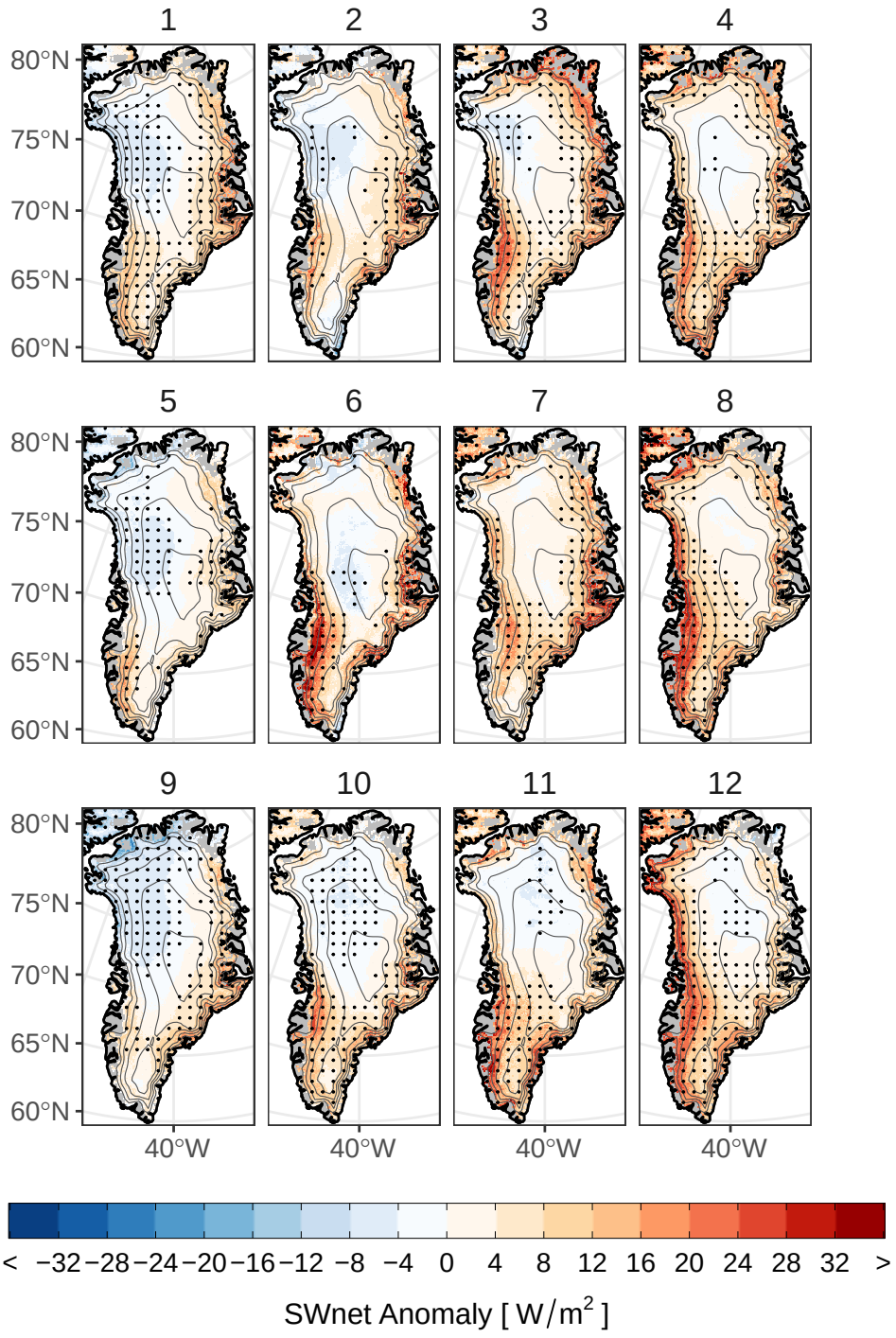
Supplementary Figure 2.9: Anomalous meltwater production (ME) composited by SOM node. Contours denote MAR elevation data. Contour interval of 500 m from 1000–3000 m. Stippling indicates significant difference between days assigned to given node and 1981–2010 JJA conditions at 95% confidence level.



Supplementary Figure 2.10: Number of blocking episode days per year (bars) and long-term linear trends (red lines) for each blocking type (columns) during JJA and for each month individually (rows). Shading indicates 95% confidence level for the best-fit lines. The Pearson's correlation coefficient (R), slope, and p-value (P) of the linear models are annotated in the upper-left corner of each panel.



Supplementary Figure 2.11: Anomalous surface albedo (AL2) composited by SOM node. contours denote MAR elevation data. Contour interval of 500 m from 1000–3000 m. Stippling indicates significant difference between days assigned to given node and 1981–2010 JJA conditions at 95% confidence level.



Supplementary Figure 2.12: Anomalous absorbed shortwave (SWnet) composited by SOM node. contours denote MAR elevation data. Contour interval of 500 m from 1000–3000 m. Stippling indicates significant difference between days assigned to given node and 1981–2010 JJA conditions at 95% confidence level.

CHAPTER 3

SUMMER ATMOSPHERIC CIRCULATION OVER GREENLAND IN RESPONSE TO ARCTIC AMPLIFICATION AND DIMINISHED SPRING SNOW COVER[2]

[2]Preece, J. R., Mote, T. L., Cohen, J., Wachowicz, L. J., Knox, J. A., & Tedesco, M. Submitted to Nature Communications.

Abstract

The exceptional atmospheric conditions that have accelerated Greenland Ice Sheet mass loss in recent decades have been repeatedly recognized as a possible dynamical response to Arctic amplification. In investigating such a relationship, this analysis reveals two potentially synergistic mechanisms linking high latitude warming to the observed increase in Greenland blocking. Consistent with a prominent hypothesis associating Arctic amplification and persistent weather extremes, we find that the summer atmospheric circulation over the North Atlantic has become wavier and link this wavier flow to more prevalent Greenland blocking. A concomitant decline in terrestrial snow cover has likely contributed to this mechanism by further amplifying warming at high latitudes; however, we also identify a direct stationary Rossby wave response to low spring North American snow cover that enforces an anomalous anticyclone over Greenland, thus helping to anchor the ridge over Greenland in this wavier atmospheric state.

3.1 Introduction

Summer atmospheric circulation in the Northern Hemisphere has undergone a pronounced shift in recent decades. Nowhere has this been more apparent than over the North Atlantic. Observations have revealed a more prevalent negative phase of the North Atlantic Oscillation (NAO) since the turn of the century and a coincident increase in the frequency of anomalous quasi-stationary anticyclonic conditions—known as atmospheric blocking—over Greenland (Bevis et al., 2019; Fettweis et al., 2013; Hanna et al., 2016; Hanna et al., 2018b).

Greenland blocking episodes transport warm, moist air from lower latitudes, which promotes widespread melt of the Greenland Ice Sheet (GrIS) through a spatially variable surface energy balance response and consequent positive feedback mechanisms (Hahn et al., 2020; Henderson et al., 2021; Mattingly et al., 2018; McLeod & Mote, 2016; Nghiem et al., 2012; Preece et al., 2022; Tedesco & Fettweis, 2020; Tedesco et al., 2016). Indeed, this dynamical forcing of the GrIS has been a primary cause of accelerating surface runoff in recent decades (Bevis et al., 2019; Fettweis et al., 2013; Hofer et al., 2017; IMBIE Team, 2020), and it has been estimated that a continuation of these more frequent anticyclonic conditions would result in approximately twice the surface mass loss projected by global climate models (Delhasse et al., 2018), which collectively fail to capture the observed shift in atmospheric circulation over Greenland (Delhasse et al., 2021; Fettweis et al., 2013; Hanna et al., 2018a). This bias has clear far-reaching implications, as it has caused even the upper range of climate projections to underestimate the contribution of GrIS surface runoff to global sea-level rise (Slater et al., 2020). Therefore, it is of critical importance to understand whether these observed changes are merely a temporary manifestation of internal variability or a continuing consequence of anthropogenic climate change.

One active area of research aims to determine whether Arctic Amplification (AA)—i.e., an elevated rate of warming at high latitudes relative to low latitudes under global climate change —causes more frequent weather extremes. A prominent hypothesis underlying this area of research contends that the reduced meridional temperature gradient caused by AA results in weaker westerlies, as dictated by the thermal wind relation, and a higher amplitude—or wavier—jet that propagates downstream more slowly, thus favoring persistent extremes such as those associated with atmospheric blocking (Francis & Vavrus, 2012). While immediate follow-up studies argued that initial results supporting this hypothesis were likely an artificial byproduct of methodology (see Barnes, 2013; Screen & Simmonds, 2013), subsequent efforts have applied more robust measures of waviness, yielding statistically significant positive trends over regional domains spanning North America in summer (Di Capua & Coumou, 2016; Vavrus et al., 2017), and the North Atlantic in both summer and winter (Cattiaux et al., 2016). However, previous studies have not focused on Greenland, as the regions examined have tended to dissect Greenland itself.

In what appears to be both a symptom and source of AA, there have been dramatic losses of both sea ice and snow cover since the second half of the 20th century (Cohen et al., 2014; Derksen & Brown, 2012; Estilow et al., 2015; Stroeve & Notz, 2018). Cryospheric response to a warming climate constitutes a positive feedback mechanism that is one of the earliest recognized sources of AA—global warming leads to retreating snow and ice cover, which lowers the surface albedo, allowing for greater absorbed shortwave radiation and further warming at high latitudes (Budyko, 1969; Pithan & Mauritsen, 2014; Serreze & Barry, 2011). Thus, diminishing sea ice and snow cover represent an important contribution to the proposed mechanism of increased waviness under AA.

Retreating snow and ice cover under AA may also impact atmospheric circulation through more direct surface-atmosphere coupling. Regional changes in snow or ice cover can elicit a stationary Rossby wave train through anomalous diabatic heating of the lower troposphere (Alexander et al., 2010; Cohen et al., 2021). Such a stationary wave response has been documented during winter in association with sea ice variability in the Sea of Okhotsk (Honda et al., 1999) as well the Barents and Kara seas (Honda et al., 2009). In summer, however, the thermal gradient between the ocean and overlying atmosphere—and thus the flux of energy between them—is minimized (Screen, 2017). Furthermore, the summer atmosphere is more sensitive to changes in terrestrial snow cover and associated soil moisture anomalies (Coumou et al., 2018), and it has been suggested that the rapid decline of spring snow cover under AA may be a primary contributor to the recent shift in summer atmospheric circulation (Overland et al., 2012).

Spring snow cover extent (SCE) has been shown to influence summer atmospheric circulation through its residual impact on soil moisture. In what is referred to as the snow-hydrological effect, anomalously low spring SCE leads to earlier depletion of soil moisture, resulting in greater sensible heating of the atmosphere in summer (Matsumura & Yamazaki, 2012; Matsumura et al., 2010; Yasunari et al., 1991), which can then influence the generation of Rossby waves. Indeed, early snowmelt over Eurasia has been linked to a stationary wave response that persists through summer with increased blocking over eastern Siberia and enhanced ridging over southeast Greenland in September (Matsumura & Yamazaki, 2012). These results suggest that spring SCE may exert a delayed influence on atmospheric circulation over Greenland; however, there has not yet been a direct investigation of possible teleconnections linking snow cover variability and Greenland blocking.

Here, we first document trends in atmospheric waviness spanning a Greenland-centered North Atlantic domain. We then look for evidence of a direct stationary

wave response to regional SCE anomalies as a potential explanation for more prevalent anticyclonic conditions over Greenland in summer. In examining these two phenomena together, we explore the hypothesis that AA has caused an increase in waviness over the North Atlantic and that, under this wavier flow regime, the stationary wave response to concomitant reductions in SCE has encouraged ridging, specifically, over Greenland.

3.2 Results

3.2.1 Summer sinuosity over the North Atlantic and its relation to Greenland blocking

To quantify the waviness of the upper-level flow in the region, we employ the sinuosity index (Cattiaux et al., 2016; Vavrus et al., 2017) over a Greenland-centered North Atlantic domain spanning 0–90°W (Figure 3.1). The sinuosity index is analogous to the index of the same name used in fluvial geomorphology that measures the degree to which a stream meanders by taking the ratio of the length along the stream bed to the valley, or straight-line, length (Vavrus et al., 2017). As such, a high sinuosity represents a stream that meanders more while a minimum possible sinuosity of one represents straight-channel flow. When applied to the atmosphere, sinuosity measures the meanders of a given isohypse (S_i) and atmospheric waviness can be quantified using the aggregate sinuosity (S_{ag}) of a selection of isohypses spanning the midlatitudes (Vavrus et al., 2017).

Over the 1979–2019 study period, JJA is the only standard meteorological season with a statistically discernible trend in S_{ag}. A linear regression of mean JJA S_{ag} against time shows an increase of 0.33 standard deviation (SD) per decade that is significant at the 95% confidence level (Supplementary Table 3.1). Examining

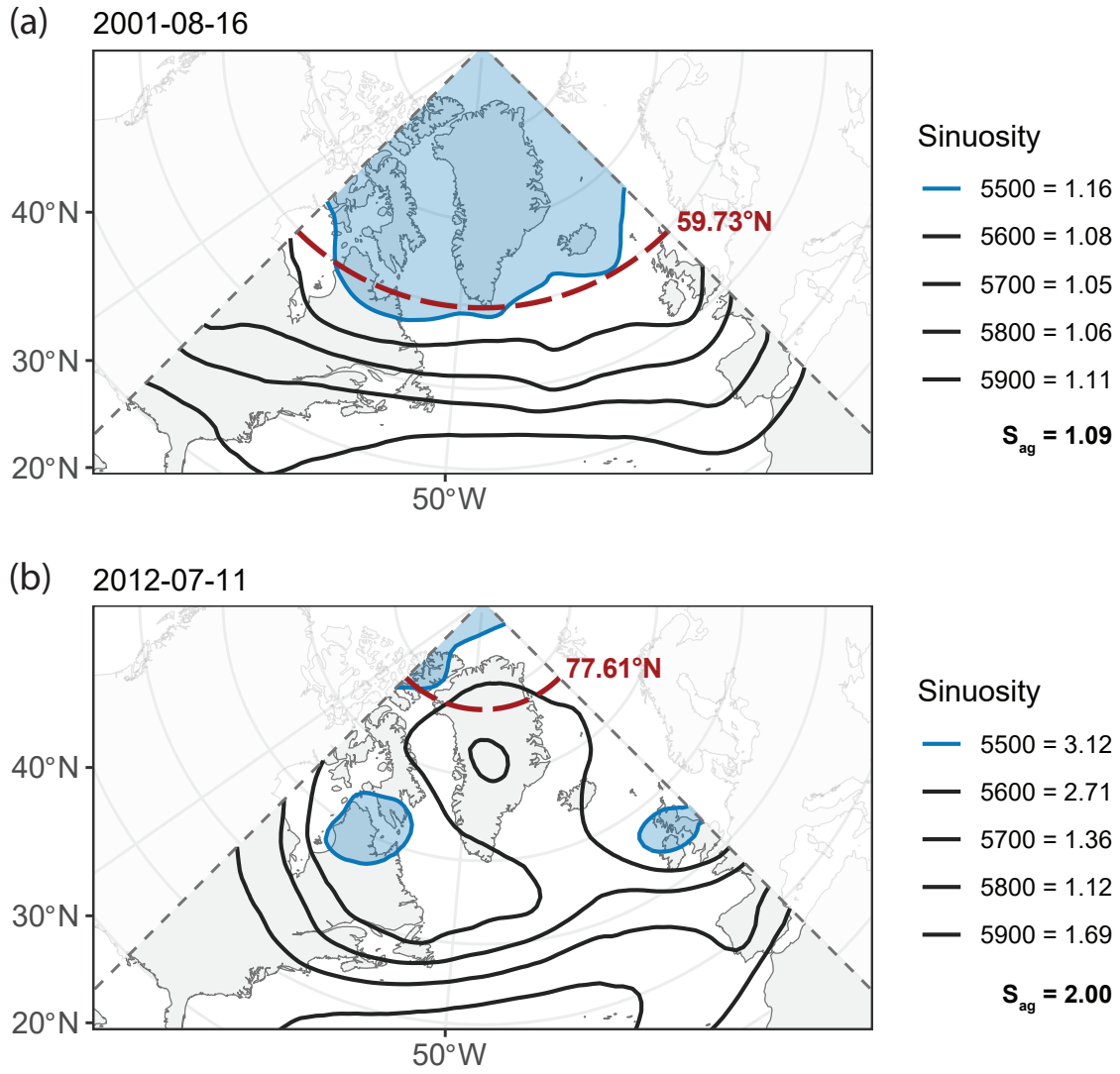


Figure 3.1: Maps illustrating the synoptic setting and S_{ag} parameters for (a) a case of low S_{ag} occurring August 16, 2001, and (b) a case of high S_{ag} occurring July 11, 2012. The value of S_{ag} as well as the sinuosity of each individual isohypse is listed to the right of each map. For each case, the calculation for the isohypse of maximum sinuosity (blue line) is shown as an example, where the blue shading shows the area used to calculate the equivalent latitude (red dashed line). Dashed gray lines show the longitude boundaries of the regional domain.

trends in S_{ag} for a range of percentile values calculated for each season and year likewise shows that JJA is the only season that displays a significant trend in waviness across any part of the distribution, and that the upper half of the distribution has undergone the greatest increase, indicating an intensification of the wavier circulation patterns occurring each summer (Supplementary Table 3.1). Figure 3.2a displays the interannual variability and long-term behavior of JJA S_{ag} alongside that of the Greenland Blocking Index (GBI) and the blocking index of Pelly and Hoskins42 (hereafter, PH03). When comparing the 5-year running mean of each index, sinuosity over the North Atlantic and Greenland blocking as measured by the GBI exhibit similar long-term behavior, with a strong increase from the mid-1990s through the early 2010s followed by high variability thereafter. Indeed, the JJA GBI has undergone a statistically significant ($\alpha = 0.05$) increase of 0.42 SD per decade, comparable to S_{ag}. The concurrence between S_{ag} and the GBI is also apparent over interannual timescales and, consequently, the two indices exhibit a strong positive correlation of $r = 0.91$ (Figure 3.2b).

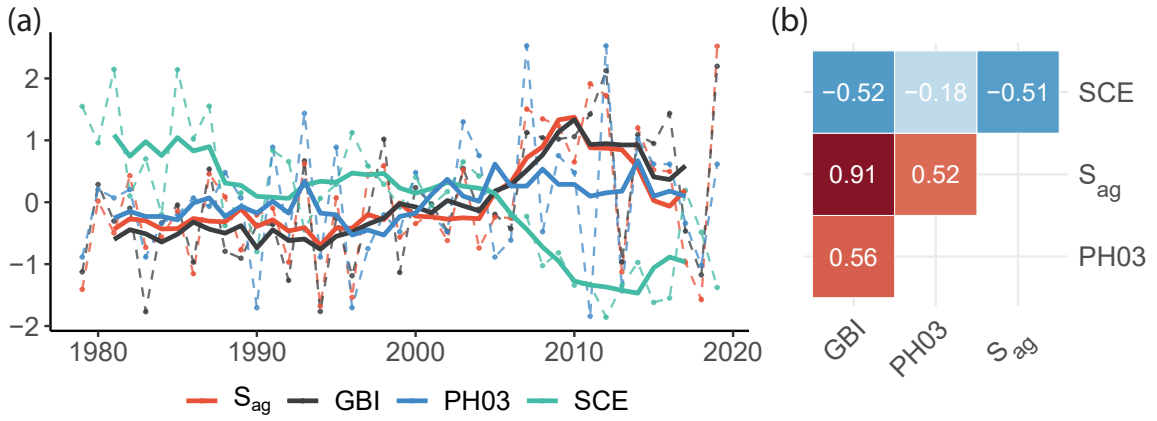


Figure 3.2: Temporal comparison of spring SCE and summer circulation over Greenland. (a) Timeseries of JJA S_{ag} (orange), GBI (gray), and PH03 (blue) plotted alongside June Northern Hemisphere SCE (green). Dashed lines show raw data. Solid lines show 5-year running means. (b) Correlation matrix comparing each of the raw timeseries in (a). White numbering presents the correlation coefficient for each variable pair and color shading corresponds to the strength of correlation

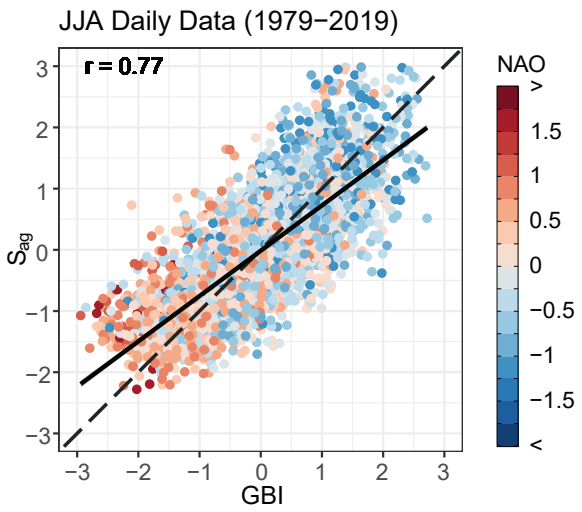


Figure 3.3: Daily standardized values of S_{ag} plotted against the corresponding standardized values of the GBI. Dashed line marks the 1:1 line. Solid line shows the linear best-fit line. Data points are color-coded according to the corresponding monthly value of the principal-component-based NAO (Hurrell et al., 2003) as shown in the color bar to the right. The associated Pearson's correlation coefficient (r) is provided in the upper-left corner.

The long-term behavior of S_{ag} and the GBI stands in contrast with the subdued trend when blocking is measured using PH03 (Fig. 2a). PH03 exhibits a much more modest increase of 0.13 SD per decade that is not statistically significant. Furthermore, PH03 exhibits a relatively weak correlation with both S_{ag} and the GBI of $r = 0.52$ and $r = 0.56$ respectively (Figure 3.2b). The low correlation between the GBI and PH03 is particularly striking given that they are both meant to measure the same phenomenon. This discrepancy may be due to well-known biases among the different categories of blocking metrics—pertinently, flow-reversal methods such as PH03 tend to underrepresent Omega blocking patterns (Barriopedro et al., 2010; Pelly & Hoskins, 2003). A previous application of the modified PH03 index utilized herein confirmed this bias over Greenland and demonstrated that an increase in Omega patterns has disproportionately contributed to the recent surge in Greenland blocking (Preece et al., 2022), which is consistent with the disparity in Figure 3.2a.

That there is a strong correlation between S_{ag} and the GBI over seasonal timescales is not surprising given the well-established increase in summer Greenland blocking in recent decades and that blocked conditions represent an anomalously meridional—i.e., wavy—circulation pattern. Thus, the increase in blocking frequency and/or magnitude signaled by an above-normal GBI, either over the

course of one summer or over the long term, would by definition act to increase North Atlantic sinuosity over the same period. However, the reverse may not necessarily be true—i.e., an increase in North Atlantic sinuosity could translate to an anomalously low GBI if the wavy circulation pattern places a trough over Greenland rather than a ridge. To explore this relationship more broadly, we examine the correlation between the two variables over daily timescales by plotting standardized values of S_{ag} against the corresponding standardized values of the GBI in Figure 3.3. We also display the associated monthly NAO index value for each data point. As expected from previous work on the relationship between the NAO and Greenland blocking (Hanna et al., 2016), anomalously high S_{ag} and GBI tend to occur under the negative phase of the NAO, while the opposite conditions prevail under its positive phase. Critically, there is a clear linear relationship between S_{ag} and the GBI, and they are highly positively correlated at $r = 0.77$, signaling a strong tendency for wavy circulation over the North Atlantic to foster anticyclonic conditions over Greenland.

The above results show an interrelated increase in waviness over the North Atlantic and blocking over Greenland in recent decades. To investigate how these changes may be a feature of Arctic amplification, we followed previous work (Vavrus et al., 2017) and calculated sinuosity as a function of latitude, then calculated seasonal trends in sinuosity at each latitude using a moving linear regression. Figure 3.4 depicts the moving linear trend in the 500 hPa sinuosity over the North Atlantic alongside that for the 850 hPa meridional temperature gradient and the 500 hPa zonal mean zonal wind. In each subplot, the change in shading in the x-direction documents the change in the linear trend through 2019 as the regression window is shortened by moving the starting year forward in time as indicated along the x-axis.

Focusing on the change in sinuosity (Figure 3.4a), it is clear that the positive trend in JJA S_{ag} evident in Figure 3.2a has been driven by changes at higher latitudes. The most pronounced trend has occurred around 60°N; however, significant increases in sinuosity are also evident extending poleward through 80°N. This is in close agreement with the latitudinal distribution of trends in sinuosity over a North America domain documented in previous work (Vavrus et al., 2017). Temporally, the slope of the trend is greatest when the regression is performed from ∼1995 onward, coinciding with the upturn in the 5-year running mean in both S_{ag} and the GBI visible in Figure 3.2a. The lack of statistical significance for trends from ∼1996 onward likely reflects both greater variability during the past decade (Figure 3.2a) and the reduction in sample size as the regression window is shortened.

Figure 3.4b shows a decrease in the strength of the meridional temperature gradient between 60 and 70°N. As

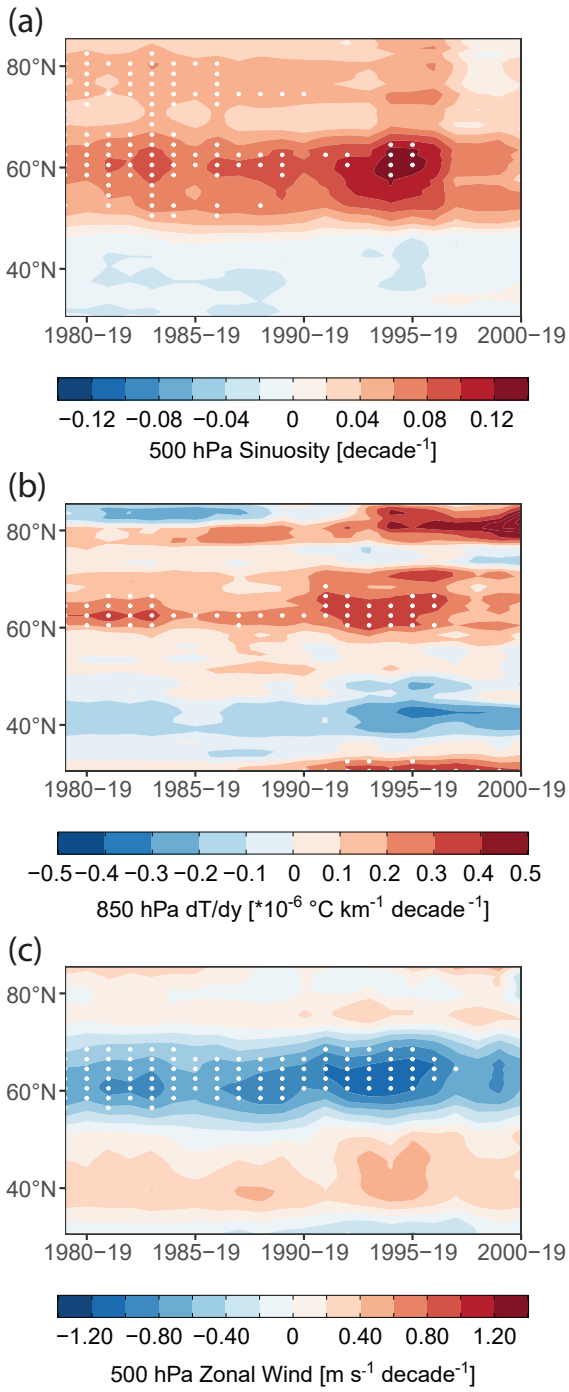


Figure 3.4: Moving linear trends for (a) 500 hPa sinuosity, (b) 850 hPa meridional temperature gradient, and (c) 500 hPa zonal wind. For each latitude along the y-axis, the shading indicates the linear trend from the start year indicated on the x-axis through the end of the study period (i.e., 2019). All quantities calculated for the North Atlantic domain (0–90° W). Stippling indicates significance at $\alpha = 0.05$.

expected from the thermal wind relation, the weakened temperature gradient in the lower troposphere is met by a reduction in the zonal mean zonal wind aloft (Figure 3.4c). In each case the strongest trend aligns with the location ($\sim$60° N) and timing (mid-1990s onward) of the observed change in sinuosity. Thus, the conditions accompanying the increase in North Atlantic sinuosity and Greenland blocking in recent decades are congruent with a leading theoretical framework (Francis & Vavrus, 2012) of midlatitude circulation change under AA.

3.2.2 Northern Hemisphere snow cover extent and atmospheric circulation over Greenland

Figure 3.2a also displays the long-term variability in June Northern Hemisphere SCE, which has undergone a decline of 0.62 SD per decade that is significant at the 95% confidence level—a trend that mirrors that of S_{ag} and the GBI. Previous work has highlighted June conditions in particular as an effective indicator of spring snow cover variability more broadly (Matsumura et al., 2014). Thus, these results indicate that the seasonal timing of this pronounced change in surface conditions precedes that of the observed change in atmospheric conditions, suggesting the possibility of a causal relationship.

The negative correlations relating spring SCE to summer S_{ag} ($r = -0.51$) and GBI ($r = -0.52$) presented in Figure 3.2b may be largely reflective of the inverse long-term trends evident in their respective 5-year running means. To investigate the matter further, Figure 3.5 presents the results of a lagged regression analysis comparing each of the three circulation indices with antecedent spring SCE. Here, we linearly detrend each time series before conducting the regression to more aptly focus on lagged covariance over interannual timescales, providing a more direct and robust examination of the lagged relationship between spring snow cover and summer atmospheric circulation.

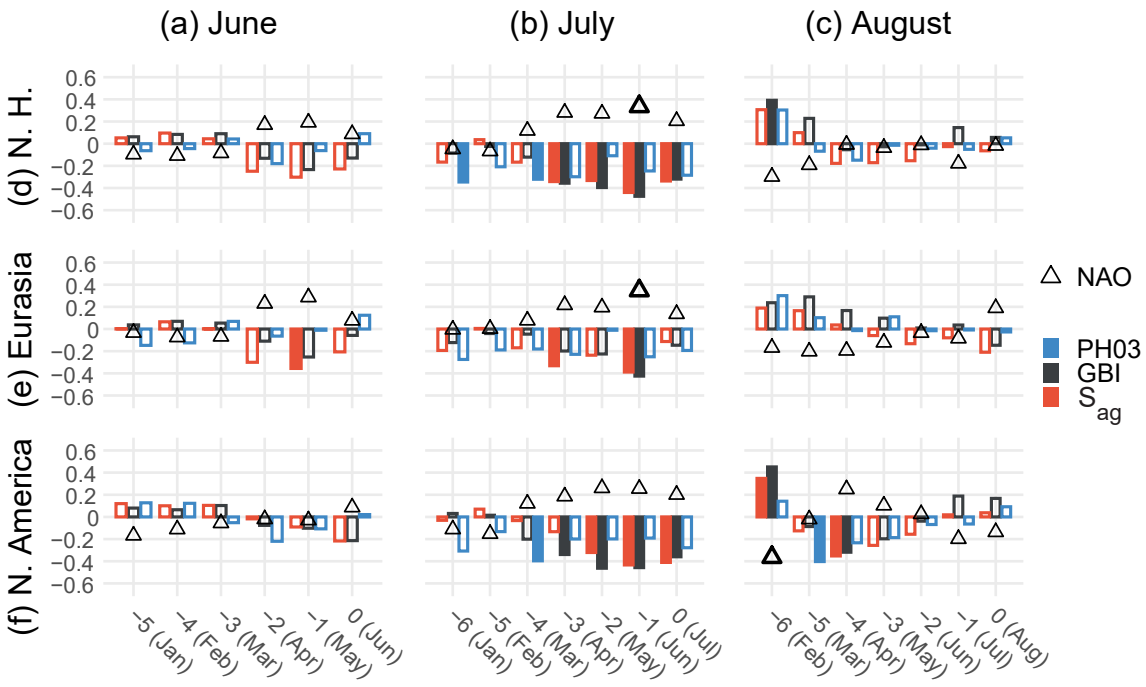


Figure 3.5: Lagged correlation plots relating (column a) June, (column b) July, and (column c) August atmospheric circulation over Greenland to antecedent monthly SCE area over (row d) the Northern Hemisphere, (row e) Eurasia, and (row f) North America. The color-coded bars in each panel document the correlation coefficient relating PH03 (blue), GBI (black), and S_{ag} (orange) measured during the summer month labeled at the top of each column to lagged monthly SCE area as noted along the x-axis. Likewise, triangles note the correlation between the principal-component-based NAO (Hurrell et al., 2003) and lagged monthly SCE area. Filled bars and bold triangles indicate statistical significance at $\alpha = 0.05$.

The top row of 3.5 details the lagged relationship between antecedent SCE area over the Northern Hemisphere as a whole and June, July, and August monthly atmospheric circulation over Greenland. Partitioning summer into its constituent months reveals a clear negative lagged correlation signature relating July S_{ag} and GBI to spring Northern Hemisphere SCE, with significant correlations extending as far back as the preceding April. The sign of the lagged correlation indicates that low spring Northern Hemisphere SCE is typically followed by an increase in July sinuosity over the North Atlantic and an attendant increase in Greenland blocking. This negative lagged correlation signature is mirrored by a positive correlation between the principal-component-based NAO index of Hurrell (Hurrell et al., 2003) and antecedent SCE; however, only the relationship with June SCE is significant at $\alpha = 0.05$. The lagged regression plots for June and August atmospheric conditions show no apparent lagged relationship with spring SCE (Figure 3.5, columns a and c).

Considering SCE area over North America and Eurasia individually likewise suggests a lack of a lagged correlation between spring SCE and either June or August circulation over Greenland (Figure 3.5, columns a and c). Examining the two continental regions separately does, however, clarify that the lagged signature evident for Northern Hemisphere as a whole is primarily driven by a relationship with snow cover over North America (Figure 3.5, rows e and f). Contrary to the results for S_{ag} and the GBI, which are closely aligned, none of the lagged regression plots indicate any relationship of note between spring SCE and PH03. This lack of agreement between PH03 and the two other circulation measures is consistent with the results of the correlation matrix in Figure 3.2b. It appears the significant correlation between the July NAO and June Northern Hemisphere SCE (Figure 3.5 column b, row d) is primarily a reflection of the relationship with SCE over Eurasia (Figure 3.5 column b, row e)—a finding that is consistent with previous work showing

that there is an increase in the poleward propagation of Rossby waves that acts to enforce the negative phase of the Northern Annular Mode during summer months in years of low June Eurasian SCE (Matsumura et al., 2014).

One way that retreating spring SCE may favor Greenland blocking is by amplifying the rate of warming at high latitudes and reducing the meridional temperature gradient, thereby contributing to the mechanisms examined in the previous section. Another possibility that we explore here is that low SCE may act to enforce ridging over Greenland via a direct stationary Rossby wave response. Figure 3.6 traces the July stationary wave response to low May North American SCE using the three-dimensional wave activity flux (WAF) (Takaya & Nakamura, 2001). We focus on the relationship with May SCE because that is the month that exhibits the earliest significant lagged relationship with July observations of both GBI and S_{ag} (Figure 3.5 column b, row f).

Figure 3.6a presents the July Z300 anomaly obtained from a linear regression of the geopotential height field against standardized May North American SCE area. Here, we inverted the SCE time series and detrended all data before conducting the regression to emphasize the response to low SCE conditions. The Z300 isopleths indicate that years of low SCE are followed by upper-level ridging over much of northeastern North America and Greenland, with a strong anomalous high-pressure center located over Baffin Bay and a weaker high over the northern Appalachians. Figure 3.6a also depicts the vertical and horizontal components of the associated WAF and its horizontal divergence. The origins of the upper-level response appear to be connected to a broad area of upward WAF that extends from the Great Plains through the Labrador Peninsula. The vectors indicate that this upward Rossby wave activity propagates in two branches—a southern branch that sustains the weaker anticyclone over the northern Appalachians and a northern branch in which wave activity propagates northeastward from its origin near Hud-

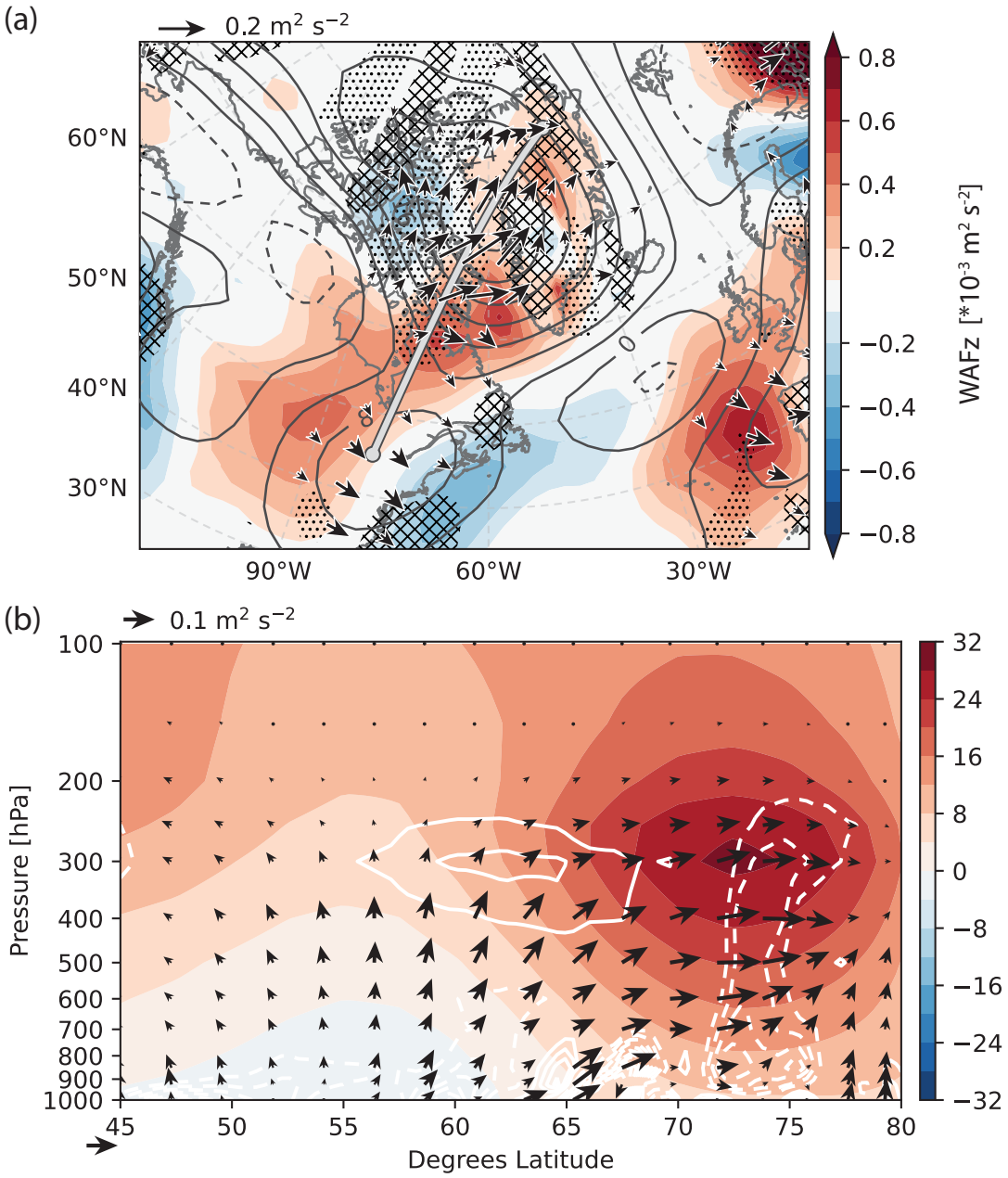


Figure 3.6: Stationary Rossby wave response to low North American SCE. (a) Anomalies of July Z300 regressed against inverted May North American SCE (contours: solid, positive; dashed, negative) presented alongside the 300 hPa horizontal component (vectors) and average 850–150 hPa vertical component (shading) of the associated WAF. Stippling (crosshatching) indicates horizontal divergence (convergence) of the Z300 WAF exceeding $\pm 10^{-7}\, m\, s^2$ *(b) Vertical cross-section along the thick gray line in (a), where vectors indicate WAF, shading indicates the geopotential height anomaly, and solid (dashed) white contours indicate WAF divergence (convergence). Contour interval:* $10^{-7}\, m\, s^2$*, zero contour omitted. The horizontal component of the vectors in (b) is 100 times that of the vertical component.*

son Bay toward northern Greenland. Divergence of the WAF is present along the upstream flank of the high-pressure center with convergence over and just downstream of the ridge axis, consistent with the pattern found to accompany strong blocking events in previous work (Takaya & Nakamura, 2001). Convergence of stationary wave activity is associated with the poleward advection of low potential vorticity and has been shown to be a key contributor to the development of blocked flows (Nakamura, 1994; Shi & Nakamura, 2021; Takaya & Nakamura, 2001). Thus, WAF convergence over western Greenland is supportive of increased blocking in years of low spring SCE.

To further investigate the ridging over Greenland, Figure 3.6b plots a vertical cross-section of the anomalous geopotential height and associated WAF along the solid gray line in Figure 3.6a. The vertical cross-section more precisely shows upward WAF near the surface at approximately 55°N—a shallow area of anomalously low pressure near the southern shoreline of Hudson Bay. The WAF vectors then turn poleward, with convergence enforcing the strong high-pressure anomaly over Baffin Bay and western Greenland that extends throughout the depth of the troposphere. This shallow cyclonic anomaly with an equivalent barotropic anticyclone positioned downstream and to the north is consistent with both linear theory and the simulated response to diabatic heating of the near-surface atmosphere in idealized modeling (Hoskins & Karoly, 1981; Walter et al., 2001). In the results that follow, we consider the snow-hydrological effect as an explanatory mechanism behind this delayed stationary wave response.

3.2.3 The snow-hydrological effect as a bridge between spring snow cover variability and summer atmospheric response

The snow-hydrological effect represents a causal chain of delayed surface-atmosphere coupling in which low spring snow cover leads to earlier depletion of soil moisture and a consequent increase in surface sensible heating that locally warms the lower troposphere in summer (Matsumura & Yamazaki, 2012; Matsumura et al., 2010; Yasunari et al., 1991). To investigate the role that this snow-hydrological effect may play in the observed July stationary wave response, we first delineate the climatological retreat of spring North American SCE and spatially resolve the relationship between spring snow cover and July Greenland blocking in Figure 3.7. Next, we illustrate the spatiotemporal progression of North American soil moisture and surface temperature anomalies in response to low May SCE in Figure 3.8 and discuss these results in the context of the observed July stationary wave response.

Figure 3.7a–c presents the frequency of observed snow cover from 1979 to 2019 for each month spanning the lagged relationship between May SCE area and July circulation over Greenland. In May, there is a region of unremitting snow cover extending from the Arctic coast to the southern end of the Hudson Bay (Figure 3.7a). South of this point, there is a zonal band of snow cover frequencies in the range of 30–70% marking the primary area of May SCE variability. Snow cover frequencies greater than 50% in June are generally confined to the Canadian Arctic tundra and the mountainous areas along the Pacific coast (Figure 3.7b). By July, the continent is predominately snow free (Figure 3.7c).

To spatially delineate the regions of SCE variability that are linked to atmospheric circulation over Greenland, we show the grid point correlation between July GBI and spring North American snow cover duration in Figure 3.7d. Here, we de-

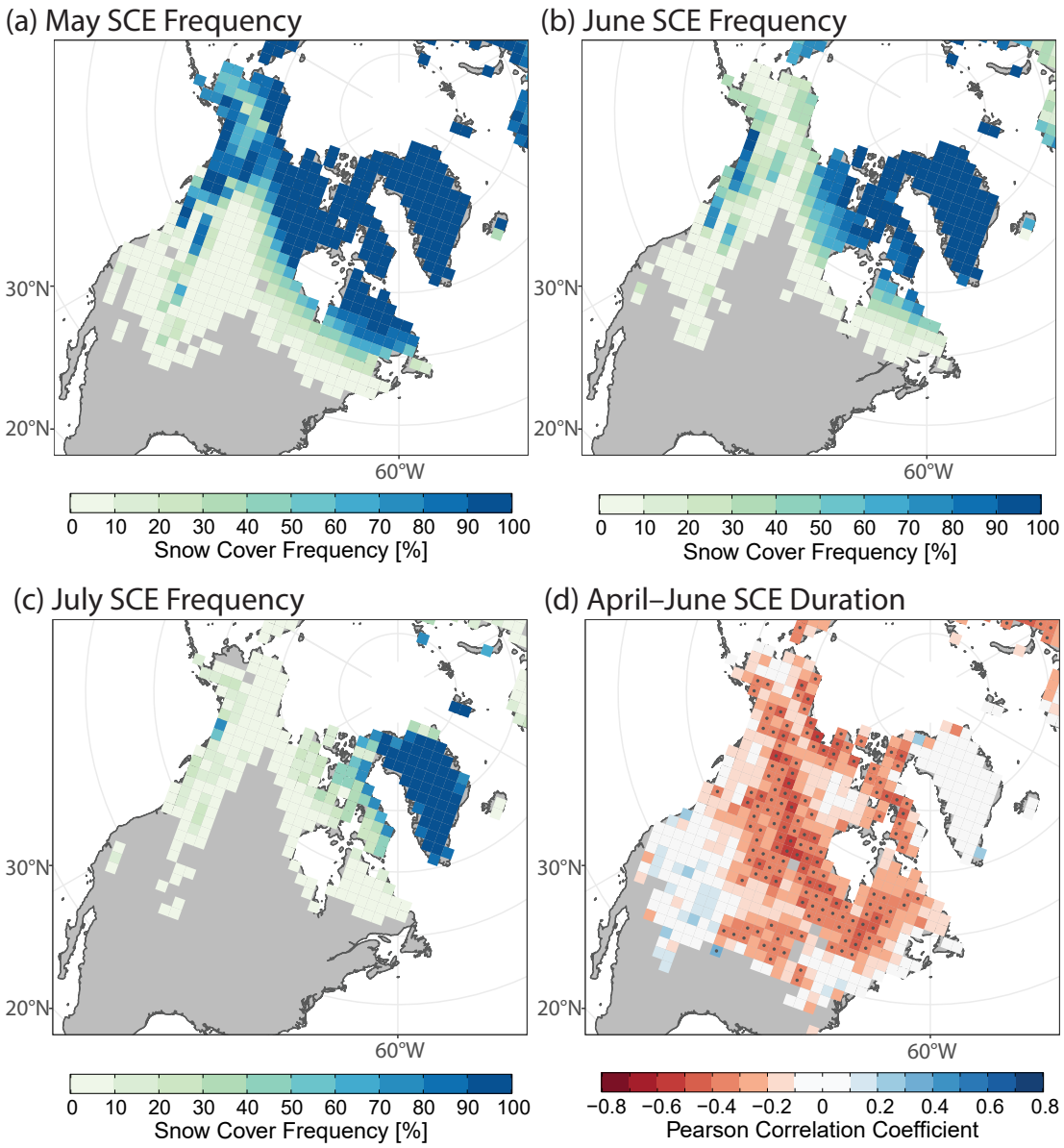


Figure 3.7: North American SCE variability as measured by the NOAA SCE CDR and its relationship with Greenland blocking. Panels a–c show the 1979–2019 frequency of weekly snow cover at each grid point during (a) May, (b) June, and (c) July. Panel (d) presents grid point Pearson correlation coefficients relating the total number of weeks with snow cover from April to June of each year and the monthly mean GBI for the following July. Note that negative values are shaded red to reflect an increase in blocking associated with a decrease in snow cover duration. Stippling indicates statistical significance at the 95% confidence level.

fine spring snow cover duration as the total number of observations from April to June of each year in which the NOAA SCE CDR indicates the presence of snow in each grid cell. The strong negative correlation values stretching zonally from southern Alaska to the Labrador Peninsula and equatorward into the interior plains of the US indicate that low spring SCE in this region is typically associated with more prominent anticyclonic conditions over Greenland in July. This region of high correlation generally aligns with the zonal band of moderate May SCE frequency in Figure 3.7a and suggests that snow cover variability in this area drives the lagged correlation documented in Figure 3.5.

Figure 3.8 chronicles the surface response to spring SCE variability by plotting anomalies of volumetric soil water content (column a) and 2 m air temperature (column b) obtained from a linear regression against standardized, inverted North American SCE area for each month spanning the lagged relationship identified in Figure 3.5 (i.e., May–July). Again, all fields were detrended prior to the regression. The regression anomalies in row c indicate that low May SCE area coincides with anomalously warm surface air temperature along the northern coastline of North America that extends just south of the Great Lakes. In June (row d), the positive temperature anomalies throughout Canada have weakened considerably. At the same time, strong negative soil moisture anomalies have emerged in conjunction with a secondary warm anomaly centered over the eastern US. The emergence of this warm anomaly well after the seasonal retreat of snow cover from the region (Figure 3.7b) is consistent with an active snow-hydrological effect. By July, negative soil moisture anomalies over the whole of North America have weakened further; however, while not statistically significant, the spatial pattern of reduced soil moisture in the eastern US aligns well with positive surface temperature anomalies running along the east coast and extending inland to the south of Hudson Bay that are significant at the 95% confidence level—conditions which suggest that the

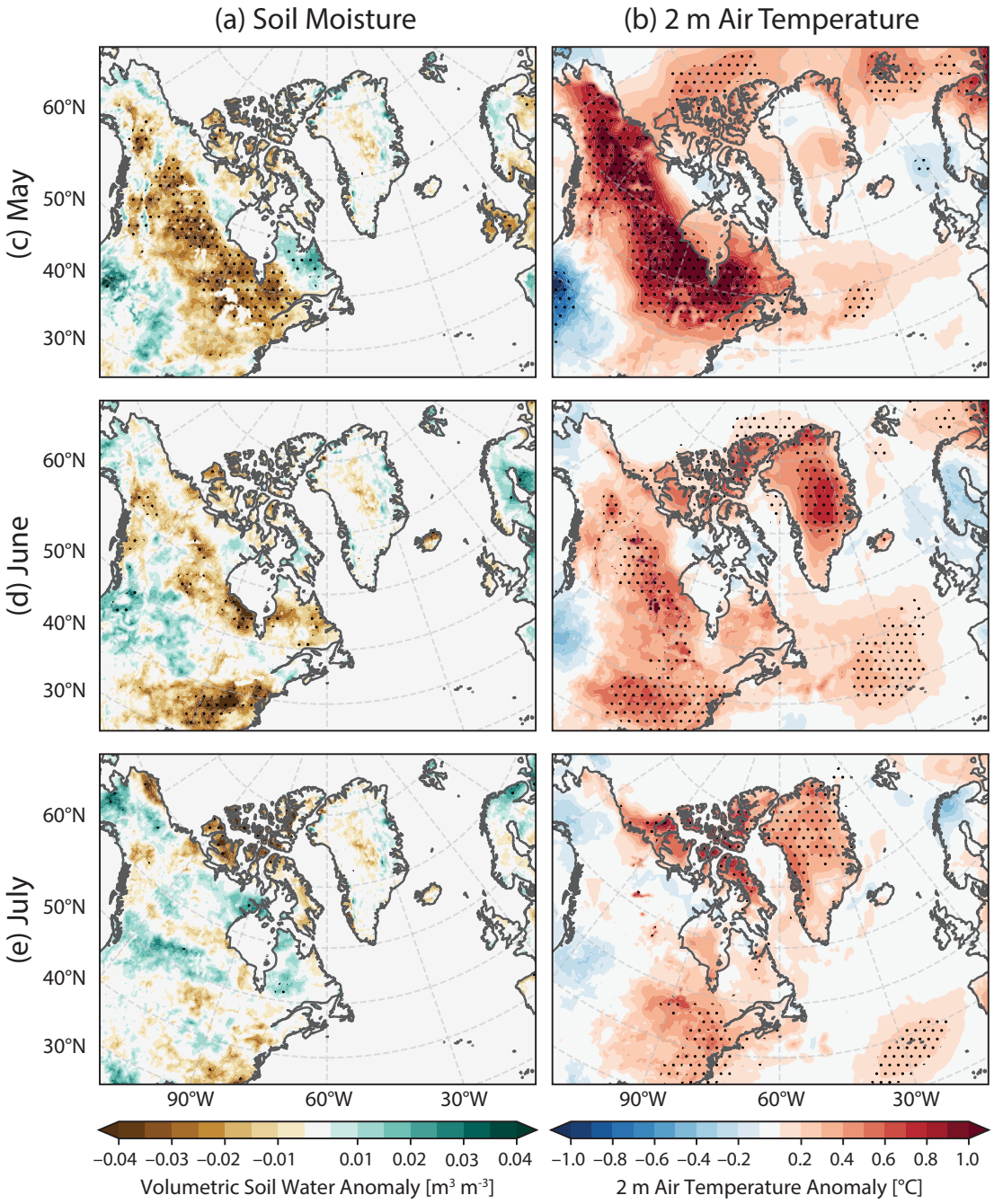


Figure 3.8: North American surface conditions following low spring SCE. Anomalies of ERA5 (column a) volumetric soil water to a depth of 28 cm and (column b) 2 m air temperature obtained from a linear regression of (row c) May, (row d) June, and (row e) July surface variables against inverted and standardized May North American SCE area. Stippling indicates significance at the 95% confidence level.

snow-hydrological effect over the eastern US persists into July when the stationary wave response is observed.

Considering these July surface conditions in the context of the concomitant stationary wave response, it is apparent that the upward WAF in Figure 3.6a generally aligns with the warm anomaly center over eastern North America (Figure 3.8 column b, row e). This is consistent with previous work, which has shown that changes in both snow cover (Matsumura & Yamazaki, 2012) and sea ice (Honda et al., 2009; Honda et al., 1996) can cause a local baroclinic response that favors upward WAF over the region of consequent diabatic heating of the near-surface atmosphere. The shallow surface low and downstream equivalent barotropic ridge visible in the cross-section in Figure 3.6b is suggestive of such a baroclinic response in association with the observed snow-hydrological effect in eastern North

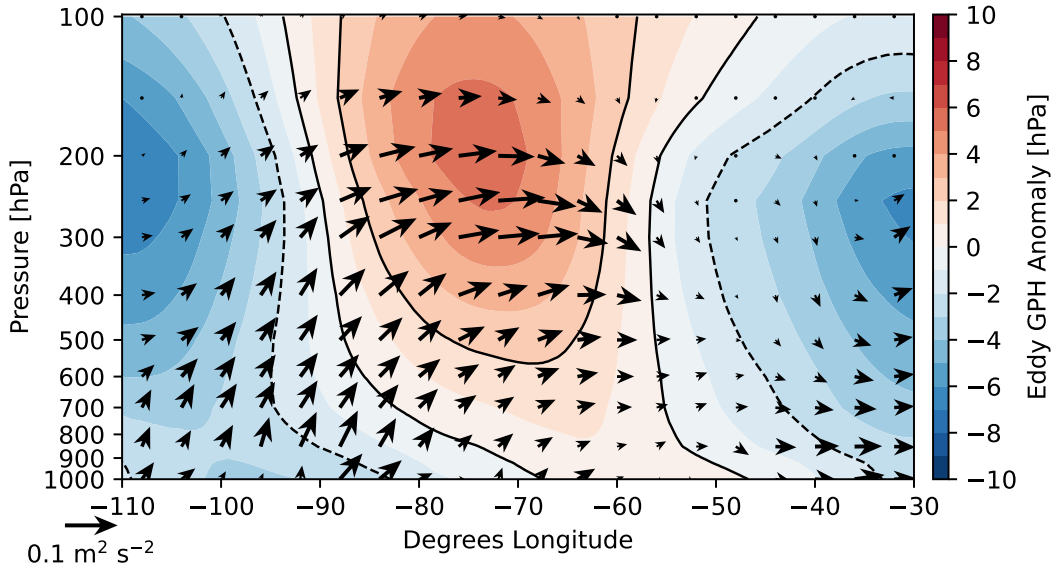


Figure 3.9: Vertical cross-section of the average 40–60 °N anomalous eddy geopotential height (shading) obtained from a linear regression against standardized, inverted May North American SCE area. The –2, 0, and 2 hPa isopleths are shown in black to more clearly visualize the vertical structure of the eddy height anomalies. Vectors show the meridional average of the associated WAF.

America. To further investigate this possibility, we focus on the eddy component of the July geopotential height response to low May North American SCE area.

Figure 3.9 presents the vertical structure of the July eddy geopotential height anomaly and associated WAF averaged over 40–60°N. Like the geopotential height anomalies in Figure 3.6, the anomaly field here was estimated from a linear regression of July eddy geopotential height against standardized, inverted May North American SCE area. As apparent from its westward tilt with height, the anomalous eddy geopotential height field exhibits a clear baroclinic structure over the warm anomaly center (i.e., ∼80–100°W) that is particularly pronounced in the lower levels of the troposphere. A westward tilt in eddy geopotential height supports the upward propagation of Rossby waves—a relationship that is visible in the WAF vectors in Figure 3.9. Thus, these results support the existence of a regionally focused snow-hydrological effect over the eastern North America that persists into July, providing a chain of physical mechanisms bridging spring SCE to the baroclinically generated stationary Rossby wave response.

3.2.4 Consequences for GrIS Surface Mass Balance

Based on the strong association between anomalous anticyclonic circulation over Greenland and GrIS surface conditions (Fettweis et al., 2013; Hahn et al., 2020; Hofer et al., 2017; Tedesco & Fettweis, 2020), one would expect the July stationary wave response to low spring snow cover to encourage meltwater runoff from the ice sheet. To directly investigate the consequences of this surface-atmosphere coupling for GrIS surface mass balance (SMB), we repeat the above lagged, linear regression analysis, this time comparing July GrIS surface conditions against May North American SCE area. The resulting regression anomalies are presented in Figure 3.10.

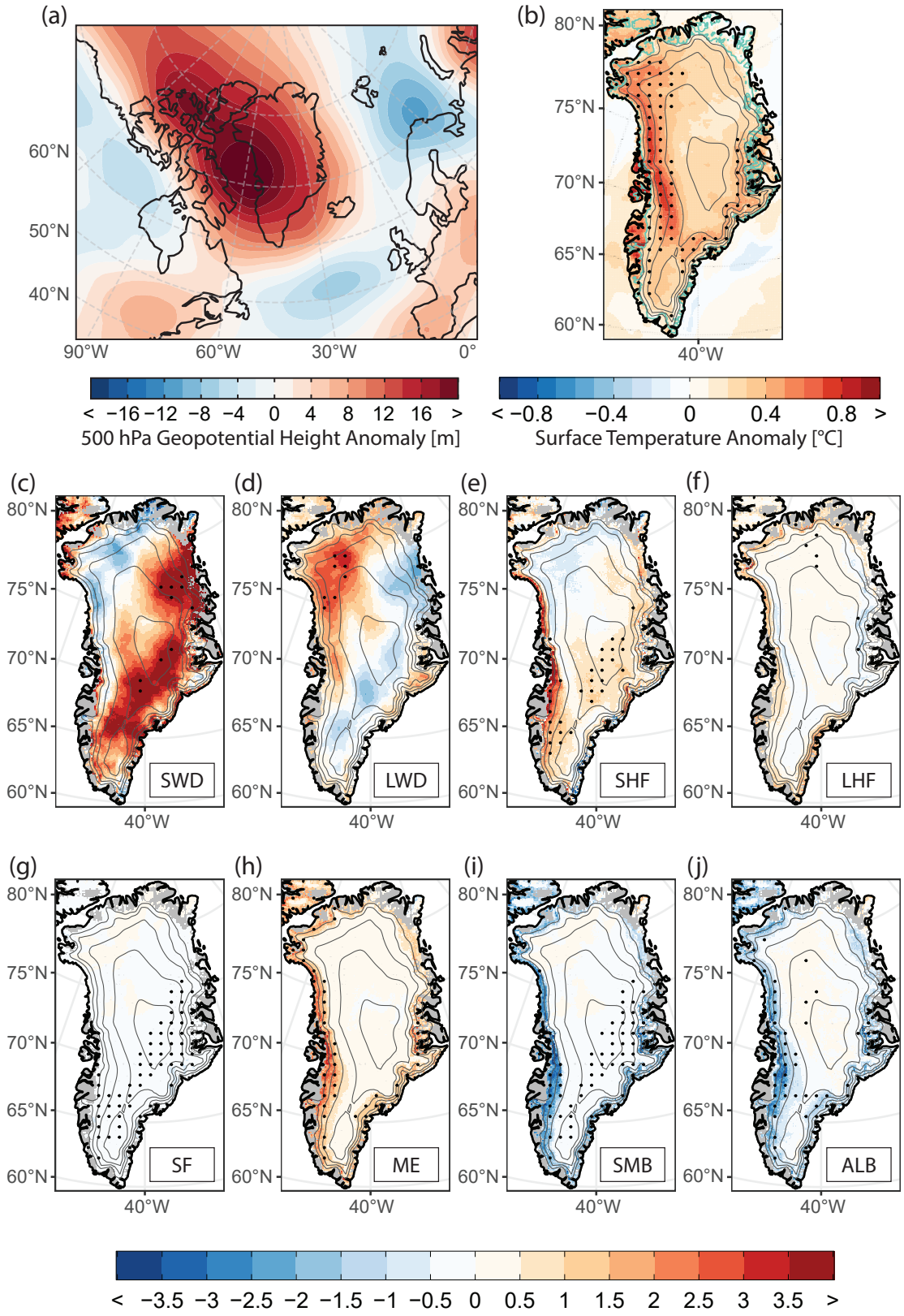


Figure 3.10: GrIS surface conditions in July following low spring SCE. (Continued on following page.)

Figure 3.10: GrIS surface conditions in July following low spring SCE. Anomalies of (a) Z500 (b) surface air temperature (c) downward shortwave radiation (SWD), (d) downward longwave radiation (LWD), (e) sensible heat flux (SHF), (f) latent heat flux (LHF), (g) snowfall (SF), (h), meltwater production (ME), (i) surface mass balance (SMB), (j) surface albedo (ALB). Z500 as represented by ERA5 reanalysis, all other variables are as simulated by the regional climate model, MAR. (c–j) share a common color bar, where (c–f) has units of Wm^{-2}, (g–i) $mmday^{-1}$ of water equivalent, (j) %. Green contour in (b) marks ice sheet edge. Anomalies obtained from a regression against inverted and standardized May North American SCE area. Stippling indicates significance at the 95% confidence level

Figure 3.10a shows the anomalous stationary ridge from Figure 3.6a at the 500 hPa level, highlighting the anomalous anticyclone that is centered over Baffin Bay. This upper level pattern is met by a northwest-southeast dipole in the radiative surface energy balance (SEB) terms, with a decrease in downward shortwave radiation to the northwest and an increase to the southeast that is mirrored by an opposing pattern in downward longwave radiation (Figure 3.10c, d). Positive anomalies in longwave radiative forcing appear to combine with above-normal sensible heat flux (Figure 3.10e) to produce a band of strong positive surface temperature anomalies that stretches along the western slope of GrIS between $\sim$65 and 80°N latitude (Figure 3.10b). The relationship between July surface air temperature and May North American SCE in this region is significant at the 95% confidence level.

This SEB response has a clear impact on the SMB of the GrIS. The enhanced longwave radiation and flux of sensible heat to the western ice sheet favor above-normal meltwater production in the region (Figure 3.10h) that aligns well with above-normal surface runoff (not shown). This increase in meltwater runoff drives a reduction in the total SMB over the western ablation zone (Figure 3.10i). Moreover, greater melt of the western ice sheet in years of low spring snow cover is collocated with a decline in surface albedo (Figure 3.10j), indicative of a positive melt-albedo feedback.

The position of the high pressure center and the associated SEB balance response following low spring SCE is consistent with the conditions that have accelerated GrIS surface mass loss in recent decades. Previous work has shown that an increase in downwelling longwave radiation accompanying more anticyclonic conditions over Baffin Bay has been instrumental in causing a disproportionate acceleration of runoff from the northern GrIS (Noël et al., 2019)—a SEB signature that is evident in the response to low SCE (Figure 3.10d). Furthermore, both the conditions that have accelerated melt of northern Greenland (Noël et al., 2019) and those following low spring North American SCE (Figure 3.10) are consistent with that of the high-amplitude Omega blocking patterns that have undergone a significant increase in recent decades (Hahn et al., 2020; Preece et al., 2022). Together, these results are suggestive a potential link between North American SCE, an increase Greenland blocking, and the rapid acceleration of runoff from the northern GrIS.

3.3 Discussion

AA has often been invoked as a possible explanation for the atmospheric conditions that have accelerated GrIS mass loss in recent decades (Francis & Vavrus, 2012; Hanna et al., 2016; Liu et al., 2016; Overland et al., 2012; Trusel et al., 2018). Our analysis directly investigated this possibility by examining the connection between AA and the waviness of atmospheric circulation over the North Atlantic, and by documenting the role of dwindling terrestrial snow cover in dictating the position of the resulting wave pattern. In pursuing this objective, we documented evidence linking AA to the observed increase in summer Greenland blocking.

Summer atmospheric sinuosity across our Greenland-centered domain has undergone a statistically significant increase that is consistent with long-term posi-

tive trends in waviness to the east and west of Greenland documented in previous studies (Cattiaux et al., 2016; Di Capua & Coumou, 2016; Vavrus et al., 2017) (Figure 3.2a, 3.4a). The increase in sinuosity is collocated with a simultaneous weakening of the meridional temperature gradient and deceleration of the zonal wind (Figure 3.4)—results that support a link between AA and persistent weather extremes in the region (Francis & Vavrus, 2012).

An increasingly meridional circulation creates favorable conditions for more frequent blocking but does not necessarily place a ridge over Greenland. A cursory look at Figure 3.2 suggests that the increase in sinuosity over the North Atlantic has indeed supported the well-established positive trend in Greenland blocking. Since a blocking anticyclone is, itself, a feature of an amplified planetary wave, it is not surprising that the long-term behavior of the GBI and that of North Atlantic sinuosity have closely tracked each other (Figure 3.2). However, our analysis goes further in demonstrating that sinuosity and the GBI exhibit a strong linear relationship over daily timescales (Figure 3.3), thereby establishing that wavier flows in the region do, in fact, favor ridging over Greenland.

Others have summarized the dynamics that encourage ridging over Greenland more generally (Hanna et al., 2018b). They note that westerly flow over the north-south oriented topography produces ridging, while katabatic outflow from the ice sheet's interior generates subsidence and adiabatic warming aloft, which increases geopotential heights. Furthermore, there is frequent cyclogenesis along the US Atlantic coast, which promotes the development of a downstream ridge over Greenland (Hanna et al., 2018b; McLeod & Mote, 2015). These factors may, on their own, anchor the ridge over Greenland during periods of wavier flow.

Given the strong linear relationship between sinuosity and the GBI, one could expect a positive trend in Greenland blocking simply by virtue of increasing waviness under AA. Retreating SCE would certainly contribute to this mechanism

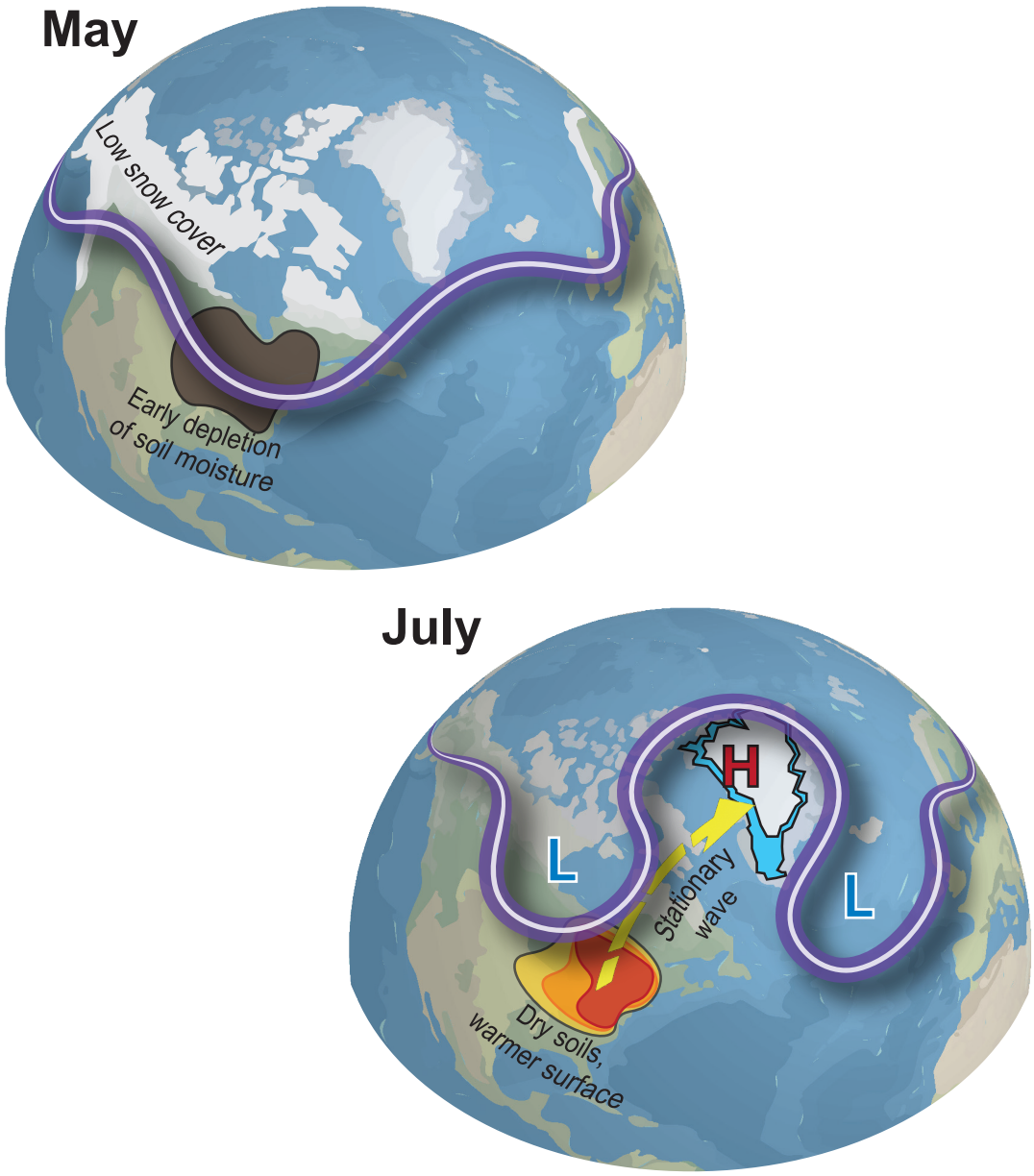


Figure 3.11: Illustration of the link between North American snow cover and atmospheric circulation over Greenland. Low spring snow cover causes early depletion of soil moisture over eastern North America (brown shading). The dry conditions that follow produce a warm surface anomaly that persists into July (orange shading). This anomalous heating of the near-surface atmosphere induces a stationary Rossby wave response that propagates northeastward (yellow arrow) and favors high-pressure ridging over Greenland—conditions which augment melt of the Greenland Ice Sheet (blue shading)

through its impact on the meridional temperature gradient, but SCE anomalies are known to exert a direct influence on the stationary wave pattern (Alexander et al., 2010; Cohen & Entekhabi, 1999; Henderson et al., 2013; Matsumura & Yamazaki, 2012), which could also act to enforce ridging over Greenland. Our results show a significant lagged relationship indicating that years of low spring North American SCE are followed by increased sinuosity and Greenland blocking the following July (Figure 3.5). This delayed atmospheric response to spring SCE appears to be the consequence of an active snow-hydrological effect that emerges over eastern North America in June and persists into July in years of low May SCE (Figure 3.8). As summarized in Figure 3.11, the anomalously warm surface temperatures that follow are associated with a baroclinic atmospheric response in July that excites a stationary Rossby wave train and enforces anomalous ridging over Greenland and encourages melt of the ice sheet (Figure 3.6, 3.9, 3.10).

It is notable that the position of the anomalous anticyclone in Figure 3.6 and the consequent impacts on GrIS surface conditions bear a striking resemblance to that of the mature Omega blocks that have driven the recent positive trend in summer Greenland blocking (Preece et al., 2022). This geographic overlap supports the notion that snow cover anomalies have directly contributed to the uptick in high-amplitude Omega blocking over Greenland.

Our results indicate that retreating SCE favors more frequent Greenland blocking both through its contribution to AA and through a direct influence on the forced Rossby wave pattern. These represent two potentially synergistic phenomena, as the atmospheric response to surface thermal forcing in the midlatitudes becomes more pronounced with a reduction in the background zonal flow (Coumou et al., 2018; Held & Ting, 1990; Hoskins & Woollings, 2015). Moreover, considering these two mechanisms together may provide additional insight into the dynamics underlying the recent increase in Greenland blocking if viewed within the traffic jam

model of blocked flows (Nakamura & Huang, 2018). Under this model, blocking is primarily governed by the column-averaged zonal flux of the local wave activity (LWA), which is a longitudinally varying, potential-vorticity-based measure of jet stream waviness (Huang & Nakamura, 2016). Like the flow of traffic on a highway, the zonal flux increases to accommodate intensifying LWA up to some capacity, after which the flux declines rapidly, leading to the buildup of LWA and the onset of blocking (Nakamura & Huang, 2018). According to the model, a more amplified stationary wave in response to retreating spring snow cover (Figure 3.6) would act to bring the LWA closer to capacity, while a weaker jet under AA (Figure 3.4c) reduces that capacity (Nakamura & Huang, 2018; Paradise et al., 2019)—changes that would both lessen the transient eddy forcing required to instigate blocking over Greenland.

While the method we used to trace the stationary wave response in this analysis emphasizes the relationship between spring SCE and the atmospheric circulation that follows, the pattern and magnitude of the regression anomalies also reflect the combined influence of other sources of internal variability within the climate system. It is difficult to disentangle these integrated processes using observations alone. Future work should therefore utilize prescribed global climate model simulations to determine whether the stationary wave response to spring North American SCE is present when accounting for other sources of variability.

3.4 Data and Methods

3.4.1 Characterizing the Large-Scale Flow Over Greenland

This analysis utilizes ERA5 reanalysis data (Hersbach et al., 2020) to represent the large-scale atmospheric setting over Greenland as quantified using three circulation metrics: the sinuosity index, the GBI, and PH03. The sinuosity of a given

isohypse is calculated as follows (Vavrus et al., 2017):

$$S_i = \frac{L_i}{L_\phi}$$

Where S_i is the sinuosity index for a given isohypse, L_i is the arc length along the isohypse, and L_ϕ is the small-circle length along the equivalent latitude. L_ϕ is determined as the parallel of latitude that contains an equal area on its poleward side as is enclosed by the isohypse in question. Thus, $S_i = 1$ would indicate an isohypse that traces a parallel of latitude. These index parameters are illustrated in Figure 3.1 where, using the 5500 hPa isohypse in Figure 3.1a as an example, the blue shading shows the area that was used to calculate an equivalent latitude of 59.73°N. As noted to the right of the map, the ratio of length along the blue line to the length of the red dashed line yields a relatively low sinuosity for the 5500 hPa isohypse of 1.16.

To characterize atmospheric circulation over the North Atlantic as a whole, we apply an aggregate sinuosity, S_{ag}, similar to that of Vavrus et al. (2017), that is simply the average S_i for five evenly distributed isohypses covering the midlatitudes. While Vavrus et al. (2017) employed the same five isohypses throughout the year, we found that a seasonally defined S_{ag} better captured the baroclinic latitudes, particularly in summer (see Supplementary Figure 3.1). Here, we use seasonally varying S_{ag} isohypses that are evenly spaced between the 1979–2019 average zonal mean Z500 at 30°N and 70°N for each standard meteorological season. From its definition, S_i should not measure less than one. While this holds true for isohypses that traverse the entire domain, in certain situations where they do not—e.g., a region of high pressure covering only the southeast corner of the domain—S_i can assume an unrealistically low value. Thus, we take the additional step of filtering all values of S_i < 1 before calculating S_{ag}.

In its atmospheric application, a low S_{ag} corresponds to more zonal flow, while a high S_{ag} corresponds to a wavier (i.e., more meridional) flow. As an example, Figure 3.1a displays the synoptic setting on August 16th, 2001 when a zonal flow pattern resulted in a low S_{ag} of 1.09. In clear contrast, Figure 3.1b shows the synoptic setting on July 11th, 2012 where an S_{ag} of 2.00 accompanied a high-amplitude Omega blocking pattern that was responsible for exceptional melt of the GrIS that eventually extended to over 98% of the ice sheet's surface (Nghiem et al., 2012).

We also followed Vavrus et al. (2017) in computing sinuosity as a function of latitude. This was done at daily time steps by first calculating S_i at 10 m increments spanning the Northern Hemisphere, then assigning the value of S_i to the latitude whose zonal-mean geopotential height matched the value of the isohypse, i.

The sinuosity index effectively indicates whether the type of wavy circulation that is conducive to persistent, anomalous weather is present over the North Atlantic. To more specifically measure whether this wavy flow produces blocking over Greenland, we employ two complementary blocking detection methods as shown in Supplementary Figure 3.2. The first of these being the GBI, which is simply the latitude-weighted mean Z500 over a domain spanning 60–80°N and 20–80°W (Fang, 2004; Hanna et al., 2013). Thus, the GBI falls into the broad category of anomaly-based blocking detection methods, as Greenland blocking episodes are often identified as positive GBI anomalies relative to the time mean (Hanna et al., 2018b; Henderson et al., 2021; McLeod & Mote, 2016; Woollings et al., 2018)—an approach that emphasizes the presence of an anomalous anticyclone as the defining feature of atmospheric blocking. The GBI has been the primary index used to study the relationship between blocking and Greenland surface mass balance(Hahn et al., 2020; Hanna et al., 2013; Hofer et al., 2017; McLeod & Mote, 2016) as well as

to establish the recent positive trend in summer Greenland blocking (Hanna et al., 2018a; Hanna et al., 2018b; Hofer et al., 2017; McLeod & Mote, 2016).

We applied PH03 as a second measure of blocking over the region. This one-dimensional, longitudinally-varying index identifies reversals of the typical meridional potential temperature gradient at the 2 potential vorticity unit (PVU) surface (Pelly & Hoskins, 2003):

$$\beta = \frac{2}{\Delta\phi}\int_{\phi_0}^{\phi_0+\Delta\phi/2} \theta \,\mathrm{d}\phi - \frac{2}{\Delta\phi}\int_{\phi_0-\Delta\phi/2}^{\phi_0} \theta \,\mathrm{d}\phi$$

Where β is the blocking index at a given longitude, $\Delta\phi = 30^\circ$ is the latitude range over which the blocking index is calculated, and θ is the potential temperature at the 2 PVU surface. The central blocking latitude, ϕ_0, is defined as the latitude of maximum 1981–2010 long-term mean eddy kinetic energy (EKE):

$$EKE = \frac{1}{2}(u' + v')^2$$

In a modification of the original PH03 index, this study uses a seasonally defined ϕ_0, as previous efforts have demonstrated it necessary to consider the seasonal migration of the storm track to effectively capture summer blocking over Greenland (Wachowicz et al., 2021). From this definition, PH03 falls in the second broad class of blocking detection methods, known as flow reversal metrics, in that $\beta > 0$ signals a reversal of the typical westerly flow along the climatological storm track (Henderson et al., 2021; Woollings et al., 2018). Here, Greenland blocking is said to occur on a given day if β is positive across at least 12 degrees of longitude within the sector encompassed by the longitudinal bounds of the GBI (i.e., 20–80°W). Thus, PH03 represents a dynamically-based definition of blocking that focuses on the disruption of the storm track as a defining characteristic and, therefore, provides an alternative perspective on blocking with respect to the GBI. Furthermore,

potential-vorticity-based flow reversal methods are more effective at detecting high latitude blocking than their geopotential-height-based counterparts (Tyrlis et al., 2021), making PH03 better suited for our application over Greenland.

3.4.2 Investigating lagged relationships between snow cover and summer atmospheric circulation over Greenland

To investigate whether summer atmospheric circulation over Greenland is influenced by Arctic-amplified changes in high-latitude snow cover, we performed a lagged linear regression of each of the three circulation indices detailed in the previous section against antecedent snow cover extent (SCE). Specifically, we examined Northern Hemisphere, Eurasian, and North American SCE area as derived from the National Oceanic and Atmospheric Administration (NOAA) Climate Data Record (CDR) of Northern Hemisphere SCE by the Rutgers University Global Snow Lab (Robinson et al., 2012). The CDR provides weekly SCE observations that are primarily produced via manual interpretation of visible satellite imagery (Estilow et al., 2015; Helfrich et al., 2007). These observations are made available on an 88x88 polar stereographic grid spanning the Northern Hemisphere and, given their course spatial resolution, are most suitable for monitoring SCE at continental scales (Estilow et al., 2015). Previous applications of the SCE CDR that are particularly relevant to this study's objectives include documenting the rapid retreat of spring snow-cover across the Northern Hemisphere as an indicator of AA (Derksen & Brown, 2012) and demonstrating the influence of Eurasian SCE variability on summer atmospheric circulation (Matsumura et al., 2014).

3.4.3 Tracing the atmospheric response to snow cover variability

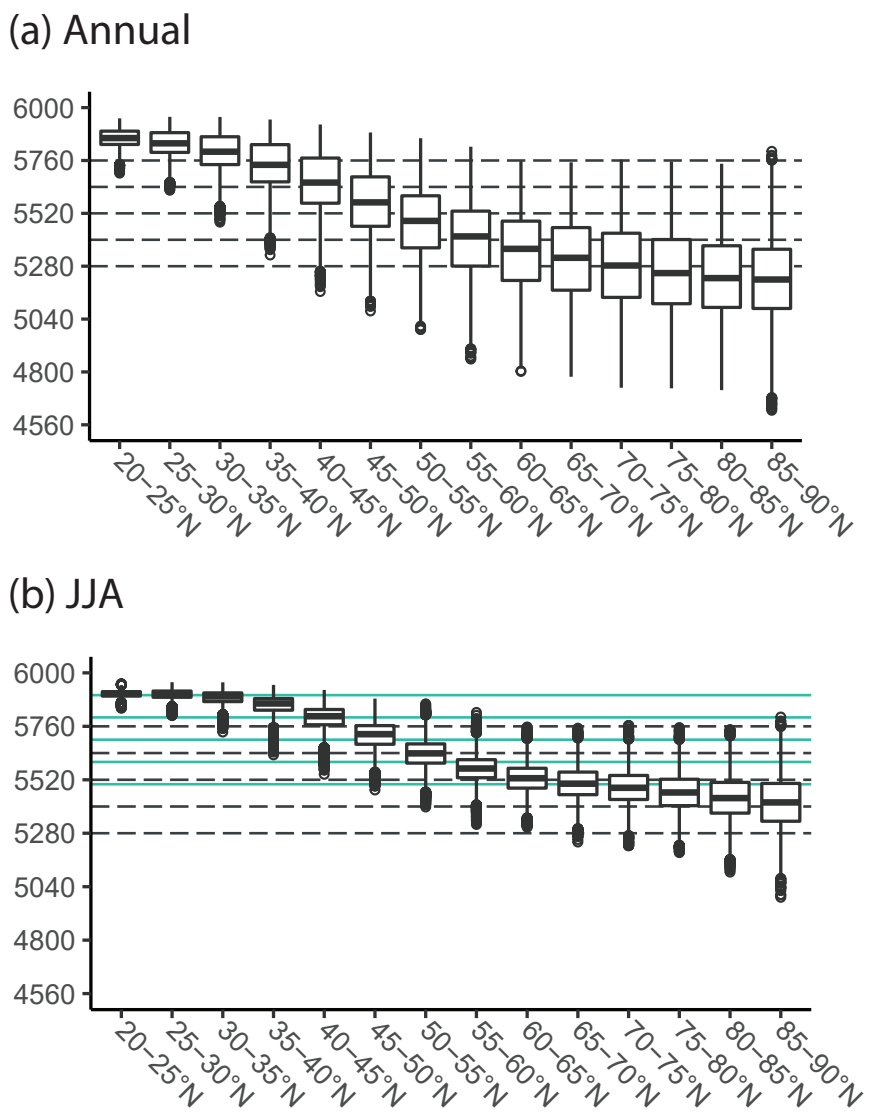
For instances where the lagged regression analysis revealed an apparent link between spring SCE and the ensuing summer atmospheric circulation over Greenland, we looked for evidence of a direct stationary Rossby wave response as a potential explanatory dynamical mechanism underlying the observed statistical relationship. This was accomplished by tracing the stationary wave response using the three-dimensional wave activity flux, where the WAF vectors run parallel to the local group velocity of the Rossby wave packet (Takaya & Nakamura, 2001).

Previous studies have applied this formulation of the WAF to demonstrate the influence of both sea ice (Honda et al., 2009; Honda et al., 1999) and snow cover variability (Matsumura & Yamazaki, 2012) on atmospheric circulation by displaying the WAF calculated from composite-difference fields representing the change in the state of the atmosphere between years of opposing surface conditions (e.g., low-minus-high SCE years). Here, we follow the general approach of T. Gong et al. (2019) by calculating the WAF from regression anomalies rather than composite differences to provide a more direct representation of the conditions captured in the lagged regression analysis. Specifically, we calculated the WAF from the geostrophic stream function anomaly obtained from the regression of ERA5 300 hPa geopotential height (Z300) against the monthly SCE area for instances of significant lagged correlation with the circulation indices outlined above. The circulation indices and Z300 were detrended prior to regression, and the regression anomalies were mapped to a 2.5°grid using first-order conservative remapping and smoothed using a Gaussian filter prior to computing the WAF.

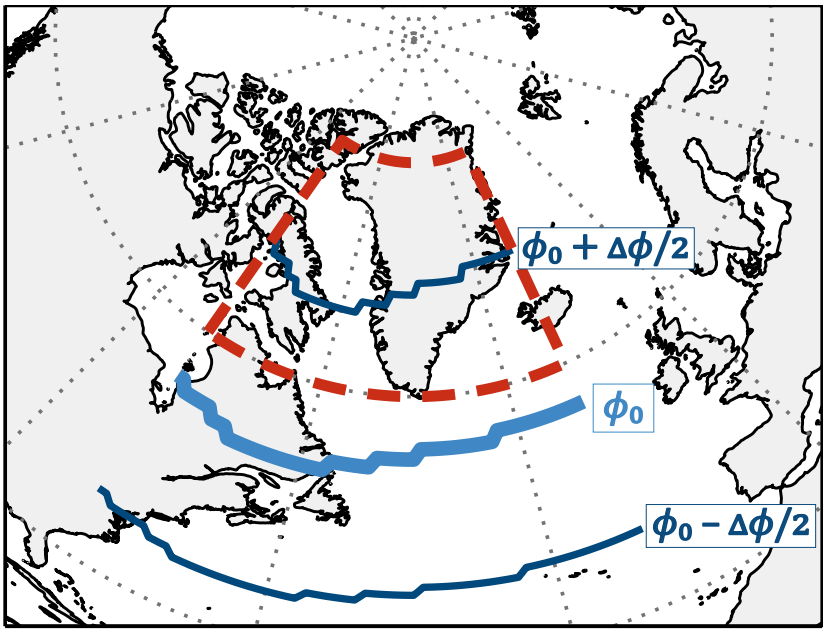
One proposed chain of mechanisms linking summer atmospheric circulation to spring surface conditions is the snow-hydrological effect, whereby diminished

spring SCE causes a depletion of soil moisture and, consequently, enhanced surface heating in summer (Matsumura & Yamazaki, 2012; Yasunari et al., 1991). To investigate this pathway, we also perform a grid point linear regression of detrended, monthly ERA5 soil moisture and surface air temperature against detrended monthly SCE. We perform the regression using monthly surface variables for each month spanning the significant lagged correlation between spring SCE and summer atmospheric circulation to illustrate the temporal chain of mechanisms in the snow hydrological effect.

We then repeat the grid point linear regression using GrIS surface variables as simulated by the regional climate model, Modèle Atmosphérique Régional (MAR) to tie the atmospheric response into the SMB of the ice sheet. MAR is fully coupled to multilayered snowpack model and has been developed for the study of GrIS SMB (Brun et al., 1992; Brun et al., 1989; Fettweis et al., 2017; Fettweis et al., 2020; Lefebre et al., 2005). Here, we examine 10-km output from MARv3.11 forced by ERA5 reanalysis. We refer the reader to Amory et al. (2021) for a more comprehensive description of MARv3.11.



Supplementary Figure 3.1: Climatology of Northern Hemisphere Z500 for (a) all days (b) JJA days during the 1979–2019 study period. Boxplots summarize daily zonal means grouped into 5° latitudinal bins spanning the midlatitudes as labeled along the x-axis. Dashed horizontal lines mark aggregate sinuosity isohypse values used in Vavrus et al. (2017). Solid green horizontal lines in (b) mark JJA S_{ag} isohypses used here.



Supplementary Figure 3.2: A representation of the two blocking detection methods employed herein. The red dashed line shows the sampling area of the GBI. Solid blue lines show PH03 parameters.

Supplementary Table 3.1: Long-term (1979–2019) seasonal trends in the mean and select percentiles of S_{ag}. Percentiles computed from daily S_{ag} for each season and year.

	Statistic	Slope (SD decade^{-1})	P-value
MAM	Mean	-0.0072	0.96
	25th %tile	-0.00005	1
	50th %tile	0.0045	0.92
	75th %tile	-0.0010	0.98
	90th %tile	-0.0048	0.93
JJA	Mean	0.33	0.01
	25th %tile	0.010	0.012
	50th %tile	0.12	0.0093
	75th %tile	0.14	0.0058
	90th %tile	0.13	0.056
SON	Mean	0.080	0.55
	25th %tile	0.049	0.12
	50th %tile	0.054	0.19
	75th %tile	-0.012	0.79
	90th %tile	-0.062	0.26
DJF	Mean	0.079	0.61
	25th %tile	0.040	0.42
	50th %tile	0.052	0.41
	75th %tile	0.026	0.72
	90th %tile	-0.0068	0.93

CHAPTER 4

ESTIMATING THE THERMODYNAMIC CONTRIBUTION TO RECENT GREENLAND ICE SHEET SURFACE MASS LOSS[3]

[3]Preece, J. R., Alexander, P. M., Fettweis, X., Tedesco, M., Kooperman, G. J., & Mote, T. L. To be submitted to The Cryosphere.

Abstract

The Greenland Ice Sheet has become the largest single frozen source of global sea level rise following a pronounced increase in meltwater runoff in recent decades. The pivotal role of anomalous anticyclonic circulation patterns in facilitating the increase in surface mass loss has been widely documented; however, this dynamical change has also occurred against a backdrop of a rapidly warming Arctic. While amplified warming at high latitudes has undoubtedly contributed to trends in mass loss, just how much is an open question. Here we apply the pseudo-global warming method of dynamical downscaling to estimate the contribution of the change in the thermodynamic background state under global warming to observed Greenland Ice Sheet surface mass loss since the turn of the century. Our analysis demonstrates that, had the recent atmospheric dynamical forcing of the Greenland Ice Sheet occurred under a preindustrial setting, anomalous surface mass loss would have been reduced by over 62% relative to observations. We show that the change in the thermodynamic environment under amplified Arctic warming has augmented melt of the ice sheet via longwave radiative effects accompanying an increase in atmospheric water vapor content. Furthermore, the thermodynamic contribution to surface mass loss over the exceptional melt years of 2012 and 2019 was less than half that of the long-term average, demonstrating a reduced influence during periods of strong synoptic-scale atmospheric forcing.

4.1 Introduction

Greenland Ice Sheet (GrIS) mass loss has rapidly accelerated since the turn of the century (IMBIE Team, 2020; Khan et al., 2015; Kjeldsen et al., 2015; Mouginot et al., 2019; Velicogna et al., 2020), becoming the largest single frozen source of global sea level rise and second largest among all sources after thermal expansion of the warming oceans (Cazenave et al., 2018; Horwath et al., 2022). While highly variable, GrIS mass loss has consistently raised global mean sea level over 0.5 mm yr^{-1} in recent decades—clearly outpacing that of the Antarctic Ice Sheet (IMBIE Team, 2018, 2020; Smith et al., 2020), and contributing at a rate that is approximately equal to that of all other glaciers combined (Cazenave et al., 2018; Zemp et al., 2019). Estimates place the total contribution at over 10 mm of sea level rise since the 1990s (IMBIE Team, 2020; Mouginot et al., 2019). Moreover, most of the impact of recent climate change on GrIS mas balance has yet to be realized. Recent work conservatively estimates another $\sim$274 mm of committed sea level rise before the GrIS achieves balance with the current climate state—i.e., even without considering the additional impact of any future warming scenario (Box et al., 2022).

Total mass balance is determined as the surface mass balance (SMB)—principally, the budget of snow accumulation minus meltwater runoff—less any solid ice discharge via marine terminating outlet glaciers. There has been both an acceleration of solid-ice discharge and a decline in SMB over the past few decades (IMBIE Team, 2020; Mankoff et al., 2019; van den Broeke et al., 2009a); however, augmented melt of the GrIS caused the SMB to decline at a rate twice that of the observed increase in dynamic ice loss (Box et al., 2022; Fettweis et al., 2020; Mote, 2007; Noël et al., 2017). Consequently, SMB reductions have surpassed discharge as the largest source of GrIS mass loss (Mouginot et al., 2019) and, according to

the latest generation of global climate models (GCM)s, SMB losses are expected to exceed mass accumulation on their own by the year 2100 unless the most ambitious mitigation efforts are implemented (Noël et al., 2021).

This stark change in GrIS surface conditions is primarily due to the recent shift in summer atmospheric circulation over the North Atlantic. The negative trend in GrIS SMB has coincided with a more persistently negative North Atlantic Oscillation (NAO) and an increase in atmospheric blocking episodes over Greenland (Bevis et al., 2019; Fettweis et al., 2013; Hanna et al., 2016; Hanna et al., 2022; Hanna et al., 2015; Hanna et al., 2018b; Hofer et al., 2017). Referred to as Greenland blocks, these persistent, anomalous anticyclones have played a key role in encouraging melt of the GrIS via multiple contrasting mechanisms.

For example, the positive trend in GrIS surface melt has been tied to Greenland blocking through the suppression of cloud cover by large-scale subsidence within the blocking ridge (Hofer et al., 2017). This reduction in cloud cover has allowed for above-normal incoming shortwave radiation over the southern ice sheet which, owing to its lower surface albedo, is more sensitive to changes in shortwave radiation than other regions of the GrIS (Hofer et al., 2017; Wang et al., 2019). Other studies, however, have demonstrated the importance of cloud longwave radiative effects, particularly in regions where albedo is high, such as the northern ice sheet and over the high-elevation accumulation zone (Gallagher et al., 2018; Lenaerts et al., 2019; Noël et al., 2019; Wang et al., 2019). Strong southerly moisture transport upstream of a blocking anticyclone in July 2012 supported the formation of low-level cloud cover that produced melt over the highest elevations of the ice sheet for the first time in over a century (Bennartz et al., 2013; Clausen et al., 1988; Mattingly et al., 2018; Meese et al., 1994; Neff et al., 2014; Nghiem et al., 2012). Additionally, the high-amplitude Omega blocking patterns that have undergone the greatest increase in recent summers deliver moisture farther poleward, generating above-

normal downward longwave radiation over the most northern portions of Greenland (Preece et al., 2022)—conditions which have caused pronounced growth of the ablation zone in the region and spurred a disproportionate increase in runoff from the northern drainages of the ice sheet (Noël et al., 2019).

A natural question is whether this shift in summer circulation may be a symptom of climate change. At the hemispheric scale, there are several theoretical frameworks that postulate a link between changes in the meridional temperature gradient under Arctic Amplification and more frequent persistent weather extremes (Cohen et al., 2014; Coumou et al., 2018; Francis & Vavrus, 2012), and there is mounting evidence of such a link during summer (Cattiaux et al., 2016; Coumou et al., 2015; Di Capua & Coumou, 2016; Kornhuber & Tamarin-Brodsky, 2021; Vavrus et al., 2017). Focusing on summer Greenland blocking more specifically, Liu et al. (2016) demonstrated a relationship between reduced Arctic sea ice and anticyclonic conditions over Greenland using both observations and modeling. However, not only have GCMs failed to capture the positive trend in Greenland blocking, they consistently predict a decline in blocking frequency in the region (Delhasse et al., 2021; Hanna et al., 2018a)—a discrepancy that constitutes a critical source of outstanding uncertainty regarding a causal link between anthropogenic climate change and the observed shift in summer circulation over Greenland.

Conversely, the change in the background thermodynamic environment, and its resulting impact on GrIS SMB, represents a more robust signal of climate change than the potential dynamical response outlined above. Multiple well-documented radiative feedbacks have helped warm the Arctic at four times the global average rate (Pithan & Mauritsen, 2014; Rantanen et al., 2022; Serreze & Barry, 2011). This constitutes a likely contributor to the nonlinear decline in GrIS SMB as surface melt would be expected to increase in frequency and magnitude in a warmer, more humid atmosphere.

While the thermodynamic environment over Greenland is surely influenced by changes occurring more broadly throughout the Arctic, local sea-surface conditions may also play an important role. Specifically, sea ice reductions over adjacent waters could further contribute to elevated temperatures over Greenland through the water vapor feedback, wherein a warmer atmosphere together with an ice free ocean increases atmospheric water vapor, which then enhances longwave radiative forcing at the surface (Pithan & Mauritsen, 2014). Thus, one of the more intuitive ways that sea ice loss could impact the GrIS is through advection of warm, moisture-enriched air from the neighboring seas. In investigating such a link, studies have revealed a relationship between changes in sea-ice concentration near Greenland and GrIS SMB (Pedersen & Christensen, 2019; Rennermalm et al., 2009); however, these studies fail to separate direct marine influence from any indirect affects that might occur via alteration of the large-scale circulation by oceanic thermal forcing (Ballinger et al., 2019; Liu et al., 2016) or relationships that might arise as a byproduct of mutual forcing of local sea ice concentration (SIC) and GrIS melt by the large-scale synoptic setting (Ballinger et al., 2018b; Stroeve et al., 2017).

Several efforts have demonstrated a minimal contribution from local SIC and SST anomalies during summers of pronounced GrIS melt (Hanna et al., 2009; Hanna et al., 2014; Noël et al., 2014). One explanation for the lack of marine influence is that persistent katabatic outflow over the ice sheet acts as a barrier to onshore advection (Hanna et al., 2014; Noël et al., 2014); however, observational evidence suggests different, seasonally varying roles for the influence of local sea-surface conditions versus that of large-scale dynamical forcing of GrIS SMB. While melt events during summer and fall are primarily a product of large-scale atmospheric conditions (Ballinger et al., 2019; Hermann et al., 2020; Noël et al., 2014), recent work has demonstrated elevated atmospheric moisture and enhanced downwelling longwave radiation over the ice sheet approximately one week following sea

ice retreat in the Baffin Bay and Davis Strait in years of early GrIS melt, suggesting local sea ice anomalies precondition the ice sheet for early melt onset (Stroeve et al., 2017).

Disentangling the relative contributions of atmospheric dynamics versus thermodynamics is an intractable problem using observations alone. Previous studies have utilized regional climate models (RCM)s to examine the sensitivity of GrIS SMB to perturbations in sea-surface conditions (Hanna et al., 2009; Hanna et al., 2014; Noël et al., 2014) or atmospheric thermodynamic fields (Delhasse et al., 2018); however, none of these efforts examined the combined influence of both atmospheric and sea-surface conditions. Furthermore, these studies either applied arbitrary perturbations to the targeted boundary fields or only examined a single melt season and, therefore, did not aim to measure the existent contribution of observed changes in these fields to GrIS mass loss since its acceleration around the turn of the century.

Here, we provide a more systematic estimate of the relative contributions of dynamical versus thermodynamic change to recent GrIS surface mass loss using the pseudo-global warming (PGW) method of dynamical downscaling. The PGW method uses adjusted reanalysis data for the initial and lateral boundary conditions of an RCM (Kawase et al., 2008; Kimura & Kitoh, 2007; Schär et al., 1996). To obtain the adjusted boundary conditions, this method applies a climate change perturbation signal that is estimated from GCM output by assuming a linear change in the boundary fields between the control period (i.e., the period of observed reanalysis data) and some alternative period of interest with a contrasting thermodynamic background state (typically some future period) (Kawase et al., 2009; Rasmussen et al., 2011; Schär et al., 1996). Thus, the PGW technique effectively emphasizes the thermodynamic component of climate change by assuming that the timing and

structure of synoptic disturbances along the RCM's boundaries will be the same in the alternative period as during the control (Lackmann, 2015).

While the PGW method is typically utilized to simulate future conditions, it can also be used to investigate how recent periods of climate or individual weather events would have behaved under past conditions. For example, Lackmann (2015) estimated the thermodynamic contribution of recent climate change to the evolution of Hurricane Sandy by comparing a control run to a PGW simulation using boundary conditions that were adjusted to reflect the climate of the late 19th Century. Likewise, Kawase et al. (2008) used a similar approach in a climate change attribution study of the Mei-yu rain band in southern China. Here we use the PGW method to quantify what the magnitude of GrIS surface melt would have been if the recent dynamical forcing of the ice sheet had occurred in a preindustrial thermodynamic setting. Specifically, this analysis aims to answer the following questions: (1) How much of the recent SMB decline can be attributed to local thermodynamic change (i.e., the combined influence of increasing background temperatures and contributions from local sea-surface conditions)? (2) What portion of the thermodynamic influence is due to adjacent SIC / SST change alone? (3) Do sea-surface conditions have a discernible impact on the timing or duration of the GrIS melt season?

4.2 Experimental Design

A model diagram outlining our approach is presented as Figure 4.1. Atmospheric conditions and GrIS SMB and surface energy balance (SEB) response were modeled using the regional climate model, Modèle Atmosphérique Régional (MAR) (Fettweis et al., 2005; Fettweis et al., 2020; Lefebre et al., 2005). MAR includes a surface-atmosphere energy and mass transfer scheme with a one-dimensional snowpack model that represents snow grain metamorphism and its impact on

albedo, and accounts for the percolation and refreeze of meltwater within the snowpack (Amory et al., 2021; Brun et al., 1992; Brun et al., 1989). For a more detailed description of MAR, we refer the reader to Amory et al. (2021). Here, we employed MAR version 3.12 forced with 6-hourly ERA5 reanalysis data and integrated over a 120X180, 20-km grid with 24 vertical atmospheric levels.

As a control, we forced MAR with ERA5 data spanning the period of 2000 to 2019 to provide a representation of observed conditions during the recent acceleration of GrIS surface melt (Figure 4.1, gray components). To simulate the preindustrial thermodynamic state (Figure 4.1, blue components), we adjusted the boundary conditions of air temperature, specific humidity, sea-surface temperature (SST), and sea ice concentration (SIC).

We adjusted air temperature and specific humidity using a climate change perturbation derived from the 40 ensemble members of the NCAR Community Earth System Model-Large Ensemble (CESM-LE) project:

$$\Delta x = \overline{x}_p - \overline{x}_c$$

Where Δx is the climate change perturbation for variable x, $\overline{x}_p$ is the ensemble-averaged, long-term monthly mean of variable x for a preindustrial reference period of 1880–1899, and $\overline{x}_c$ is the ensemble-averaged, long-term monthly mean of variable x for a control period of 2000–2019. We then linearly interpolated the monthly climate change perturbations to a 6-hourly timestep before adding them to the corresponding ERA5 boundary fields.

Figure 4.2 shows the monthly surface air temperature and specific humidity perturbation fields over the entirety of the MAR integration domain utilized herein for an equally spaced subset of months. Seasonally, CESM-LE simulates the greatest temperature difference in fall and winter, where conditions over the surrounding

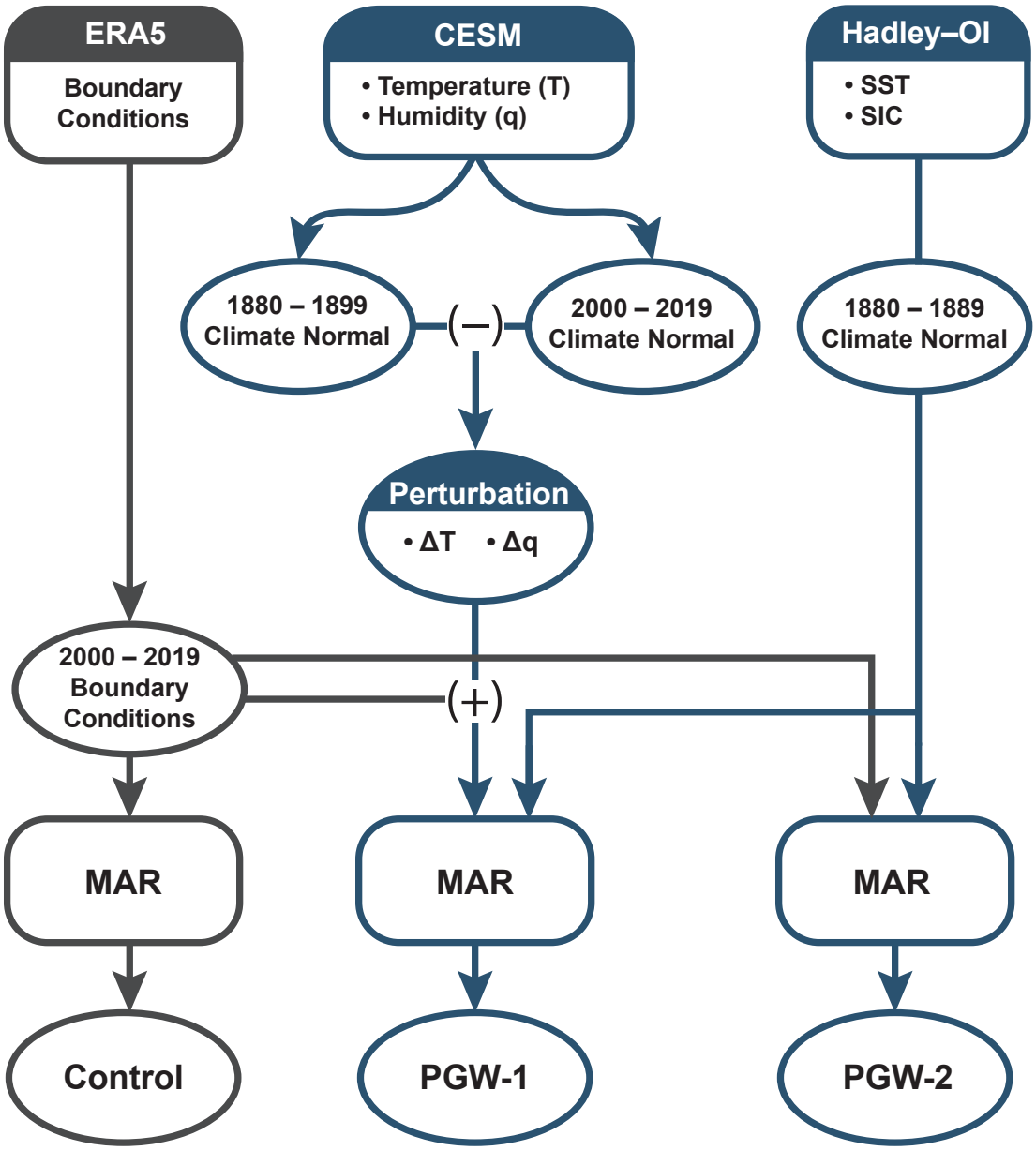


Figure 4.1: Model diagram illustrating the design of the control run (gray outlines) pseudo-global warming experiments (blue outlines).

seas were more than 3 °C cooler during the preindustrial period than in the current climate (Figure 4.2, top row). The spatial distribution and seasonality of this temperature perturbation signal is consistent with what should be expected under Arctic amplification, which is, in large part, driven by sea ice loss (Screen & Simmonds, 2010). Differences in atmospheric moisture are largely reflective of the Clausius-Clapeyron relation, with drier conditions mirroring locations of cooler temperatures in the preindustrial climate (Figure 4.2, bottom row).

While global climate models (GCMs) should resolve the periodicity of internal climate variability, the precise timing of a particular mode of variability differs between individual ensemble members. Considering a single GCM simulation alone would risk enhancing or suppressing the magnitude of the climate perturbation signal if the control and alternative periods are characterized by opposing phases of a relevant mode of internal variability. The same is true for observations. For example, summer atmospheric circulation has been characterized by an anomalously negative North Atlantic Oscillation (NAO) since the turn of the century—an atmospheric setting that favors the advection of warm, moist air over Greenland (Fettweis et al., 2013; Hanna et al., 2013; Henderson et al., 2021; Mattingly et al., 2018; Mote, 1998; Tedesco et al., 2016). Since our intent is to isolate the contribution of background thermodynamic change to GrIS mass loss, deriving a perturbation signal from observations would overestimate the change in temperature and humidity around Greenland because it would also include the dynamical contribution of an anomalously negative NAO during our control period. Taking an ensemble mean of the CESM-LE effectively removes the noise of internal climate variability by averaging across the differing phases resolved by each ensemble member for a given date, thereby providing a more appropriate estimate of the change in the mean climate state under global warming.

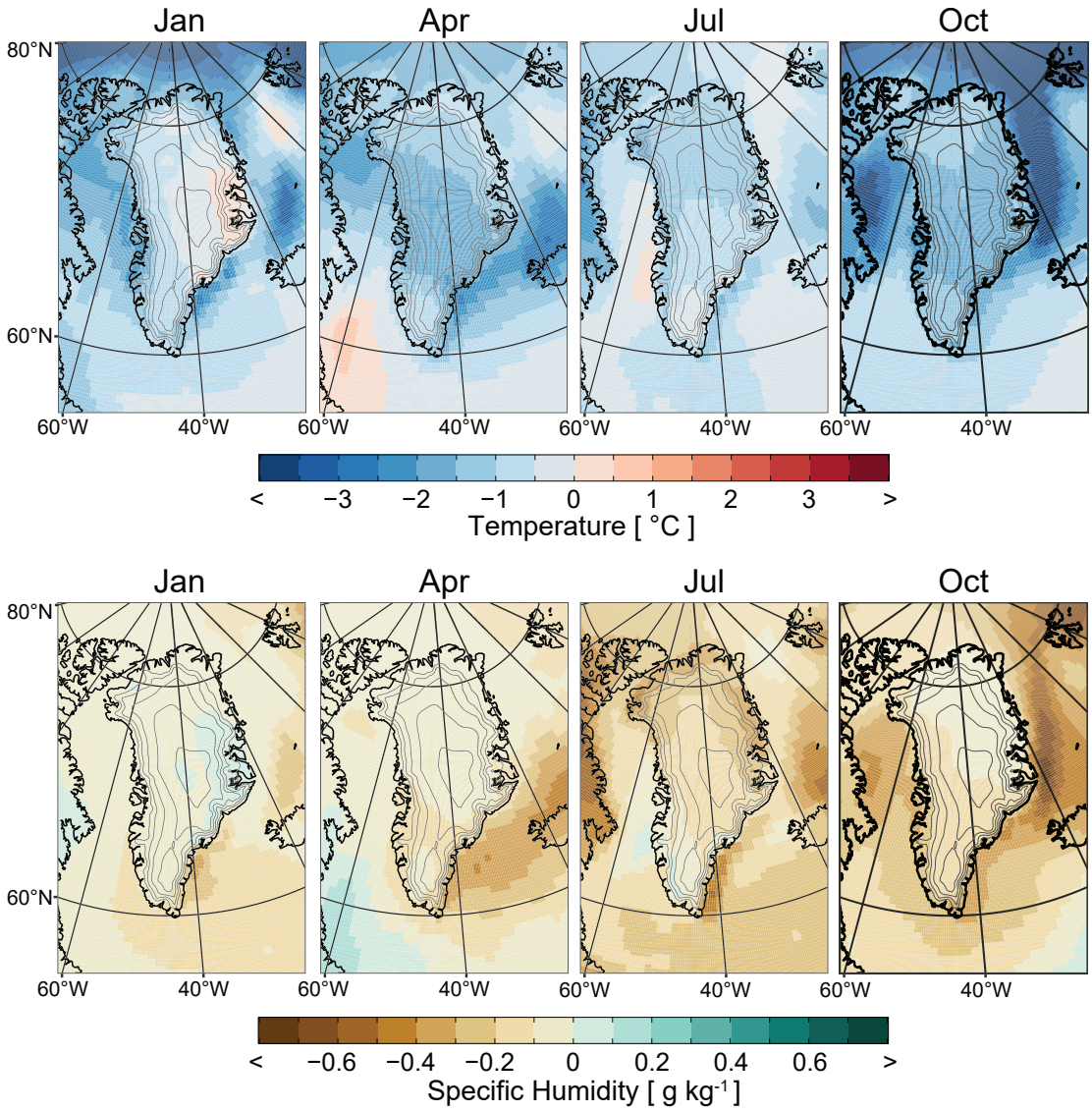


Figure 4.2: Climate change perturbation fields for surface air temperature (top row) and specific humidity (bottom row) shown for a selection of months equally spaced throughout the year as labeled at the top of each panel. Perturbation fields shown for the lowermost model level after vertically interpolating to the same ECMWF L137 hybrid sigma-pressure levels as the ERA5 boundary conditions. Contour interval: 500 m. Range: 1000–3000 m.

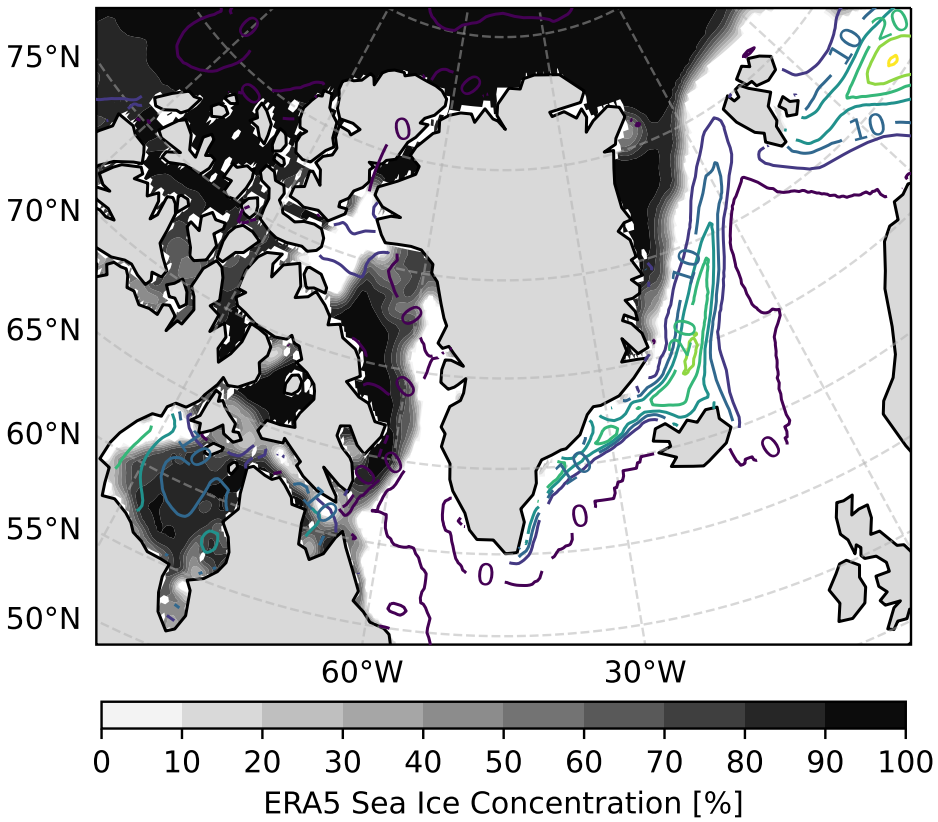


Figure 4.3: Comparison of observed sea ice concentration on June 15, 2018 (shading) and the corresponding CESM-LE climate perturbation signal (contours, 5% interval).

The use of a GCM-derived perturbation signal presents issues, however, when dealing with sea ice. The change in SIC is greatest along the sharply defined sea ice front and the GCM's representation may not geographically align with observations. This misalignment is quite apparent when comparing the perturbation signal to the sub-daily observations used to force the RCM. Figure 4.3 presents one such comparison for June 15, 2018, which occurs during a month of exceptionally low SIC in the Greenland Sea. There is a considerable gap between the observed sea ice front and area of greatest SIC change according to CESM-LE, such that the application of this perturbation signal would result in a local minimum in SIC stretching along the original sea ice front, followed by a band of higher SIC stretching from Iceland to Svalbard. To avoid this unrealistic circumstance, and to ensure consistency between SIC and SST, we prescribed sea-surface conditions in our experimental simulations using 1880–1899 long-term monthly means calculated from the merged Hadley-OI observational dataset (Shea et al., 2020) and interpolated to a 6-hourly timestep.

Figure 4.4 illustrates the long-term mean difference in sea-surface conditions between the 2000–2019 ERA5 fields used to force the control simulation and the 1880–1899 Hadley-OI fields that were prescribed for the PGW experiment. Contrary to global SST trends, the red shading in Figure 4.4 indicates extensive areas where SST during preindustrial period was warmer than during the current period—i.e., much of the region around Greenland has undergone SST cooling since the preindustrial period. This is most apparent during winter and spring when warmer SST is observed throughout the northern subpolar gyre to the southeast of Greenland, and extending from the southern Greenland coast along the sea ice edge to Svalbard. In summer, the more prevalent blue shading signals SST throughout much of the region was cooler during preindustrial period. The spatial and seasonal pattern SST cooling since the preindustrial period matches the fingerprint of the

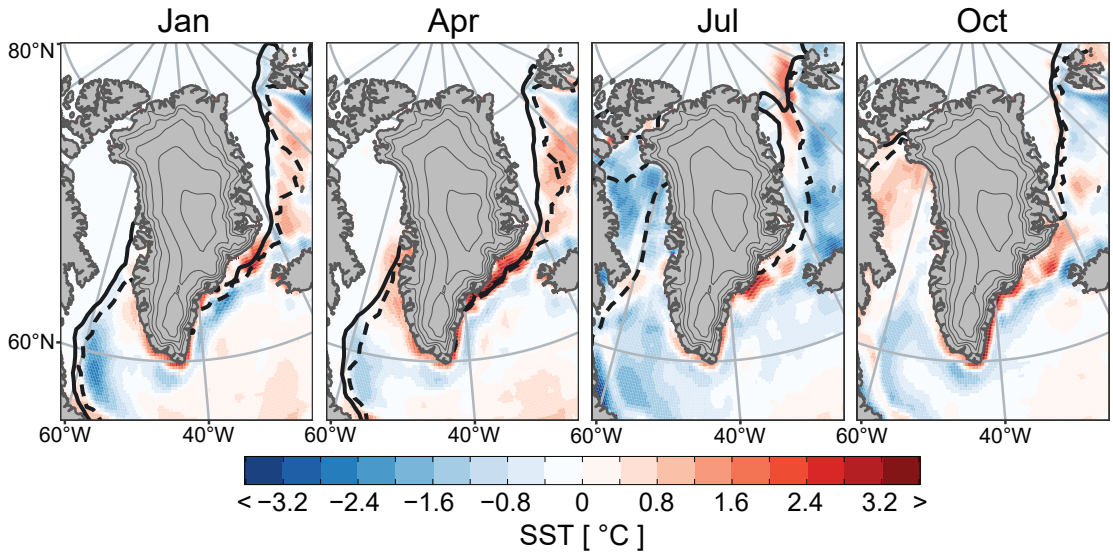


Figure 4.4: Change in sea-surface conditions around Greenland. Maps show the difference in SST (shading) and the location of the sea ice edge (black contours) between the prescribed 1880–1899 Hadley-OI fields used in the PGW experiments and the 2000–2019 ERA5 sea-surface conditions used in the control. Differences are shown for a selection of months equally spaced throughout the year as labeled at the top of each panel. Positive values (red shading) indicate warmer SST during the preindustrial period than during the control. Solid contour demarcates the sea ice edge for the control period, dashed for the preindustrial period. Sea ice edge is defined using a threshold of $\geq 50\%$ *SIC.*

so-called North Atlantic warming hole—an observed decrease in subpolar North Atlantic SST that has been attributed to a weakening of the Atlantic meridional overturning circulation and associated poleward oceanic heat transport as a consequence of global climate change (Caesar et al., 2018). In all months, sea ice extent is greater during the preindustrial period (dashed contour) than during the current period (solid contour).

After interpolating to a 6-hourly timestep, we applied the following adjustments based on the work of Hurrell et al. (2008) to further ensure consistency between SST and SIC:

- If an interpolated grid cell had a SIC $>$ 90%, we set the SST of that cell to the sea ice freezing point of -1.8 °C.

- Where 15% $<$ SIC $<$ 90% we adjusted SST as follows:

$$SST = 9.328(0.729 - (SIC/100)^3) - 1.8$$

- SIC was set to zero if SST $>$ 4.97 °C.

- Where -1.8 °C $<$ SST $<$ 4.97 °C we adjusted SIC as follows:

$$SIC = 100(0.729 - (SST + 1.8)/9.328)^{\frac{1}{3}}$$

This analysis includes two PGW simulations (Figure 4.1). For each model simulation, we allotted 5 years of spin-up time to allow the snowpack model to adjust to the altered boundary conditions. In PGW-1, we adjusted the boundary forcing fields of temperature, specific humidity, SST, and SIC to reflect preindustrial conditions using the procedures detailed above. Thus, by comparing PGW-1 to the control simulation, we quantify the thermodynamic contribution to recent GrIS surface mass loss. For PGW-2, we adjusted SST and SIC to reflect preindustrial conditions, while leaving the temperature and humidity fields unaltered. In doing so, we quantify the portion of recent surface mass loss that is due to changes in local sea-surface conditions alone.

The design of PGW-2 also allows us to test the theory of Stroeve et al. (2017) that low spring SIC in the seas surrounding Greenland preconditions the GrIS for melt in early melt onset years. Following Stroeve et al. (2017), we define melt onset as the first instance of five or more consecutive days of melt. The date of freeze onset is then defined as the first day following the last instance of five or more consecutive days of melt and melt season length as the number of days spanning the two dates. We calculated all measures of the melt season at each MAR grid point, then test for significant differences between the PGW simulations and the

control using a paired Wilcoxon signed-rank test with a predetermined significance level of $\alpha = 0.05$.

4.3 Results

4.3.1 Thermodynamic Contribution to GrIS SMB Change

Figure 4.5 presents a comparison of the cumulative SMB anomaly between the control run and each of the PGW simulations. The control run (Figure 4.5, gray line) shows a cumulative SMB anomaly of –1852 GT over the study period of 2000 to 2019, congruent with other estimates (IMBIE Team, 2020). This decline in the SMB equates to just over 5 mm of global sea level rise. A gradual shift to a negative cumulative SMB occurs around 2005, coinciding with the transition to more a persistently negative NAO and rise in Greenland blocking frequency (Hanna et al., 2015; Hofer et al., 2017). The first instance of pronounced mass loss is evident as a sharp decrease in 2007—a year of unprecedented surface melt up to that point in the satellite record (Mote, 2007). Instances of marked mass loss are frequently evident in the years that follow; however, the exceptional melt years of 2012 and 2019 are readily apparent as precipitous drops in the control time series.

Comparing the control with PGW1 (Figure 4.5, blue dashed line) clearly highlights the substantial thermodynamic contribution to the recent change in GrIS SMB. A difference in cumulative SMB between the two simulations of 1145 GT amounts to a 62% reduction in surface mass loss in PGW1 relative to the control. Under the preindustrial thermodynamic setting of PGW1, the GrIS maintains a positive SMB through 2009, and while the dynamical forcing of the ice sheet is still evident in the negative anomalies that occur during individual summers, the mass loss for each melt season is much more subdued relative to the control.

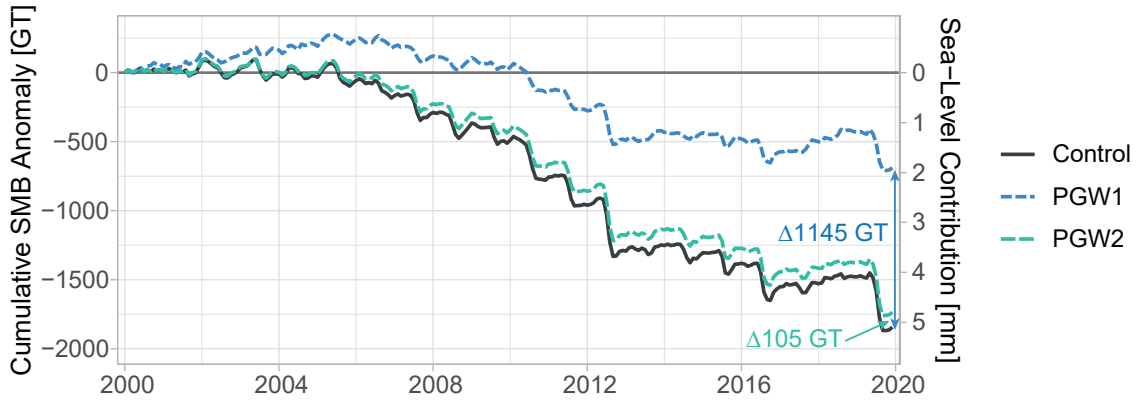


Figure 4.5: Temporal evolution of the GrIS SMB under contrasting thermodynamic background conditions. Shown are the cumulative SMB anomaly time series for the control (gray), PGW1 (blue dashed), and PGW2 (green dashed) simulations. Anomalies calculated with respect to the 1980-1989 reference period. Left axis shows cumulative SMB anomaly; right axis shows the equivalent sea-level contribution. Annotations detail the difference in the final cumulative SMB between each of the PGW simulations and the control.

Furthermore, while the rate of mass loss is much reduced from 2013 to 2018 in the control, this period undergoes a slight surface mass gain in PGW1.

The cumulative SMB anomaly in PGW2 (Figure 4.5, green dashed line) is 105 GT greater than that for the control. This relatively small difference indicates that there has been minimal influence by changes in local SST and SIC over the study period—a result that is consistent with previous studies showing low GrIS sensitivity to local sea-surface conditions (Hanna et al., 2009; Hanna et al., 2014; Noël et al., 2014). Together, these results demonstrate that changes occurring more widely throughout the Arctic dominate the thermodynamic contribution to GrIS mass loss.

Figure 4.6 provides a spatial representation of the comparisons made in Figure 4.5. The map of cumulative SMB over the study period as modeled by the control (Figure 4.6a) shows a band of negative SMB along the perimeter of the ice sheet that clearly demarcates the ablation zone, where annual surface mass loss exceeds accumulation. The greatest accumulation occurs along the southeast

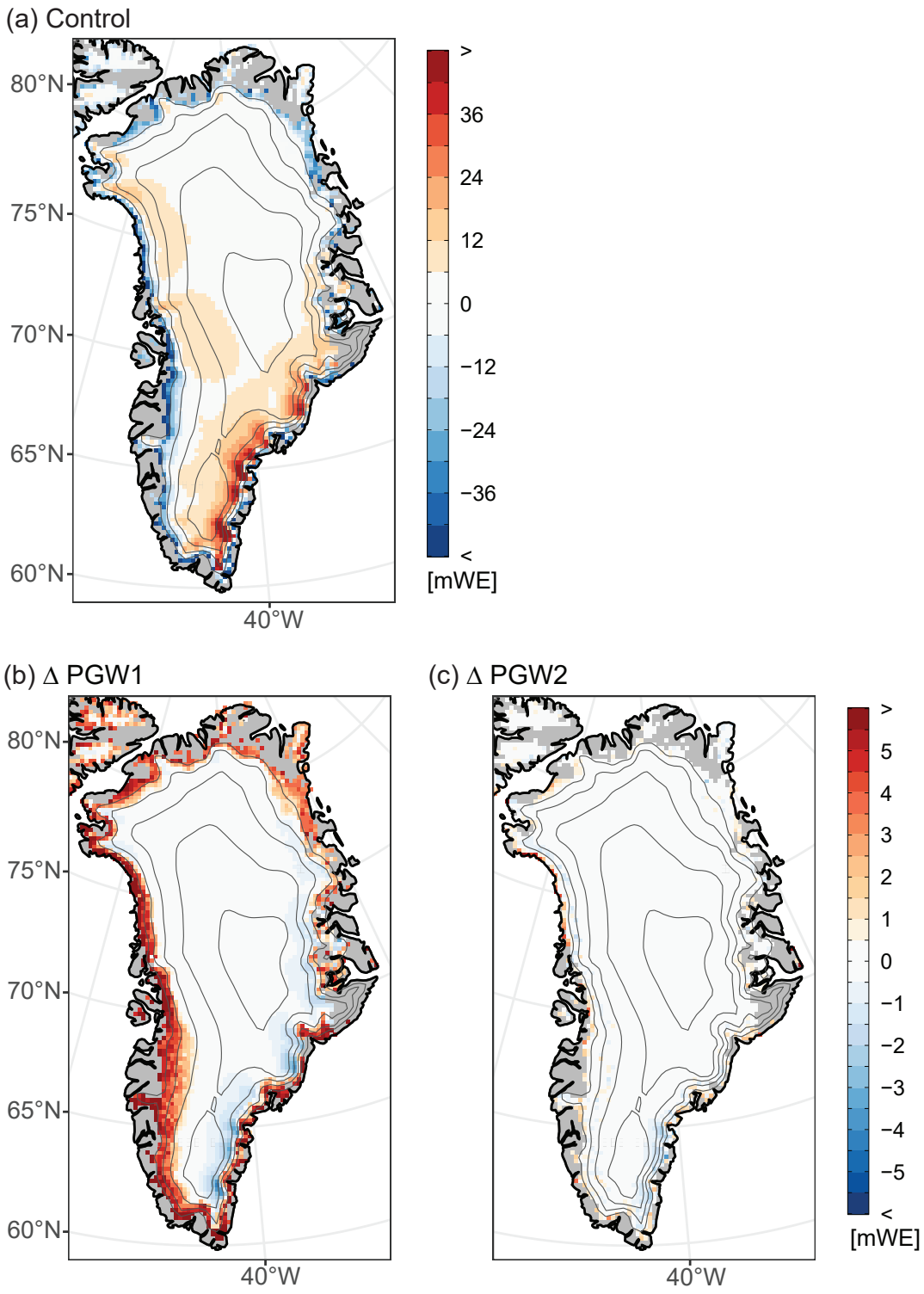


Figure 4.6: Spatial distribution of GrIS SMB change under contrasting thermodynamic background conditions. (a) The observed cumulative SMB over the full study period of 2000–2019 as represented by the control simulation. (b) PGW1 cumulative SMB minus the control. (c) PGW2 cumulative SMB minus the control. Contour interval: 500 m. Range: 1000–3000 m.

coast of Greenland and is a product of orographic enhancement of precipitation associated with lee-side cyclones that form in westerly flow over southern Greenland (Bromwich et al., 1998; Rogers et al., 2004; Schuenemann et al., 2009). Other areas of notable SMB gains include west and northwest Greenland. Snow accumulation in these areas is fueled by bouts of intense water vapor transport through the Davis Strait that have increased in frequency in recent decades (Mattingly et al., 2018; Mattingly et al., 2016).

Relative to the control, PGW1 yields a greater cumulative SMB in a band that stretches around perimeter of the ice sheet, exceeding 2000 m elevation in some locations in southwest Greenland (Figure 4.6b). This positive anomaly with respect to the control is a consequence of decreased meltwater runoff in the preindustrial setting (Supplementary Figure 4.1a). At higher elevations over much of eastern Greenland and, to a lesser extent over the northwest ice sheet near Qaanaaq, a reduction in snowfall in the cooler and dryer atmosphere of PGW1 results in a lower SMB compared to the control (Figure 4.6b, Supplementary Figure 4.1b).

Figure 4.7 shows the average seasonal progression of the principal SMB components for each model simulation. The greatest differences in surface runoff between PGW1 and the control are centered on the peak of the melt season in mid-to-late July (Figure 4.7a). The relative mass loss over high elevations evident in Figure 4.6b is driven a reduction in snowfall throughout the cool season; however this impact on snow accumulation is most apparent in fall and early winter when the greatest change in background conditions have occurred under Arctic amplification (Figure 4.2, Figure 4.7b) (Serreze & Barry, 2011). In contrast with the rest of the year, there is a slight increase in summer snowfall in PGW1 that coincides with a reduction in rainfall (Figure 4.7c), consistent with greater partitioning toward frozen precipitation under the cooler preindustrial setting.

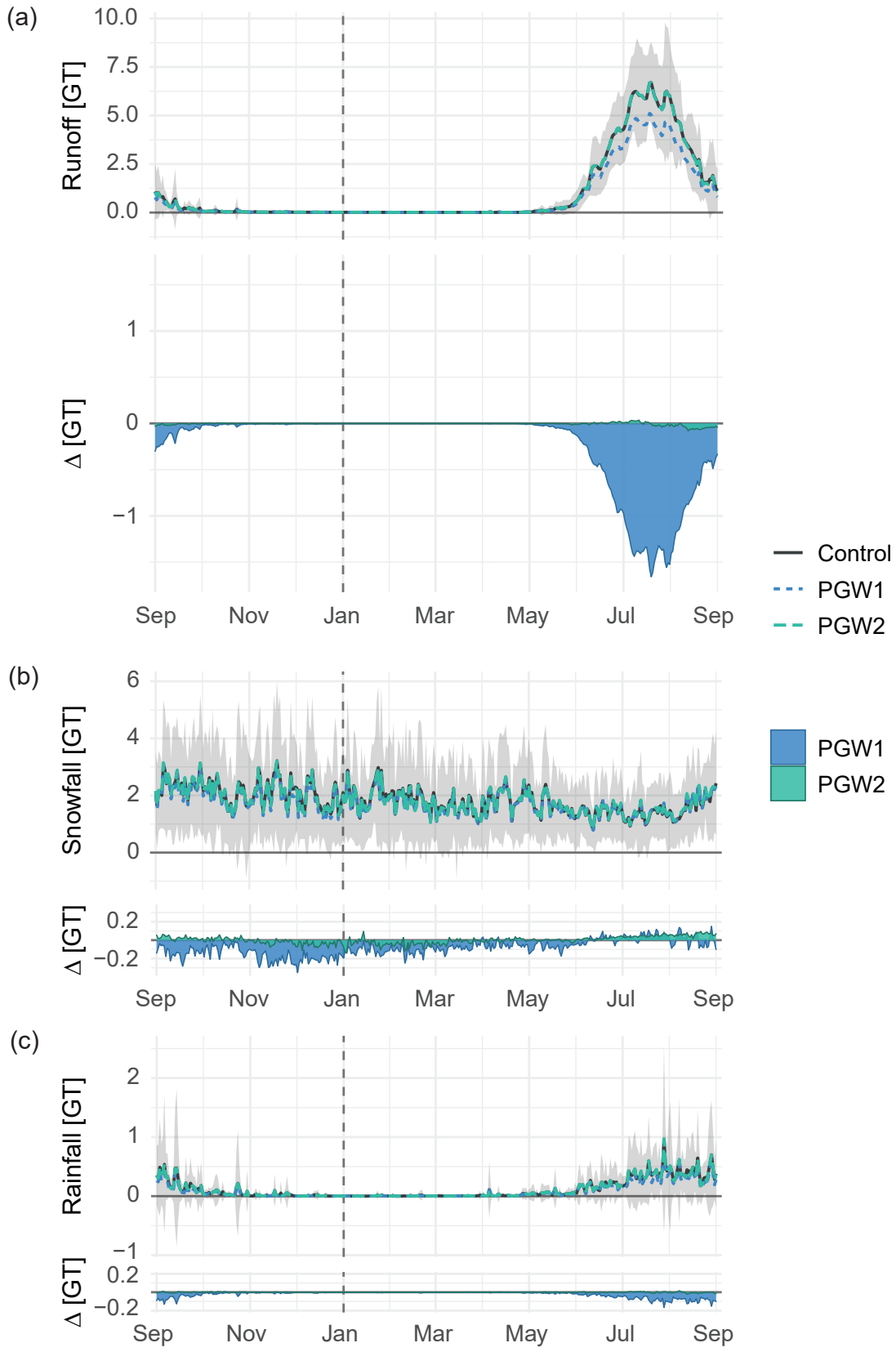


Figure 4.7: Seasonal evolution of GrIS SMB under contrasting thermodynamic background conditions. (Continued on following page.)

Figure 4.7: Seasonal evolution of GrIS SMB under contrasting thermodynamic background conditions. Panels depict the seasonal progression of three principle SEB components: (a) Surface runoff, (b) snowfall, (c) rainfall. Top portion of each panel shows the 2000–2019 long-term mean progression of each SMB component throughout the melt season for the control (gray), PGW1 (blue dashed), and PGW2 (green dashed) simulations. Time series represent the spatially integrated sum of a given variable over the entire ice mask. Gray shading shows the 1σ range about the mean for the control simulation. Bottom portion shows the difference between each PGW simulation (PGW1, blue; PGW2, green) and the control ($\Delta = PGW - Control$). The scale of the y-axis on the bottom portion is kept constant across all panels to facilitate comparison between SMB terms.

The differences between PGW2 and the control show a similar pattern as observed for PGW1; however they are reduced in both magnitude and scale (Figure 4.6c). The change in sea-surface conditions in PGW2 reduces meltwater runoff resulting in higher SMB (Figure 4.6c, Supplementary Figure 4.1d). Unlike PGW1, this response is largely confined to grid cells along the terminus of the ice sheet. The isolated impact of sea-surface conditions on snowfall is most evident along the southeast margin of the ice sheet and above $\sim$1000 m near Qaanaaq. In contrast with PGW1, in which runoff was diminished throughout the entire melt season, the impact of sea-surface conditions alone on surface melt emerges later in the melt season (Figure 4.7a), likely reflecting the stronger coupling between ocean and atmosphere as the thermal gradient between them increases into the fall (Screen, 2017).

While a decrease in snowfall relative to the control in the PGW simulations partially compensates for the relative mass gains at lower elevations, it is clear that the reduction in meltwater runoff is the primary determinant of the differences in cumulative SMB observed in Figure 4.5. Thus, the influence of recent thermodynamic change on GrIS SMB has been consequential during the melt season. Recognizing this, the next section focuses on the extended melt season to better understand the mechanisms by which thermodynamic change has dictated GrIS surface runoff.

4.3.2 Thermodynamic drivers of GrIS surface runoff

Figure 4.8 contrasts the SEB of the GrIS between the control and PGW simulations. The preindustrial thermodynamic state of PGW1 is associated with an increase in downward shortwave radiation (SWD) (Figure 4.8a, e) and a decrease in downward longwave radiation (LWD) (Figure 4.8b, f) throughout the melt season. For both variables, the differences between the control and PGW1 are maximized over the northern ice sheet. The time series in Figure 4.8c and d indicate that the turbulent fluxes are generally diminished in PGW1 relative to the control. The magnitude of these differences are far less than what is observed for the radiative terms; however, this is partly attributable to a spatially heterogeneous response. Differences in the turbulent heat fluxes are focused along the outer margins of the ice sheet, where lower elevations display a decrease in both sensible (SHF) and latent heat flux (LHF) in PGW1 that is mirrored by differences of the opposite sign over higher elevations (Figure 4.8g, h). Regardless, it is clear that longwave radiative effects have exerted a commanding role in the total SEB response to recent thermodynamic change.

The juxtaposition in the response of the turbulent fluxes in PGW1 appears to arise from opposing direct and indirect responses to the change in background conditions. Along the ice sheet margins, a decrease in both SHF an LHF is consistent with a direct reduction in the flux of heat and moisture to the surface of the ice sheet in a colder, drier preindustrial atmosphere. Conversely, above normal turbulent fluxes over higher elevations follows indirectly from changes in the near-surface wind field. Figure 4.9a shows the long-term mean May–Sep 10 m winds for the control period, clearly illustrating the persistent katabatic wind signature over Greenland. Lower water vapor content in PGW1 (Figure 4.2) reduces the longwave emissivity of the atmosphere, which would act to lower surface temperatures, in-

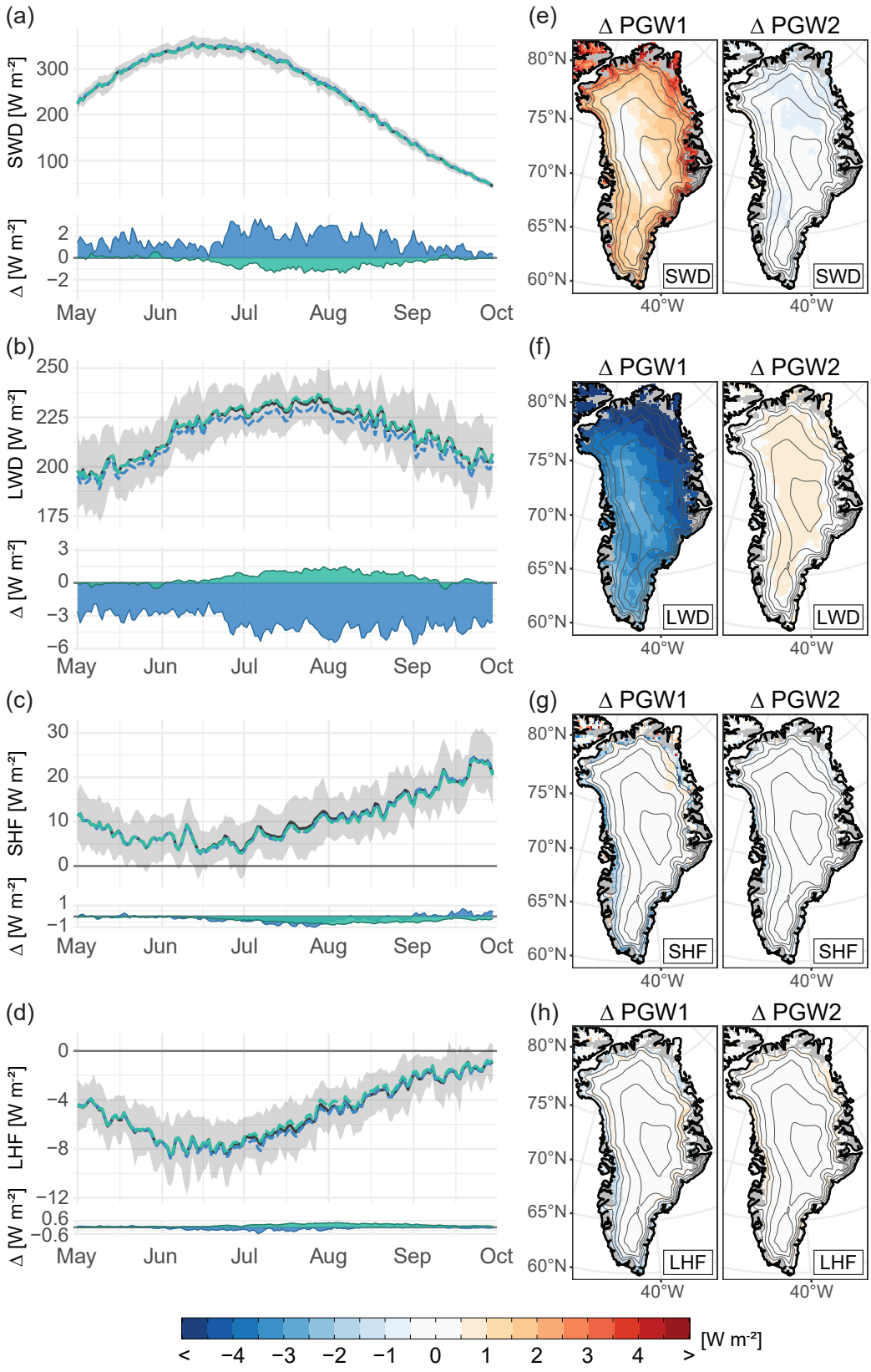


Figure 4.8: The SEB of the GrIS under contrasting thermodynamic background conditions.
(Continued on following page.)

Figure 4.8: The SEB of the GrIS during the melt season under contrasting thermodynamic background conditions. (a–d) Top portion of each panel shows the 2000–2019 long-term mean progression of each SEB component throughout the melt season for the control (gray), PGW1 (blue dashed), and PGW2 (green dashed) simulations. Time series represent the spatial average taken over the entire ice mask for a given variable. Gray shading shows the 1σ range about the mean for the control simulation. Bottom portion shows the difference between each PGW simulation (PGW1, blue; PGW2, green) and the control ($\Delta = PGW - Control$). The scale of the y-axis on the bottom portion is kept constant across all panels to facilitate comparison between SEB terms. (e–f) Maps depicting the difference between the 2000–2019, May–Sep long-term mean of each SEB component between each PGW simulations (PGW1, left; PGW2, right) and the control. SEB components are organized by row: (a, e) downward shortwave radiation (SWD); (b, f) downward longwave radiation (LWD); (c, g) sensible heat flux (SHF); (d, h) latent heat flux (LHF). Contour interval: 500 m. Range: 1000–3000 m.

crease the near-surface potential temperature deficit, and thereby strengthen the katabatic winds over the upper portion of the steep margins of the GrIS (Figure 4.9b) (Gorter et al., 2014; van den Broeke et al., 2009b). Stronger katabatic winds then increase turbulent heat flux by mixing relatively warm air through the stable boundary layer to the surface (Figure 4.8g, h).

While the differences in the radiative terms considerably outweigh that of the turbulent fluxes in PGW1, this is not the case for PGW2. Although the minor differences in SWD and LWD are more widespread (Figure 4.8e, f), the magnitude of the impact of sea-surface conditions on turbulent heat flux is greater in some locations along the ice sheet margins, particularly as is evident in the reduction in SHF along the northern and central portions of the western ablation zone (Figure 4.8g). This appears to be primarily a consequence of the indirect katabatic wind adjustment. The lower SST and higher SIC in PGW2 reduces the horizontal temperature gradient between the ice sheet and surrounding seas which, as has been documented in previous work (Noël et al., 2014), causes a weakening of the katabatic wind along the ice sheet margins (Figure 4.9c) (Noël et al., 2014). The

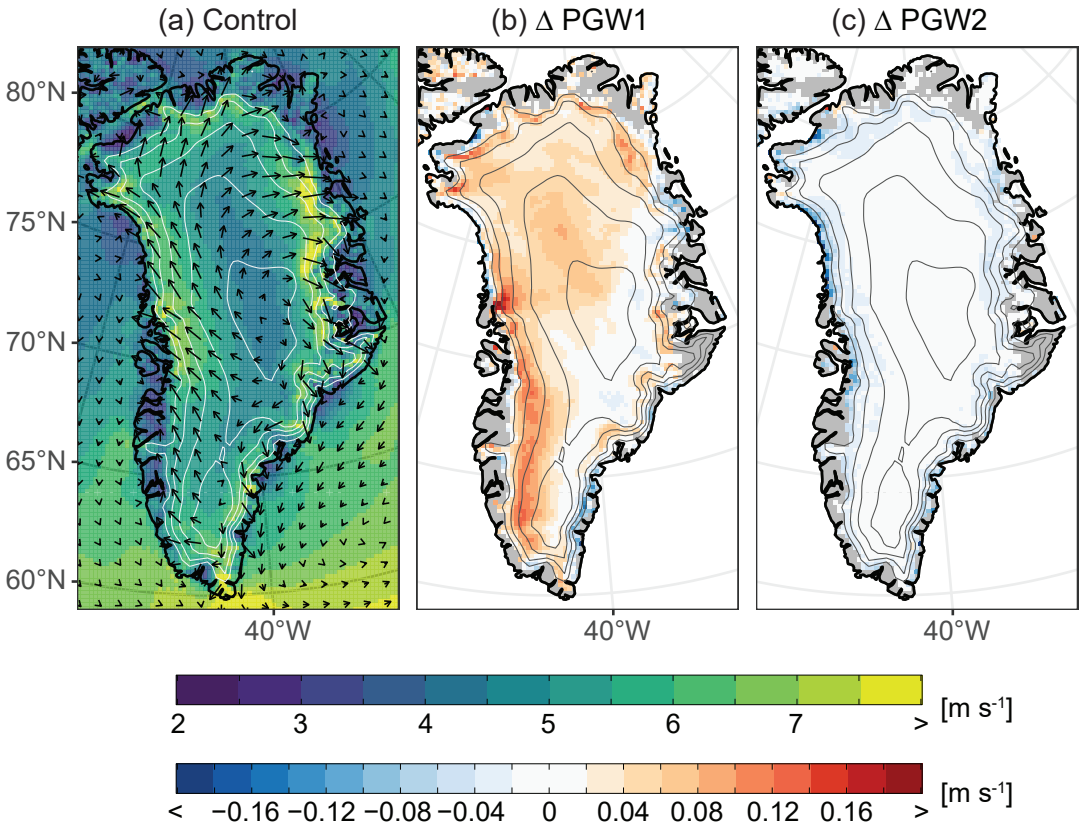


Figure 4.9: Melt season katabatic wind field under contrasting thermodynamic background conditions. (a) 2000–2019 long-term mean May–Sep 10 m wind speed (shading) and direction (vectors). (b) Difference in 10 m wind speed between PGW1 and the control. (c) Difference in the 10 m wind speed between PGW2 and the control. $\Delta = PGW - Control$*. Contour interval: 500 m. Range: 1000–3000 m.*

decrease in the near-surface wind field would reduce turbulent mixing, and thus SHF, to the surface, while also causing a reduction in evaporation / sublimation, resulting in an increase in LHF relative to the control.

The consistent and widespread reduction in LWD that is visible for PGW1 (Figure 4.8b and f) is not surprising given the drier atmospheric conditions that prevailed during the preindustrial period. The assimilated specific humidity perturbation signal that was applied to PGW1 (see Figure 4.2) is manifest in the integrated water vapor (IWV) over the ice sheet (Figure 4.10a, e). The spatial distribution of the IWV anomalies with respect to the control closely resemble that for LWD (c.f. Figures 4.10e and 4.8f)—highlighting the effectiveness of water vapor as a greenhouse gas and nicely illustrating the cause of the longwave radiative response.

The consequence of this water vapor feedback can be seen in the ice-sheet-wide drop in surface temperature simulated by PGW1. Here, the differences in the seasonality, magnitude, and spatial distribution of the maximum (Tmax) and minimum (Tmin) daily temperature response reflects seasonal and diurnal variations in the relative importance of longwave radiative effects, as well as geographical variations in surface albedo (see Lenaerts et al., 2019; Wang et al., 2018; Wang et al., 2019). The magnitude of the Tmax and Tmin anomalies in PGW1 relative to the control both increase from spring into fall (Figure 4.10b, c). This seasonal pattern is consistent with stronger Arctic amplification, and thus a greater water vapor feedback, in the fall than in spring, as well as a decline in incoming shortwave radiation as the solar declination decreases into winter, which elevates the relative contribution of longwave radiative effects to the SEB. There is a distinct north-south gradient in the maximum daily surface air temperature (Tmax) response (Figure 4.10f). The weaker Tmax differences over southern Greenland in PGW1 are a consequence of both a higher sun angle at lower latitudes and the lower surface albedo of the southern ice sheet, both of which decrease the relative longwave contribution

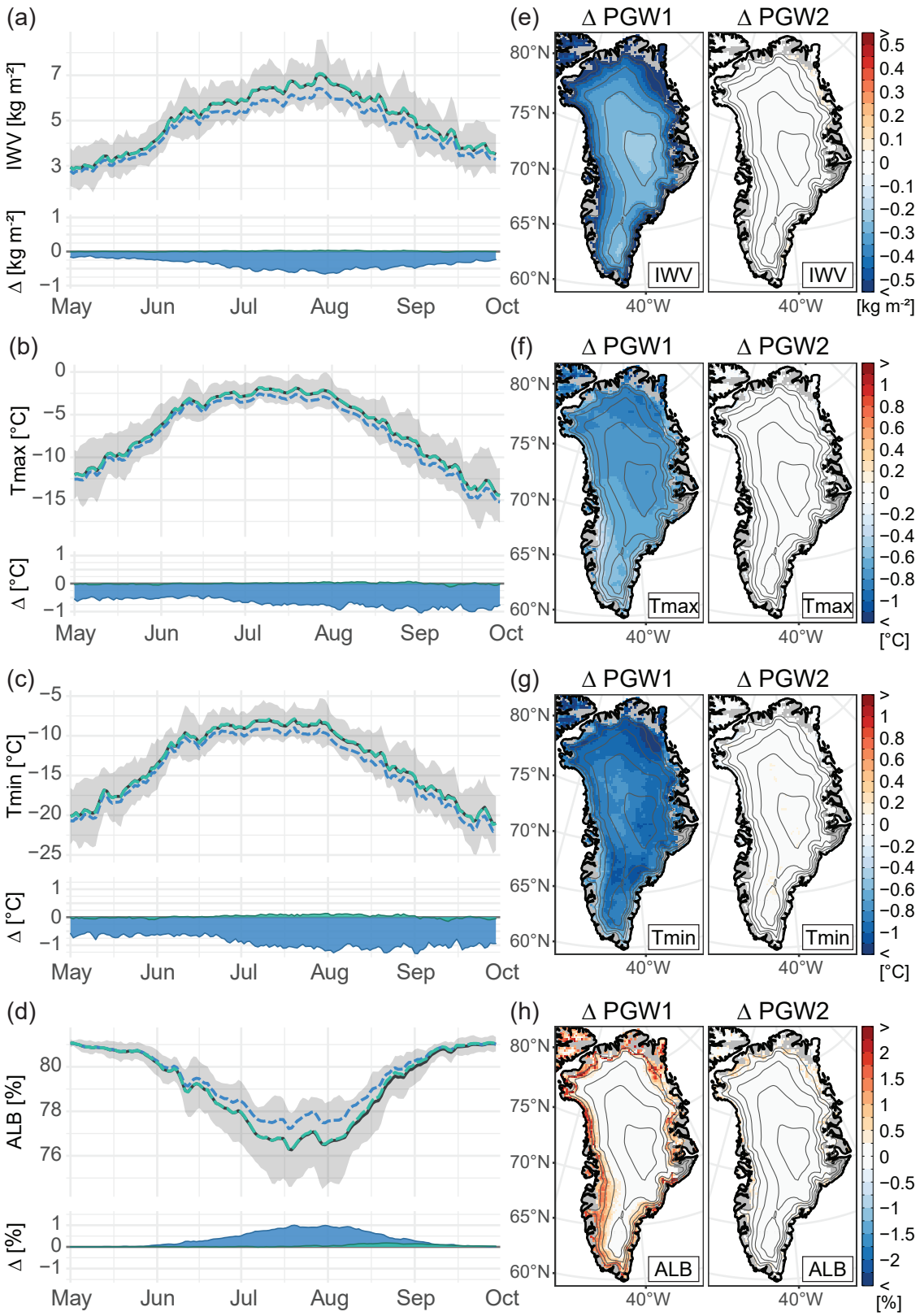


Figure 4.10: Thermodynamic mechanisms of GrIS SMB change. (Continued on following page.)

Figure 4.10: Thermodynamic mechanisms of GrIS SMB change. (a–d) Top portion of each panel shows the 2000–2019 long-term mean progression of each variable throughout the melt season for the control (gray), PGW1 (blue dashed), and PGW2 (green dashed) simulations. Gray shading shows the 1σ range about the mean for the control simulation. Time series represent the spatial average taken over the entire ice mask for a given variable. Bottom portion shows the difference between each PGW simulation (PGW1, blue; PGW2, green) and the control ($\Delta = PGW - Control$). (e–f) Maps depicting the difference between the 2000–2019, May–Sep long-term mean of each variable between the PGW simulations (PGW1, left; PGW2, right) and the control. Variables are organized by row: (a, e) integrated water vapor (IWV); (b, f) daily maximum surface air temperature (Tmax); (c, g) daily minimum surface air temperature (Tmin); (d, h) surface albedo (ALB). Contour interval: 500 m. Range: 1000–3000 m.

to the SEB. The impact of surface albedo is particularly evident in the weak Tmax response over the southwest ablation zone (Figure 4.10f). At night, LWD constitutes the sole radiative input to the SEB. Consequently, the Tmin response is notably greater than Tmax and it more closely resembles that of IWV (Figure 4.10e) and LWD (Figure 4.8f).

PGW1 exhibits a band of higher surface albedo throughout the melt season that runs along the perimeter of the GrIS (Figure 4.10d, h) and closely aligns with areas where IWV (Figure 4.10e), Tmin, (Figure4.10g), SHF (Figure 4.8g), and surface runoff (Supplementary Figure 4.1a) are reduced in PGW1 relative to the control. Thus, lower surface runoff under the preindustrial setting of PGW1 appears to be largely a consequence of the longwave radiative response to reduced water vapor content combined with lower SHF in a cooler atmosphere. The reduction in water vapor decreases LWD, which allows for lower Tmin. These changes would reduce runoff directly, by increasing the portion of meltwater that is refrozen within the snowpack, and indirectly, by diminishing the ice-albedo feedback. That the strongest signal in these variables is located over the northern Greenland and aligned with some of the largest increases in surface albedo supports previous

work demonstrating the importance of this longwave radiative mechanism to runoff from the northern GrIS (Noël et al., 2019).

Focusing on PGW2, the lack of inland influence by local sea-surface conditions is starkly illustrated in Figure 4.10e–g. There is no clear pattern of influence on IWV, near surface air temperature over the GrIS (Figure 4.10e–g). There is, however, an increase in surface albedo along the western and northern margins of the ice sheet in PGW2 relative to the control that occurs late in the melt season (Figure 4.10d, h) and appears to be the product of the collocated reduction in SHF (Figure 4.8g).

4.3.3 Thermodynamic change and GrIS melt timing

Consistent with previous studies (Hanna et al., 2009; Hanna et al., 2014; Noël et al., 2014), the above results suggest that local marine influence on GrIS melt is limited to the outermost margins of the ice sheet. Furthermore, these results demonstrate that the influence of local sea-surface conditions is an order of magnitude less than what is observed for the full thermodynamic forcing of PGW1 (Figure 4.5). This, combined with the lack of a IWV or surface air temperature signal over the ice sheet in PGW2 (Figure 4.10), would seem to contradict the possibility raised by Stroeve et al. (2017) that early sea ice loss in Baffin Bay may have an appreciable impact on meltwater production in extreme melt years by preconditioning the ice sheet for early melt onset via downward longwave radiative forcing.

To examine this hypothesis more directly, Figure 4.11 presents the results of a paired, signed-rank test comparing differences in median GrIS melt timing between the control and each of the PGW simulations. Over lower elevations where melt occurs consistently on an interannual basis, melt onset during the 2000–2019 study period typically occurs between early-May and mid-June (Figure 4.11a) while

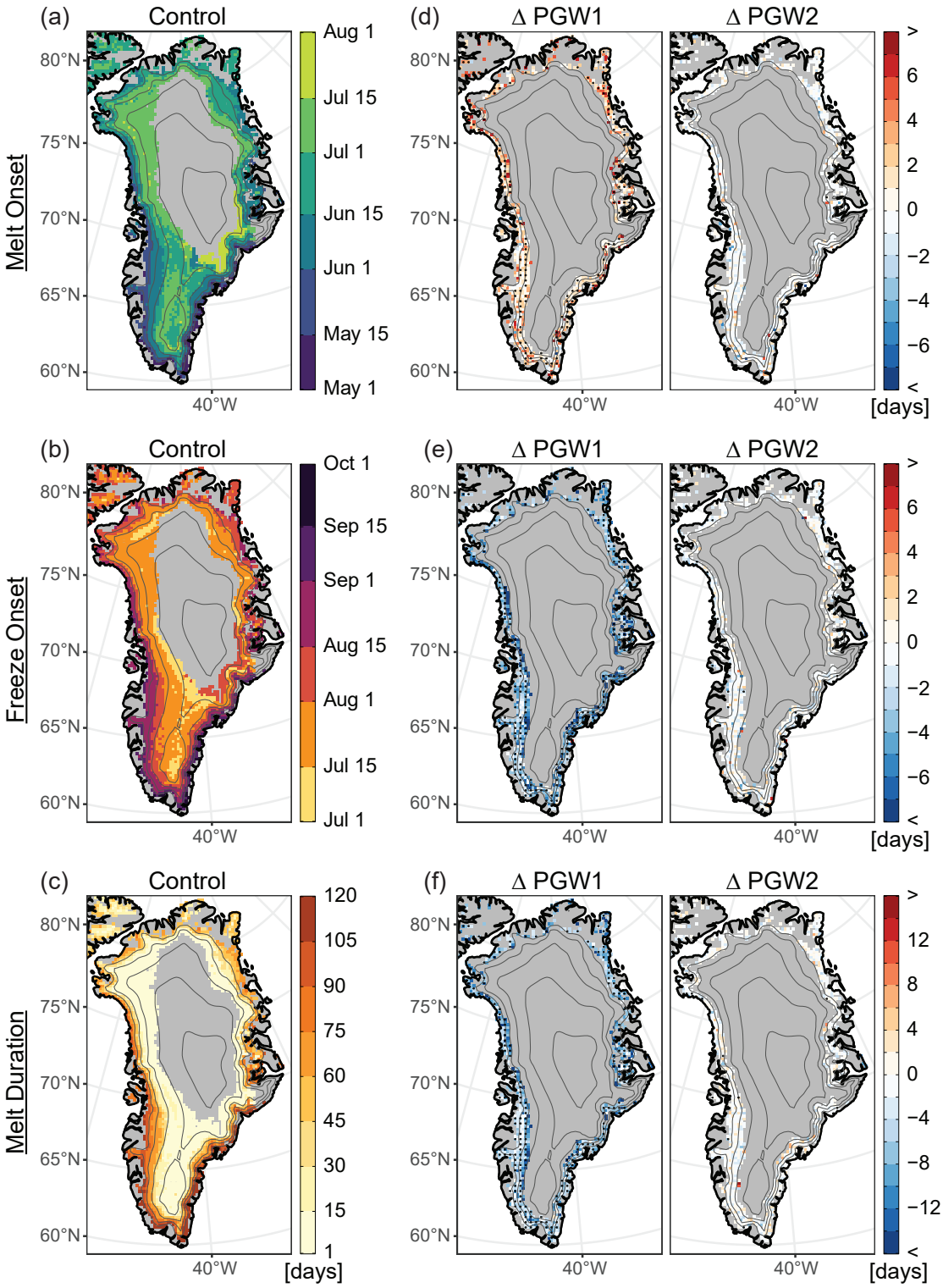


Figure 4.11: The impact of thermodynamic change on GrIS melt timing. The observed median date of (a) melt onset, (b) freeze onset and (c) median melt season duration for the control simulation alongside (d–f) the difference between the PGW simulations (PGW1, left; PGW2, right) and the control ($\Delta = PGW - Control$) for each metric as organized by row and labeled on the left. Contour interval: 500 m. Range: 1000–3000 m.

freeze onset occurs from early-August through September (Figure 4.11b). Later melt onset and earlier freeze onset is evident over higher elevations; however, melt in these regions is typically short-lived (Figure 4.11c) and infrequent. Accordingly, and as mentioned in the experimental design, the comparisons of melt timing between the PGW simulations and the control are limited to lower elevation locations with a sufficient sample of years experiencing melt.

Relative to the control, the median date of melt onset in PGW1 occurs, on average, $\sim$2.5 days later across those regions of the GrIS that consistently experience melt, while in the upper quartile grid cells experienced delays in median melt onset of $\geq$4 days (Figure 4.11d). The thermodynamic impact on the close of the melt season was even greater—the median date of freeze onset advanced, on average, by $\sim$3.7 days and freeze onset in the upper quartile of grid cells shifted to $\geq$5.5 days earlier in the fall (Figure 4.11e). Combined, these changes shortened the median melt season duration by an average of $\sim$6.7 days, while melt duration in the upper quartile of grid cells shortened by $\geq$9 days. For all melt timing metrics, the differences between the PGW1 and the control that were deemed statistically significant at the 95% confidence level are widespread across the examined grid cells. In contrast, differences between PGW2 and the control exhibit a weak and inconsistent signal for all melt timing metrics and yielded only sporadic instances of statistically significant results. In summary, while these results do show a widespread impact on the duration of the melt season by the full thermodynamic forcing of PGW1, and thus changes occurring more widely throughout the Arctic, the lack of a signal in PGW2 does not support any direct influence on either melt or freeze onset by local sea-surface conditions.

4.3.4 The exceptional melt years of 2012 and 2019

Embedded in the long-term GrIS SMB decline (Figure 4.5), 2012 and 2019 stand out as exceptional years of surface mass loss. According to the control, there was a cumulative SMB anomaly of –364 GT during the 2011–2012 hydrological year (Figure 4.12a). The melt season of 2012 was characterized by recurrent episodes of intense surface runoff (Figure 4.12b), spurred by anomalous atmospheric forcing of the ice sheet (Hanna et al., 2014). During this stretch of melt events, pronounced atmospheric ridging over Greenland promoted southerly advection of warm, moist air from low latitudes to the western ice sheet (Hermann et al., 2020; Neff et al., 2014), generating strong turbulent heat fluxes that drove high-volume meltwater production over the western ablation zone (Cullather et al., 2020; Fausto et al., 2016b). Adiabatic cooling of remotely-sourced moist air that ascended the western slope of the GrIS on July 12 prompted the formation of low-level, liquid clouds that supplied the requisite longwave radiative forcing for widespread melt over high elevations (Bennartz et al., 2013; Neff et al., 2014), generating a single day melt extent that covered over 98% of the ice sheet's surface (Nghiem et al., 2012).

The cumulative SMB anomaly over the 2018–2019 hydrological year totaled –376 GT (Figure 4.12e), exceeding the surface mass loss of 2012. The melt season of 2019 was heavily influenced by a blocking anticyclone, with origins in the European heatwave of the same year (Cullather et al., 2020), that produced tremendous surface runoff during a melt event centered around July 31 (Figure 4.12f). The air mass, which was transported west from Europe, was warmer and drier in comparison with that which was responsible for the mid-July, 2012 melt event and, consequently, did not produce the same low-level cloud cover that was instrumental to melt of the accumulation zone in 2012 (Tedesco & Fettweis, 2020). Thus, while

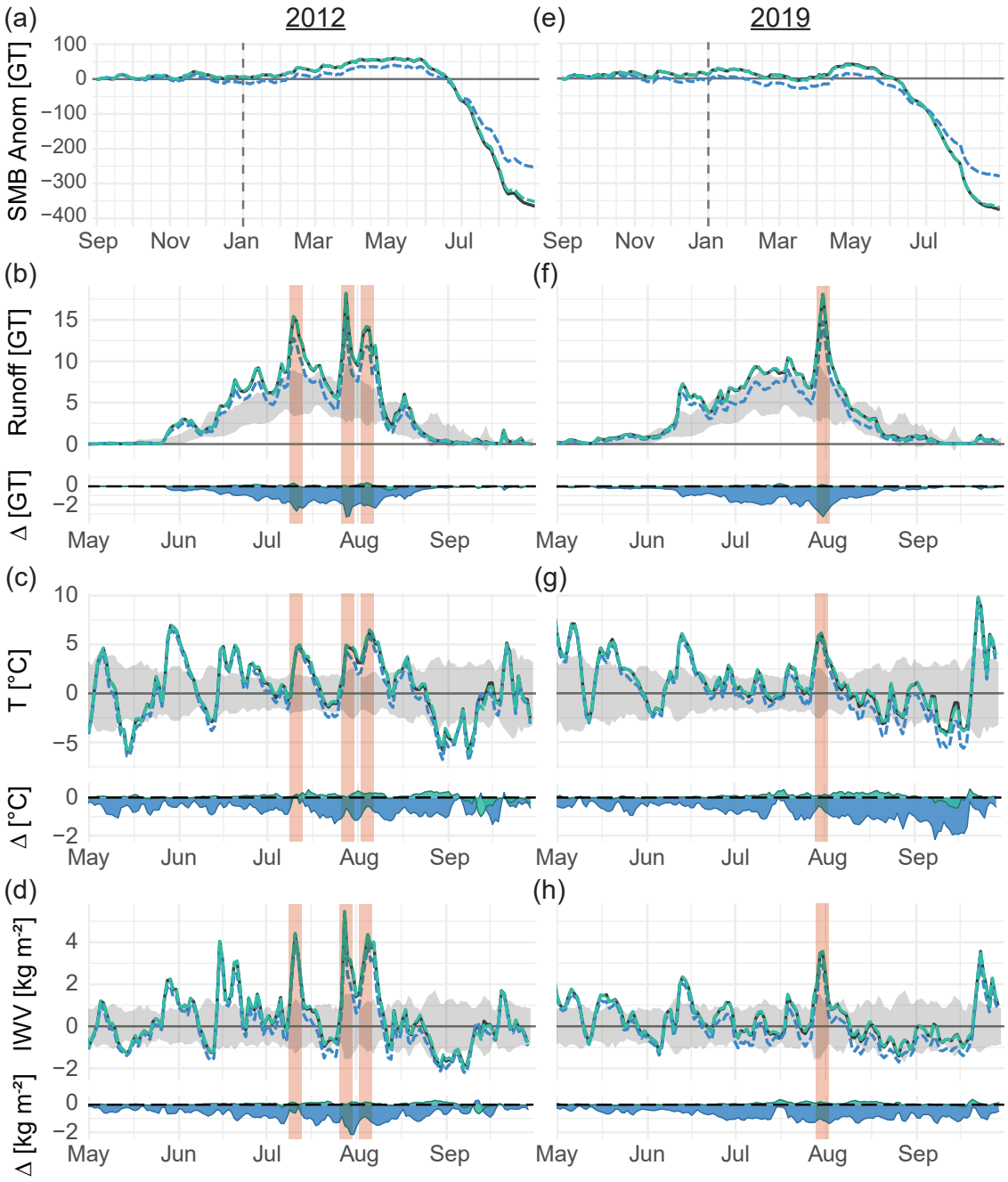


Figure 4.12: Thermodynamic contribution to surface mass loss during years of exceptional GrIS melt. Panels show (a, e) the cumulative SMB anomaly spanning the Sep–Aug hydrological year alongside (b, f) meltwater runoff, (c, g) average daily near-surface air temperature anomaly, and (d, h) integrated water vapor anomaly during the exceptional melt years of (a–d) 2012 and (e–h) 2019. In all panels, time series are presented for the control (gray), PGW1 (blue dashed), and PGW2 (green dashed) simulations. Bottom portion of b–d and f–h shows the difference between each PGW simulation (PGW1, blue; PGW2, green) and the control ($\Delta = PGW - Control$). Red vertical shading highlights periods of strong synoptic-scale forcing. Anomalies calculated with respect to the entire 2000–2019 study period. Cumulative anomalies calculated with respect to the 1980–1989 reference period.

the total surface mass loss was greater in 2019 than in 2012, the maximum daily melt extent of ∼73% of the ice sheet's surface was lower.

For both years, the portion of observed GrIS surface mass loss that is attributable to changes in the local background thermodynamic environment was far less than the average for the study period—whereas the total mass loss over the entire 2000–2019 study period was ∼62% less in PGW1 relative to the control, the reduction in mass loss was a relatively modest 30% and 25% in 2012 and 2019, respectively (Figure 4.12a, e). This suggests that the relative importance of a changing background state under global climate change may be minimized during periods of strong synoptic-scale atmospheric forcing. Indeed, this disparity is also evident over synoptic timescales—the periods of strong dynamical forcing of the GrIS, marked by the red, vertical bars in Figure 4.12, correspond to local minima in the differences in daily-mean near-surface air temperature between PGW1 and the control. The production of meltwater and consequent surface runoff during high-volume melt events is largely driven by turbulent heat fluxes (Fausto et al., 2016a; Fausto et al., 2016b). It follows that the longwave radiative effects of the water vapor feedback that are strongly dictated by changes in the thermodynamic environment assume a lesser role during these periods of intense melt. Consistent with the results for the full study period, the minimal difference between PGW2 and the control suggests no appreciable contribution by the observed change in local sea-surface conditions to runoff production during these exceptional melt years.

Meltwater that exits the ice sheet as runoff is primarily sourced from the ablation zone and is therefore controlled by processes, such as turbulent heat flux, that exert a strong influence along the margins of the GrIS. As was highlighted above, melt in the high-elevation accumulation zone is more dependent on longwave radiative effects. Figure 4.12d and h shows that atmospheric water vapor content is consistently reduced throughout both 2012 and 2019 in PGW1 relative to

the control, particularly during periods outside the highlighted instances of strong synoptic-scale atmospheric forcing. Thus, the influence of thermodynamic change may be more visible in the frequency of melt over the accumulation zone than for total meltwater runoff.

To investigate this possibility, Figure 4.13 presents a comparison of the number of days that underwent surface melt during the melt seasons of 2012 and 2019 in each of the model simulations. Focusing on the control (Figure 4.13a, c), melt frequencies across the ice sheet were generally greater in 2012 than 2019. The difference between the two years is quite evident over the southern portion of the ice sheet, where locations above 2500 m in elevation recorded over 40 days of melt in 2012 (Figure 4.13a). Melt was also more frequent above $\sim$1500 m over the northern GrIS in 2012, but 2019 underwent more frequent melt at lower elevations of the most northern margin of the ice sheet. These results align with previous work demonstrating greater runoff from the northern drainages of the GrIS but lower total melt extent in 2019 relative to 2012 (Cullather et al., 2020; Tedesco & Fettweis, 2020).

Broadly across the GrIS, the difference between PGW1 and the control show that the thermodynamic contribution to melt frequency was greater in 2019 than in 2012 (Figure 4.13b, d). Unlike 2019, intense water vapor transport accompanied the extensive melt events of 2012 (Hermann et al., 2020; Neff et al., 2014; Tedesco & Fettweis, 2020). Thus, the longwave radiative forcing necessary for melt over the high-albedo accumulation zone was provided by anomalous atmospheric moisture supplied by the large-scale circulation, which likely resulted in less sensitivity to changes in local thermodynamic conditions. In both years, the greatest differences in melt frequency between PGW1 and the control are located just above the ablation zone, where perennial snow cover raises the albedo of the ice sheet, making it more susceptible to the longwave radiative effects that accompany the change in

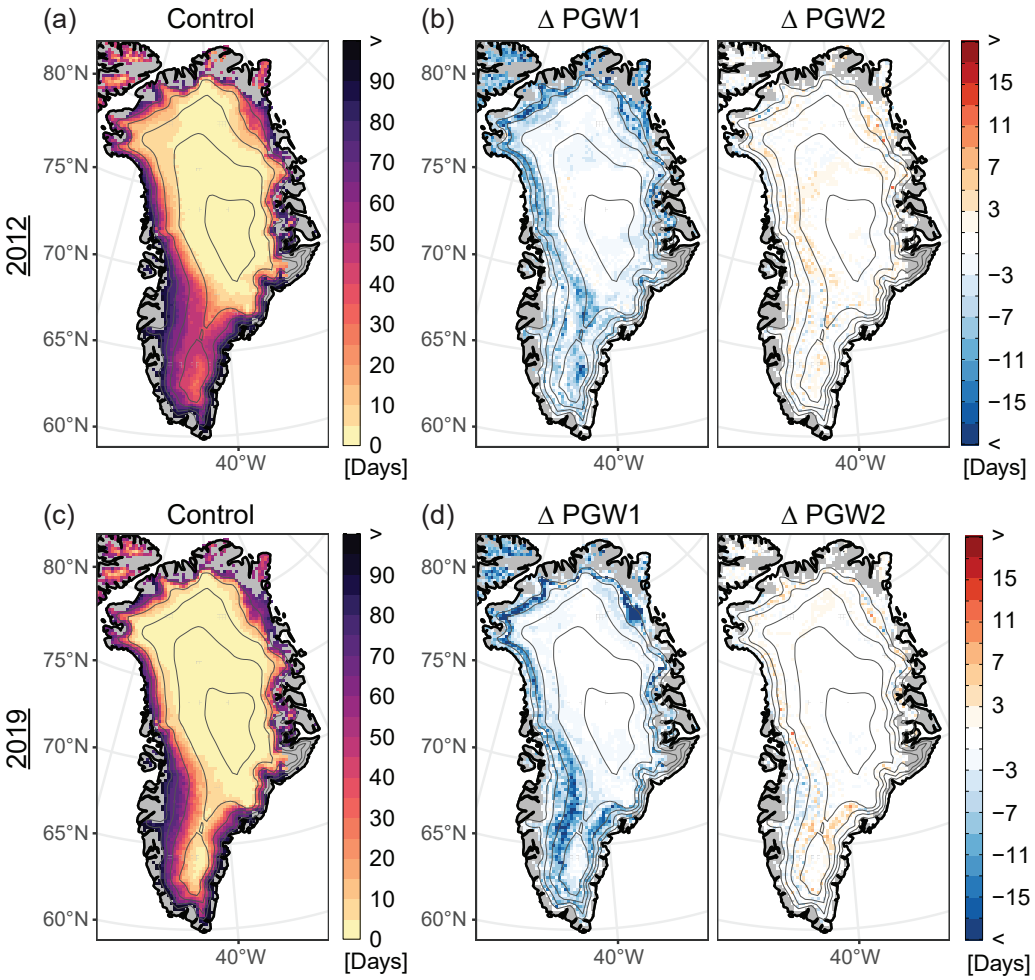


Figure 4.13: Comparison of GrIS melt frequency between PGW simulations during years of exceptional GrIS surface mass loss. (a, c) The number of days in which the control simulation indicated $\geq$5 mm melt in a given grid cell and (b, d) the difference between the PGW simulations and the control (PGW1, left; PGW2, right) for the exceptional melt years of (a, b) 2012 and (c, d) 2019. $\Delta = PGW - Control$ Contour interval: 500 m. Range: 1000–3000 m.

background conditions (Figure 4.13b, d). The spatial distribution of the differences in melt frequency in PGW1 also highlights the thermodynamic contribution to the maximum elevation of GrIS melt extent. This is most evident when considering the decline in melt frequency over high elevations in the context of the total number of melt days simulated by the control. While the reduction in melt frequency of 1 to 5 days above $\sim$2000 m in northern and central Greenland is low compared to other regions of the ice sheet, it is comparable to the total observed number of melt days simulated by the control (c.f. Figure 4.13a, c and b, d), demonstrating that melt over much of the high accumulation zone would not have occurred if not for recent climate warming. Contrary to PGW1, the changes in the number of PGW2 melt days relative to the control are minimal and generally do not exhibit a coherent spatial signal (Figure 4.13b, d); however, there is some indication of a decline in 2019 melt frequency over the western slope of the southern ice sheet that is opposed by an increase in melt frequency above 2000 m (Figure 4.13d).

4.4 Discussion

Much of the work examining the recent, marked increase in GrIS meltwater runoff has rightfully focused on the role of atmospheric dynamics in facilitating this change (Bevis et al., 2019; Fettweis et al., 2013; Hanna et al., 2016; Hanna et al., 2022; Hanna et al., 2015; Hanna et al., 2018b; Hofer et al., 2017). While some have presented evidence of a relationship between global climate change and the shift in summer atmospheric circulation that has promoted melt of the GrIS (Liu et al., 2016), a conclusive link remains a subject of investigation. In contrast, the accelerated rate of warming in the Arctic represents a robust climate change signal that has undoubtedly contributed to recent GrIS SMB trends (Boers & Rypdal, 2021; Hanna et al., 2008). This work represents the first systematic attempt to quantify

the contribution of the local change in background thermodynamic conditions to recent GrIS surface mass loss.

Our efforts indicate that had recent atmospheric dynamical forcing occurred in a preindustrial climate, surface mass loss from the GrIS would have been reduced by over 62% (Figure 4.5), highlighting the substantial contribution of external climate forcing. The mechanisms by which local thermodynamic background conditions contribute to SMB change appear to be dominated by longwave radiative effects stemming from the water vapor feedback. The amplified rate of warming in the Arctic has augmented surface runoff by promoting an increase in atmospheric moisture content and associated downwelling longwave radiation (Figures 4.10a, e and 4.8b, f), which disproportionately increases daily minimum temperatures (Figure 4.10c, g). Combined with increased SHF along the margins of the GrIS (Figure 4.8c, g), these changes have reduced the surface albedo (Figure 4.10d, h), further increasing meltwater runoff (Figure 4.7a). The role of longwave radiative effects that is emphasized in these results is consistent with the recent findings of Noël et al. (2019), who show that an increase in downwelling longwave radiation has caused a disproportionate increase in surface runoff from the northern drainages of the GrIS by efficiently promoting melt and expanding the ablation zone in this region of high albedo, as well as by increasing daily minimum temperatures, which reduces meltwater refreeze within the firn layer. While the authors point to the advection of moisture-rich air to the northern ice sheet by anomalously anticyclonic summer circulation over Greenland, the results of this analysis suggest that the increase in background temperature constitutes an important contribution to this mechanism on its own.

The contribution of local thermodynamic background conditions to total surface mass loss during the exceptional melt years of 2012 and 2019 was less than half that which was observed for the entire 2000–2019 study period (c.f. Figures

4.5 and 4.12a, e), demonstrating that the relative contribution by the local thermodynamic state is reduced during periods of strong large-scale atmospheric forcing. Indeed, this is also evident over synoptic timescales, where the difference in surface air temperature between PGW1 and the control is minimized on days of exceptionally high-volume surface runoff; rather, the greatest differences in surface temperature appear to emerge during periods encompassing temporal minima in air temperature (Figure 4.12). This pattern of influence likely reflects the increased contribution of remotely sourced heat and moisture during strong large-scale forcing—reducing the relative importance of the background thermodynamic state—as well as the efficacy of the longwave radiative effects that typify the response to changes in the thermodynamic background state in regulating minimum temperatures. In other words, recent local thermodynamic change around Greenland appears to have promoted GrIS surface runoff by raising the floor of the temperature distribution more so than by exacerbating warm extremes.

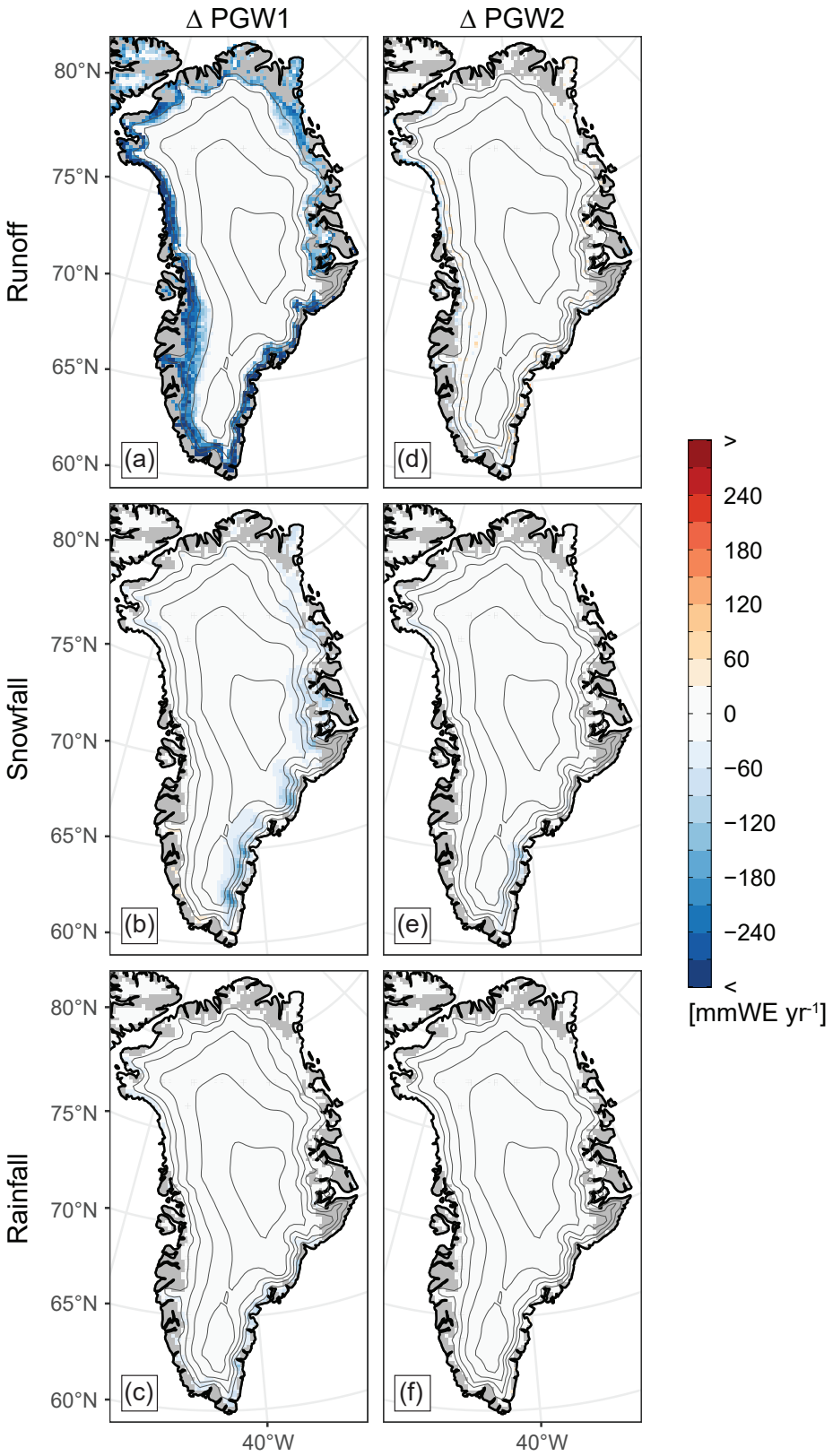
It is important to note that the same large-scale atmospheric conditions that typify our control period and have encouraged GrIS mass loss also foster below-normal sea ice in the region (Ballinger et al., 2018a; Ogi & Wallace, 2007; Stroeve et al., 2017). Thus, the 1880–1899 sea ice climatology that we prescribe here may often exceed the SIC that would have occurred if recently observed atmospheric circulation had occurred under preindustrial conditions. Recognizing this potential bias, our results likely represent an aggressive estimate of the contribution of sea-surface conditions to recent GrIS surface mass loss. Even so, this analysis reveals a minimal influence. Not only does this support previous work showing low SMB sensitivity to adjacent sea-sea surface conditions due to the barrier to onshore advection from the marine layer presented by consistent katabatic outflow over the ice sheet (Hanna et al., 2009; Hanna et al., 2014; Noël et al., 2014), but it also shows that any bias due to our treatment of sea-surface conditions likely had a

negligible impact on our estimate of the total local thermodynamic contribution to recent surface mass loss.

Contrary to the hypothesis put forth by Stroeve et al. (2017) that warmer SST and lower SIC may promote earlier melt onset in the spring which acts to precondition the ice sheet for later melt, the evidence here suggests very limited impact of sea-surface conditions on recent GrIS surface melt volume and no significant impact on seasonal melt timing (Figure 4.5 and 4.11). In fact, the little impact by sea-surface conditions that does occur is maximized later in the melt season when ocean-atmosphere heat exchange is greater than during spring (Figures 4.7, 4.8, 4.10) (Screen, 2017). However, when considering the change in atmospheric thermodynamic fields (i.e., PGW1), these results show an advance in melt onset and an even greater delay in freeze onset in response to a warming atmosphere that has lead to an overall lengthening of the melt season (Figure 4.11).

Because MAR assumes a fixed ice sheet geometry, the results presented herein strictly describe the thermodynamic influence on the SMB of the ice sheet; however, GrIS surface runoff and solid ice dynamics are not independent. Strong pulses of meltwater can cause rapid drainage through moulins that overwhelms the subglacial drainage network (Chu, 2014; Schoof, 2010). The consequent buildup of pressure increases basal sliding, causing a surge in ice velocity that increases glacial discharge and accelerates ice sheet thinning (Andersen et al., 2011; Chu, 2014; Schoof, 2010). Thus, it is likely that the thermodynamic influence on GrIS surface melt documented here has indirectly contributed further to sea-level rise via its impact on ice sheet dynamics. Regardless, these results demonstrate that while the shift in summer atmospheric circulation over Greenland has been key to the acceleration of runoff from the GrIS, the change in the background thermodynamic state under Arctic amplification has significantly enhanced the observed surface

mass loss beyond that which would have occurred if not for anthropogenic climate change.



Supplementary Figure 4.1: Comparison of individual SMB terms between the PGW simulations and the control. (Continued on following page.)

Supplementary Figure 4.1: Comparison of individual SMB terms between the PGW simulations and the control. (a–c) difference between PGW1 and the control, (d–f) difference between PGW2 and the control for each SEB component as organized by row as labeled to the left: (a, d) runoff; (b, e) snowfall; (c, f) rainfall. $\Delta = PGW - Control$. Contour interval: 500 m. Range: 1000–3000 m.

CHAPTER 5

CONCLUSION

Considered in isolation, the change in Greenland Ice Sheet (GrIS) surface conditions since the turn of the century certainly fits within the broader global trend toward more frequent heatwaves that is clearly linked to changes in the thermodynamic environment under anthropogenic climate change (Fischer & Knutti, 2015; Perkins et al., 2012). However, the existing literature is clear regarding the critical role of more frequent Greenland blocking in driving the observed decline in GrIS surface mass balance (SMB), and while there are several theories of how the observed amplified rate of warming in the Arctic could lead to more persistent summer heat extremes (Coumou et al., 2018), whether this regionally-specific dynamical change over Greenland is linked to global warming or simply product of internal variability is still an open question. Furthermore, it is unclear how much the impact of this dynamical forcing of GrIS meltwater runoff has been exacerbated by the anthropogenic change in the local thermodynamic environment. This dissertation informs on this subject by presenting a comprehensive look at dynamical and thermodynamic drivers of GrIS surface mass loss during the current period of Arctic amplification.

In the first of three primary research areas, which is presented as Chapter 2, this dissertation elucidated the mechanisms by which Greenland blocking promotes melt of the GrIS by considering spatiotemporal differences in the pattern of the mid-tropospheric circulation and associated surface response between blocking episodes. Indices such as those that have been used to establish the increasing trend in blocking over Greenland are an essential tool for distilling complex environmental processes into a more digestible form that can be used to reveal patterns in long-term behavior and identify relationships between various components of the earth system. However, this practical reduction in dataset dimensionality can come at the cost of losing important spatiotemporal details.

To regain some of those details, this work utilized self-organizing maps to objectively classify the large-scale atmospheric circulation on days which occurred during Greenland blocking episodes as identified using two complimentary blocking detection methods. This approach revealed three predominate Greenland blocking types, each with their own distinct GrIS surface energy balance (SEB) signature: (1) A lower-amplitude, stationary summer ridge pattern that produces greater melt over the southern ice sheet relative to other blocking types through the delivery of moisture to the southwest ablation zone, generating above-normal downwelling longwave radiation and increased sensible heat flux in the region. (2) A cyclonic wave breaking pattern, which brings relatively more melt to northeast Greenland through an apparent foehn effect where cross-barrier flow generates above-normal incoming shortwave radiation and enhanced sensible heat flux. (3) A high-amplitude, Omega blocking pattern that drives relatively greater melt across the northern GrIS in response to onshore moisture transport over the northwestern and northern coastlines, which generates above-normal longwave radiative forcing over northern Greenland. Critically, this classification of Greenland blocking also revealed that it has been an increase in Omega blocking, specifically, that has been primarily

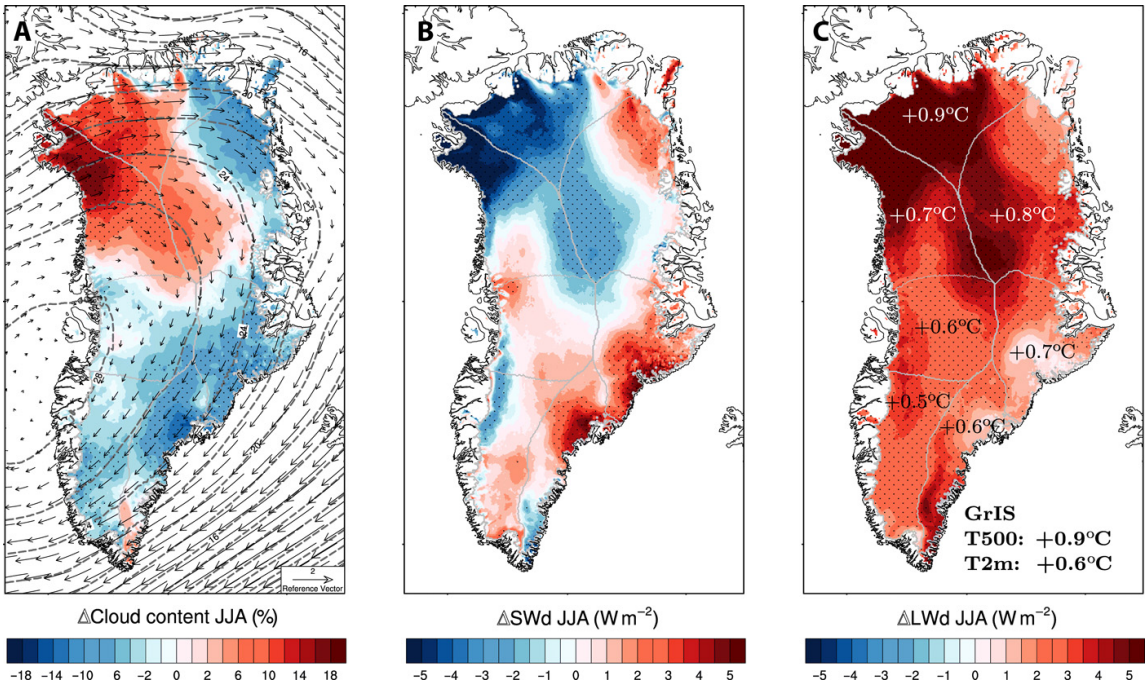


Figure 5.1: The change in conditions accompanying the recent GrIS SMB decline. Panels show the difference in the 1991–2017 summer (A) 500 hPa geopotential height (contours), winds (vectors), and mid-tropospheric cloud cover, (B) downward shortwave radiation, and (C) downward longwave radiation relative to that of 1958–1990. The annotations in panel (C) note the change in 2 m temperature for each of the sectors illustrated by the gray outlines. Figure reprinted from Noël et al. (2019), with permission granted by the Creative Commons Attribution 4.0 License: https://creativecommons.org/licenses/by/4.0/legalcode.

responsible for the positive trend in summer blocking in the region. Over the 1979–2019 study period, the frequency of Omega blocking patterns increased by 0.22 days per year, while cyclonic wave breaking pattern increased by 0.15 days per year and stationary summer ridge patterns showed no statistically discernible trend.

Recently, Noël et al. (2019) demonstrated that GrIS surface mass loss has been driven by a disproportionate increase in runoff from the most northern drainages of the ice sheet. They show that this change has occurred as a consequence of anomalous anticyclonic circulation relative to pre-1990 conditions over the Davis Strait—an anomalous pattern that they show enhances cloud longwave radiation over northern Greenland (Figure 5.1). This anomalous longwave

radiative forcing promotes runoff through the expansion of bare-ice area over low elevations and by raising daily minimum temperatures, which reduces meltwater refreeze within the firn layer at higher elevations (Noël et al., 2019). Both the position anomalous high pressure center since the early 1990s and the pattern of longwave radiative forcing over northern Greenland closely align with that of the high-amplitude Omega blocks that have undergone a pronounced increase in recent decades, suggesting that the trend in Omega blocks has been an important driving force behind the surge in runoff from the northern GrIS.

While the above results clarify the mechanisms by which blocking has encouraged melt of the GrIS, there is still the open question of why Omega blocking has become more common. Chapter 3 presents the results of the second research area of this dissertation, which explores potential remote sources of the observed shift in summer atmospheric circulation over Greenland. This analysis shows that, consistent with the prominent hypothesis of dynamical change under Arctic amplification of Francis and Vavrus (2012), a reduction in the magnitude of the meridional temperature gradient and a consequent weakening of the westerly flow at $\sim$60 to 70°N has spatially and temporally coincided with wavier atmospheric circulation over the North Atlantic. It also demonstrates that wavier flows in the region show a strong linear correlation with the Greenland Blocking Index over daily timescales ($r = 0.77$), thereby establishing that wavier circulation patterns over the North Atlantic tend to produce atmospheric riding over Greenland.

Chapter 3 also reveals a clear lagged correlation signal indicating that low May North American snow cover is followed by more frequent Greenland blocking in July. It then presents evidence that the mechanism underlying this delayed atmospheric response is an active snow-hydrological effect, in which low spring cover leads to early depletion of soil moisture and enhanced surface heating over eastern North America. Using the three-dimensional wave activity flux of Takaya and

Nakamura (2001), the analysis traces a stationary wave response that originates at the surface over the warm anomaly center, then propagates northeastward, favoring anticyclonic conditions that, as was the case for the Omega blocking patterns identified in Chapter 2, are centered over the Davis Strait and Baffin Bay. Unsurprisingly given the similarities in the large-scale upper-level flow, this stationary wave pattern is associated with a SEB signature, with enhanced downwelling longwave radiation over northern Greenland, that closely mirrors that of both Omega blocking patterns and the post-1990 conditions identified by Noël et al. (2019) (c.f. Figures 2.2, 2.5, 3.10, 5.1). Thus, these findings suggest that diminishing North American snow cover may produce conditions favorable to the formation of Omega blocks and thereby encourage melt of the northern GrIS. Together, the results presented in Chapter 3 suggest potentially synergistic mechanisms where arctic Amplification weakens the midlatitude flow while shrinking North American snow cover enhances the stationary ridge pattern over Greenland, both of which increase the likelihood of blocking (Nakamura & Huang, 2018; Paradise et al., 2019).

While it is true that atmospheric circulation has been pivotal to the magnitude of recent GrIS mass loss, this dynamical change has occurred against the backdrop of a rapidly evolving thermodynamic environment. This dissertation presented the most comprehensive estimate of the thermodynamic contribution to recent GrIS surface mass loss to date, demonstrating that—if not for the change in background thermodynamic conditions due to global warming—GrIS mass loss during the recent period of anomalous summer atmospheric circulation would have been $\sim$62% less than observed. This stark difference is primarily a byproduct of reduced longwave radiative forcing in a drier preindustrial atmosphere that acts as an important control on the left tail of the temperature distribution—underscoring the importance of the water vapor feedback to the thermodynamic contribution to GrIS surface mass loss. Furthermore, there has been minimal direct influence

on the cumulative GrIS SMB by observed changes in local sea-surface conditions. Thus, it is the local atmospheric thermodynamic fields, which are reflective of the integrated effects of changes occurring more broadly throughout the Arctic, that have dominated the thermodynamic contribution to recent mass loss. The analysis also demonstrates that, relative to the study period as a whole, the contribution of the change in the local thermodynamic environment to GrIS SMB is reduced during periods of strong dynamical forcing—the exceptional melt years of 2012 and 2019 showed only a 30% and 25% reduction, respectively, in surface mass loss during the preindustrial setting relative to the control. This disparity is presumably due to increased turbulent fluxes of remotely sourced heat and moisture during strong synoptic-scale forcing (Hermann et al., 2020; Mattingly et al., 2020).

This dissertation adds to the extensive body of work documenting the atmospheric forcing of recent GrIS mass loss by framing the observed dynamical change over Greenland within the context Arctic Amplification. It clarifies the mechanisms by which blocking encourages melt of the GrIS by considering spatiotemporal differences between common Greenland blocking patterns and provides evidence of a link between Arctic amplification and more frequent blocked flows over Greenland, both through hemispheric-scale changes in the meridional temperature gradient that favor wavier atmospheric circulation states, and through a more direct stationary wave response to shrinking North American snow cover. Thus, these results provide evidence in support of a link between global climate change and recent dynamical forcing of the GrIS that suggests that these exceptional atmospheric conditions may be expected to continue into the near future.

Additional work should build on these results by examining the representation of this snow-cover-induced surface-atmosphere coupling in the latest generation of earth system models. The existence of the stationary Rossby wave response in either ensemble output from fully-coupled earth system models or atmosphere-only

models with prescribed snow cover would increase confidence in these results and inform near-term projections of GrIS contribution to global sea-level rise. While similarities between the GrIS SEB signature during Omega blocking episodes and that which is observed in years of low North American spring snow cover suggest a link between the two, future work should be targeted at better understanding the dynamics of Omega blocking patterns relative to other blocking types. Knowledge of how the background zonal flow, stationary wave pattern, transient eddy forcing, and the role of diabatic processes differs for each blocking type may shed light on the failure of global climate models to resolve the observed increase in Greenland blocking and further speak to the existence—or lack thereof—of a link between climate change and the observed shift in summer atmospheric circulation over Greenland. Regardless, this dissertation emphasizes the substantial contribution of the background thermodynamic environment to observed surface mass loss, clearly demonstrating an anthropogenic fingerprint in the recent pronounced melt of the GrIS.

BIBLIOGRAPHY

Alexander, M. A., Bhatt, U. S., Walsh, J. E., Timlin, M. S., Miller, J. S., & Scott, J. D. (2004). The atmospheric response to realistic arctic sea ice anomalies in an agcm during winter. *Journal of Climate*, *17*(5), 890–905. https://doi.org/10.1175/1520-0442(2004)017<0890:TARTRA>2.0.CO;2

Alexander, M. A., Tomas, R., Deser, C., & Lawrence, D. M. (2010). The atmospheric response to projected terrestrial snow changes in the late twenty-first century. *Journal of Climate*, *23*(23), 6430–6437. https://doi.org/10.1175/2010JCLI3899.1

Alley, R. B., & Anandakrishnan, S. (1995). Variations in melt-layer frequency in the gisp2 ice core: Implications for holocene summer temperatures in central greenland. *Annals of Glaciology*, *21*, 64–70. https://doi.org/10.3189/S0260305500015615

Amory, C., Kittel, C., Le Toumelin, L., Agosta, C., Delhasse, A., Favier, V., & Fettweis, X. (2021). Performance of mar (v3.11) in simulating the drifting-snow climate and surface mass balance of adélie land, east antarctica. *Geoscientific Model Development*, *14*(6), 3487–3510. https://doi.org/10.5194/gmd-14-3487-2021

Andersen, M. L., Nettles, M., Elosegui, P., Larsen, T. B., Hamilton, G. S., & Stearns, L. A. (2011). Quantitative estimates of velocity sensitivity to surface melt

variations at a large greenland outlet glacier. *Journal of Glaciology*, *57*(204), 609–620. https://doi.org/10.3189/002214311797409785

Arrigo, K. R., Dijken, G. L. v., Castelao, R. M., Luo, H., Rennermalm, Å. K., Tedesco, M., Mote, T. L., Oliver, H., & Yager, P. L. (2017). Melting glaciers stimulate large summer phytoplankton blooms in southwest greenland waters. *Geophysical Research Letters*, *44*(12), 6278–6285. https://doi.org/10.1002/2017GL073583

Aschwanden, A., Fahnestock, M. A., Truffer, M., Brinkerhoff, D. J., Hock, R., Khroulev, C., Mottram, R., & Khan, S. A. (2019). Contribution of the greenland ice sheet to sea level over the next millennium. *Science Advances*, *5*(6), eaav9396. https://doi.org/10.1126/sciadv.aav9396

Bader, J., Mesquita, M. D. S., Hodges, K. I., Keenlyside, N., Østerhus, S., & Miles, M. (2011). A review on northern hemisphere sea-ice, storminess and the north atlantic oscillation: Observations and projected changes. *Atmospheric Research*, *101*(4), 809–834. https://doi.org/10.1016/j.atmosres.2011.04.007

Ballinger, T. J., Hanna, E., Hall, R. J., Cropper, T. E., Miller, J., Ribergaard, M. H., Overland, J. E., & Høyer, J. L. (2018a). Anomalous blocking over greenland preceded the 2013 extreme early melt of local sea ice. *Annals of Glaciology*, *59*(76pt2), 181–190. https://doi.org/10.1017/aog.2017.30

Ballinger, T. J., Hanna, E., Hall, R. J., Miller, J., Ribergaard, M. H., & Høyer, J. L. (2018b). Greenland coastal air temperatures linked to baffin bay and greenland sea ice conditions during autumn through regional blocking patterns. *Climate Dynamics*, *50*(1–2), 83–100. https://doi.org/10.1007/s00382-017-3583-3

Ballinger, T. J., Mote, T. L., Mattingly, K., Bliss, A. C., Hanna, E., van As, D., Prieto, M., Gharehchahi, S., Fettweis, X., Noël, B., Smeets, P. C. J. P., Ribergaard, M. H., & Cappelen, J. (2019). Greenland ice sheet late-season melt: Investi-

gating multi-scale drivers of k-transect events. *The Cryosphere Discussions*, 1–23. https://doi.org/10.5194/tc-2018-285

Barnes, E. A. (2013). Revisiting the evidence linking arctic amplification to extreme weather in midlatitudes: Arctic amplification and weather. *Geophysical Research Letters*, *40*(17), 4734–4739. https://doi.org/10.1002/grl.50880

Barrett, B. S., Henderson, G. R., McDonnell, E., Henry, M., & Mote, T. (2020). Extreme greenland blocking and high-latitude moisture transport. *Atmospheric Science Letters*, *21*(11), e1002. https://doi.org/https://doi.org/10.1002/asl.1002

Barriopedro, D., García-Herrera, R., & Trigo, R. M. (2010). Application of blocking diagnosis methods to general circulation models. part i: A novel detection scheme. *Climate Dynamics*, *35*(7), 1373–1391. https://doi.org/10.1007/s00382-010-0767-5

Bennartz, R., Shupe, M. D., Turner, D. D., Walden, V. P., Steffen, K., Cox, C. J., Kulie, M. S., Miller, N. B., & Pettersen, C. (2013). July 2012 greenland melt extent enhanced by low-level liquid clouds. *Nature*, *496*(74437443), 83–86. https://doi.org/10.1038/nature12002

Bevis, M., Harig, C., Khan, S. A., Brown, A., Simons, F. J., Willis, M., Fettweis, X., Broeke, M. R. v. d., Madsen, F. B., Kendrick, E., Caccamise, D. J., Dam, T. v., Knudsen, P., & Nylen, T. (2019). Accelerating changes in ice mass within greenland, and the ice sheet's sensitivity to atmospheric forcing. *Proceedings of the National Academy of Sciences*, *116*(6), 1934–1939. https://doi.org/10.1073/pnas.1806562116

Bhatt, U. S., Alexander, M. A., Deser, C., Walsh, J. E., Miller, J. S., Timlin, M. S., Scott, J., & Tomas, R. A. (2013). The atmospheric response to realistic reduced summer arctic sea ice anomalies. In E. T. DeWeaver, C. M. Bitz, &

L.-B. Tremblay (Eds.), *Geophysical monograph series* (pp. 91–110). American Geophysical Union. https://doi.org/10.1029/180GM08

Boers, N., & Rypdal, M. (2021). Critical slowing down suggests that the western greenland ice sheet is close to a tipping point. *Proceedings of the National Academy of Sciences*, *118*(21), e2024192118. https://doi.org/10.1073/pnas.2024192118

Box, J. E., Fettweis, X., Stroeve, J. C., Tedesco, M., Hall, D. K., & Steffen, K. (2012). Greenland ice sheet albedo feedback: Thermodynamics and atmospheric drivers. *The Cryosphere*, *6*(4), 821–839. https://doi.org/https://doi.org/10.5194/tc-6-821-2012

Box, J. E., Hubbard, A., Bahr, D. B., Colgan, W. T., Fettweis, X., Mankoff, K. D., Wehrlé, A., Noël, B., van den Broeke, M. R., Wouters, B., Bjørk, A. A., & Fausto, R. S. (2022). Greenland ice sheet climate disequilibrium and committed sea-level rise. *Nature Climate Change*, 1–6. https://doi.org/10.1038/s41558-022-01441-2

Brodzik, M. J., Billingsley, B., Haran, T., Raup, B., & Savoie, M. H. (2012). Ease-grid 2.0: Incremental but significant improvements for earth-gridded data sets. *ISPRS International Journal of Geo-Information*, *1*(11), 32–45. https://doi.org/10.3390/ijgi1010032

Brodzik, M. J., Billingsley, B., Haran, T., Raup, B., & Savoie, M. H. (2014). Correction: Brodzik, m.j., et al. ease-grid 2.0: Incremental but significant improvements for earth-gridded data sets. isprs international journal of geo-information 2012, 1, 32–45. *ISPRS International Journal of Geo-Information*, *3*(33), 1154–1156. https://doi.org/10.3390/ijgi3031154

Bromwich, D. H., Cullather, R. I., Chen, Q.-s., & Csathó, B. M. (1998). Evaluation of recent precipitation studies for greenland ice sheet. *Journal of Geophysical*

Research: Atmospheres, *103*(D20), 26007–26024. https://doi.org/10.1029/98JD02278

Brun, E., David, P., Sudul, M., & Brunot, G. (1992). A numerical model to simulate snow-cover stratigraphy for operational avalanche forecasting. *Journal of Glaciology*, *38*(128), 13–22. https://doi.org/10.3189/S0022143000009552

Brun, E., Martin, E., Simon, V., Gendre, C., & Coléou, C. (1989). An energy and mass model of snow cover suitable for operational avalanche forecasting. *J. Glaciol.*, *35*, 333. https://doi.org/10.1017/S0022143000009254

Budyko, M. I. (1969). The effect of solar radiation variations on the climate of the earth. *Tellus*, *21*(5), 611–619. https://doi.org/10.1111/j.2153-3490.1969.tb00466.x

Caesar, L., Rahmstorf, S., Robinson, A., Feulner, G., & Saba, V. (2018). Observed fingerprint of a weakening atlantic ocean overturning circulation. *Nature*, *556*(77007700), 191–196. https://doi.org/10.1038/s41586-018-0006-5

Cattiaux, J., Peings, Y., Saint-Martin, D., Trou-Kechout, N., & Vavrus, S. J. (2016). Sinuosity of midlatitude atmospheric flow in a warming world. *Geophysical Research Letters*, *43*(15), 8259–8268. https://doi.org/10.1002/2016GL070309

Cazenave, A., Palanisamy, H., & Ablain, M. (2018). Contemporary sea level changes from satellite altimetry: What have we learned? what are the new challenges? *Advances in Space Research*, *62*(7), 1639–1653. https://doi.org/10.1016/j.asr.2018.07.017

Charney, J. G., Shukla, J., & Mo, K. C. (1981). Comparison of a barotropic blocking theory with observation. *Journal of the Atmospheric Sciences*, *38*(4), 762–779. https://doi.org/10.1175/1520-0469(1981)038<0762:COABBT>2.0.CO;2

Cheung, H. N., Zhou, W., Mok, H. Y., Wu, M. C., & Shao, Y. (2013). Revisiting the climatology of atmospheric blocking in the northern hemisphere. *Advances in Atmospheric Sciences*, *30*(2), 397–410. https://doi.org/10.1007/s00376-012-2006-y

Christidis, N., & Stott, P. A. (2015). Changes in the geopotential height at 500 hpa under the influence of external climatic forcings. *Geophysical Research Letters*, *42*(24), 10, 798–10, 806. https://doi.org/10.1002/2015GL066669

Chu, V. W. (2014). Greenland ice sheet hydrology: A review. *Progress in Physical Geography: Earth and Environment*, *38*(1), 19–54. https://doi.org/10.1177/0309133313507075

Clausen, H. B., Gundestrup, N. S., Johnsen, S. J., Bindschadler, R., & Zwally, J. (1988). Glaciological investigations in the crête area, central greenland: A search for a new deep-drilling site. *Annals of Glaciology*, *10*, 10–15. https://doi.org/10.3189/S0260305500004080

Cohen, J. (2016). An observational analysis: Tropical relative to arctic influence on midlatitude weather in the era of arctic amplification. *Geophysical Research Letters*, *43*(10), 5287–5294. https://doi.org/10.1002/2016GL069102

Cohen, J., Agel, L., Barlow, M., Garfinkel, C. I., & White, I. (2021). Linking arctic variability and change with extreme winter weather in the united states. *Science*, *373*(6559), 1116–1121. https://doi.org/10.1126/science.abi9167

Cohen, J., Barlow, M., Kushner, P. J., & Saito, K. (2007). Stratosphere-troposphere coupling and links with eurasian land surface variability. *Journal of Climate*, *20*(21), 5335–5343. https://doi.org/10.1175/2007JCLI1725.1

Cohen, J., & Entekhabi, D. (1999). Eurasian snow cover variability and northern hemisphere climate predictability. *Geophysical Research Letters*, *26*(3), 345–348. https://doi.org/10.1029/1998GL900321

Cohen, J., Furtado, J. C., Barlow, M. A., Alexeev, V. A., & Cherry, J. E. (2012). Arctic warming, increasing snow cover and widespread boreal winter cooling. *Environmental Research Letters*, *7*(1), 014007. https://doi.org/10.1088/1748-9326/7/1/014007

Cohen, J., & Rind, D. (1991). The effect of snow cover on the climate. *Journal of Climate*, *4*(7), 689–706. https://doi.org/10.1175/1520-0442(1991)004<0689:TEOSCO>2.0.CO;2

Cohen, J., Screen, J. A., Furtado, J. C., Barlow, M., Whittleston, D., Coumou, D., Francis, J., Dethloff, K., Entekhabi, D., Overland, J., & Jones, J. (2014). Recent arctic amplification and extreme mid-latitude weather. *Nature Geoscience*, *7*(9), 627–637. https://doi.org/10.1038/ngeo2234

Cohen, J., Zhang, X., Francis, J., Jung, T., Kwok, R., Overland, J., Ballinger, T. J., Bhatt, U. S., Chen, H. W., Coumou, D., Feldstein, S., Gu, H., Handorf, D., Henderson, G., Ionita, M., Kretschmer, M., Laliberte, F., Lee, S., Linderholm, H. W., ... Yoon, J. (2019). Divergent consensuses on arctic amplification influence on midlatitude severe winter weather. *Nature Climate Change*. https://doi.org/10.1038/s41558-019-0662-y

Coumou, D., Di Capua, G., Vavrus, S., Wang, L., & Wang, S. (2018). The influence of arctic amplification on mid-latitude summer circulation. *Nature Communications*, *9*(1), 2959. https://doi.org/10.1038/s41467-018-05256-8

Coumou, D., Lehmann, J., & Beckmann, J. (2015). The weakening summer circulation in the northern hemisphere mid-latitudes. *Science*, *348*(6232), 324–327. https://doi.org/10.1126/science.1261768

Cullather, R. I., Andrews, L. C., Croteau, M. J., Digirolamo, N. E., Hall, D. K., Lim, Y.-K., Loomis, B. D., Shuman, C. A., & Nowicki, S. M. J. (2020). Anomalous circulation in july 2019 resulting in mass loss on the greenland ice sheet.

Geophysical Research Letters, *47*(17), e2020GL087263. https://doi.org/https://doi.org/10.1029/2020GL087263

Cullather, R. I., & Nowicki, S. M. J. (2018). Greenland ice sheet surface melt and its relation to daily atmospheric conditions. *Journal of Climate*, *31*(5), 1897–1919. https://doi.org/10.1175/JCLI-D-17-0447.1

Cvijanovic, I., & Caldeira, K. (2015). Atmospheric impacts of sea ice decline in co2 induced global warming. *Climate Dynamics*, *44*(5), 1173–1186. https://doi.org/10.1007/s00382-015-2489-1

Delhasse, A., Fettweis, X., Kittel, C., Amory, C., & Agosta, C. (2018). Brief communication: Impact of the recent atmospheric circulation change in summer on the future surface mass balance of the greenland ice sheet. *The Cryosphere*, *12*(11), 3409–3418. https://doi.org/10.5194/tc-12-3409-2018

Delhasse, A., Hanna, E., Kittel, C., & Fettweis, X. (2021). Brief communication: Cmip6 does not suggest any atmospheric blocking increase in summer over greenland by 2100. *International Journal of Climatology*, *41*(4), 2589–2596. https://doi.org/10.1002/joc.6977

Derksen, C., & Brown, R. (2012). Spring snow cover extent reductions in the 2008-2012 period exceeding climate model projections: Spring snow cover extent reductions. *Geophysical Research Letters*, *39*(19), L19504. https://doi.org/10.1029/2012GL053387

Deser, C., Tomas, R., Alexander, M., & Lawrence, D. (2010). The seasonal atmospheric response to projected arctic sea ice loss in the late twenty-first century. *Journal of Climate*, *23*(2), 333–351. https://doi.org/10.1175/2009JCLI3053.1

Deser, C., Tomas, R. A., & Sun, L. (2015). The role of ocean-atmosphere coupling in the zonal-mean atmospheric response to arctic sea ice loss. *Journal of Climate*, *28*(6), 2168–2186. https://doi.org/10.1175/JCLI-D-14-00325.1

Deser, C., Walsh, J. E., & Timlin, M. S. (2000). Arctic sea ice variability in the context of recent atmospheric circulation trends. *Journal of Climate*, *13*(3), 617–633. https://doi.org/10.1175/1520-0442(2000)013<0617:ASIVIT>2.0.CO;2

Di Capua, G., & Coumou, D. (2016). Changes in meandering of the northern hemisphere circulation. *Environmental Research Letters*, *11*(9), 094028. https://doi.org/10.1088/1748-9326/11/9/094028

Dole, R. M., & Gordon, N. D. (1983). Persistent anomalies of the extratropical northern hemisphere wintertime circulation: Geographical distribution and regional persistence characteristics. *Monthly Weather Review*, *111*(8), 1567–1586. https://doi.org/10.1175/1520-0493(1983)111<1567:PAOTEN>2.0.CO;2

Doyle, S. H., Hubbard, A., van de Wal, R. S. W., Box, J. E., van As, D., Scharrer, K., Meierbachtol, T. W., Smeets, P. C. J. P., Harper, J. T., Johansson, E., Mottram, R. H., Mikkelsen, A. B., Wilhelms, F., Patton, H., Christoffersen, P., & Hubbard, B. (2015). Amplified melt and flow of the greenland ice sheet driven by late-summer cyclonic rainfall. *Nature Geoscience*, *8*(8), 647–653. https://doi.org/10.1038/ngeo2482

Dunn-Sigouin, E., & Son, S.-W. (2013). Northern hemisphere blocking frequency and duration in the cmip5 models. *Journal of Geophysical Research: Atmospheres*, *118*(3), 1179–1188. https://doi.org/https://doi.org/10.1002/jgrd.50143

Duynkerke, P. G., & van den Broeke, M. R. (1994). Surface energy balance and katabatic flow over glacier and tundra during gimex-91. *Global and Planetary Change*, *9*(1), 17–28. https://doi.org/10.1016/0921-8181(94)90004-3

Estilow, T. W., Young, A. H., & Robinson, D. A. (2015). A long-term northern hemisphere snow cover extent data record for climate studies and monitoring.

Earth System Science Data, *7*(1), 137–142. https://doi.org/10.5194/essd-7-137-2015

Fang, Z.-F. (2004). Statistical relationship between the northern hemisphere sea ice and atmospheric circulation during wintertime. In *Observation, Theory and Modeling of Atmospheric Variability* (pp. 131–141). WORLD SCIENTIFIC. https://doi.org/10.1142/9789812791139_0006

Fausto, R. S., van As, D., Box, J. E., Colgan, W., & Langen, P. L. (2016a). Quantifying the surface energy fluxes in south greenland during the 2012 high melt episodes using in-situ observations. *Frontiers in Earth Science*, *4*. https://doi.org/10.3389/feart.2016.00082

Fausto, R. S., van As, D., Box, J. E., Colgan, W., Langen, P. L., & Mottram, R. H. (2016b). The implication of nonradiative energy fluxes dominating greenland ice sheet exceptional ablation area surface melt in 2012. *Geophysical Research Letters*, *43*(6), 2649–2658. https://doi.org/10.1002/2016GL067720

Fettweis, X. (2022). Modèle atmosphérique régional (mar) version 3.11 regional climate model output, 1979–2019, greenland domain, 10 kilometer (km) horizontal resolution. *Arctic Data Center*. https://doi.org/doi:10.18739/A23T9D74T

Fettweis, X., Box, J. E., Agosta, C., Amory, C., Kittel, C., Lang, C., van As, D., Machguth, H., & Gallée, H. (2017). Reconstructions of the 1900–2015 greenland ice sheet surface mass balance using the regional climate mar model. *The Cryosphere*, *11*(2), 1015–1033. https://doi.org/10.5194/tc-11-1015-2017

Fettweis, X., Gallée, H., Lefebre, F., & van Ypersele, J.-P. (2005). Greenland surface mass balance simulated by a regional climate model and comparison with satellite-derived data in 1990–1991. *Climate Dynamics*, *24*(6), 623–640. https://doi.org/10.1007/s00382-005-0010-y

Fettweis, X., Hanna, E., Lang, C., Belleflamme, A., Erpicum, M., & Gallée, H. (2013). Brief communication: "important role of the mid-tropospheric atmospheric circulation in the recent surface melt increase over the greenland ice sheet". *The Cryosphere*, *7*(1), 241–248. https://doi.org/10.5194/tc-7-241-2013

Fettweis, X., Hofer, S., Krebs-Kanzow, U., Amory, C., Aoki, T., Berends, C. J., Born, A., Box, J. E., Delhasse, A., Fujita, K., Gierz, P., Goelzer, H., Hanna, E., Hashimoto, A., Huybrechts, P., Kapsch, M.-L., King, M. D., Kittel, C., Lang, C., ... Zolles, T. (2020). Grsmbmip: Intercomparison of the modelled 1980–2012 surface mass balance over the greenland ice sheet. *The Cryosphere*, *14*(11), 3935–3958. https://doi.org/https://doi.org/10.5194/tc-14-3935-2020

Fichefet, T., Poncin, C., Goosse, H., Huybrechts, P., Janssens, I., & Treut, H. L. (2003). Implications of changes in freshwater flux from the greenland ice sheet for the climate of the 21st century. *Geophysical Research Letters*, *30*(17). https://doi.org/10.1029/2003GL017826

Fischer, E. M., & Knutti, R. (2015). Anthropogenic contribution to global occurrence of heavy-precipitation and high-temperature extremes. *Nature Climate Change*, *5*(66), 560–564. https://doi.org/10.1038/nclimate2617

Francis, J. A., & Vavrus, S. J. (2012). Evidence linking arctic amplification to extreme weather in mid-latitudes: Arctic links to mid-latitude weather. *Geophysical Research Letters*, *39*(6), L06801. https://doi.org/10.1029/2012GL051000

Francis, J. A., & Vavrus, S. J. (2015). Evidence for a wavier jet stream in response to rapid arctic warming. *Environmental Research Letters*, *10*(1), 014005. https://doi.org/10.1088/1748-9326/10/1/014005

Francis, J. A., Vavrus, S. J., & Cohen, J. (2017). Amplified arctic warming and mid-latitude weather: New perspectives on emerging connections: Amplified

arctic warming and mid-latitude weather. *Wiley Interdisciplinary Reviews: Climate Change*, *8*(5), e474. https://doi.org/10.1002/wcc.474

Gallagher, M. R., Chepfer, H., Shupe, M. D., & Guzman, R. (2020). Warm temperature extremes across greenland connected to clouds. *Geophysical Research Letters*, *47*(9), e2019GL086059. https://doi.org/10.1029/2019GL086059

Gallagher, M. R., Shupe, M. D., & Miller, N. B. (2018). Impact of atmospheric circulation on temperature, clouds, and radiation at summit station, greenland, with self-organizing maps. *Journal of Climate*, *31*(21), 8895–8915. https://doi.org/10.1175/JCLI-D-17-0893.1

Gibson, P. B., Perkins-Kirkpatrick, S. E., Uotila, P., Pepler, A. S., & Alexander, L. V. (2017). On the use of self-organizing maps for studying climate extremes. *Journal of Geophysical Research: Atmospheres*, *122*(7), 3891–3903. https://doi.org/10.1002/2016JD026256

Gong, G., Cohen, J., Entekhabi, D., & Ge, Y. (2007). Hemispheric-scale climate response to northern eurasia land surface characteristics and snow anomalies. *Global and Planetary Change*, *56*(3), 359–370. https://doi.org/10.1016/j.gloplacha.2006.07.025

Gong, G., Entekhabi, D., & Cohen, J. (2003). Relative impacts of siberian and north american snow anomalies on the winter arctic oscillation. *Geophysical Research Letters*, *30*(16). https://doi.org/10.1029/2003GL017749

Gong, T., Feldstein, S. B., & Lee, S. (2019). Rossby wave propagation from the arctic into the midlatitudes: Does it arise from in situ latent heating or a trans-arctic wave train? *Journal of Climate*, *33*(9), 3619–3633. https://doi.org/10.1175/JCLI-D-18-0780.1

Gorter, W., van Angelen, J. H., Lenaerts, J. T. M., & van den Broeke, M. R. (2014). Present and future near-surface wind climate of greenland from high reso-

lution regional climate modelling. *Climate Dynamics*, *42*(5–6), 1595–1611. https://doi.org/10.1007/s00382-013-1861-2

Hahn, L. C., Storelvmo, T., Hofer, S., Parfitt, R., & Ummenhofer, C. C. (2020). Importance of orography for greenland cloud and melt response to atmospheric blocking. *Journal of Climate*, *33*(10), 4187–4206. https://doi.org/10.1175/JCLI-D-19-0527.1

Häkkinen, S., Hall, D. K., Shuman, C. A., Worthen, D. L., & DiGirolamo, N. E. (2014). Greenland ice sheet melt from modis and associated atmospheric variability. *Geophysical Research Letters*, *41*(5), 1600–1607. https://doi.org/https://doi.org/10.1002/2013GL059185

Hanna, E., Cappelen, J., Fettweis, X., Huybrechts, P., Luckman, A., & Ribergaard, M. H. (2009). Hydrologic response of the greenland ice sheet: The role of oceanographic warming. *Hydrological Processes*, *23*(1), 7–30. https://doi.org/10.1002/hyp.7090

Hanna, E., Cappelen, J., Fettweis, X., Mernild, S. H., Mote, T. L., Mottram, R., Steffen, K., Ballinger, T. J., & Hall, R. J. (2021). Greenland surface air temperature changes from 1981 to 2019 and implications for ice-sheet melt and mass-balance change. *International Journal of Climatology*, *41*(S1), E1336–E1352. https://doi.org/10.1002/joc.6771

Hanna, E., Cropper, T. E., Hall, R. J., & Cappelen, J. (2016). Greenland blocking index 1851-2015: A regional climate change signal: Greenland blocking index 1851-2015. *International Journal of Climatology*, *36*(15), 4847–4861. https://doi.org/10.1002/joc.4673

Hanna, E., Cropper, T. E., Hall, R. J., Cornes, R. C., & Barriendos, M. (2022). Extended north atlantic oscillation and greenland blocking indices 1800–2020 from new meteorological reanalysis. *Atmosphere*, *13*(33), 436. https://doi.org/10.3390/atmos13030436

Hanna, E., Cropper, T. E., Jones, P. D., Scaife, A. A., & Allan, R. (2015). Recent seasonal asymmetric changes in the nao (a marked summer decline and increased winter variability) and associated changes in the ao and greenland blocking index. *International Journal of Climatology*, *35*(9), 2540–2554. https://doi.org/10.1002/joc.4157

Hanna, E., Fettweis, X., & Hall, R. J. (2018a). Brief communication: Recent changes in summer greenland blocking captured by none of the cmip5 models. *The Cryosphere*, *12*(10), 3287–3292. https://doi.org/10.5194/tc-12-3287-2018

Hanna, E., Fettweis, X., Mernild, S. H., Cappelen, J., Ribergaard, M. H., Shuman, C. A., Steffen, K., Wood, L., & Mote, T. L. (2014). Atmospheric and oceanic climate forcing of the exceptional greenland ice sheet surface melt in summer 2012. *International Journal of Climatology*, *34*(4), 1022–1037. https://doi.org/10.1002/joc.3743

Hanna, E., Hall, R. J., Cropper, T. E., Ballinger, T. J., Wake, L., Mote, T., & Cappelen, J. (2018b). Greenland blocking index daily series 1851–2015: Analysis of changes in extremes and links with north atlantic and uk climate variability and change. *International Journal of Climatology*, *38*(9), 3546–3564. https://doi.org/10.1002/joc.5516

Hanna, E., Huybrechts, P., Steffen, K., Cappelen, J., Huff, R., Shuman, C., Irvine-Fynn, T., Wise, S., & Griffiths, M. (2008). Increased runoff from melt from the greenland ice sheet: A response to global warming. *Journal of Climate*, *21*(2), 331–341. https://doi.org/10.1175/2007JCLI1964.1

Hanna, E., Jones, J. M., Cappelen, J., Mernild, S. H., Wood, L., Steffen, K., & Huybrechts, P. (2013). The influence of North Atlantic atmospheric and oceanic forcing effects on 1900-2010 Greenland summer climate and ice

melt/runoff. *International Journal of Climatology*, *33*(4), 862–880. https://doi.org/10.1002/joc.3475

Hassanzadeh, P., & Kuang, Z. (2015). Blocking variability: Arctic amplification versus arctic oscillation. *Geophysical Research Letters*, *42*(20), 8586–8595. https://doi.org/10.1002/2015GL065923

Held, I. M., & Ting, M. (1990). Orographic versus thermal forcing of stationary waves: The importance of the mean low-level wind. *Journal of the Atmospheric Sciences*, *47*(4), 495–500. https://doi.org/10.1175/1520-0469(1990)047<0495:OVTFOS>2.0.CO;2

Helfrich, S. R., McNamara, D., Ramsay, B. H., Baldwin, T., & Kasheta, T. (2007). Enhancements to, and forthcoming developments in the interactive multisensor snow and ice mapping system (ims). *Hydrological Processes*, *21*(12), 1576–1586. https://doi.org/10.1002/hyp.6720

Henderson, G. R., Barrett, B. S., Wachowicz, L. J., Mattingly, K. S., Preece, J. R., & Mote, T. L. (2021). Local and Remote Atmospheric Circulation Drivers of Arctic Change: A Review. *Frontiers in Earth Science*, *9*. https://doi.org/https://doi.org/10.3389/feart.2021.709896

Henderson, G. R., Leathers, D. J., & Hanson, B. (2013). Circulation response to eurasian versus north american anomalous snow scenarios in the northern hemisphere with an agcm coupled to a slab ocean model. *Journal of Climate*, *26*(5), 1502–1515. https://doi.org/10.1175/JCLI-D-11-00465.1

Henderson, G. R., Peings, Y., Furtado, J. C., & Kushner, P. J. (2018). Snow-atmosphere coupling in the northern hemisphere. *Nature Climate Change*, *8*(11), 954–963. https://doi.org/10.1038/s41558-018-0295-6

Hermann, M., Papritz, L., & Wernli, H. (2020). A lagrangian analysis of the dynamical and thermodynamic drivers of large-scale greenland melt events

during 1979–2017. *Weather and Climate Dynamics*, *1*(2), 497–518. https://doi.org/10.5194/wcd-1-497-2020

Hernández-Henríquez, M. A., Déry, S. J., & Derksen, C. (2015). Polar amplification and elevation-dependence in trends of northern hemisphere snow cover extent, 1971–2014. *Environmental Research Letters*, *10*(4), 044010. https://doi.org/10.1088/1748-9326/10/4/044010

Hersbach, H., Bell, B., Berrisford, P., Hirahara, S., Horányi, A., Muñoz-Sabater, J., Nicolas, J., Peubey, C., Radu, R., Schepers, D., Simmons, A., Soci, C., Abdalla, S., Abellan, X., Balsamo, G., Bechtold, P., Biavati, G., Bidlot, J., Bonavita, M., ... Thépaut, J.-N. (2020). The era5 global reanalysis. *Quarterly Journal of the Royal Meteorological Society*, *146*(730), 1999–2049. https://doi.org/https://doi.org/10.1002/qj.3803

Hewitson, B. C., & Crane, R. G. (2002). Self-organizing maps: Applications to synoptic climatology. *Climate Research*, *22*(1), 13–26. https://doi.org/10.3354/cr022013

Hofer, S., Tedstone, A. J., Fettweis, X., & Bamber, J. L. (2017). Decreasing cloud cover drives the recent mass loss on the greenland ice sheet. *Science Advances*, *3*(6), e1700584. https://doi.org/10.1126/sciadv.1700584

Honda, M., Inoue, J., & Yamane, S. (2009). Influence of low arctic sea-ice minima on anomalously cold eurasian winters. *Geophysical Research Letters*, *36*(8), L08707. https://doi.org/10.1029/2008GL037079

Honda, M., Yamazaki, K., Nakamura, H., & Takeuchi, K. (1999). Dynamic and thermodynamic characteristics of atmospheric response to anomalous sea-ice extent in the sea of okhotsk. *Journal of Climate*, *12*(12), 3347–3358. https://doi.org/10.1175/1520-0442(1999)012<3347:DATCOA>2.0.CO;2

Honda, M., Yamazaki, K., Tachibana, Y., & Takeuchi, K. (1996). Influence of okhotsk sea-ice extent on atmospheric circulation. *Geophysical Research Letters*, *23*(24), 3595–3598. https://doi.org/10.1029/96GL03474

Horwath, M., Gutknecht, B. D., Cazenave, A., Palanisamy, H. K., Marti, F., Marzeion, B., Paul, F., Le Bris, R., Hogg, A. E., Otosaka, I., Shepherd, A., Döll, P., Cáceres, D., Müller Schmied, H., Johannessen, J. A., Nilsen, J. E. Ø., Raj, R. P., Forsberg, R., Sandberg Sørensen, L., ... Benveniste, J. (2022). Global sea-level budget and ocean-mass budget, with a focus on advanced data products and uncertainty characterisation. *Earth System Science Data*, *14*(2), 411–447. https://doi.org/10.5194/essd-14-411-2022

Hoskins, B. J., & Karoly, D. J. (1981). The steady linear response of a spherical atmosphere to thermal and orographic forcing. *Journal of the Atmospheric Sciences*, *38*(6), 1179–1196. https://doi.org/10.1175/1520-0469(1981)038<1179:TSLROA>2.0.CO;2

Hoskins, B. J., & Woollings, T. (2015). Persistent extratropical regimes and climate extremes. *Current Climate Change Reports*, *1*(3), 115–124. https://doi.org/10.1007/s40641-015-0020-8

Huang, C. S. Y., & Nakamura, N. (2016). Local finite-amplitude wave activity as a diagnostic of anomalous weather events. *Journal of the Atmospheric Sciences*, *73*(1), 211–229. https://doi.org/10.1175/JAS-D-15-0194.1

Hurrell, J. W., Hack, J. J., Shea, D., Caron, J. M., & Rosinski, J. (2008). A new sea surface temperature and sea ice boundary dataset for the community atmosphere model. *Journal of Climate*, *21*(19), 5145–5153. https://doi.org/10.1175/2008JCLI2292.1

Hurrell, J. W., Kushnir, Y., Ottersen, G., & Visbeck, M. (2003). An overview of the north atlantic oscillation. In *The north atlantic oscillation: Climatic signifi-*

cance and environmental impact (pp. 1–35). American Geophysical Union (AGU). https://doi.org/10.1029/134GM01

IMBIE Team, T. (2018). Mass balance of the antarctic ice sheet from 1992 to 2017. *Nature*, *558*(77097709), 219–222. https://doi.org/10.1038/s41586-018-0179-y

IMBIE Team, T. (2020). Mass balance of the greenland ice sheet from 1992 to 2018. *Nature*, *579*(77987798), 233–239. https://doi.org/10.1038/s41586-019-1855-2

Jaiser, R., Nakamura, T., Handorf, D., Dethloff, K., Ukita, J., & Yamazaki, K. (2016). Atmospheric winter response to arctic sea ice changes in reanalysis data and model simulations. *Journal of Geophysical Research: Atmospheres*, *121*(13), 7564–7577. https://doi.org/10.1002/2015JD024679

Joughin, I., Das, S. B., King, M. A., Smith, B. E., Howat, I. M., & Moon, T. (2008). Seasonal speedup along the western flank of the greenland ice sheet. *Science*, *320*(5877), 781–783. https://doi.org/10.1126/science.1153288

Kawase, H., Yoshikane, T., Hara, M., Ailikun, B., Kimura, F., & Yasunari, T. (2008). Downscaling of the climatic change in the mei-yu rainband in east asia by a pseudo climate simulation method. *SOLA*, *4*, 73–76. https://doi.org/10.2151/sola.2008-019

Kawase, H., Yoshikane, T., Hara, M., Kimura, F., Yasunari, T., Ailikun, B., Ueda, H., & Inoue, T. (2009). Intermodel variability of future changes in the baiu rainband estimated by the pseudo global warming downscaling method. *Journal of Geophysical Research*, *114*(D24), D24110. https://doi.org/10.1029/2009JD011803

Kelleher, M. E., Ayarzagüena, B., & Screen, J. A. (2020). Interseasonal connections between the timing of the stratospheric final warming and arctic sea ice.

Journal of Climate, *33*(8), 3079–3092. https://doi.org/10.1175/JCLI-D-19-0064.1

Khan, S. A., Aschwanden, A., Bjørk, A. A., Wahr, J., Kjeldsen, K. K., & Kjær, K. H. (2015). Greenland ice sheet mass balance: A review. *Reports on Progress in Physics*, *78*(4), 046801. https://doi.org/10.1088/0034-4885/78/4/046801

Khan, S. A., Kjær, K. H., Bevis, M., Bamber, J. L., Wahr, J., Kjeldsen, K. K., Bjørk, A. A., Korsgaard, N. J., Stearns, L. A., van den Broeke, M. R., Liu, L., Larsen, N. K., & Muresan, I. S. (2014). Sustained mass loss of the northeast greenland ice sheet triggered by regional warming. *Nature Climate Change*, *4*(4), 292–299. https://doi.org/10.1038/nclimate2161

Kidston, J., Taschetto, A. S., Thompson, D. W. J., & England, M. H. (2011). The influence of southern hemisphere sea-ice extent on the latitude of the mid-latitude jet stream. *Geophysical Research Letters*, *38*(15). https://doi.org/10.1029/2011GL048056

Kim, B.-M., Son, S.-W., Min, S.-K., Jeong, J.-H., Kim, S.-J., Zhang, X., Shim, T., & Yoon, J.-H. (2014). Weakening of the stratospheric polar vortex by arctic sea-ice loss. *Nature Communications*, *5*(1), 4646. https://doi.org/10.1038/ncomms5646

Kimura, F., & Kitoh, A. (2007). Downscaling by pseudo global warming method. *The Final Report of ICCAP*, *4346*.

Kjeldsen, K. K., Korsgaard, N. J., Bjørk, A. A., Khan, S. A., Box, J. E., Funder, S., Larsen, N. K., Bamber, J. L., Colgan, W., van den Broeke, M., Siggaard-Andersen, M.-L., Nuth, C., Schomacker, A., Andresen, C. S., Willerslev, E., & Kjær, K. H. (2015). Spatial and temporal distribution of mass loss from the greenland ice sheet since ad 1900. *Nature*, *528*(7582), 396–400. https://doi.org/10.1038/nature16183

Klingaman, N. P., Hanson, B., & Leathers, D. J. (2008). A teleconnection between forced great plains snow cover and european winter climate. *Journal of Climate*, *21*(11), 2466–2483. https://doi.org/10.1175/2007JCLI1672.1

Kohonen, T. (1990). The self-organizing map. *Proceedings of the IEEE*, *78*(9), 1464–1480. https://doi.org/10.1109/5.58325

Kornhuber, K., & Tamarin-Brodsky, T. (2021). Future changes in northern hemisphere summer weather persistence linked to projected arctic warming. *Geophysical Research Letters*, *48*(4), e2020GL091603. https://doi.org/10.1029/2020GL091603

Lackmann, G. M. (2015). Hurricane sandy before 1900 and after 2100. *Bulletin of the American Meteorological Society*, *96*(4), 547–560. https://doi.org/10.1175/BAMS-D-14-00123.1

Lefebre, F., Fettweis, X., Gallée, H., Van Ypersele, J.-P., Marbaix, P., Greuell, W., & Calanca, P. (2005). Evaluation of a high-resolution regional climate simulation over greenland. *Climate Dynamics*, *25*(1), 99–116. https://doi.org/10.1007/s00382-005-0005-8

Lejenäs, H., & Økland, H. (1983). Characteristics of northern hemisphere blocking as determined from a long time series of observational data. *Tellus A*, *35A*(5), 350–362. https://doi.org/https://doi.org/10.1111/j.1600-0870.1983.tb00210.x

Lenaerts, J. T. M., Medley, B., van den Broeke, M. R., & Wouters, B. (2019). Observing and modeling ice sheet surface mass balance. *Reviews of Geophysics*, *57*(2), 376–420. https://doi.org/https://doi.org/10.1029/2018RG000622

Liptak, J., & Strong, C. (2014). The winter atmospheric response to sea ice anomalies in the barents sea. *Journal of Climate*, *27*(2), 914–924. https://doi.org/10.1175/JCLI-D-13-00186.1

Liu, C., & Barnes, E. A. (2015). Extreme moisture transport into the arctic linked to rossby wave breaking: Extreme moisture flux and wave breaking. *Journal of Geophysical Research: Atmospheres*, *120*(9), 3774–3788. https://doi.org/10.1002/2014JD022796

Liu, J., Chen, Z., Francis, J., Song, M., Mote, T., & Hu, Y. (2016). Has arctic sea ice loss contributed to increased surface melting of the greenland ice sheet? *Journal of Climate*, *29*(9), 3373–3386. https://doi.org/10.1175/JCLI-D-15-0391.1

Luo, D. (2005). A barotropic envelope rossby soliton model for block-eddy interaction. part i: Effect of topography. *Journal of the Atmospheric Sciences*, *62*(1), 5–21. https://doi.org/10.1175/1186.1

Luo, D., & Yao, Y. (2014). On the blocking flow patterns in the euro-atlantic sector: A simple model study. *Advances in Atmospheric Sciences*, *31*(5), 1181–1196. https://doi.org/10.1007/s00376-014-3197-1

Mankoff, K. D., Colgan, W., Solgaard, A., Karlsson, N. B., Ahlstrøm, A. P., As, D. V., Box, J. E., Khan, S. A., Kjeldsen, K. K., Mouginot, J., & Fausto, R. S. (2019). Greenland ice sheet solid ice discharge from 1986 through 2017. *Earth System Science Data*, *11*(2), 769–786. https://doi.org/10.5194/essd-11-769-2019

Markus, T., Stroeve, J. C., & Miller, J. (2009). Recent changes in arctic sea ice melt onset, freezeup, and melt season length. *Journal of Geophysical Research: Oceans*, *114*(C12). https://doi.org/10.1029/2009JC005436

Masato, G., Hoskins, B. J., & Woollings, T. (2013). Winter and summer northern hemisphere blocking in cmip5 models. *Journal of Climate*, (18), 7044–7059. https://doi.org/10.1175/JCLI-D-12-00466.1

Matsumura, S., & Yamazaki, K. (2012). Eurasian subarctic summer climate in response to anomalous snow cover. *Journal of Climate*, *25*(4), 1305–1317. https://doi.org/10.1175/2011JCLI4116.1

Matsumura, S., Yamazaki, K., & Tokioka, T. (2010). Summertime land-atmosphere interactions in response to anomalous springtime snow cover in northern eurasia. *Journal of Geophysical Research: Atmospheres*, *115*(D20). https://doi.org/10.1029/2009JD012342

Matsumura, S., Zhang, X., & Yamazaki, K. (2014). Summer arctic atmospheric circulation response to spring eurasian snow cover and its possible linkage to accelerated sea ice decrease. *Journal of Climate*, *27*(17), 6551–6558. https://doi.org/10.1175/JCLI-D-13-00549.1

Mattingly, K. S., Mote, T. L., & Fettweis, X. (2018). Atmospheric river impacts on greenland ice sheet surface mass balance. *Journal of Geophysical Research: Atmospheres*, *123*(16), 8538–8560. https://doi.org/10.1029/2018JD028714

Mattingly, K. S., Mote, T. L., Fettweis, X., van As, D., Van Tricht, K., Lhermitte, S., Pettersen, C., & Fausto, R. S. (2020). Strong summer atmospheric rivers trigger greenland ice sheet melt through spatially varying surface energy balance and cloud regimes. *Journal of Climate*, *33*(16), 6809–6832. https://doi.org/10.1175/JCLI-D-19-0835.1

Mattingly, K. S., Ramseyer, C. A., Rosen, J. J., Mote, T. L., & Muthyala, R. (2016). Increasing water vapor transport to the greenland ice sheet revealed using self-organizing maps. *Geophysical Research Letters*, *43*(17), 9250–9258. https://doi.org/https://doi.org/10.1002/2016GL070424

McKenna, C. M., Bracegirdle, T. J., Shuckburgh, E. F., Haynes, P. H., & Joshi, M. M. (2018). Arctic sea ice loss in different regions leads to contrasting

northern hemisphere impacts. *Geophysical Research Letters*, *45*(2), 945–954. https://doi.org/10.1002/2017GL076433

McLeod, J. T., Ballinger, T. J., & Mote, T. L. (2018). Assessing the climatic and environmental impacts of mid-tropospheric anticyclones over alaska. *International Journal of Climatology*, *38*(1), 351–364. https://doi.org/https://doi.org/10.1002/joc.5180

McLeod, J. T., & Mote, T. L. (2015). Assessing the role of precursor cyclones on the formation of extreme greenland blocking episodes and their impact on summer melting across the greenland ice sheet. *Journal of Geophysical Research: Atmospheres*, *120*(24), 12357–12377. https://doi.org/https://doi.org/10.1002/2015JD023945

McLeod, J. T., & Mote, T. L. (2016). Linking interannual variability in extreme greenland blocking episodes to the recent increase in summer melting across the greenland ice sheet: Extreme greenland blocking and summer melting across the greenland ice sheet. *International Journal of Climatology*, *36*(3), 1484–1499. https://doi.org/10.1002/joc.4440

Meese, D. A., Gow, A. J., Grootes, P., Mayewski, P. A., Ram, M., Stuiver, M., Taylor, K. C., Waddington, E. D., & Zielinski, G. A. (1994). The accumulation record from the gisp2 core as an indicator of climate change throughout the holocene. *Science*, *266*(5191), 1680–1682.

Miljković, D. (2017). Brief review of self-organizing maps. *2017 40th International Convention on Information and Communication Technology, Electronics and Microelectronics (MIPRO)*, 1061–1066. https://doi.org/10.23919/MIPRO.2017.7973581

Mote, T. L. (1998). Mid-tropospheric circulation and surface melt on the greenland ice sheet. part i: Atmospheric teleconnections. *International Journal*

of Climatology, *18*(2), 111–129. https://doi.org/10.1002/(SICI)1097-0088(199802)18:2<111::AID-JOC227>3.0.CO;2-X

Mote, T. L. (2007). Greenland surface melt trends 1973–2007: Evidence of a large increase in 2007. *Geophysical Research Letters*, *34*(22). https://doi.org/10.1029/2007GL031976

Mote, T. L. (2008). On the role of snow cover in depressing air temperature. *Journal of Applied Meteorology and Climatology*, *47*(7), 2008–2022. https://doi.org/10.1175/2007JAMC1823.1

Mote, T. L. (2014). Measures greenland surface melt daily 25km ease-grid 2.0, version 1 [itemType: dataset]. *NASA National Snow and Ice Data Center Distributed Active Archive Center.* https://doi.org/doi:https://doi.org/10.5067/MEASURES/CRYOSPHERE/nsidc-0533.001.

Mouginot, J., Rignot, E., Bjørk, A. A., van den Broeke, M. R., Millan, R., Morlighem, M., Noël, B., Scheuchl, B., & Wood, M. (2019). Forty-six years of greenland ice sheet mass balance from 1972 to 2018. *Proceedings of the National Academy of Sciences*, *116*(19), 9239–9244. https://doi.org/10.1073/pnas.1904242116

Mullen, S. L. (1987). Transient eddy forcing of blocking flows. *Journal of the Atmospheric Sciences*, *44*(1), 3–22. https://doi.org/10.1175/1520-0469(1987)044<0003:TEFOBF>2.0.CO;2

Nakamura, H. (1994). Rotational evolution of potential vorticity associated with a strong blocking flow configuration over europe. *Geophysical Research Letters*, *21*(18), 2003–2006. https://doi.org/10.1029/94GL01614

Nakamura, N., & Huang, C. S. Y. (2018). Atmospheric blocking as a traffic jam in the jet stream. *Science*, *361*(6397), 42–47. https://doi.org/10.1126/science.aat0721

Neff, W. (2018). Atmospheric rivers melt greenland. *Nature Climate Change*, *8*(10), 857–858. https://doi.org/10.1038/s41558-018-0297-4

Neff, W., Compo, G. P., Martin Ralph, F., & Shupe, M. D. (2014). Continental heat anomalies and the extreme melting of the greenland ice surface in 2012 and 1889: Melting of greenland in 1889 and 2012. *Journal of Geophysical Research: Atmospheres*, *119*(11), 6520–6536. https://doi.org/10.1002/2014JD021470

Nghiem, S. V., Hall, D. K., Mote, T. L., Tedesco, M., Albert, M. R., Keegan, K., Shuman, C. A., DiGirolamo, N. E., & Neumann, G. (2012). The extreme melt across the greenland ice sheet in 2012. *Geophysical Research Letters*, *39*(20). https://doi.org/10.1029/2012GL053611

Noël, B., Berg, W. J. v. d., Lhermitte, S., & van den Broeke, M. R. (2019). Rapid ablation zone expansion amplifies north greenland mass loss. *Science Advances*, *5*(9), eaaw0123. https://doi.org/10.1126/sciadv.aaw0123

Noël, B., Fettweis, X., van de Berg, W. J., van den Broeke, M. R., & Erpicum, M. (2014). Sensitivity of greenland ice sheet surface mass balance to perturbations in sea surface temperature and sea ice cover: A study with the regional climate model mar. *The Cryosphere*, *8*(5), 1871–1883. https://doi.org/10.5194/tc-8-1871-2014

Noël, B., van de Berg, W. J., Lhermitte, S., Wouters, B., Machguth, H., Howat, I., Citterio, M., Moholdt, G., Lenaerts, J. T. M., & van den Broeke, M. R. (2017). A tipping point in refreezing accelerates mass loss of greenland's glaciers and ice caps. *Nature Communications*, *8*(11), 14730. https://doi.org/10.1038/ncomms14730

Noël, B., van Kampenhout, L., Lenaerts, J. T. M., van de Berg, W. J., & van den Broeke, M. R. (2021). A 21st century warming threshold for sus-

tained greenland ice sheet mass loss. *Geophysical Research Letters*, *48*(5), e2020GL090471. https://doi.org/10.1029/2020GL090471

Ogi, M., & Wallace, J. M. (2007). Summer minimum arctic sea ice extent and the associated summer atmospheric circulation. *Geophysical Research Letters*, *34*(12). https://doi.org/10.1029/2007GL029897

Oliver, H., Luo, H., Castelao, R. M., Dijken, G. L. v., Mattingly, K. S., Rosen, J. J., Mote, T. L., Arrigo, K. R., Rennermalm, Å. K., Tedesco, M., & Yager, P. L. (2018). Exploring the potential impact of greenland meltwater on stratification, photosynthetically active radiation, and primary production in the labrador sea. *Journal of Geophysical Research: Oceans*, *123*(4), 2570–2591. https://doi.org/10.1002/2018JC013802

Overland, J. E., Ballinger, T. J., Cohen, J., Francis, J. A., Hanna, E., Jaiser, R., Kim, B.-M., Kim, S.-J., Ukita, J., Vihma, T., Wang, M., & Zhang, X. (2021). How do intermittency and simultaneous processes obfuscate the arctic influence on midlatitude winter extreme weather events? *Environmental Research Letters*, *16*(4), 043002. https://doi.org/10.1088/1748-9326/abdb5d

Overland, J. E., Francis, J. A., Hall, R., Hanna, E., Kim, S.-J., & Vihma, T. (2015). The melting arctic and midlatitude weather patterns: Are they connected? *Journal of Climate*, *28*(20), 7917–7932. https://doi.org/10.1175/JCLI-D-14-00822.1

Overland, J. E., Francis, J. A., Hanna, E., & Wang, M. (2012). The recent shift in early summer arctic atmospheric circulation. *Geophysical Research Letters*, *39*(19), L19804. https://doi.org/10.1029/2012GL053268

Overland, J. E., & Wang, M. (2018). Resolving future arctic/midlatitude weather connections. *Earth's Future*, *6*(8), 1146–1152. https://doi.org/10.1029/2018EF000901

Paradise, A., Rocha, C. B., Barpanda, P., & Nakamura, N. (2019). Blocking statistics in a varying climate: Lessons from a “traffic jam” model with pseudostochastic forcing. *Journal of the Atmospheric Sciences*, *76*(10), 3013–3027. https://doi.org/10.1175/JAS-D-19-0095.1

Pedersen, R. A., & Christensen, J. H. (2019). Attributing greenland warming patterns to regional arctic sea ice loss. *Geophysical Research Letters*, *46*(17–18), 10495–10503. https://doi.org/10.1029/2019GL083828

Pelly, J. L., & Hoskins, B. J. (2003). A New Perspective on Blocking [Publisher: American Meteorological Society]. *Journal of the Atmospheric Sciences*, *60*(5), 743–755. https://doi.org/10.1175/1520-0469(2003)060<0743:ANPOB>2.0.CO;2

Perkins, S. E., Alexander, L. V., & Nairn, J. R. (2012). Increasing frequency, intensity and duration of observed global heatwaves and warm spells. *Geophysical Research Letters*, *39*(20). https://doi.org/10.1029/2012GL053361

Petoukhov, V., & Semenov, V. A. (2010). A link between reduced barents-kara sea ice and cold winter extremes over northern continents. *Journal of Geophysical Research: Atmospheres*, *115*(D21). https://doi.org/10.1029/2009JD013568

Petrie, R. E., Shaffrey, L. C., & Sutton, R. T. (2015). Atmospheric response in summer linked to recent arctic sea ice loss. *Quarterly Journal of the Royal Meteorological Society*, *141*(691), 2070–2076. https://doi.org/10.1002/qj.2502

Pfahl, S., Schwierz, C., Croci-Maspoli, M., Grams, C. M., & Wernli, H. (2015). Importance of latent heat release in ascending air streams for atmospheric blocking. *Nature Geoscience*, *8*(88), 610–614. https://doi.org/10.1038/ngeo2487

Pithan, F., & Mauritsen, T. (2014). Arctic amplification dominated by temperature feedbacks in contemporary climate models. *Nature Geoscience*, *7*(3), 181–184. https://doi.org/10.1038/ngeo2071

Preece, J. R., Wachowicz, L. J., Mote, T. L., Tedesco, M., & Fettweis, X. (2022). Summer greenland blocking diversity and its impact on the surface mass balance of the greenland ice sheet. *Journal of Geophysical Research: Atmospheres*, *127*(4), e2021JD035489. https://doi.org/10.1029/2021JD035489

Rajewicz, J., & Marshall, S. J. (2014). Variability and trends in anticyclonic circulation over the greenland ice sheet, 1948-2013: Rajewicz and marshall: Atmospheric circulation over greenland. *Geophysical Research Letters*, *41*(8), 2842–2850. https://doi.org/10.1002/2014GL059255

Rantanen, M., Karpechko, A. Y., Lipponen, A., Nordling, K., Hyvärinen, O., Ruosteenoja, K., Vihma, T., & Laaksonen, A. (2022). The arctic has warmed nearly four times faster than the globe since 1979. *Communications Earth & Environment*, *3*(11), 1–10. https://doi.org/10.1038/s43247-022-00498-3

Rasmussen, R., Liu, C., Ikeda, K., Gochis, D., Yates, D., Chen, F., Tewari, M., Barlage, M., Dudhia, J., Yu, W., Miller, K., Arsenault, K., Grubišić, V., Thompson, G., & Gutmann, E. (2011). High-resolution coupled climate runoff simulations of seasonal snowfall over colorado: A process study of current and warmer climate. *Journal of Climate*, *24*(12), 3015–3048. https://doi.org/10.1175/2010JCLI3985.1

Rennermalm, A. K., Smith, L. C., Stroeve, J. C., & Chu, V. W. (2009). Does sea ice influence greenland ice sheet surface-melt? *Environmental Research Letters*, *4*(2), 024011. https://doi.org/10.1088/1748-9326/4/2/024011

Reusch, D. B., Alley, R. B., & Hewitson, B. C. (2005). Relative performance of self-organizing maps and principal component analysis in pattern extraction

from synthetic climatological data. *Polar Geography*, *29*(3), 188–212. https://doi.org/10.1080/789610199

Rignot, E., & Kanagaratnam, P. (2006). Changes in the velocity structure of the greenland ice sheet. *Science*, *311*(5763), 986–990. https://doi.org/10.1126/science.1121381

Robinson, D. A., Estilow, T. W., & Program, N. C. D. R. (2012). Noaa climate data record (cdr) of northern hemisphere (nh) snow cover extent (sce), version 1 [DOI: 10.7289/V5N014G9]. *NOAA National Centers for Environmental Information*. https://doi.org/10.7289/V5N014G9

Rogers, J. C., Bathke, D. J., Mosley-Thompson, E., & Wang, S.-H. (2004). Atmospheric circulation and cyclone frequency variations linked to the primary modes of greenland snow accumulation. *Geophysical Research Letters*, *31*(23). https://doi.org/https://doi.org/10.1029/2004GL021048

Saito, K., Cohen, J., & Entekhabi, D. (2001). Evolution of atmospheric response to early-season eurasian snow cover anomalies. *Monthly Weather Review*, *129*(11), 2746–2760. https://doi.org/10.1175/1520-0493(2001)129<2746:EOARTE>2.0.CO;2

Schär, C., Frei, C., Lüthi, D., & Davies, H. C. (1996). Surrogate climate-change scenarios for regional climate models. *Geophysical Research Letters*, *23*(6), 669–672. https://doi.org/10.1029/96GL00265

Schoof, C. (2010). Ice-sheet acceleration driven by melt supply variability. *Nature*, *468*(7325), 803–806. https://doi.org/10.1038/nature09618

Schuenemann, K. C., Cassano, J. J., & Finnis, J. (2009). Synoptic forcing of precipitation over greenland: Climatology for 1961–99. *Journal of Hydrometeorology*, *10*(1), 60–78. https://doi.org/10.1175/2008JHM1014.1

Screen, J. A. (2013). Influence of arctic sea ice on european summer precipitation. *Environmental Research Letters*, *8*(4), 044015. https://doi.org/10.1088/1748-9326/8/4/044015

Screen, J. A. (2017). Simulated atmospheric response to regional and pan-arctic sea ice loss. *Journal of Climate*, *30*(11), 3945–3962. https://doi.org/10.1175/JCLI-D-16-0197.1

Screen, J. A., & Simmonds, I. (2010). The central role of diminishing sea ice in recent arctic temperature amplification. *Nature*, *464*(72937293), 1334–1337. https://doi.org/10.1038/nature09051

Screen, J. A., & Simmonds, I. (2013). Exploring links between arctic amplification and mid-latitude weather. *Geophysical Research Letters*, *40*(5), 959–964. https://doi.org/10.1002/grl.50174

Screen, J. A., Simmonds, I., Deser, C., & Tomas, R. (2013). The atmospheric response to three decades of observed arctic sea ice loss. *Journal of Climate*, *26*(4), 1230–1248. https://doi.org/10.1175/JCLI-D-12-00063.1

Serreze, M. C., & Barry, R. G. (2011). Processes and impacts of arctic amplification: A research synthesis. *Global and Planetary Change*, *77*(1–2), 85–96. https://doi.org/10.1016/j.gloplacha.2011.03.004

Shea, D., Hurrell, J., & Phillips, A. (2020). Merged hadley-oi sea surface temperature and sea ice concentration data set. https://doi.org/10.5065/R33V-SV91

Sheridan, S. C., & Lee, C. C. (2011). The self-organizing map in synoptic climatological research. *Progress in Physical Geography: Earth and Environment*, *35*(1), 109–119. https://doi.org/10.1177/0309133310397582

Shi, N., & Nakamura, H. (2021). A new detection scheme of wave-breaking events with blocking flow configurations. *Journal of Climate*, *34*(4), 1467–1483. https://doi.org/10.1175/JCLI-D-20-0037.1

Slater, T., Hogg, A. E., & Mottram, R. (2020). Ice-sheet losses track high-end sea-level rise projections. *Nature Climate Change*, *10*(1010), 879–881. https://doi.org/10.1038/s41558-020-0893-y

Smith, B., Fricker, H. A., Gardner, A. S., Medley, B., Nilsson, J., Paolo, F. S., Holschuh, N., Adusumilli, S., Brunt, K., Csatho, B., Harbeck, K., Markus, T., Neumann, T., Siegfried, M. R., & Zwally, H. J. (2020). Pervasive ice sheet mass loss reflects competing ocean and atmosphere processes. *Science*, *368*(6496), 1239–1242. https://doi.org/10.1126/science.aaz5845

Steinfeld, D., & Pfahl, S. (2019). The role of latent heating in atmospheric blocking dynamics: A global climatology. *Climate Dynamics*, *53*(9), 6159–6180. https://doi.org/10.1007/s00382-019-04919-6

Stroeve, J. C., Mioduszewski, J. R., Rennermalm, A., Boisvert, L. N., Tedesco, M., & Robinson, D. (2017). Investigating the local-scale influence of sea ice on greenland surface melt. *The Cryosphere*, *11*(5), 2363–2381. https://doi.org/https://doi.org/10.5194/tc-11-2363-2017

Stroeve, J. C., & Notz, D. (2018). Changing state of arctic sea ice across all seasons. *Environmental Research Letters*, *13*(10), 103001. https://doi.org/10.1088/1748-9326/aade56

Stroeve, J. C., Serreze, M. C., Holland, M. M., Kay, J. E., Malanik, J., & Barrett, A. P. (2012). The arctic's rapidly shrinking sea ice cover: A research synthesis. *Climatic Change*, *110*(3–4), 1005–1027. https://doi.org/10.1007/s10584-011-0101-1

Sun, L., Deser, C., & Tomas, R. A. (2015). Mechanisms of stratospheric and tropospheric circulation response to projected arctic sea ice loss. *Journal of Climate*, *28*(19), 7824–7845. https://doi.org/10.1175/JCLI-D-15-0169.1

Takaya, K., & Nakamura, H. (2001). A Formulation of a Phase-Independent Wave-Activity Flux for Stationary and Migratory Quasigeostrophic Eddies on a

Zonally Varying Basic Flow [Publisher: American Meteorological Society]. *Journal of the Atmospheric Sciences*, *58*(6), 608–627. https://doi.org/10.1175/1520-0469(2001)058<0608:AFOAPI>2.0.CO;2

Tedesco, M., Fettweis, X., van den Broeke, M. R., van de Wal, R. S. W., Smeets, C. J. P. P., van de Berg, W. J., Serreze, M. C., & Box, J. E. (2011). The role of albedo and accumulation in the 2010 melting record in greenland. *Environmental Research Letters*, *6*(1), 014005. https://doi.org/10.1088/1748-9326/6/1/014005

Tedesco, M., & Fettweis, X. (2020). Unprecedented atmospheric conditions (1948-2019) drive the 2019 exceptional melting season over the greenland ice sheet. *Cryosphere*, *14*, 1209–1223. https://doi.org/10.5194/tc-14-1209-2020

Tedesco, M., Mote, T., Fettweis, X., Hanna, E., Jeyaratnam, J., Booth, J. F., Datta, R., & Briggs, K. (2016). Arctic cut-off high drives the poleward shift of a new greenland melting record. *Nature Communications*, *7*(1), 11723. https://doi.org/10.1038/ncomms11723

Thompson, D. W. J., & Wallace, J. M. (1998). The arctic oscillation signature in the wintertime geopotential height and temperature fields. *Geophysical Research Letters*, *25*(9), 1297–1300. https://doi.org/10.1029/98GL00950

Tibaldi, S., & Molteni, F. (1990). On the operational predictability of blocking. *Tellus A*, *42*(3), 343–365. https://doi.org/https://doi.org/10.1034/j.1600-0870.1990.t01-2-00003.x

Trusel, L. D., Das, S. B., Osman, M. B., Evans, M. J., Smith, B. E., Fettweis, X., McConnell, J. R., Noël, B. P. Y., & van den Broeke, M. R. (2018). Nonlinear rise in greenland runoff in response to post-industrial arctic warming. *Nature*, *564*(7734), 104–108. https://doi.org/10.1038/s41586-018-0752-4

Tyrlis, E., & Hoskins, B. J. (2008). Aspects of a northern hemisphere atmospheric blocking climatology. *Journal of the Atmospheric Sciences*, *65*(5), 1638–1652. https://doi.org/10.1175/2007JAS2337.1

Tyrlis, E., Bader, J., Manzini, E., & Matei, D. (2021). Reconciling different methods of high-latitude blocking detection. *Quarterly Journal of the Royal Meteorological Society*, *147*(735), 1070–1096. https://doi.org/10.1002/qj.3960

van den Broeke, M. R., Bamber, J., Ettema, J., Rignot, E., Schrama, E., Berg, W. J. v. d., Meijgaard, E. v., Velicogna, I., & Wouters, B. (2009a). Partitioning recent greenland mass loss. *Science*, *326*(5955), 984–986. https://doi.org/10.1126/science.1178176

van den Broeke, M. R., Box, J., Fettweis, X., Hanna, E., Noël, B., Tedesco, M., van As, D., van de Berg, W. J., & van Kampenhout, L. (2017). Greenland ice sheet surface mass loss: Recent developments in observation and modeling. *Current Climate Change Reports*, *3*(4), 345–356. https://doi.org/10.1007/s40641-017-0084-8

van den Broeke, M. R., & Gallée, H. (1996). Observation and simulation of barrier winds at the western margin of the greenland ice sheet. *Quarterly Journal of the Royal Meteorological Society*, *122*(534), 1365–1383. https://doi.org/10.1002/qj.49712253407

van den Broeke, M. R., Smeets, P., & Ettema, J. (2009b). Surface layer climate and turbulent exchange in the ablation zone of the west greenland ice sheet. *International Journal of Climatology*, *29*(15), 2309–2323. https://doi.org/10.1002/joc.1815

van Angelen, J. H., van den Broeke, M. R., Wouters, B., & Lenaerts, J. T. M. (2014). Contemporary (1960–2012) evolution of the climate and surface mass balance of the greenland ice sheet. *Surveys in Geophysics*, *35*(5), 1155–1174. https://doi.org/10.1007/s10712-013-9261-z

Vavrus, S. J. (2007). The role of terrestrial snow cover in the climate system. *Climate Dynamics*, *29*(1), 73–88. https://doi.org/10.1007/s00382-007-0226-0

Vavrus, S. J., Wang, F., Martin, J. E., Francis, J. A., Peings, Y., & Cattiaux, J. (2017). Changes in North American Atmospheric Circulation and Extreme Weather: Influence of Arctic Amplification and Northern Hemisphere Snow Cover [Publisher: American Meteorological Society]. *Journal of Climate*, *30*(11), 4317–4333. https://doi.org/10.1175/JCLI-D-16-0762.1

Velicogna, I., Mohajerani, Y., A, G., Landerer, F., Mouginot, J., Noel, B., Rignot, E., Sutterley, T., van den Broeke, M., van Wessem, M., & Wiese, D. (2020). Continuity of ice sheet mass loss in greenland and antarctica from the grace and grace follow-on missions. *Geophysical Research Letters*, *47*(8), e2020GL087291. https://doi.org/10.1029/2020GL087291

Vial, J., & Osborn, T. J. (2012). Assessment of atmosphere-ocean general circulation model simulations of winter northern hemisphere atmospheric blocking. *Climate Dynamics*, *39*(1–2), 95–112. https://doi.org/10.1007/s00382-011-1177-z

Vihma, T. (2014). Effects of arctic sea ice decline on weather and climate: A review. *Surveys in Geophysics*, *35*(5), 1175–1214. https://doi.org/10.1007/s10712-014-9284-0

Wachowicz, L. J., Preece, J. R., Mote, T. L., Barrett, B. S., & Henderson, G. R. (2021). Historical trends of seasonal Greenland blocking under different blocking metrics. *International Journal of Climatology*, *41*(S1), E3263–E3278. https://doi.org/https://doi.org/10.1002/joc.6923

Walsh, J. E., Tucek, D. R., & Peterson, M. R. (1982). Seasonal snow cover and short-term climatic fluctuations over the united states. *Monthly Weather*

Review, *110*(10), 1474–1486. https://doi.org/10.1175/1520-0493(1982)110<1474:SSCAST>2.0.CO;2

Walter, K., Luksch, U., & Fraedrich, K. (2001). A response climatology of idealized midlatitude thermal forcing experiments with and without a storm track. *Journal of Climate*, *14*(4), 467–484. https://doi.org/10.1175/1520-0442(2001)014<0467:ARCOIM>2.0.CO;2

Wang, W., Zender, C. S., & As, D. v. (2018). Temporal characteristics of cloud radiative effects on the greenland ice sheet: Discoveries from multiyear automatic weather station measurements. *Journal of Geophysical Research: Atmospheres*, *123*(20), 11, 348–11, 361. https://doi.org/https://doi.org/10.1029/2018JD028540

Wang, W., Zender, C. S., As, D. v., Fausto, R. S., & Laffin, M. K. (2021). Greenland surface melt dominated by solar and sensible heating. *Geophysical Research Letters*, *48*(7), e2020GL090653. https://doi.org/https://doi.org/10.1029/2020GL090653

Wang, W., Zender, C. S., As, D. v., & Miller, N. B. (2019). Spatial distribution of melt season cloud radiative effects over greenland: Evaluating satellite observations, reanalyses, and model simulations against in situ measurements. *Journal of Geophysical Research: Atmospheres*, *124*(1), 57–71. https://doi.org/10.1029/2018JD028919

Ward, J. L., Flanner, M. G., & Dunn-Sigouin, E. (2020). Impacts of greenland block location on clouds and surface energy fluxes over the greenland ice sheet. *Journal of Geophysical Research: Atmospheres*, *125*(22), e2020JD033172. https://doi.org/https://doi.org/10.1029/2020JD033172

Woollings, T., Barriopedro, D., Methven, J., Son, S.-W., Martius, O., Harvey, B., Sillmann, J., Lupo, A. R., & Seneviratne, S. (2018). Blocking and its re-

sponse to climate change. *Current Climate Change Reports*, *4*(3), 287–300. https://doi.org/10.1007/s40641-018-0108-z

Wu, B., Zhang, R., D'Arrigo, R., & Su, J. (2013). On the relationship between winter sea ice and summer atmospheric circulation over eurasia. *Journal of Climate*, *26*(15), 5523–5536. https://doi.org/10.1175/JCLI-D-12-00524.1

Wu, Y., & Smith, K. L. (2016). Response of northern hemisphere midlatitude circulation to arctic amplification in a simple atmospheric general circulation model. *Journal of Climate*, *29*(6), 2041–2058. https://doi.org/10.1175/JCLI-D-15-0602.1

Xu, L., & Dirmeyer, P. (2011). Snow-atmosphere coupling strength in a global atmospheric model. *Geophysical Research Letters*, *38*(13). https://doi.org/10.1029/2011GL048049

Yao, Y., Luo, D., Dai, A., & Simmonds, I. (2017). Increased quasi stationarity and persistence of winter ural blocking and eurasian extreme cold events in response to arctic warming. part i: Insights from observational analyses. *Journal of Climate*, *30*(10), 3549–3568. https://doi.org/10.1175/JCLI-D-16-0261.1

Yasunari, T., Kitoh, A., & Tokioka, T. (1991). Local and remote responses to excessive snow mass over eurasia appearing in the northern spring and summer climate: A study with the mri gcm. *Journal of the Meteorological Society of Japan. Ser. II*, *69*(4), 473–487. https://doi.org/10.2151/jmsj1965.69.4_473

Zemp, M., Huss, M., Thibert, E., Eckert, N., McNabb, R., Huber, J., Barandun, M., Machguth, H., Nussbaumer, S. U., Gärtner-Roer, I., Thomson, L., Paul, F., Maussion, F., Kutuzov, S., & Cogley, J. G. (2019). Global glacier mass changes and their contributions to sea-level rise from 1961 to 2016. *Nature*, *568*(77527752), 382–386. https://doi.org/10.1038/s41586-019-1071-0